Influence of Fluid Structure Interaction on Human Eye Biomechanics Under Air Puff Non-Contact Tonometry

Osama Mohamed Yousef Maklad

School of Engineering

University of Liverpool

'This Thesis is submitted in accordance with the requirements of the University of Liverpool for the degree of Doctor of Philosophy in Biomechanical Engineering.'

School of Engineering June 2019

I would like to dedicate this thesis to my loving parents, my brothers, my wife, my supervisors and The University of Liverpool.

Declaration

I hereby declare that except where specific reference is made to the work of others, the contents of this dissertation are original and have not been submitted in whole or in part for consideration for any other degree or qualification in this, or any other university. The research was carried out, unless otherwise stated, by the author at school of Engineering at the University of Liverpool between 01/05/2015 and 30/04/2019.

Some parts of this thesis have been published or submitted for publication in the following papers:

- Eliasy A, Chen KJ, Vinciguerra R, Maklad O, et al. Ex-vivo experimental validation of biomechanically-corrected intraocular pressure measurements on human eyes using the CorVis ST. Exp Eye Res. 2018;175(June):98-102. doi:10.1016/j.exer.2018.06.013

- Maklad O, Theofilis V, Elsheikh A. Fluid Structure Interaction (FSI) Simulation of the human eye under the air puff tonometry using Computational Fluid Dynamics (CFD). In: ICCFD10. Barcelona; 2018. http://www.iccfd.org/iccfd10/proceedings.html.

- Maklad O, Theofilis V, Elsheikh A. Role of impinging jets in the biomechanical correction of the intraocular pressure (IOP) measurement. In: ICFD13. Cairo; 2018:ICFD13-EG-6095. http://icfd-egypt.com/index.html.

- Maklad O, Eliasy A, Chen K, Theofilis V, Elsheikh A. Influence of Fluid Structure Interaction (FSI) on Prediction of Corneal Biomechanics under the Effect of Air Puff Tonometry. Journal of the Royal Society Interface. Submitted manuscript 06/03/2019.

- Maklad O, Eliasy A, Chen K, Theofilis V, Elsheikh A. Introducing a new biomechanically corrected IOP and cornea material parameter using Fluid Structure Interaction (FSI) simulation of healthy human eye under the air puff tonometry. Exp Eye Res. Manuscript under internal review.

Osama Mohamed Yousef Maklad

June 2019

Acknowledgements

I would like to acknowledge everyone who assisted me in my journey until i write these words. I am very grateful to Prof. Ahmed Elsheikh for his wonderful support and guidance all the way during my time in the PhD. Also, would like to thank Prof. Vassilis Theofilis for his constructive feedback and generous support. All acknowlegement to the Vincieye Clinic in Milan, Italy and Rio de Janeiro Corneal Tomography and Biomechanics Study Group – Rio de Janeiro, Brazil for permission to work on the clinical data provided. Great appreciation to OCULUS Optikgeräte GmbH for their support with CorVis-ST. Thanks to the great scholars and scientists in the field that motivated me with their academic contributions to finish my study. My appreciation goes to my colleagues Ashkan Eliasy and Kai-Jung Chen for their support and cooperation during all my PhD stages. Thanks to the personal development program at University of Liverpool and the continuous help and support whenever needed. Thanks to Mansoura University for giving me the needed support during my study leave. Last but foremost, my huge thanks go to my family (My parents, brothers and my wife Yasmin Mehanna) for their advices and endless support.

Abstract

Biomechanical properties of biological tissues are important health indicators and multiple clinical decisions and surgical planning can be made based on their dynamic response to loading. But until now, some of the mechanical and dynamic responses are not fully understood due to the non-linearity and viscoelastic behaviour of biological tissues. The relevant biological tissues of interest in the current study are the cornea and sclera of the human ocular globe. Cornea contributes with two thirds of the optical focusing power of the eye beside intraocular lens and ocular fluids. The air puff tonometry test is a non-contact method with direct interaction to cornea in order to estimate the intraocular pressure which helps with early Glaucoma diagnosis. The gab in research of this area is considering the fluid structure interaction effect between cornea, the air puff and the eye internal fluid. Numerical model of the air puff test was constructed in the context of a coupled model between computational fluid dynamics (CFD) and finite element analysis (FEA) using Arbitrary Lagrangian-Eulerian (ALE) deforming mesh. The time span of the jet is 30 ms and maximum Reynolds number ($R_e = 2.3 \times 10^4$), with jet orifice diameter 2.4 mm and impinging distance 11 mm. The present study was the first to take fluid structure interaction between the air puff and cornea into account, in IOP and cornea material behaviour estimations. It was found that pressure distribution and corneal deformations change with different eye biomechanical

parameters and numerical models will have high uncertainty if deformation of the cornea wasn't coupled with the CFD model of the air puff using adaptive deformable mesh.

A clinical dataset of 476 healthy patients from the Vincieye Clinic in Milan, Italy and Rio de Janeiro Corneal Tomography and Biomechanics Study Group were used to validate the numerical fluid structure interaction (FSI) model. A parametric study was done for 110 numerical tests of ocular globe with IOP range of (10:25 mmHg), central corneal thickness (CCT) (445:645 μm), corneal radius (R) (7.4:8.4 mm) and different material properties representing age (stiffening) effect. Analysis of the turbulent air puff model showed the significant effect of fluid structure interaction on air puff pressure distribution and corneal deformations compared to applying the same puff on a rigid, non-deformable, cornea and having a region of negative pressure between 2-4 mm from cornea centre. The parametric study showed that pressure distribution of the air puff is different from model to another based on cornea biomechanical parameters. The parametric study was used to develop an estimation algorithm for intraocular pressure measurement taking into account, fluid structure interaction effect between cornea and the air puff. The new algorithm was validated against the clinical dataset and experimental measurements of true IOP on ex-vivo human eye specimens. An estimation algorithm for corneal material behaviour was also developed to accurately represent the corneal biomechanical behaviour in numerical analysis. The new material estimation algorithm showed good performance when validated against clinical and inverse analysis data.

Keywords: Human eye, Non-Contact Tonometry, Ocular biomechanics, Glaucoma, Intra-Ocular Pressure (IOP), Computational Fluid Dynamics (CFD), Finite Element Analysis (FEA), Fluid Structure Interaction (FSI), Impinging jets, Aeroelasticity, Arbitrary Lagrangian-Eulerian (ALE)

Table of contents

Nomenclature

IOP	Intraocular Pressure
CCT	Central Corneal Thickness
CFD	Computational Fluid Dynamics
FE	Finite Element
FSI	Fluid Structure Interaction
ALE	Arbitrary Lagrangian-Eulerian
$CorVis-ST$	Corneal Visualisation Scheimpflug Technology
ORA	Ocular Response Analyser
CF	Concentrated Force
U_R	Reduced Velocity
D	Displacement number
$\bar{q}$	Solid displacement
$\bar{f}$	Loads causing solid deformations
$\tilde{U}$	Fluid velocity
$\phi(x)$	Shape function
C_Y	Cauchy number
$\tilde{p}$	Pressure forces on the fluid
R_E	Reynolds number
F_R	Froude number
$\tilde{\nu}$	Kinematic turbulent eddy viscosity
HCR	Highest Concavity Radius
PD	Peak Distance
SP	Stiffness Parameter
CDR	Corneal Deformation Response

Chapter 1

Introduction

1.1 Preface

The ocular globe is the most valuable sense organ in the human body. It helps providing three dimensional, coloured and moving image. The human eye can differentiate between

10 million different colours and even is able to detect a single photon [1]. It contains a viscoelastic fluid called vitreous humour which has a pressure that gives the eye its spherical shape called Intraocular pressure (IOP). The IOP is crucial in eye biomechanical analysis and important to understand it in terms of how it is controlled and accurately measured. There are many ocular diseases connected directly or indirectly to IOP, if it is deviated from its normal values. Glaucoma, Ocular Hypertension and Retinal Detachment are examples of these diseases. Glaucoma, for instance, is considered the second cause of blindness in the world [2] and it develops when the eye internal fluid cannot drain properly and the intraocular pressure builds up. This can damage the optic nerve and nerve fibres from the retina (the light-sensitive nerve tissue that lines back of the eye), Figure 1.1. These diseases can be treated with eye drops, laser treatment or surgery, but early diagnosis is highly desired, as any damage to the eye cannot be reversed. There are several comprehensive tests that can be carried out to perform this diagnosis and it is important to do it as early and accurate as possible. The technique used to measure the IOP is called Tonometry, which can be contact or non-contact method.

Goldmann applanation tonometer (GAT) is one of the contact tonometrs and it is considered the gold standard of IOP measurements [3, 2, 4]. It depends on applying contact force to flaten the front part of the cornea and relate between the applied force and intraocular pressure. This technique was found to be affected by corneal material stiffness, central thickness of the cornea and corneal curvature which are different between patients [5, 6].

The air puff test is one of the non-contact tonometry techniques which uses a rapid jet of air to deform the cornea in order to estimate the value of intraocular pressure and measure the mechanical reponse of corneal material. The air puff test is commonly used nowadays, since it's easy to use and non-invasive. Studying the dynamic deformation following an air-puff has recently been proposed in different biomedical areas (skin [7], bacteria [8], cornea [9], soft tissue tumours [10]) to noninvasively assess biomechanical properties. In most cases

the degree of deformation of the sample is empirically related to mechanical parameters. A major limitation with the air puff tonometry technique is the lack of consideration of fluid structure interaction effect between air puff and the cornea. These changes are not likely to be uniform due to the viscoelastic properties of the cornea and intra-ocular fluid.

1.2 Background

In ophthalmology, ocular biomechanics are essential for basic research, clinical evaluation, prognosis and treatment [11, 12]. The demand for measuring biomechanical properties of biological tissue in-vivo and non-invasively is high, because tissue biomechanics play a key role in a wide range of diseases' diagnosis as a health indicator. Biomechanical properties are also indicative of muscle function and the effects of disease, wound healing, ageing or cosmetics [11].

1.2.1 Cornea Biomechanics

Cornea is the dome-shaped clear surface that covers front of the eye with typical diameter of 11.5 mm. It allows the light to enter to back of the eye through the transparent liquid filling the eye and through the intra-ocular lens. The cornea plays a vital role in the focusing power of the eye as it contributes with 65 to 75 % of the refractive power [13].

The cornea consists of five different layers, [14] as shown in Figure 1.1:

- The Epithelium: It is the outer layer of the cornea and is filled with a large number of small nerve endings which hurts if any dust or foreign material tried to enter the eye. Also, it absorbs the nutrients and oxygen from tears to deliver it to the other cornea layers. It measures about 50 microns which is 5 to 7 cells thick [14].

- Bowman's membrane: The adjacent layer just after the Epithelium is composed of collagen fibres. If it's injured, it may leave a scar behind after it heals and might cause a vision loss if it's centrally located. It's a thin layer of about 8 to 14 microns [14].

- Stroma Layer: It's the thickest layer of the cornea and it gives the cornea most of its elasticity and strength. Water and collagen fibres are the main constituents of the stroma. The micro structure and arrangement of the collagen greatly affects the biomechanical properties of cornea and the light transparency. It has a thickness of, approximately, a half millimetre which is about 90% of corneal thickness [14].

- Descemet's membrane: It's a thin but strong membrane and works as a protective shield against injuries and infections. It heals easily if been injured. Its thickness changes with age from 5 microns in children to 15 microns in older adults [14].

- Endothelium layer: It is the layer exactly adjacent to the aqueous humour liquid and measures about 5 microns which is one layer of cells only. It has an important job to pump any excess fluid that might leak into the stroma. If it failed to pump properly, the stroma might become opaque and swell with water [14].

Functional response of cornea and ocular vision, are greatly influenced by biomechanics of the cornea. The viscoelastic properties of cornea are given by its physical composition, which has a mixture between behaviour of soft elastic material and high viscous fluids. This mixed behaviour gives the cornea, hysteresis effect which is a history effect or time delay that cornea experience when regaining the original shape after stress unloading. Structural integrity of the cornea can be affected by any corneal disease or after refractive surgeries if the collagen fibre network is disrupted which will lead to vision distortion [15]. Corneal ectasia and Keratoconus are examples of these pathologies and early detection of corneas at risk is an important decision before any surgery. This is done through eye tests and cornea imaging.

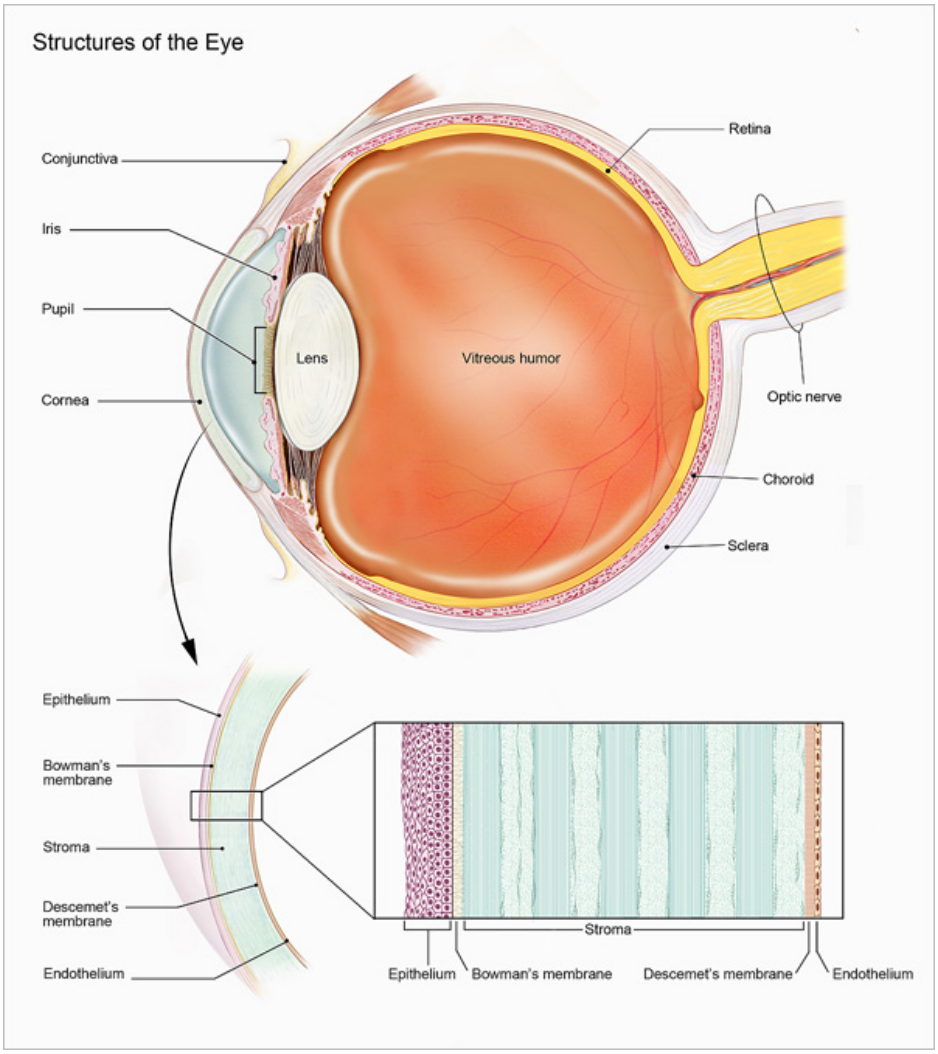

Figure 1.1 Human Eye and Cornea structure [14]

Keratoconus is a progressive disease associated with irregularities in the fibre network and conical protrusion causing astigmatism and high myopia. The techniques which were developed to measure mechanical properties of the cornea are classified to be in-vivo non destructive testing and ex-vivo destructive testing.

In-vivo non destructive testing

There are several techniques and methods that were tested to measure the corneal biomechanical properties in-vivo and the application of these techniques is different from device to another.

In-vivo methods have the advantage of avoiding error of removing the ocular tissue from its working environment, but on the other hand, they have a lot of limitations on the tools that can be used and the scope of investigation [16–18]. The Ocular Response Analyser (ORA; Reichert, Inc., Buffalo, NY) [19, 20] and the CorVis-ST (Oculus Optikgerate GmbH, Wetzlar, Germany) [21], are the most common devices to give direct analysis of biomechanical properties of the cornea and they are under research and development to give better understanding of corneal behaviour which will assist in diagnosing many diseases such as corneal Ectasia or Keratoconus and help in ocular surgical planning. They depend on a puff of air to deform the cornea and at the same time an infra-red beam or Scheimpflug imaging monitor shape of the cornea at forward and backward applanation times. A lot of valuable information can be obtained from analysis of the waveform signal generated by the infrared beam. The difference between pressure forces applied by the air puff at applanation times is the value of the corneal hysteresis (CH). Corneal hysteresis (CH) was reported to change in different disease conditions and after eye refractive surgeries [16–18].

Ex-vivo destructive testing

Many experimental studies were performed on ex-vivo preserved ocular tissues for donated eyes [5, 6, 22–25]. This technique provides more flexibility on performing parametric studies and reduce tools limitations as it was for in-vivo testing, but sacrificing accuracy of the tissue being within the human body and trying to mimic the in-vivo conditions by close experimental set-ups. The information obtained from ex-vivo testing including material properties, loading geometry and boundary conditions will feed into numerical simulations of these particular tissues. Some studies used uniaxial testing on parts of cornea or sclera and some used inflation testing to parts or the whole eye globe [5, 6]. Stretching forces range from tensile testing and measurine the tissue deformation in response to tension or eye

inflation using a pressure system fo internal stresses. The same devices that were applied to the eye in-vivo can be used on the ex-vivo eyes for validation purposes.

1.2.2 Glaucoma

Glaucoma is the disease of irreversible blindness due to build-up of the pressure inside the ocular globe [26, 27]. Accurate measurement of the intraocular pressure (IOP) is essential in management of Glaucoma and diagnosis of other diseases. The two most common types of Glaucoma are Open Angle Glaucoma (OAG) and Angle Closure Glaucoma (ACG). In 2010, more than 44.7 million patients, worldwide, are diseased with OAG and 15.7 million patients with ACG. The numbers are expected to increase in 2020 to 58.6 million OAG patients and 21 million ACG patients, [26–28]. Moreover, large number of patients can have normal IOP values, but have the condition and they are subject to optic nerve damage and gradual sight loss which is known as normal tension Glaucoma (NTG), [29, 30]. Some recent studies looked at the effect of age on stiffness of the cornea and on the IOP measurement as a result, [6, 31, 32]. Statistical studies, using clinical datasets, were carried out to improve the IOP measurement accuracy, [26].

1.2.3 Impinging jet theory

The basic theory of the air puff simulation is the round jet diffusion and impingement theory. Impinging jets have different variety of important applications such as cooling and drying, they are also representative models for the jets in, vertical take-off and landing, aircrafts and rockets or in simulation of the atmospheric microbursts. Flow characteristics of impinging jets depend on different parameters including; jet orifice diameter, nozzle to impingement surface distance, jet confinement, radial distance from stagnation point, angle of impingement, surface curvature & roughness, nozzle exit geometry and turbulence intensity, [33], [34], [35]. The round jet is characterized by the continuous increase of boundary shear layer

thickness. This boundary shear layer has two corresponding factors, decrease of the jet core cross section and increase of the jet diameter as shown in Figure 1.2. The core length depends on the inner angle of diffusion, about 5^o for the jet core and around 8.5^o for the outer jet diameter for highly turbulent impinging jets [36].

Figure 1.2 shows three observed regions from an impinging jet: the “free” jet region; the impingement or stagnation region, and the wall-jet region. Beltaos and Rajaratnam (1973) [36] have studied the free and impinging jet phenomena and provided a detailed experimental and analytical study of plane turbulent impinging jets.

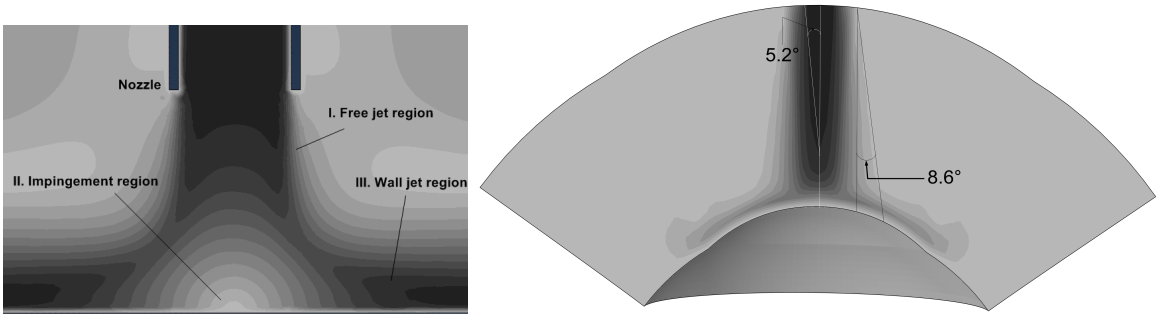

(a) (b)

Figure 1.2 The impinging jet different regions (a), Round impinging jet diffusion (b)

Free jet region

From the name "free", it indicates the remote part of the jet from the wall in which the turbulence is due to the mean velocity fluctuations. The surrounding fluid is entrained or swept along the jet with a flat-topped velocity profile. Miller and Comings (1957) [37] have studied the static pressure distribution and turbulence properties in the free turbulent jets. Sometimes, it is also called the flow establishment region which starts from the nozzle outlet to the potential core apex. The potential core is the central part of the flow in which the velocity stays equal to outlet velocity of the nozzle [33]. The flow in this region is axisymmetric and depends on the dimensionless number "Reynolds number" which is

characterized by three parameters the jet velocity U_j, the jet orifice diameter D and the kinematic viscosity of the fluid ν

$$R_e = \frac{U_j.D}{\nu} \tag{1.1}$$

As the jet grows, the velocity decays and the jet diameter increases according to the following equations:

$$\frac{U_x}{U_J} = \frac{B}{(X - X_0)/d} \tag{1.2}$$

Where U_x is the velocity at distance X from the nozzle; B is the velocity decay constant; d is the nozzle diameter.
And the jet spreads linearly with a spread rate (S) of:

$$S \equiv \frac{dr_{1/2}(x)}{dx} \tag{1.3}$$

As the distance go further from the jet orifice, the axial velocity decreases and the half width $r_{1/2}$ increases [33].

Impingement jet region

As the jet approaches the impingement surface, it experiences a velocity decay in a rate depends on the initial jet profile due to the adverse pressure gradient. In the impingement jet region, closer to the surface, streamlines will diverge away from the jet centreline. Then the fluid accelerates again when it starts moving away in the transverse direction to form a radial wall jet [38, 39].

Wall jet region

In the wall jet region, which is the direct vicinity of the impingement surface, there are strong shear stresses and velocity fluctuations greater than any normal boundary layer and a recirculation zone also, may be observed above the wall jet region [35]. It can be divided into two layers; the inner layer adjacent to the wall, where wall effect is more dominant, and the outer layer where the free turbulent flow features appear.

1.2.4 Aeroelasticity

Aeroelasticity deals with the combined features of fluid mechanics and solid mechanics. There are many applications based on this part of science including; air-crafts' wing design, turbo-machinery, bridges and skyscrapers design, electric transmission lines, artificial heart valves and the air puff test, moreover it is considered the foundation of modern biomechanics [40–43]. In most of aeroelasticity applications, it is normally assumed that the external loading acting on a structure is, in general, independent of the deformation of that structure and this was the assumption made in the literature when simulating the air puff test, but actually deformations of the cornea are in the same order of magnitude of air velocity compared to the eye and cornea size which will have an effect on the applied aerodynamic force by the air jet if it is ignored [44, 45].

1.3 Scope of the study

Intraocular pressure measurement is of a significant importance in diagnosis of multiple diseases. Glaucoma is the most emerging disease affected by IOP measurement. Improving accuracy of tonometry devices has been growing in the past decade and drew attention of many research groups. As a result, a collaboration between ophthalmologists, materials and mechanical engineers is required to achieve that important goal. The current study

concentrates on the air puff tonometry to improve and compensate the biomechanical effects on IOP measurements through studying the fluid structure interaction effect between cornea and the air puff. Computational Fluid Dynamics and turbulence modelling were used to simulate the turbulent air puff and finite element analysis was used to simulate the human eye with patient-specific topography. The main challenge was the two-way coupling between the two models and exchanging the data between them to accurately predict pressure distribution on the cornea, as input to finite element model of the eye and influence of fluid structure interaction on corneal mechanical response. After validation of the numerical model, it was used to develop estimation algorithms for intraocular pressure and corneal material behaviour.

1.4 Aim and Objectives

The main aim of this study is to produce estimation algorithms of intraocular pressure measurement and corneal material behaviour by non-contact air puff method taking into account, fluid structure interaction effects between the air puff and cornea via a parametric study with different eye geometry, material parameters and pressure loadings.

The objectives of this study were to:

- Study the Fluid Structure Interaction effect on corneal deformation profiles and air puff pressure distribution.
- Conduct Parametric study to understand the association of different Eye parameters on IOP measurement and corneal biomechanical behaviour.
- Produce an estimation algorithm of intraocular pressure with no association with eye biomechanical parameters.

- Expand and calibrate existing material models of the ocular globe based on in-vivo and ex-vivo measurements.
- Develop a biomechanical material behaviour algorithm to represent the hyperelastic non-linear nature of ocular tissues.

1.5 Structure of the thesis

The thesis consists of six chapters summarising the work that was performed to produce a validated fully coupled fluid structure interaction model of the human eye under air puff tonometry and use it to produce estimation algorithms for intraocular pressure and corneal material behaviour.

Chapter 1: Introduction

This chapter is introducing to the field of ocular biomechanics and giving a background about the human cornea, different tonometry techniques and ocular diseases. It also introduces the role of impinging jets in the biomechanical correction of IOP and corneal material characterisation. Scope of the study along with its objectives and thesis contribution are presented as well.

Chapter 2: Literature review

This chapter is giving a review of the literature and previous work that was conducted in air puff tonometry simulation, IOP accurate estimation and ocular tissues' material characterisation. The influence of biomechanical parameters on IOP measurements and corneal material behaviour are also presented.

Chapter 3: Analytical and dimensional analysis

In this chapter, the analytical and dimensional analysis of the air puff test problem are introduced. Classification of fluid structure interaction problems based on the key dimensionless numbers for both the fluid and solid models is also presented. Governing equations of CFD and finite element methods that were used in simulation of the air puff test are dicussed to provide the mathematical basis of the work.

Chapter 4: Research methodology

Chapter 4 explains the research methodology that was used to answer the research questions. It illustrates the numerical methods that were used in modelling of the air puff test and validation process of the numerical model. This chapter also illustrates the methodology followed in building and validating the parametric study and estimation algorithms of intraocular pressure and corneal material behaviour taking into account the fluid structure interaction effect.

Chapter 5: Presentation of results

Chapter 5 provides presentation of results obtained on validation of the CFD code used in the modelling and presents the coupled fluid structure interaction model of the air puff and the human eye. This chapter provides a full analysis of the air puff, pressure distribution on the cornea and FSI effect on the corneal deformations. Clinical validation of the numerical dynamic corneal response is presented against clinical and experimental data. The estimation algorithms of intraocular pressure and corneal material behaviour along with their validation against clinical and experimental data are also presented.

Chapter 6: Overall discussion and conclusions

This last chapter provides an overall discussion of the findings and stressing on the novel conclusions of the current study. Limitations of the present study and recommendations for future research are also be provided.

1.6 Contribution of the thesis

The novel contributions of this study are:

- A novel numerical simulation of the non-contact tonometry test was presented. This model provides realistic representation of the air puff, the ocular globe and the multi-physics fluid structure interaction coupling between the two models. It is the first time for the air puff test to be modelled using arbitrary Lagrangian-Eulerian adaptive mesh on patient specific human eyes. It was found that pressure distribution and corneal deformations change with different eye biomechanical parameters and numerical models will have high uncertainty if deformation of the cornea wasn't coupled with CFD model of the air puff using adaptive deformable mesh.
- A novel estimation algorithm for intraocular pressure measurement, based on a parametric study conducted on the numerical model and validated against clinical and experimental data. This algorithm corrects influence of cornea biomechanical parameters and fluid structure interaction on IOP measurement.
- A corneal material behaviour algorithm is presented to provide more flexibility and accuracy of material representation in numerical modelling depending on patient-specific corneal response parameters not only patient's age.

Chapter 2

Literature review

2.1 Introduction

Biomechanical properties of biological tissues are important health indicators and multiple clinical decisions and surgical planning can be made based on these properties and their dynamic response to loading. But till the moment there are some mechanical and dynamic responses are not fully understood or predictable. That is because of the different variables and parameters that control the response of this biological tissue,in-vivo, when it's functioning within the human body. In order to build such accurate understanding of the dynamic response, two routes are available, the experimental route or the numerical simulation route. Experimentally, this is quite expensive and needs very skilled hands and sophisticated

experimental setups, preparations and materials. Numerically, can be easier and faster, especially using the current available optimization tools and computational abilities. But of course sacrificing the in-vivo conditions, therefore, any numerical simulation needs to be validated and verified against some experimental testing in-vivo or ex-vivo.

The relevant biological tissue of interest in this study is cornea and sclera of the ocular globe. Especially cornea, why it is very important to understand how it behaves and responds to mechanical loading?. The answer to that question is; since the cornea is a vital area in any refractive surgery to correct vision errors which are outcome of many diseases, including Myopia, Hyperopia and Astigmatism, named as lower order aberrations. Cornea contributes with almost two thirds of the optical focusing power of the eye [46]. Refractive surgery is very fastly growing due to the development and improvement of laser technologies and surface ablation algorithms which based on new assessment techniques like wavefront analysis [47]. From here it comes importance of getting biomechanical properties of the cornea and its vital role in accuracy of any instrument or measurement device dealing with the human eye. The air puff test is one of non-contact methods with direct interaction with the cornea to estimate intraocular pressure for Glaucoma diagnosis and regular eye tests. Accuracy of intraocular pressure continued to be a big issue due to the effect of various parameters related to biomechanics of the eye.

This chapter is gathering the most important and relevant literature to the study, introducing to the corneal biomechanics and their influence on IOP measurement's accuracy and corneal material behaviour estimation. A review of tonometry techniques, used in intraocular pressure measurement, is presented including a survey on previous effort that were made to simulate the air puff test from different perspectives, theoretically, clinically, from the material and finite element analysis point of view, from the CFD and fluid structure interaction point of view.

2.1.1 Intraocular pressure (IOP)

Intraocular pressure (IOP) value is one of the important measurements in eye clinics to diagnose ocular diseases, especially, glaucoma. It is a common visual disorder that can lead to complete vision loss if the optic nerve is severely affected. Intraocular pressure is a risk factor of glaucoma progression and important to accurately monitor its value regularely, however, some cases are diagnosed with glaucoma and their IOP is in the normal range which has not yet been fully understood [28, 27]. From here comes the motivation to improve accuracy of measurement techniques to separate any error from the correct diagnosis of glaucomatous eyes. Measurement errors can be misleading and recommend false treatements. There are multiple reasons can lead to increased pressure level inside the eye which can be considered the same causes of glaucoma [29, 30]. Some of these reasons are listed below:

- The aqueous humour is a renewable fluid produced by the ciliary body located behind the iris. It flows via the pupil to fill the anterior chamber. The trabecular meshwork and Schlemm's canal are the drainage pathways for aqueous liquid located at the anterior chamber periphery, Figure 2.1. If any blockage occured at this meshwork, for whatever clinical reason, it will lead to excessive production of the aqueous humour over the drainage rate causing build up of pressure inside the eye [26, 48, 49].

- Some medications can have influence on production or drainage rate of aqueous from the eye as a side effect to treating another condition, for instance steroid drops after LASIK surgery can increase eye pressure and patients are advised to monitor their IOP level for some time after surgery [26, 49].

- Any injury or accident can cause blockage to the drainage pathways leading to increased eye pressure level even after months or years after the trauma.

The normal value of intraocular pressure is different between people and ethnic groups, but it ranges between 10 and 20 mmHg. If IOP increases above this range, the patient

might be in risk of Glaucoma [50, 51]. In numerical simulations, despite there are multiple components inside the eye including ocular lens, iris, aqueous and vitreous, the human eye is dealt with as a deformable pressure vessel that has internal pressure equal to IOP applied using a fluid cavity taking into account the cahnge in pressure with change in volume.

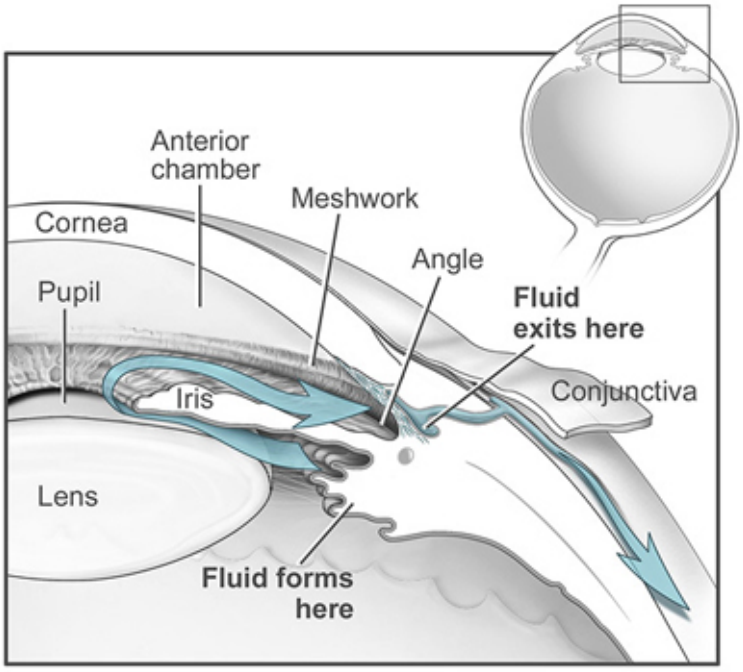

Figure 2.1 Flow of aqueous fluid inside the eye [26, 48]

2.2 Tonometry techniques

It goes back to the tenth century when some individuals noted the eye firmness in conditions of vision loss due to glaucoma and associated it with increased pressure level inside the eye. In 17^{th} century, IOP was estimated by finger pressure and this method lasted for decades until the first instrument developed in the 19^{th} century by Von Graefe [52, 53]. At end of 19^{th} century, the first reasonably accurate mechanical tonometer was developed by Maklakoff [52, 53]. Early in the 20^{th} century, Schiötz developed an indentation device that was used for five decades as the gold standard of IOP measurements, until 1950, the

Goldmann's applanation tonometer was invented and became the new gold standard which is still being used widely in the world until today [3, 53]. More recently in the 21^{st} century, the non-contact tonometers (NCT) were developed; the air puff applanation tonometer and the dynamic contour tonometer (DCT). Their development is fastly growing to improve their accuracy to be independent of corneal biomechanical properties [52–54].

Manometry technique is the most precise method to measure the pressure inside the eye, however it is an invasive technique suitable only for experimental laboratory measurements. A hollow needle is inserted to the anterior chamber of the eye and connected to a reservoir of fluid and raised to a height calibrated to represent the intraocular pressure. IOP fluctuations with time also can be monitored by a strain gauge sensing the fluid level change in the reservoir.

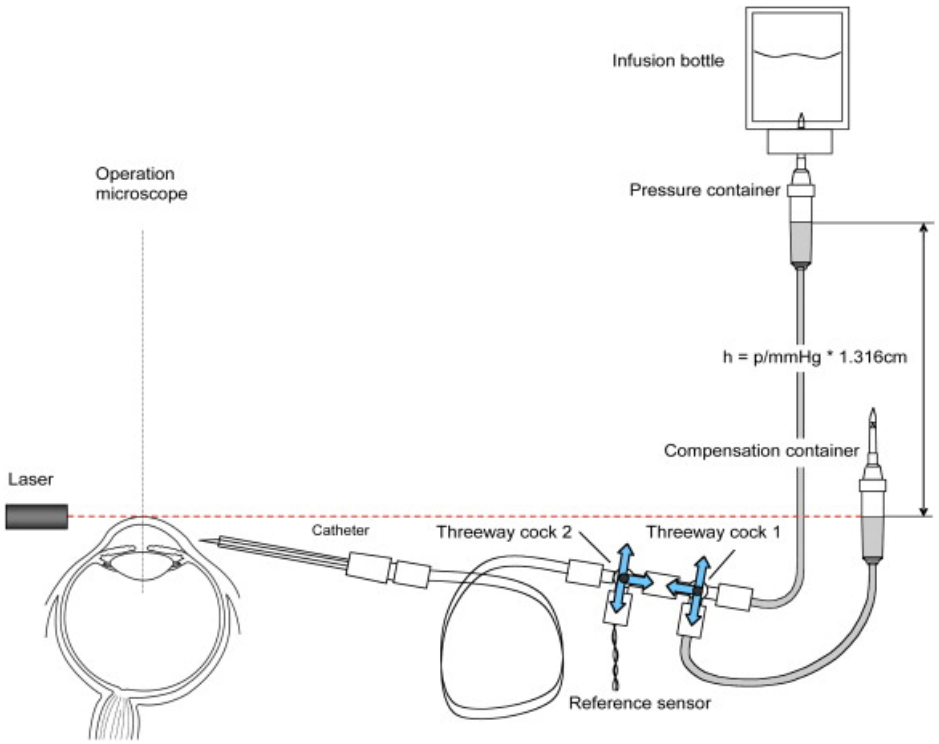

Figure 2.2 Operation principle of eye pressure measurement by manometry [52, 55]

The Goldmann applantion tonometer, Figurre 2.3, is considered the gold standard for intraocular pressure measurements [2–4, 55]. Its priciple of operation depends on estimation of the force required to applanate the cornea and relate it to the value of IOP, Equation 2.1.

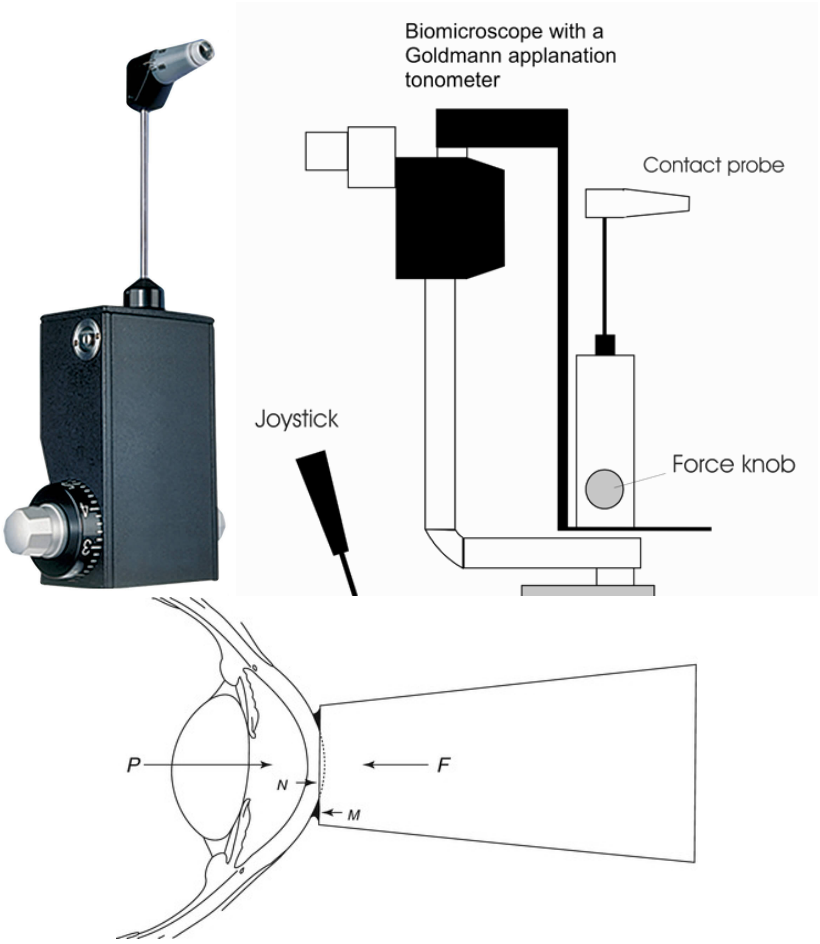

Figure 2.3 Goldmann applanation tonometer and its principle of operation [3, 55, 56]

$$P = \frac{F + M - N}{S} \tag{2.1}$$

where P is the intraocular pressure (IOP), F is the applanation force applied by the tonometer, M is the meniscus surface tension force of the tear film adhering cornea to the applanation surface, N is the elastic opposition force of the cornea, S is the flatened surface area at the applanation moment.

Some approximations were made in order to get IOP estimation via this method assuming the cornea is a very thin membrane, perfectly elastic and spherical, which is not necessarily accurate for the human cornea. Therefore, accuracy of IOP measurements were found affected by biomechanical properties of the cornea including central corneal thickness (CCT), corneal curvature (R) and corneal stiffness variations from person to another. Several studies were conducted in order to provide multivariable correction algorithms to the GAT measurement to reduce or eliminate its dependence on corneal biomechanical parameters [57–64].

The Ocular Response Analyser (ORA; Reichert, Inc., Buffalo, NY) is an air puff tonometer that applies an air pulse to flatten or applanate the cornea and uses the corresponding applanation pressures to estimate the IOP. It was mainly produced to reduce the errors in GAT applanation measurements. The temporal pressure distribution of the air jet on the cornea assumed in the literature for simulating the air puff test is shown in figure 2.4 [5, 20, 65, 66]. It is based on an experimental study conducted by Reichert [19, 20].

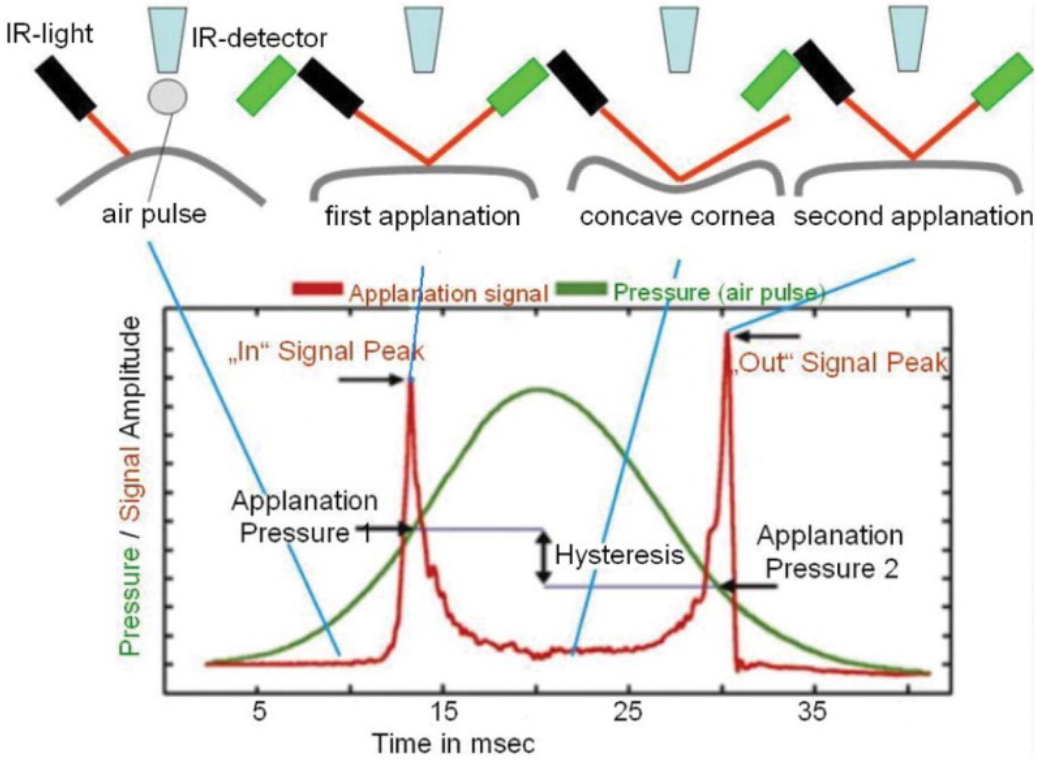

Figure 2.4 Operation principle of the Ocular Response Analyzer (ORA) [19, 67]

As a review on the history of intraocular pressure and its measurement techniques, Stamper et al. [52, 53], Sampaolesi et al. [55] and Elsheikh et al. [54] provided a detailed overview on IOP and the different measurement methods including the air puff non-contact method.

2.2.1 Simulation of non-contact air puff tonometry test

The air puff tonometry test is the main interest in the present study and it has been the focus for many previous studies due to its non-intrusive advantage and ease of use around the world. The Ocular Response Analyser (ORA; Reichert, Inc., Buffalo, NY) [19, 67] was the first developed device that uses an air puff to quantify ocular biomechanics, but recently CorVis-ST (Oculus Optikgeräte GmbH, Wetzlar, Germany) [68, 21] has provided the user with digital Scheimpflug imaging to capture the dynamic response of cornea to the air puff instead of the infrared signals in ORA, which acquires valuable information about the biomechanical behaviour of the cornea. The present study was based on the air puff of CorVis-ST and it was used in the experimental validations. Below is a survey on previous efforts that were made to simulate the air puff test from different perspectives, theoretically, clinically, from the material and finite element analysis point of view, from the CFD and fluid structure interaction point of view.

Theoretical modelling

Theoretically, the air puff test was simulated as a harmonic oscillator model (1DOF) to model behaviour of the cornea under action of the air puff test as shown in figure 2.5 by Zhaolong, Han et al. [69] to investigate the air puff induced corneal vibrations and their effect on the intraocular pressure (IOP), viscoelasticity and mass of the cornea based on theoretical approach and some clinical observations. They have used a kinematic viscoelastic corneal model to simulate the corneal movement during the air puff deformation involving

mass of the cornea, elasticity, damping coefficient and IOP. A parametric study has been conducted to see how these factors affect the corneal deformations. They have used two clinical ocular instruments to observe the corneal dynamic behaviour, CorVis ST (Oculus Optikgeräte GmbH, Wetzlar, Germany) and the Ocular Response Analyzer (ORA; Reichert, Inc., Buffalo, NY). The numerical results showed that there are vibrations with the corneal deformations and damping viscoelastic response of cornea reduced the vibration amplitude and with stiffer cornea, the overall vibration amplitude and inward motion depths are smaller.

Moreover, Anna Pandolfi et al. [70] used two different approaches to estimate the intraocular pressure and the other eye parameters, the first approach was modelling the corneal system as a harmonic oscillator. In the second approach they used patient specific geometries and finite element models to simulate the dynamic test on surgically treated corneas. The qualitative response of the two models was similar in spite of the different level of approximation in their assumptions. The finite element calculations reproduced the observed clinical deformations of cornea including the two applanation configurations provided by ocular response analyzer, suggesting that the mechanical response of cornea to the air puff test was driven only by elasticity of the stromal tissue. Furthermore, Kaneko et al. [71] modelled the human eyeball as a 1-DOF and 2-DOF systems to assess the dynamic response of the cornea and eyeball to the air puff test as shown in Figure 2.6.

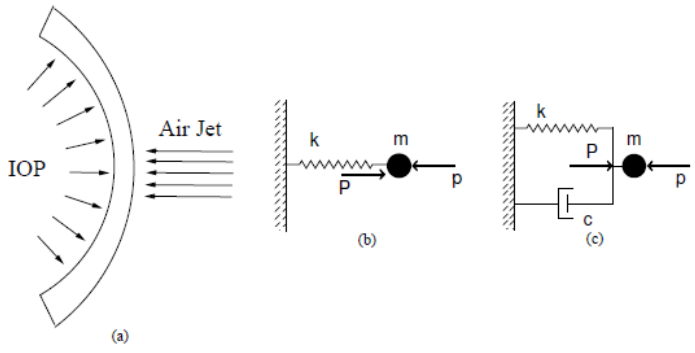

Figure 2.5 Simple one degree of freedom model. (a) Schematic of the air puff test and corresponding one-degree-of-freedom rheologic models. (b) Elastic oscillator. (c) Viscoelastic oscillator [70, 69]

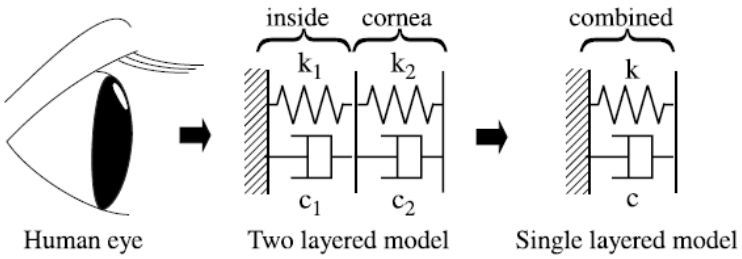

Figure 2.6 Dynamic model of the human eye [71]

Numerical modelling

Numerically, Finite element method and CFD were used to simulate the air puff test. Kling et al. [11] presented a two-dimensional axis-symmetric finite element model which predicts the deformation patterns of the cornea during air puff test to get its elastic and viscoelastic properties. They validated the results against experimental testing on porcine and human eyes to get the spatial pressure profile. They developed 2D axis-symmetric CFD model for the air jet impinging on different solid configurations of the cornea. The presented model and pressure distribution on the cornea are shown in Figures 2.7. They haven't considered effect of corneal deformations on pressure distribution of the air puff and the cornea was simulated as rigid geometry. An inverse modelling was performed to find the corneal biomechanical properties at different experimental conditions. Their parametric study revealed significant contributions of the intraocular pressure and corneal thickness to the corneal deformation, besides the corneal biomechanical properties. The results also showed that the capability of dynamic imaging to reveal inherent biomechanical properties in vivo.

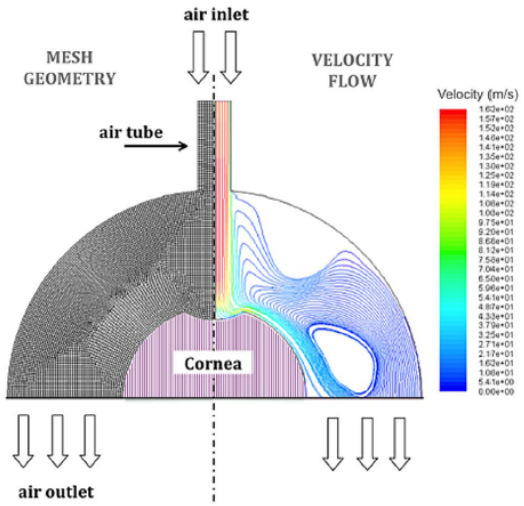

Figure 2.7 Geometry model of the cornea at maximal deformation [11]

The interplay between corneal geometry, material properties and loading in the non-contact air jet tonometry were studied by Ariza-Gracia et al. [72] . A patient specific finite element model of a healthy eye was used, taking account of the stress free configuration. The cornea was modelled as an anisotropic hyperelastic material with two preferential directions. Three sets of parameters within the healthy human range, based on inflation tests, were considered. Four pressure levels (10-28 mmHg) were considered to study the influence of IOP, whereas the corneal thickness varied uniformally (300-600 microns). A 2D CFD simulation of the air jet was used to obtain pressure loading exerted on the anterior surface of the cornea, results of pressure distribution is shown in Figure 2.8. The maximum apex deformation showed linear relationship with IOP for all the examined materials, although it showed a cubic variation with the corneal thickness. They also concluded the significant change of apical displacement with corneal stiffness.

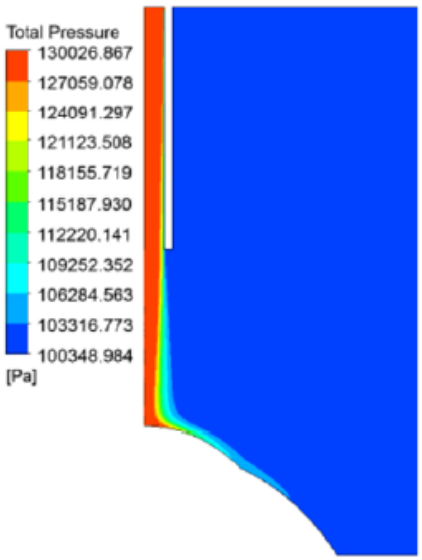

Figure 2.8 Symmetrical pressure profile obtained from the CFD simulation [72]

In another study performed by Muench et al. [73], they identified the normal and shear stress profiles on cornea resulting from an air puff to present a universal equation of the pressure distribution on cornea to use it for corneal material inverse analyses. Their method was based on experimental characterisation of the air puff produced by CorVis-ST and CFD simulation of the air puff test using ANSYS CFX. As a calibration of the CFD simulations, they applied the air puff to a rigid eye model which was hung up through a yarn and positioned in front of the nozzle exit, Figure 2.9. Based on the eye movement, they calculated the reaction force and considered it the boundary condition to a CFD inverse problem to get the time-dependent pressure profile at the nozzle exit.

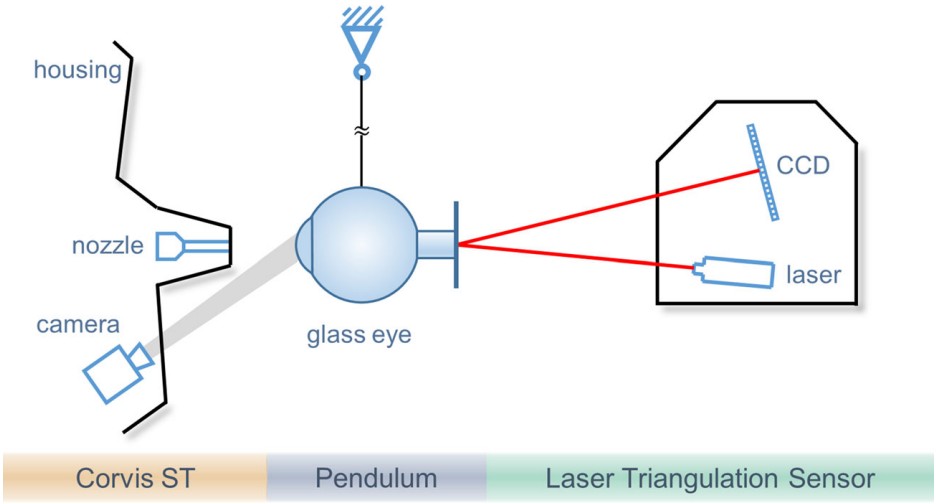

Figure 2.9 Set up of the pendulum experiment of a rigid glass eye in front of CorVis-ST nozzle and a laser sensor to record movement time curve [73]

Muench et al. used eleven corneal deformation configurations to apply them in the CFD model of the rigid eye glass model as shown in Figure 2.10. The outcomes showed dependency of pressure distribution on cornea on corneal deformations with minor effect of shear stress component on corneal deformations Which is a motivation to perform the present study and take corneal deformations into account when simulating the air puff. In order to add a realistic modelling of the human eye, they considered the human face to see its influence on the pressure distribution on cornea, Figure 2.11. They demonstrated that pressure and shear stress distributions were not rotationally symmetric when applying the air puff to real human eyes [73].

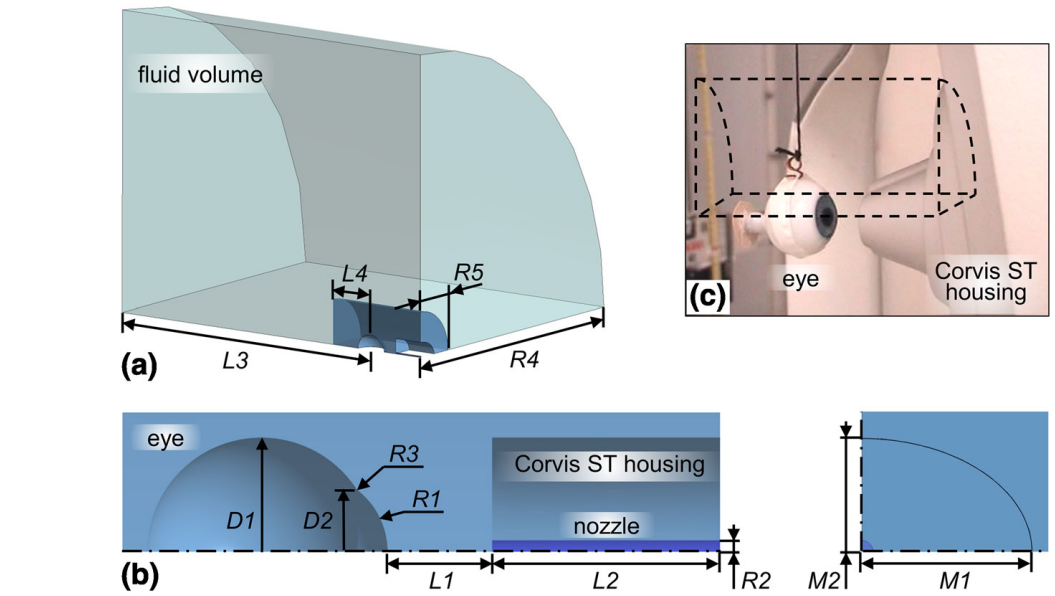

Figure 2.10 Three dimensional CFD model of the air puff test fro a rigid eye glass. (a) Isometric view, (b) Front and side views of CFD inner volume, (c) the physical model [73]

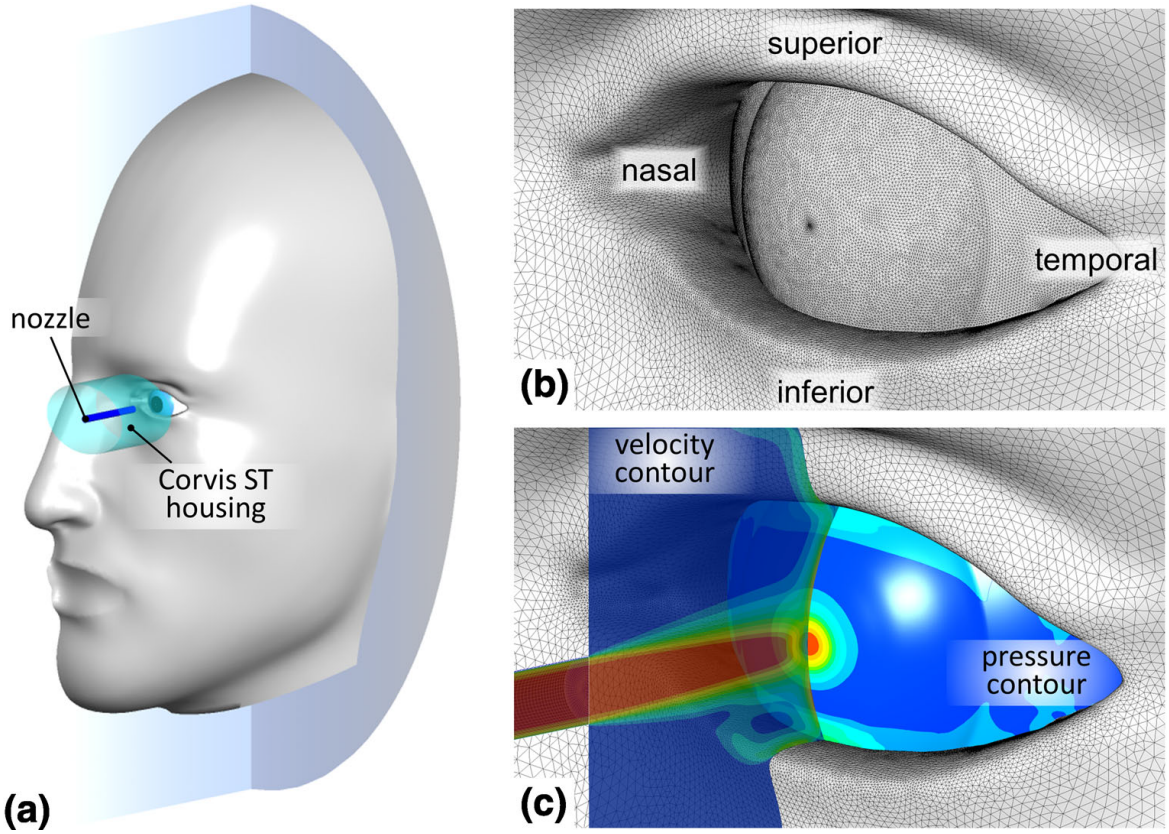

Figure 2.11 Model of the human face. (a) Isometric view, (b) surface mesh of the model, (c) velocity and pressure contours on cornea [73]

Fluid structure interaction modelling

From the Fluid Structure Interaction (FSI) point of view, Sinha Roy et al. [74], estimated the corneal biomechanical properties by developing a new 3D patient specific inverse finite element model of the air puff applanation. Highlight of this model was the inclusion of patient specific corneal tomography, cross links between collagen lamellae, epithelium layer and fiber dependent hyperelastic model. A lumped mass dashpot and spring model was introduced to model the resistance to motion and deformation of the eye globe caused by the air puff effect. Ten normal eyes were used for the study and customised routines were scripted to perform the inverse analysis. The study concluded that the inverse method that they have used was effective to quantify the material properties with sensitivity to IOP variation, especially the in vivo fiber-dependent hyperelastic biomechanical behaviour of the cornea which was introduced for the first time. A 2D axisymmetric CFD simulation of the air puff was used to compute the normal pressure force distribution and applied as a load on the anterior corneal surface. The CFD and finite element models of the air puff test are shown in Figure 2.12, 2.13.

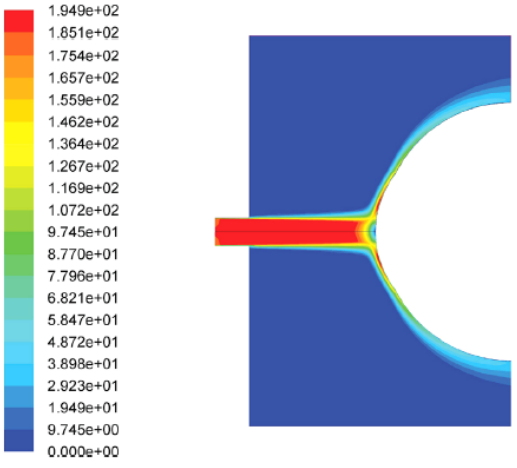

Fig. 3 – Contour plot of axial velocity distribution at peak air-puff pressure.

Figure 2.12 Contour plot of axial velocity distribution at peak air-puff pressure [74]

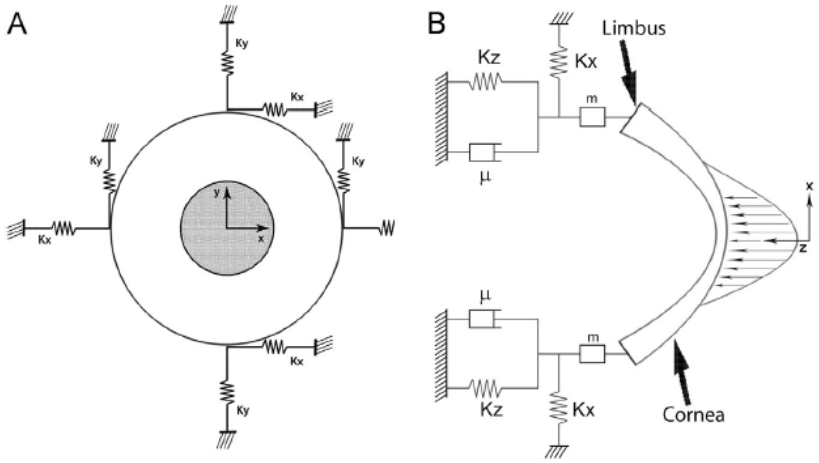

Figure 2.13 (A)Top-view of the cornea in the 3-D inverse finite element model of human eye. The shaded circular region shows a schematic of the area where the air-puff was incident on the cornea, (B) cross-section view of the cornea with lumped mass (m) and parallel network spring–dashpot model. [74]

Edward P, Furlani et al. [75] used a multiscale modelling approach to make full two way coupling fluid structure interaction model to predict the stress and strain through the whole eye as a result of applying the intraocular pressure and introducing the challenges and opportunities of using this approach to develop understanding of the biomechanical behaviour of the human eye. The results are shown in Figure 2.14.

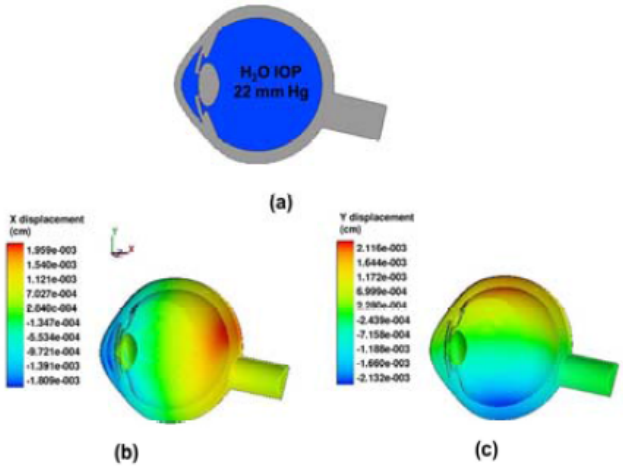

Figure 2.14 CFD-FSI strain analysis: (a) applied IOP, (b) X-displacement, (c) Y-displacement [75]

The first coupled fluid structure interaction model of the air puff test to establish some basic parameters for future wide scale studies was introduced by Nouran, Bahr et al.[76]. They used CFD simulation for the air jet and finite element model for the cornea and used Corvis-ST to validate the numerical results. They employed Neo-Hookean model to simulate the cornea material behaviour. The FSI framework within ANSYS was used upon a multi-field analysis (MFX) solver and they assumed that the corneal deformation is insignificant compared with the enclosure size and performed one-way fluid structure interaction analysis, the transient air force applied to the cornea was calculated in CFX and then passed to the finite element solver. They have applied a constant normal pressure against back of the cornea to mimic the effect of IOP, Figure 2.15.

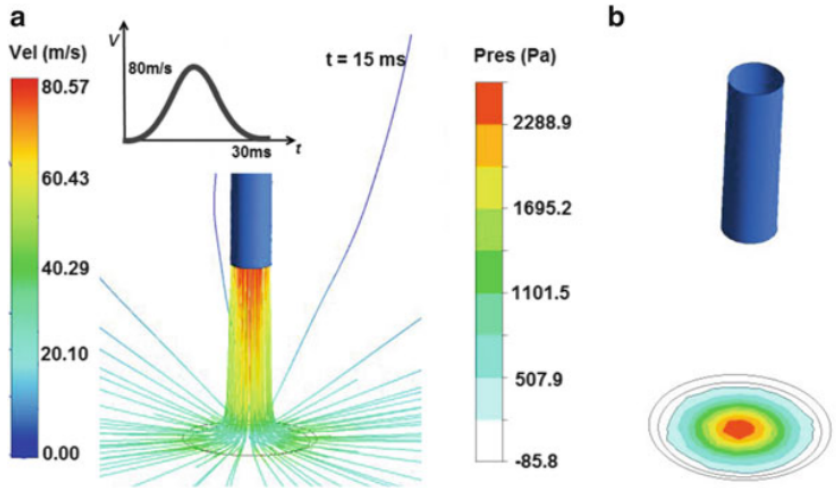

Figure 2.15 (a)Air flow velocity along the flow streamline, (b) the pressure force acting on the cornea [76]

The closest fluid structure interaction simulation of the non-contact tonometry test was done by Ariza-Garcia et al. [77]. They explored four different approaches starting from structural analysis to considering the fluid structure interaction with the air puff from outside and with the aqueous humour from inside, figure 2.16. However, the model was created based on 2D-axisymmetric porcine eyes. These four modelling methodologies were compared against each other by considering biomechanical parameters of the cornea. The

results indicated importance of considering fluid structure interaction effect on the pressure distribution and corneal deformations which will lead to an overestimated IOP measurments and biased corneal stiffness when performing the inverse finite element analysis [78]. To the best of my knowledge, the current study is the first attempt to, further, quantify the influence of fluid structure interaction on corneal behaviour predictions for 3D patient-specific eye models using the Arbitrary Lagrangian- Eulerian (ALE) deforming mesh, with more focus on air puff dynamics and extending the model for a larger parametric study to develop IOP and corneal material estimation algorithms.

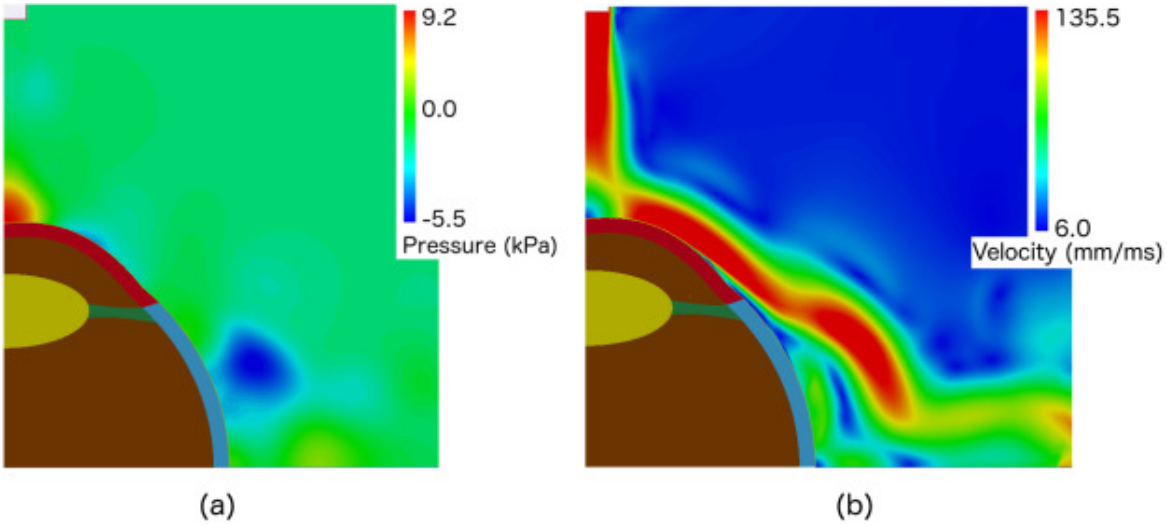

Figure 2.16 Pressure (a) and velocity (b) distribution on the cornea for the CFD simulation of the non-contact tonometry test, by Ariza-Garcia et al. [77]

Another approach to relate between the changes of eye vibration and the value of IOP, S. Salimi et al. [79] were studying variation of vibration characteristics of the eye with changes in intraocular pressure by introducing a fluid structure interaction model, which has the potential to provide an improved measurement techniques over the traditional ones. They have developed a finite element model of the eye subject to vibration. The eye is modelled as a shell structure filled with an inviscid pressurized fluid with no mean flow. The model is verified by comparing its vibrational characteristics with an Experimental Modal Analysis (EMA) of an elastic spherical shell filled with water. The structural dynamics are

examined due to the change of fluid pressure. They concluded that the frequency response of this fluid-structure coupled system has a clear direct relationship between the natural frequency and the fluid pressure. They extended the model to include the lens to improve the accuracy of modelling the eye and study its effect on the corneal vibrations. They have studied influence of biomechanical properties such as the corneal thickness and the eye dimensions on changing the measured natural frequencies and compared them to the similar influences in the Goldmann applanation models. Dynamic response of the eye was found to be less affected by the biomechanical parameters than applanation tonometry models , Figure 2.17, 2.18.

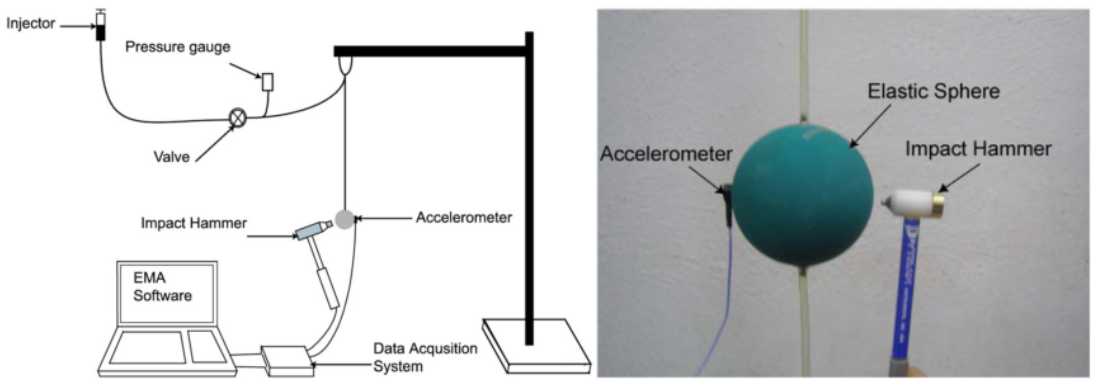

Figure 2.17 EMA set up on the elastic ball (a) schematic diagram (b) impact hammer test [79]

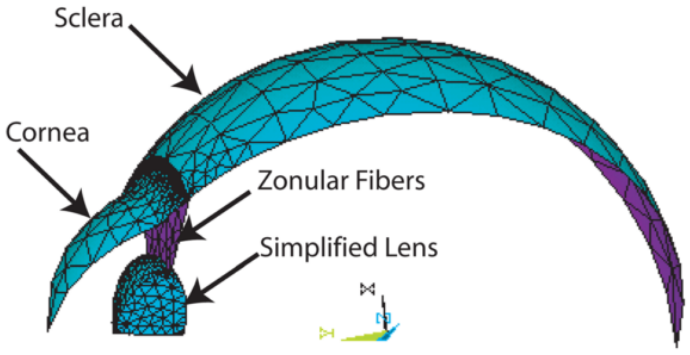

Figure 2.18 Mesh of the simplified lens FE model [79]

2.2.2 Corneal material behaviour estimation

A deep understanding of the corneal biomechanical behaviour is of a great importance in several clinical applications, for instance, refractive surgery [80, 81], contact lens design [82–84], tonometry [52, 53], and trauma treatment [85–87]. The corneal biomechancal parameters play a vital role in preserving the curved corneal geometry which is important for clear vision and refraction of light [88]. Many previous studies worked on the characterisation of corneal material properties using three main experimental techniques, tensile uniaxial testing [22–25], whole eye inflation testing [89–92] and compression testing [93]. The main issue was expanding these ex-vivo experimental findings to clinical in-vivo tests as always there are limitations and assumptions made when testing the tissues ex-vivo. Some studies performed finite element analyses to simulate the in-vivo conditions such as eye inflation, air puff tonometry and LASIK surgery. Some studies considered the corneal material to behave as linear homogenous elastic material [94, 95], other studies provided hyperelastic non-linear behaviour [96, 91, 97, 98]. An experimental study was done by Elsheikh et al. to determine the stress-strain curves of corneal material behaviour and their variation with age. Fifty seven ex-vivo preserved human corneas with age range between 30 and 90 years were tested under posterior pressure up to 60 mmHg [6]. Corneal tissues showed hyper-elastic stress-strain curves that nearly match an exponential growth without crossing over each other with some bias towards age above 80 years, Figure 2.19. They also demonstrated a clear increase in the corneal stiffness in relation to age observed at all pressure levels [5, 6]. Generic stress-strain equations were developed for implementaion in ocular biomchanical behaviour simulations, Equation 2.2. Figure 2.20 shows the stress strain curves after applying the generic equation and its stiffness becomes higher as age increases.

$$\sigma = (35\times10^{-9}age^2 + 1.4\times10^{-6}age + 1.03\times10^{-3}) \times [e^{(0.0013age^2+0.013age+99)\varepsilon} - 1], \quad (2.2)$$

where σ is the stress in MPa, ε is the strain and age is in years.

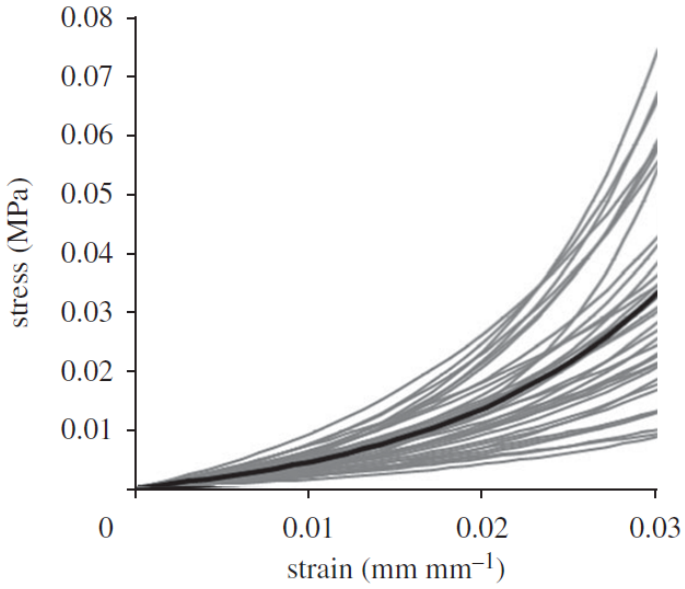

Figure 2.19 Experimental stress-strain curves for corneas with age range between 30 and 90 years. Solid black line represents the average behaviour [6]

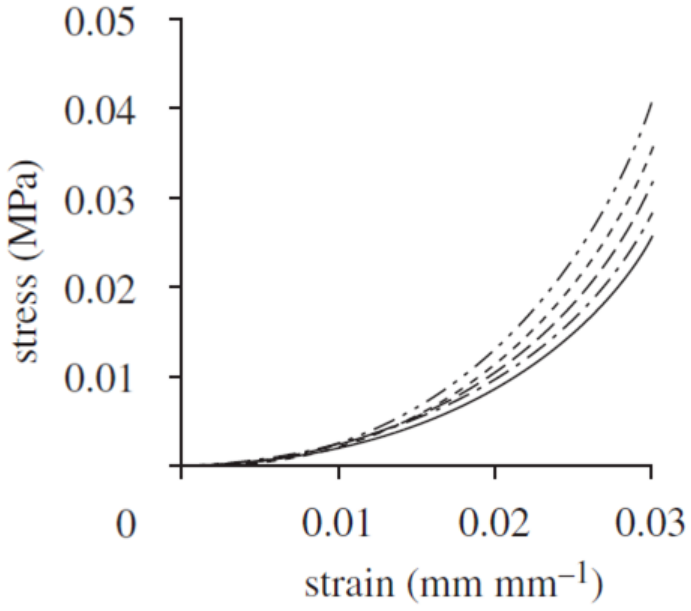

Figure 2.20 Stress-strain curves for as obtained from Equation 2.2. Solid line represents age 55 years; dash dotted line, age 65 years; long-dashed line, 75 years; short-dashed line, 85 years; dashed double-dotted line, 95 years [6]

In a numerical study conducted by Elsheikh et al., a hyper-elastic Ogden material model was used in material definition of different segments of the eye with different values for model input coefficients (μ *and* α) as obtained from uniaxial experimental analysis of corneal and scleral tissues [5, 6, 65]. Ogden models were first produced by Raymond Ogden [99], to describe the material behaviour through strain energy density function. They were primarily used to define non-linear stress-strain behaviour of complex materials such as biological tissues and rubber-like materials. Ogden model applies a strain energy potential function ($\prod$) which defines the stored energy in unit volume of the material, Equation 2.3 [100–102, 99]. Finite element analyses try to minimise this strain energy functional.

$$\prod = \sum_{i=1}^{N} \frac{2\mu_i}{\alpha_i^2}(\bar{\lambda}_1^{\alpha_i} + \bar{\lambda}_2^{\alpha_i} + \bar{\lambda}_3^{\alpha_i} - 3) + \sum_{i=1}^{N} \frac{1}{D_i}(J^{el} - 1)^{2i}, \tag{2.3}$$

where $\bar{\lambda}_i$ are the deviatoric principal stretches which are related to the deformations at constant volume as outcome of shear stresses [100, 103]; N defines the order of the Ogden model with maximum of sixth order (N=6); μ and α are material parameters; J^{el} is the elastic volume ratio related to thermal expansion and D_i defines the material compressibility.

Several previous studies have demonstrated the influence of central corneal thickness (CCT) and the other biomechanical metrics of cornea on IOP measurements using Ocular response Analyzer (ORA) and CorVis-ST [104–106]. Riccardo et al. [107] have evaluated the influence of IOP and pachymetry on the corneal response parameters and provided normative values for the CorVis-ST parameters in helthy patients. They used dataset of 705 healthy patients in multilocation study to incorpotrate variant ethnic origins. They have used the analysis of corneal response parameters to see their influence on the clinically corrected IOP (IOPcc) and the biomechanically corrected IOP (bIOP). Also, they have investigated the effect of age and material stiffening.

Chapter 3

Fluid structure interaction workflow

3.1 Introduction

Studying the physical problems using mathematical models is an important stage towards solving this problem and can make difficult matters easy to understand. In the current chapter, analytical and dimensional analysis of the air puff test are introduced to put our hands on the key dimensionless numbers controling fluid structure interaction problems and the govering equations for numerical methods used in the simulation.

3.2 Analytical approach of the fluid structure interaction effect on impingement surfaces

In the air puff test, the cornea acts as an impingement surface in front of the jet, which means that the impingement surface is deformable during the impingement time. Figures 3.1, 3.2 show the difference between jet impact on a rigid stationary flat plate and a moving flat plat (White, Frank M. 1979)[108].

- Impact of a jet on a stationary plate

  By applying the momentum equation in the horizontal direction

$$\Sigma F_x = \dot{m}(V_{jet} - V_{plate})$$
$$\therefore R_x = \rho A V_{jet}(V_{jet} - 0)$$
$$\therefore R_{x1} = \rho A V_{jet}^2 \tag{3.1}$$

  where ΣF_x is the net force in the X-direction; $\dot{m}$ is the fluid mass flow rate; V_{jet} is the jat average velocity and R_x is the reaction force from the wall in X-direction.

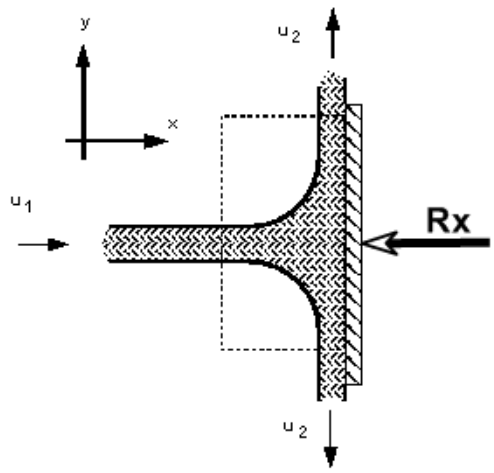

Figure 3.1 Impact of a jet on a stationary plate [108]

- Impact of a jet on a moving plate

$$\Sigma F_x = \dot{m}(V_{jet} - V_{plate})$$

$$\therefore R_{x2} = \rho A V_{jet}(V_{jet} - V_{plate}) \tag{3.2}$$

So $R_{x2} < R_{x1}$ which proves the fluid structure interaction effect on corneal deformations and IOP measurements.

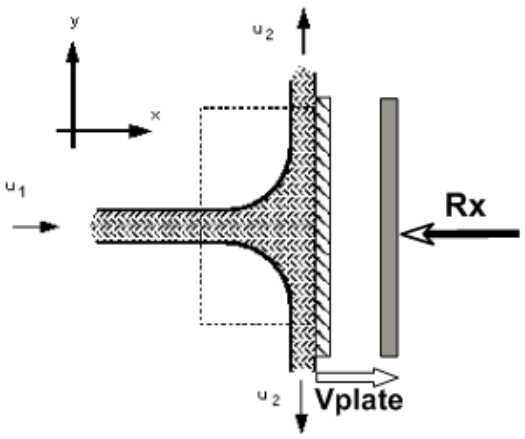

Figure 3.2 Impact of a jet on a moving plate [108]

3.2.1 The difference between static and stagnation (Pitot) pressure

Static pressure is often used in fluid dynamics' publications instead of "pressure" to avoid confusion, because the concepts of dynamic and stagnation pressures are vital in the study of fluid flows. There are two components of the pressure in any flow stream; the static and dynamic pressures [109–111]. The stagnation, or Pitot, pressure is the summation of these two components, or in other words, it equals the static pressure at a stagnation point in the flow stream, Equation 3.3. At this stagnation point all the kinetic energy has converted into pressure energy [109–111].

$$P_{Stagnation} = P_{Static} + P_{Dynamic} = P_{Static} + \frac{1}{2}\rho v^2 \tag{3.3}$$

ρ is the fluid density and v is the fluid velocity.

The famous "Bernoulli's equation" summarises this concept of stagnation pressure. It has three main components; the static, dynamic and head pressures which give the total pressure [109, 112, 113]. Figure 3.3 shows the streamlines of a flow around an oval body. The total pressure at points 1,2 and S has to be equally the same, energy can convert from one form to another, but the total energy is conserved, Equation 3.4. As the velocity at the stagnation point S equals zero, then the third part of the equation will equal the stagnation pressure.

$$P_1 + \frac{1}{2}\rho v_1^2 = P_2 + \frac{1}{2}\rho v_2^2 = P_S + \frac{1}{2}\rho v_S^2 \tag{3.4}$$

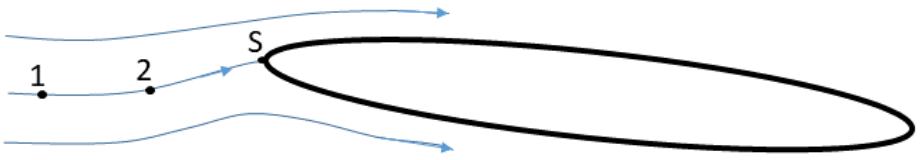

Figure 3.3 Flow around an oval: Bernoulli and stagnation pressure principles

Pressure coeffiecient (C_p)

Pressure coefficient is an important dimensionless figure in studying fluid flows as it equals the ratio between pressure forces and inertial forces. Equation 3.5 gives the value of C_p as the ratio between static and dynamic pressures. Along the flow, there is a continous conversion between inertial forces and pressure forces especially close to boundaries and obstacles to the flow stream [109, 112, 113]. Sometimes the inertial forces are refered to the dynamic pressure while the pressure forces refered to static pressure. For impinging jets, the dynamic pressure is converted completely to static pressure at the stagnation point where the velocity is zero such as point S in Figure 3.3.

$$C_p = \frac{p - p_\infty}{\frac{1}{2}\rho_\infty V_\infty^2} \tag{3.5}$$

where C_p is the pressure coefficient; p is the static pressure at the point of interest in the flow stream; p_∞ is the free stream static pressure; ρ_∞ is the free stream fluid density and V_∞ is the free stream fluid velocity. For inviscid and steady flows, using Bernoulli's equation, the equation for C_p can be simplified more as in Equation 3.6 [109, 112, 113].

$$C_p = 1 - (\frac{u}{u_\infty})^2 \tag{3.6}$$

where u is velocity of the flow at point of interest and u_∞ is the free stream velocity. C_p equals zero at the free stream flow and equals one at the stagnation point.

3.3 Classification of fluid structure interaction problems

In fluid mechanics, solids are considered as boundary conditions only and not in terms of what they are made of. For instance, in a flow around a cylinder, the cylinder deviates the uniform flow, and prevents the fluid from penetrating the body of the cylinder. On the other

hand, in solid mechanics, we solve for deformations of the solid under loading. Some of these loadings can be due to the presence of a fluid such as a deformation of a submarine under external pressure or inflation of a balloon under internal pressure or a building or a bridge subject to the the wind. Usually the fluid is considered a cause of a loading at the boundary [114, 44, 45]. The two approaches can work separately in many applications with acceptable results, but in other applications, separate solutions are not accurate enough and consideration of fluid-structure interaction becomes necessary. These interactions mostly driven by practical and industrial applications such as biomechanics, aerospace, nuclear and civil engineering.

3.3.1 Dimensional analysis

Dimensionless numbers are effective tools to classify FSI problems. For instance, the well known Reynolds number is used to classify the flow to be creeping flow at low values or detached flow at high values. More generally in multi-physics problems, physical laws should be expressed in terms of dimensionless quantities as this can simplify analysis steps and reduce unknowns [114, 44, 45]. Table 3.1 shows the dimensional quantities for the fluid and the solid models.

Table 3.1 Fluid and solid dimensional quantities

Quantity	Solid	Fluid
Coordinates	x	x
Time	t	t
Studied field	Displacement ξ	Velocity U
Material property	Stiffness E	Viscosity μ
Size	L_s	L_f
Gravity	g	g
Density	ρ_s	ρ_f
Initial conditions	Displacement data ξ_0	Velocity data U_0

3.3.2 Fluid domain dimensionless numbers

The function $f(U,x,t,\mu,L,g,\rho,U_0)=0$ describing the fluid flow in the dimensional quantities form is converted into a dimensionless form as $F(\frac{U}{U_0},\frac{x}{L},\frac{U_0 t}{L},\frac{\rho U_0 L}{\mu},\frac{U_0}{\sqrt{gL}})=0$, which contains five variables instead of eight [114, 44, 45]. In this form:
$\frac{U}{U_0}$ is the dimensionless velocity
$\frac{x}{L}$ is the dimensionless coordinate
$\frac{U_0 t}{L}=\frac{t}{T_{Fluid}}$ is the dimensionless time , where $T_{Fluid}=\frac{L}{U_0}$ which is the time taken by a fluid particle to travel at velocity U_0 across distance L which is describing the convection in the fluid
$\frac{\rho U_0 L}{\mu}$ is Reynolds number R_E
$\frac{U_0}{\sqrt{gL}}$ is the Froude number F_R

3.3.3 Solid domain dimensionless numbers

The function $f(\xi,x,t,E,L,g,\rho_s,\xi_0)=0$ describing the solid deformation in the dimensional quantities form can be converted into a dimensionless form as $F(\frac{\xi}{L},\frac{x}{L},\frac{t\sqrt{\frac{E}{\rho_s}}}{L},\frac{\xi_0}{L},\frac{\rho_s g L}{E})=0$ [114, 44, 45, 115]. In this form:
$\frac{\xi}{L}$ is the dimensionless displacement
$\frac{x}{L}$ is the dimensionless coordinate
$\frac{t\sqrt{\frac{E}{\rho_s}}}{L}=\frac{t}{T_{Solid}}$ is the dimensionless time, where $T_{Solid}=\frac{L}{c}$ is the time that the elastic wave takes to travel across the solid length L at velocity c
$\frac{\xi_0}{L}$ is the displacement number D, which describes how big the displacement is compared to the length scale of the problem and it plays a vital role in the classification
$\frac{\rho_s g L}{E}$ is the elastogravity number G, which describes the deformations induced by gravity

3.3.4 Fluid-solid coupled dimensionless numbers

To remove the separation between the above sets of dimensionless numbers, they can be combined into a new set of coupled dimensionless numbers.

Now the function $g(U,x,t,\mu,\rho,U_0,L,g,E,\rho_s,\xi_0)=0$ with 11 dimensional quantities will become dimensionless as $G(\frac{U}{U_0},\frac{x}{L},\frac{U_0 t}{L},\frac{\rho U_0 L}{\mu},\frac{U_0}{\sqrt{gL}},\frac{\xi_0}{L},\frac{\rho_s g L}{E},A)$ with eight independent dimensionless quantities, five for the fluid alone, two for the solid alone and the last quantity is the coupled dimensionless number A, which cannot be a combination of the other numbers, but be a parameter of the form $A=\frac{Fluid}{Solid}$, which is the core of the classification of any problem. (A) can be one of three choices based on the application [44, 115]:

1. Mass Number ($M=\frac{\rho_f}{\rho_s}$)
2. Reduced Velocity ($U_R=\frac{U_0}{c}=\frac{T_{Solid}}{T_{Fluid}}$)
3. Cauchy Number ($C_Y=\frac{\rho U^3}{E}$)

The governing equations for the CFD model are the continuity and momentum equations. On the other hand the solid deformations are governed by the oscillator equation which includes mass, stiffness and force matrices. To create coupling between the two models, two conditions have to be satisfied at the interface; the kinematic condition and the dynamic condition. The kinematic condition is satisfied by equating the velocities of the two models at the interface which means no sliding and no mixing between the two materials, while the dynamic condition is satisfied by equating the forces at the interface, including the pressure and the viscous shear forces from the fluid model to be transferred to the force matrix of the structure model [44, 45, 115]. Figure 3.4 explains the dimensionless governing equations for both models and at the interface. The reduced velocity, displacement number, Cauchy number, Froude number and Reynolds number appear in the dimensionless equations. These equations will be explained in details in Section 3.4.

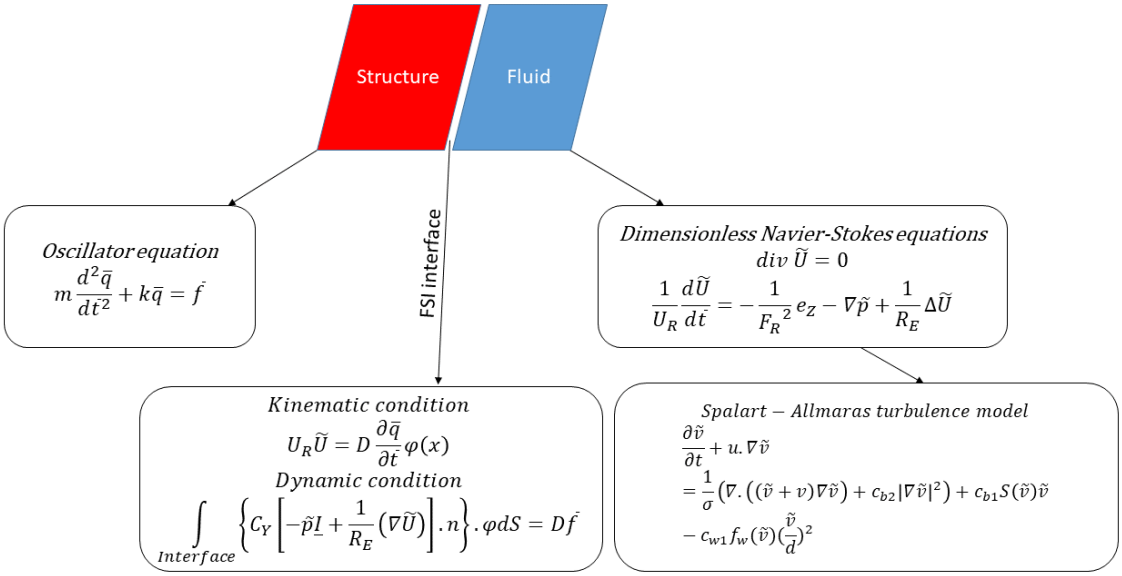

Figure 3.4 Coupled dimensionless governing equations

3.3.5 Reduced velocity (U_R) as a key classification tool

The reduced velocity ($U_R = \frac{T_{Solid}}{T_{Fluid}}$) is a vital dimensionless number to be quantified. For a small reduced velocity close to zero, the time scale of the fluid domain is much larger than the time scale of the solid domain. In other words, velocity of the fluid can be compensatedin the structural model without the need to consider a separate fluid model. Simulating a boat oscillating in still water or offshore designs are examples of such problems. This assumption of neglecting the fluid velocity simplifies the general equations allowing the two domains to be solved separately. The effect of the fluid on the solid will be in a form of fluid induced stiffness to the oscillator equation, and based on the value of Stokes number ($S_T = \frac{R_E}{U_R}$), fluid induced damping (viscous effect) (Low S_T), fluid induced mass (inertia effect) (high S_T) or memory effect (intermediate S_T) is added to the solid equation, such as coupling between a solid tank and sloshing water [44, 45, 115].

For high reduced velocities in order of magnitude of 100, the solid deformations are coupled with fast flow, making the time scale of the fluid much smaller than the time scale of the solid. In aerospace engineering, this concept is called aeroelasticity approximation or quasi-static aeroelasticity, which neglects the velocity of the solid structure and considers the solid domain deformation is frozen in time. However, these deformations have to be calculated at different time intervals, and this is done separately as there is a separation between the two time scales. The effect of the fluid on the solid domain will be an added stiffness which depends totally, in terms of sign and magnitude, on the fluid velocity. This may lead, in some cases, to static instabilities if the added stiffness is negative and cause the structure to vibrate at high frequencies that can destroy the structure if it's a plane wing for example. There is a critical velocity for the flow, before which these static instabilities occur and for systems with two modes of vibrations like torsion and plunge in the case of an airfoil, dynamic instabilities occur when a coincidence between the frequencies of the two modes take place, generating what's known as the coupled-mode flutter of an airfoil [44, 45, 115].

For intermediate reduced velocities in order of magnitude close to the displacement number, the problems become more complicated as the two time scales are in the same order of magnitude and there is no model that is dominant over the other, so both models have to be solved simultaneously which is known as coupling with slow flow. The most general case will be when the interface has deformation, velocity and acceleration. In the case of Pseudo-static aeroelasticity, acceleration of the interface is neglected and the velocity is considered constant with time as this can be simpler and computationally more economic.

Figure 3.5 explains the broad range of the reduced velocity and influence of this dimensionless number on classification of the problem and method of solution. The most general case, which requires full coupling between the two models, is when the reduced velocity is in order of magnitude around the displacement number which is the case in the air puff test. The reduced velocity of the air puff test ranges between 0 and 10 at the maximum

velocity. The displacement number of the eye model is in order of magnitude of $10^{-}2$. So any approximation or selection to another method, rather than the full coupling between the two models, will have a major impact on accuracy of the solution [44, 45, 115].

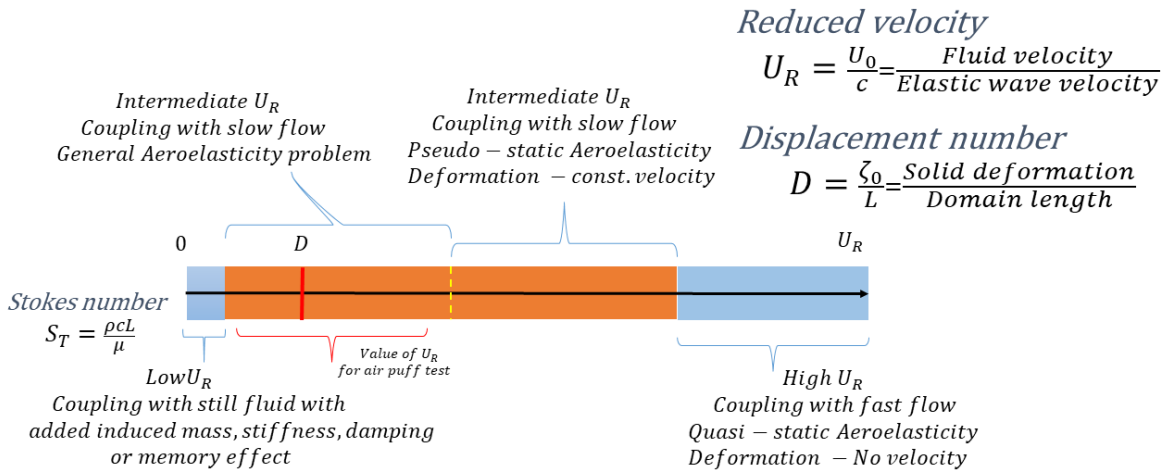

Figure 3.5 classification of fluid structure interaction problems based on the value of the reduced velocity U_R [44, 115]

3.4 CFD governing equations

To simulate the turbulent jet of the air puff test, Navier-Stokes equations were solved with an appropriate turbulence model, possibly using the Unsteady Reynolds Averaged Navier-Stokes equations (URANS) to capture the turbulent eddies. To solve these partial differential equations, Abaqus/CFD uses an integral form for momentumand continuity equations. For unsteady problems, which is the case for air puff test, an advanced second-order projection method was used for the air deforming domain. A node-centered finite element discretization was used for the pressure equation and and a cell-centered finite volume discretisation of all other transported variables (such as velocity, temperature, turbulence, etc.)[100, 116]. This hybrid meshing approach removes the need for any artificial dissipation, while preserving the traditional conservation properties associated with the finite volume method. The main concept of projection methods is the separation between the velocity and the pressure fields

for more efficient solutions of Navier-Stokes equations. The projection purpose is to separate the divergence free part of the velocity field using Helmholtz decomposition providing that the boundary conditions are satisfied [100, 117, 116].

There are multiple turbulence models available in Abaqus-CFD including "Spalart-Allmaras" as a one-equation RANS model, "RNG and Realizable K-ε models" and "K-ω model" as two-equations RANS model [100, 114]. Navier-Stokes equations consist of four equations with four unknowns in the case of laminar flows; one equation for mass conservation and three momentum conservation equations in the three dimensions. Therefore, this system of equations can be solved, but in case of turbulent flows there are velocity fluctuations in the three dimensions and changing with time which can't be captured by the laminar equations [113, 118, 117]. In this case, number of unknowns exceeds number of equations, creating what is called a "Closure Problem". As a result, there is a need for additional equations to enable solving this problem and reducing number of unknowns by finding relationships between these equations and the unknowns describing turbulent fluctuations and turbulent stresses [113, 118, 117].

Unsteady Reynolds Averaged Navier-Stokes equations (URANS)

- Averaged incompressible continuity equation:

$$\frac{\partial \overline{u}}{\partial x}+\frac{\partial \overline{v}}{\partial y}+\frac{\partial \overline{w}}{\partial z}=0, \;\; Or \;\; \nabla.\overline{u_i}=0 \tag{3.7}$$

- Averaged Momentum equation:

$$\frac{\partial \overline{u_i}}{\partial t}+\overline{u_i}.\nabla\overline{u_i}=-\frac{1}{\rho}\nabla.\overline{P}+\nu\frac{\partial^2\overline{u_i}}{\partial x_i\partial x_j}-\frac{\partial\overline{u_i'u_j'}}{\partial x_j} \tag{3.8}$$

where,

ρ is the fluid density

$\overline{u_i}$ are the averaged fluid velocity components

i,j are counters, each one equal to [1,2,3] used to represent the three dimensions

$\overline{P}$ is the averaged fluid pressure

ν is the kinematic viscosity of the fluid

$-\overline{u_i' u_j'}$ is the Reynolds stress tensor

The above averaged Navier-Stokes equations are not closed because of the six new unknowns of the Reynolds stress tensor. From Boussinesq Approximation:

$$\tau_{ij}^R = -\rho\overline{u_i' u_j'} = 2\mu_t S_{ij} - \frac{2}{3}\rho k \delta_{ij} \tag{3.9}$$

where,

μ_t is the effective turbulent viscosity

$S_{ij} = \frac{1}{2}(\frac{\partial \overline{u_i}}{\partial x_j} + \frac{\partial \overline{u_j}}{\partial x_i})$

k is the turbulent kinetic energy

Therefore, the role of turbulence models is to quantify magnitude of the effective turbulent viscosity in the flow to be resolved and the turbulent eddies to be captured, [118].

3.4.1 One-equation Spalart-Allmaras model

The Spalart-Allmaras model is a one-equation turbulence model that solves nonlinear transport equation for the kinematic turbulent eddy viscosity. It was originally designed for aerospace and turbo machinery applications, which include wall-bounded flows, and has been calibrated for two-dimensional mixing layers, wakes, and flat plate boundary layers [119]. The model produces reasonably accurate predictions of turbulent flows with adverse pressure gradient and flows with separation [100, 119]. It requires the perpendicular distance

from the wall used in the damping functions for turbulence near wall treatment. Abaqus/CFD provides the advantage of automatically computing the normal distance function, permitting simple specification of the boundary conditions.

- The transient form of the turbulent viscosity transport equation used is given by:

$$\frac{\partial \overline{\nu}}{\partial t} + u \,.\nabla \overline{\nu} = \frac{1}{\sigma}(\nabla.((\overline{\nu}+\nu)\nabla\overline{\nu}) + c_{b2}|\nabla\overline{\nu}|^2) + c_{b1}\overline{S}(\overline{\nu})\overline{\nu} - c_{w1}f_w(\overline{\nu})(\frac{\overline{\nu}}{d})^2 \quad (3.10)$$

  where,

  $\overline{S}(\overline{\nu}) = S + \frac{\overline{\nu}}{\kappa^2 d^2} f_{v2}(x).$

- Wall functions and near wall treatment

  With the built-in low Reynolds number damping functions available in the Spalart-Allmaras model, the inner layer of the turbulent boundary layer can be resolved. However, the model usually requires fine near-wall resolutions in the order of $y^+ < 2$ to accurately predict the eddy viscosity in the entire boundary layer [100], this near-wall resolution requirement is a crucial constraint in the complex high Reynolds number flow problems. Therefore, Abaqus-CFD implements a wall-function approach to relax the near-wall resolution. The wall function approach is based on the law of the wall, which is a semi-empirical universal velocity profile in the equilibrium wall-bounded flows [120]. The wall function is defined as:

$$V^+_{(y^+)} = \begin{cases} y^+ & \text{if } y^+ \leq y^+_c \\ \frac{1}{\kappa}\ln(Ey^+) & \text{if } y^+ > y^+_c \end{cases} \quad (3.11)$$

  where,

  $V^+ = \frac{V}{\upsilon_\tau},$

υ_τ is the friction velocity (known as viscous units or wall units),

$$\upsilon_\tau = \sqrt{\frac{\tau_{wall}}{\rho}},$$

$y^+ = \dfrac{y\upsilon_\tau}{\nu}$, τ_{wall} is the shear stress at the wall,

y_c^+ is the intersection point of the linear and logarithmic velocity profile,

κ and E are constants with values 0.41 and 8.4, respectively.

A powerful advantage in Abaqus-CFD is that the above wall function is adapted to provide results for coarse meshes identical to a wall function free approach for fine meshes so it's independent of the near-wall resolution, which can be named as a hybrid wall function [121–126]. The law of the wall implemented needs to accurately predict the viscous-sublayer, the logarithmic-layer, and the buffer-layer (the region that connects the viscous and logarithmic zones), so the cell-center adjacent to the wall can be located anywhere within the inner layer producing the same results for coarser meshes [100].

3.4.2 Two-equation RNG k-ε model (Renormalization Group)

- The transport equation for turbulent kinetic energy k is:

$$\frac{\partial \rho k}{\partial t} + div[\rho k u] = div[\frac{\mu_t}{\sigma_k} grad k] + 2\mu_t S_{ij} S_{ij} - \rho\varepsilon \tag{3.12}$$

- The transport equation for dissipation of kinetic energy ε is:

$$\frac{\partial \rho \varepsilon}{\partial t} + div[\rho \varepsilon u] = div[\frac{\mu_t}{\sigma_\varepsilon} grad \varepsilon] + C_{1\varepsilon}\frac{\varepsilon}{k} 2\mu_t S_{ij} S_{ij} - C_{2\varepsilon}\rho\frac{\varepsilon^2}{k} \tag{3.13}$$

where,

u represents velocity component in the corresponding direction

S_{ij} represents component of rate of deformation

μ_t represents eddy viscosity

$$\mu_t = \rho C_\mu \frac{k^2}{\varepsilon} \tag{3.14}$$

The values of constants are

$C_\mu = 0.0845, \sigma_k = 0.72, \sigma_\varepsilon = 0.72, C_{1\varepsilon} = 1.42, C_{2\varepsilon} = 1.68$, [118]

- The turbulence quantities initial conditions

  1. Turbulence kinetic energy

  $$k = \frac{3}{2}(UI)^2 \tag{3.15}$$

  Where,

  U represents the initial velocity magnitude

  I represents the initial turbulence intensity, given below.

  $$I = 0.16 R_e^{-1/8} \tag{3.16}$$

  2. Turbulence kinetic energy dissipation rate

  $$\varepsilon = C_\mu^{3/4} k^{3/2} l^{-1} \tag{3.17}$$

  Where,

  l represents the turbulence or eddy length scale, given below.

  C_μ = 0.0845, a $k-\varepsilon$ model parameter whose value is the same as in Equation 3.14

  $$l = 0.07L \tag{3.18}$$

Where L is the characteristic length.

3.5 Finite element analysis governing equations

Finite element analysis is used, in general, to solve physical, engineering and design problem, but in the current study it was used to solve the structural model of the eye. According to the flowchart in Figure 3.6, the physical problem which describes the actual structural design that is subjected to different loads, is modelled mathematicaly with appropriate differential equations, but this mathematical modelling involves some assumptions to the actual problem [127, 128, 116]. The finite element analysis with all its procedure solves this mathematical model.

Finite element analysis procedure start with discretising the continous bulk domain into finite elements assembly through preprocessing program. These elements are connected to each other via nodes, each node has a value for unknown variable. Values inside the elements are calculated through numerical interpolation functions. In order to produce matrix equations relating between the nodal values and the element properties such as material characteristics, Galerkin method or variational formulation are the most convenient methods for this task [127, 128, 116]. The produced system of linear equations for the element assemply is solved by linear algebra after defining appropriate boundary conditions for the problem. Below is a detailed explanation of the process of producing the system of equation assemply.

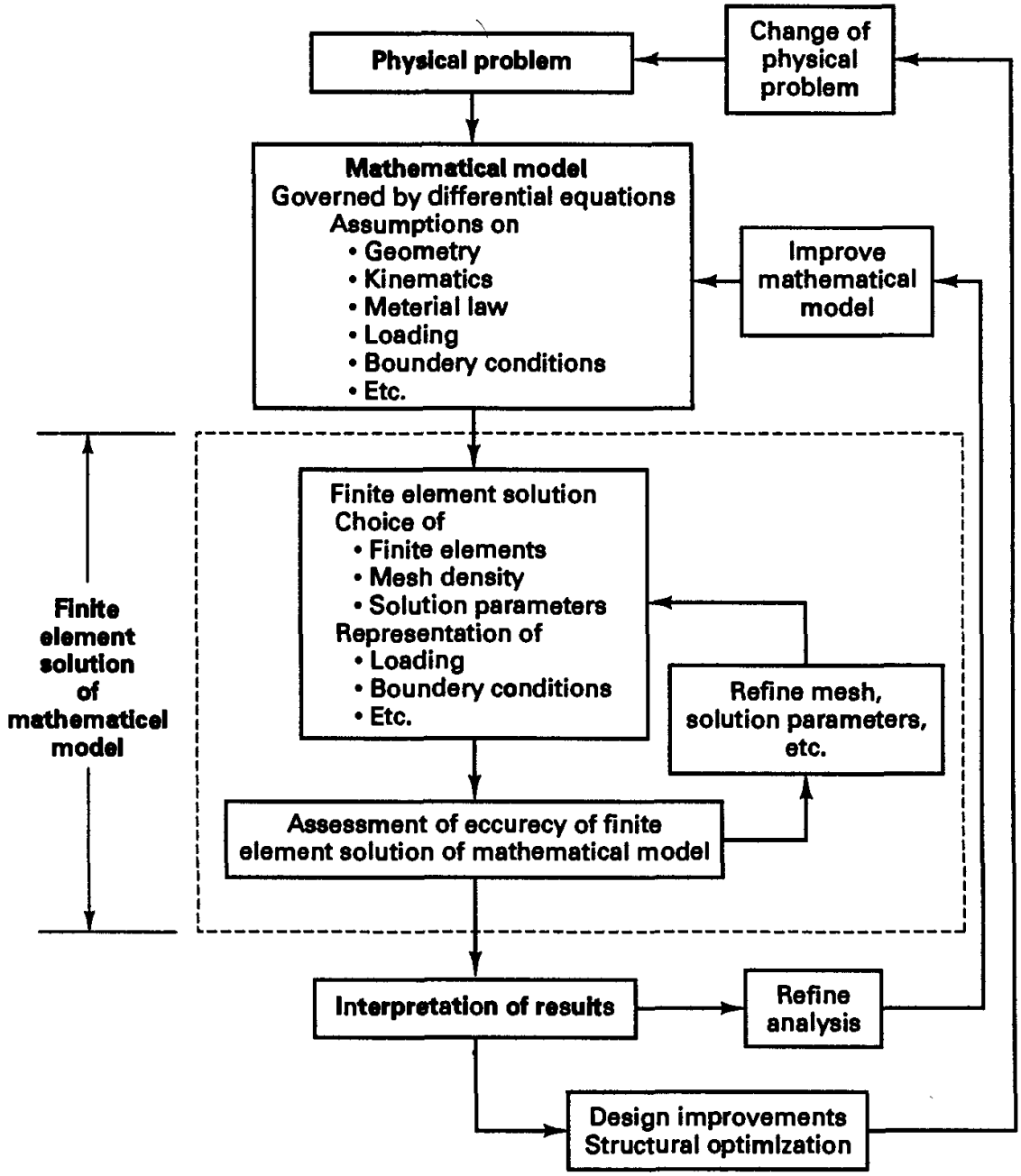

Figure 3.6 The flow chart of finite element analysis as a part of physical problem solving [127]

For a three-dimensional finite element, the nodal displacement vector (q) contains the displacement values at every node and takes the form in Equation 3.19. Using the

interpolation or shape functions (N), the displacements at any point in the element can be quantified using Equation 3.20.

$$\{q\} = \{u_1\ v_1\ w_1\ u_2\ v_2\ w_2\ ....\} \tag{3.19}$$

$$\{U\} = [N]\{q\},\ [N] = \begin{bmatrix} N_1 & 0 & 0 & N_2 & ... \\ 0 & N_1 & 0 & 0 & ... \\ 0 & 0 & N_1 & 0 & ... \end{bmatrix} \tag{3.20}$$

The strain matrix consists of the six strain componenets in equation 3.21 and can be calculated from the displacement matrix by multiplying the diffrenitiation opertor (D) as explained in Equation 3.22.

$$\{\varepsilon\} = \{\varepsilon_x\ \varepsilon_y\ \varepsilon_z\ \gamma_{xy}\ \gamma_{yz}\ \gamma_{zx}\} \tag{3.21}$$

$$\{\varepsilon\} = [D]\{U\},\ [D] = \begin{bmatrix} \partial/\partial x & 0 & 0 \\ 0 & \partial/\partial y & 0 \\ 0 & 0 & \partial/\partial z \\ \partial/\partial y & \partial/\partial x & 0 \\ 0 & \partial/\partial z & \partial/\partial y \\ \partial/\partial z & 0 & \partial/\partial x \end{bmatrix} \tag{3.22}$$

The stress tensor consists of the six stress components in Equation 3.23 which are related to strains by Hook's law for elastic materials as in Equation 3.24.

$$\{\sigma\} = \{\sigma_x\ \sigma_y\ \sigma_z\ \tau_{xy}\ \tau_{yz}\ \tau_{zx}\} \tag{3.23}$$

$$\{\sigma\} = [E]\{\varepsilon\},\ [E] = \begin{bmatrix} \lambda+2\mu & \lambda & \lambda & 0 & 0 & 0 \\ \lambda & \lambda+2\mu & \lambda & 0 & 0 & 0 \\ \lambda & \lambda & \lambda+2\mu & 0 & 0 & 0 \\ 0 & 0 & 0 & \mu & 0 & 0 \\ 0 & 0 & 0 & 0 & \mu & 0 \\ 0 & 0 & 0 & 0 & 0 & \mu \end{bmatrix} \tag{3.24}$$

where λ *and* μ are elastic constants in terms of modulus of elasticity (E) and poisson's ratio (ν) of the elastic material, Equation 3.25.

$$\lambda = \frac{\nu E}{(1+\nu)(1-2\nu)},\ \mu = \frac{E}{2(1+\nu)} \tag{3.25}$$

The final solution for the finite element analysis is to find the minimum of functional of the strain energy potential ($\prod$) which defines the stored energy in unit volume of the material, Equation 3.26 [127, 128, 116].

$$\prod = \int_V \frac{1}{2}\{\varepsilon\}^T\{\sigma\}dV - \int_V \{U\}^T\{p^V\}^T dV - \int_S \{U\}^T\{p^S\}^T dS \tag{3.26}$$

where $\{p^V\}$ is the body force and $\{p^S\}$ is the surface forces on the element.

Ogden hyper-elastic material model

In case of the corneal and scleral tissues of the eye, they behave non-elastically, or in other words, they have a hyper-elastic non-linear behaviour based on prior experimental studies [5, 6, 20, 129]. The hyper-elastic materials have a rubber-like material behaviour and the strain energy potential function is different than elastic materials and it takes multiple forms. The Ogden form was the one applied in the finite elment model of the human eye as shown in Equation 3.27 [100–102, 99].

$$\prod = \sum_{i=1}^{N} \frac{2\mu_i}{\alpha_i^2}(\bar{\lambda}_1^{\alpha_i} + \bar{\lambda}_2^{\alpha_i} + \bar{\lambda}_3^{\alpha_i} - 3) + \sum_{i=1}^{N} \frac{1}{D_i}(J^{el} - 1)^{2i}, \tag{3.27}$$

where $\bar{\lambda}_i$ are the deviatoric principal stretches which are related to the deformations at constant volume as outcome of shear stresses [100, 103]; N defines the order of the Ogden model with maximum of sixth order (N=6); μ and α are material parameters; J^{el} is the elastic volume ratio related to thermal expansion and D_i defines the material compressibility.

Chapter 4

Research methodology

4.1 Introduction

Understanding the mechanical behaviour of biological soft tissues is a challenging task which requires development of accurate tools and processes to be capable of predicting the tissues' response to different loadings. In order to predict biomechanical response of the cornea to internal and external loadings in the air puff test, a set of parametric studies have to be performed to include the most influential factors affecting corneal deformation. The parametric studies, in general, can be experimental on ex-vivo eyes, clinical on real patients or numerical using computer analysis. In the current study, these methods were employed to validate the obtained results according to the validation and verification guidelines in computational biomechanics [130–132]. The main objectives in the present study, are to produce a biomechanical estimation algorithm for the intraocular pressure taking into account fluid structure interaction effect on air pressure distribution on the cornea during air puff test and use this in efforts to estimate the material behaviour of corneal tissue in-vivo.

The work started with the development of numerical tools for analysis, followed by their validation of against clinical and experimental data, then using them to answer the research questions, Figure 4.1. The main aim of this study is to improve understanding of the importance of fluid structure interaction in analysis of corneal behaviour in dynamic air pressure testing via producing an accurate numerical simulation of the air puff test. The air puff tonometry test is an interaction between a transient air jet and a model of the eye globe with hyper-elastic material. This means dealing with two different models with

different governing equations; one is a structural model analysed using finite element method to calculate deformations and stresses in ocular tissue material, and a computaional fluid dynamics (CFD) model to simulate the air puff and calculate the pressure acting on the eye globe. The most challenging part is the multi-physics fluid-structure interaction (FSI) coupling between the two models and analysing them at the same time.

The interaction includes the exchange of data and results between the two models. As shown in Figure 4.2, the structural model calculates the deformations (line 1) and sends them to the fluid model (line 2) which in turn calculates the pressure loads(line 3) and returns them back to the structural model (line 4). This process takes place at each time step (Δt) of the computation time and is repeated through the analysis. Table 4.1 shows a comparison between available finite element software packages and the availability of FSI simulation capabilities within their codes. The finite element model of the whole eye created by bespoke software of the biomechanics group was used as the structural model [5, 20, 101, 129], in which the hyper-elastic and viscoelastic properties of the ocular vessel were defined. In previous attempts made on that eye model to simulate the tonometry test, the air puff pressure was applied as an external static pressure load with a fixed spatial and temporal distribution as provided by Oculus, which didn't take into account the effect of fluid structure interaction [19, 20, 66].

There are various options for fluid structure interaction simulation, CFD solvers such as ANSYS CFX or FLUENT, Star-CCM+, COMSOL, OpenFoam can be coupled to the finite element model of the eye built in ABAQUS, but each software will need an intermediate interface to control the coupling. What was employed in the present study is ABAQUS CFD (Version 6.14 , Dassault Systemes Simulia Inc., USA) [100] as there is a co-simulation engine (CSE) in ABAQUS which enables two-way coupling between the structure and the fluid models. This coupling mechanism was tried, tested and validated in the present study.

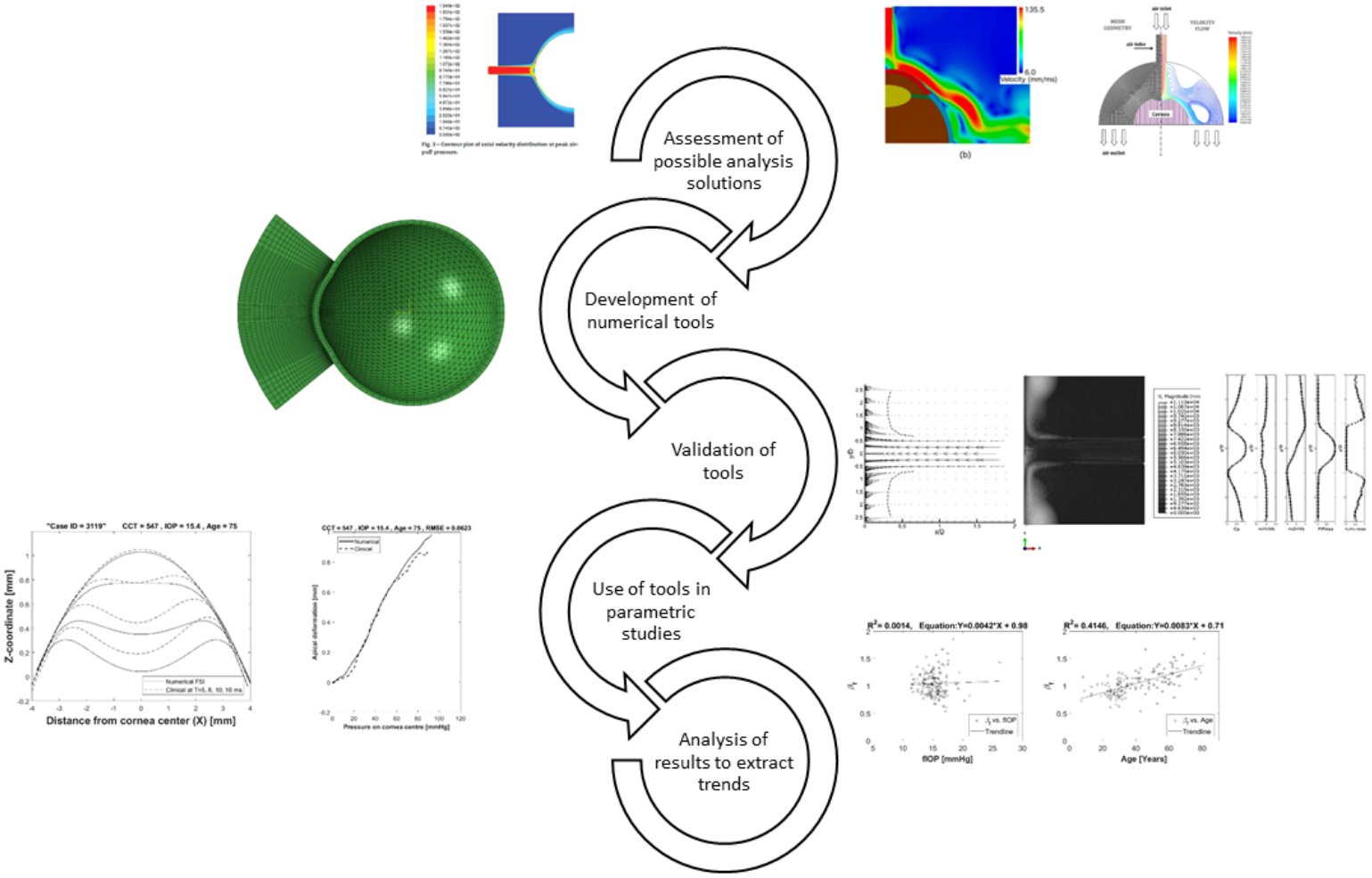

Figure 4.1 Flow chart of research progress

Table 4.1 FEA software packages and their capabilities in modelling fluid structure interaction [133]

Software	Graphical geometry modeler	Graphical manual meshing	CAD import	Units aware	Linear static	Non-linear large displacements	Non-linear contact	Transient linear	Transient non-linear	Acoustic	Heat transfer	Fluid flow	Fluid structure interaction	Anisotropic materials	Hyperelastic materials	Plasticity
Abaqus/CAE	✓	✓	✓	×	✓	✓	✓	✓	✓	✓	✓	✓	✓	✓	✓	✓
LS-DYNA	✓	✓	✓	✓	✓	✓	✓	✓	✓	✓	✓	✓	✓	✓	✓	✓
ADINA	✓	✓	✓	✓	✓	✓	✓	✓	✓	✓	✓	✓	✓	✓	✓	✓
ANSYS Mechanical	✓	✓	✓	✓	✓	✓	✓	✓	✓	✓	✓	✓	✓	✓	✓	✓
midasNFX	✓	✓	✓	✓	✓	✓	✓	✓	✓	×	✓	✓	✓	✓	✓	✓
NISA Mechanical	×	×	✓	✓	✓	✓	✓	✓	✓	×	✓	✓	✓	✓	✓	✓
AMPS	✓	✓	×	✓	✓	✓	✓	✓	✓	×	✓	✓	✓	✓	✓	✓
COMSOL Multiphysics	✓	✓	✓	✓	✓	✓	✓	✓	✓	✓	✓	✓	✓	✓	✓	✓
MSC Nastran	×	×	✓	✓	✓	✓	✓	✓	✓	✓	✓	×	✓	✓	✓	✓

Table 4.1 FEA software packages and their capabilities in modelling fluid structure interaction [133]

Software	Graphical geometry modeler	Graphical manual meshing	CAD import	Units aware	Linear static	Non-linear large displacements	Non-linear contact	Transient linear	Transient non-linear	Acoustic	Heat transfer	Fluid flow	Fluid structure interaction	Anisotropic materials	Hyperelastic materials	Plasticity
NX Simcenter 3D	✓	✓	✓	✓	✓	✓	✓	✓	✓	✓	✓	✓	✓	✓	✓	✓
Elmer	×	×	✓	×	✓	✓	×	✓	✓	×	✓	✓	✓	✓	×	×
FEBio with PreView	✓	×	×	×	✓	✓	×	✓	✓	×	✓	✓	×	✓	✓	✓
Code_Aster	×	×	×	×	✓	✓	✓	✓	✓	×	✓	×	✓	✓	✓	✓
Cast3M	×	×	×	×	✓	✓	✓	✓	✓	×	✓	✓	✓	✓	✓	✓
CalculiX	×	×	×	×	✓	✓	✓	✓	✓	×	✓	✓	×	✓	✓	✓

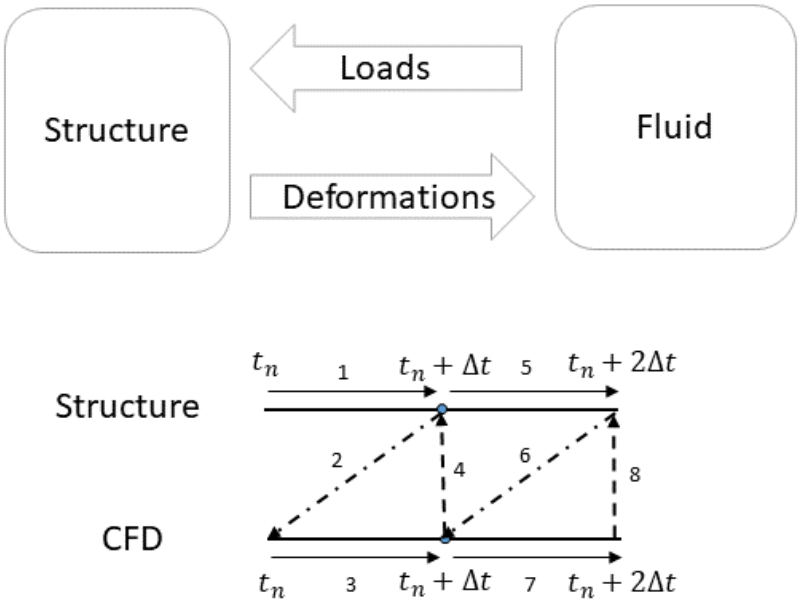

Figure 4.2 Components of fluid structure interaction (FSI) analysis and flow of information at each time step

4.2 Numerical Methods

The numerical model of the air puff test is constructed in the context of a coupled Computational Fluid Dynamics (CFD) and Finite Element Analysis (FEA), as implemented in the software package ABAQUS. The air puff test simulation consists of three components:

1. Three dimensional finite element model of the eye and material models for ocular tissue
2. Three dimensional CFD turbulence model of the air puff impinging on the cornea
3. Fluid structure interaction (FSI) between the two models

4.2.1 Three dimensional eye model

The eye model consisted of 3676 fifteen-nodded continuum elements (C3D15H), a general purpose element with 9 integration points, arranged over two layers based on earlier element

type study findings [134], distributed along 15 rings in the cornea and 35 rings in the sclera. This construction was based on a mesh sensitivity analysis, whose results are reported in Section 5.3.1. The corneal topography was based on the Pentacam's measurements of topography and thickness profile. The Pentacam is a combined ocular device that employs a Scheimpflug camera and an illumination system which rotates around the eye to scan its topography, [135]. The model also incorporated attributes to represent in-vivo conditions including the non-uniform thickness of cornea and sclera, weak inter-lamellar adhesion in corneal stroma and aspherity of the cornea's anterior and posterior surfaces [101].

The eye model included different material definitions for cornea and sclera behaving hyper-elastically [5, 6, 20, 129]. The materials are known to behave differently under loading and unloading. Their stiffness increases gradually under loading and it follows an S-shaped stress-strain path [129]. With these important features, the model was capable of selecting which stress-strain path (under loading or unloading) that each element would follow based on its strain history [101]. The constitutive material model representing mechanical response of the cornea and sclera was the first order Ogden hyper-elastic model [101, 102, 99].

The finite element model of the eye was prevented from rigid body motion in the Z-direction (anterior-posterior) at the equatorial nodes. Also, the posterior and anterior pole nodes were restricted in both X and Y directions but were free to move in the Z-direction (anterior-posterior), see Figure 4.3. Before analysis, the stress-free geometry of the eye, under zero IOP, was estimated. It is important to calculate the un-deformed configuration of the eye before applying the IOP internal stresses because deformed geometry of the eye will not be suitable for applying different values of IOP. An iterative approach is used to gradually subtract deformations from the nodes' coordinates to reach the stress-free (relaxed) configuration of the ocular tissue [101, 136]. An initial numerical model was generated based on a measured value of IOP and patient-specific geometry of the ocular tissue. The

calculated deformations are then subtracted from the stressed geometry to get the relaxed (stress-free) geometry.

Fluid cavity was the technique used to represent IOP inside the eye. This technique is mainly used to simulate fluid-filled structures such as pressure vessels, hydraulic or pneumatic actuators and automotive air bags. The fluid cavity behaviour governs the relationship between cavity pressure, structure deformation and volume. The fluid cavity calculates the change in IOP and internal volume during application of the air puff and corneal deformations. The fluid cavity was filled with a fluid with a density of (1,000 Kg/m3) and bulk modulus of (2.2×10^3 MPa) [137]. A reference node was specified inside the cavity to represent the applied pressure and used in the volume calculations. Despite there are multiple components inside the eye including ocular lens, iris, aqueous and vitreous, the human eye was dealt with as a deformable pressure vessel that has internal pressure equal to IOP applied using a fluid cavity taking into account the change in pressure with the change in volume.

4.2.2 Three dimensional CFD turbulence model of the air puff

Model of the air puff consisted of 25920 six-nodded 3-D fluid continuum elements (FC3D6) based on the mesh sensitivity analysis conducted in Section 5.3.1 and uses a turbulence model (Spallart-Almaras or RNG K-ε) [119, 118] to simulate the turbulence in the air jet. The air model domain and its mesh are created over the cornea and a 4 mm ring of the sclera by projecting coordinates of the anterior surface nodes to a distance of 11 mm from the cornea apex as the typical distance for an air puff test in eye clinics as shown in Figure 4.4. It is based on the concept of similar triangles to project the known coordinates of the cornea to calculate the new coordinates of air domain. Equation 4.1 clarifies this concept and based on shape of the mesh, and how fine it is, the layer thickness was specified and applied to the (X,Y, and Z) coordinates of the targeted area.

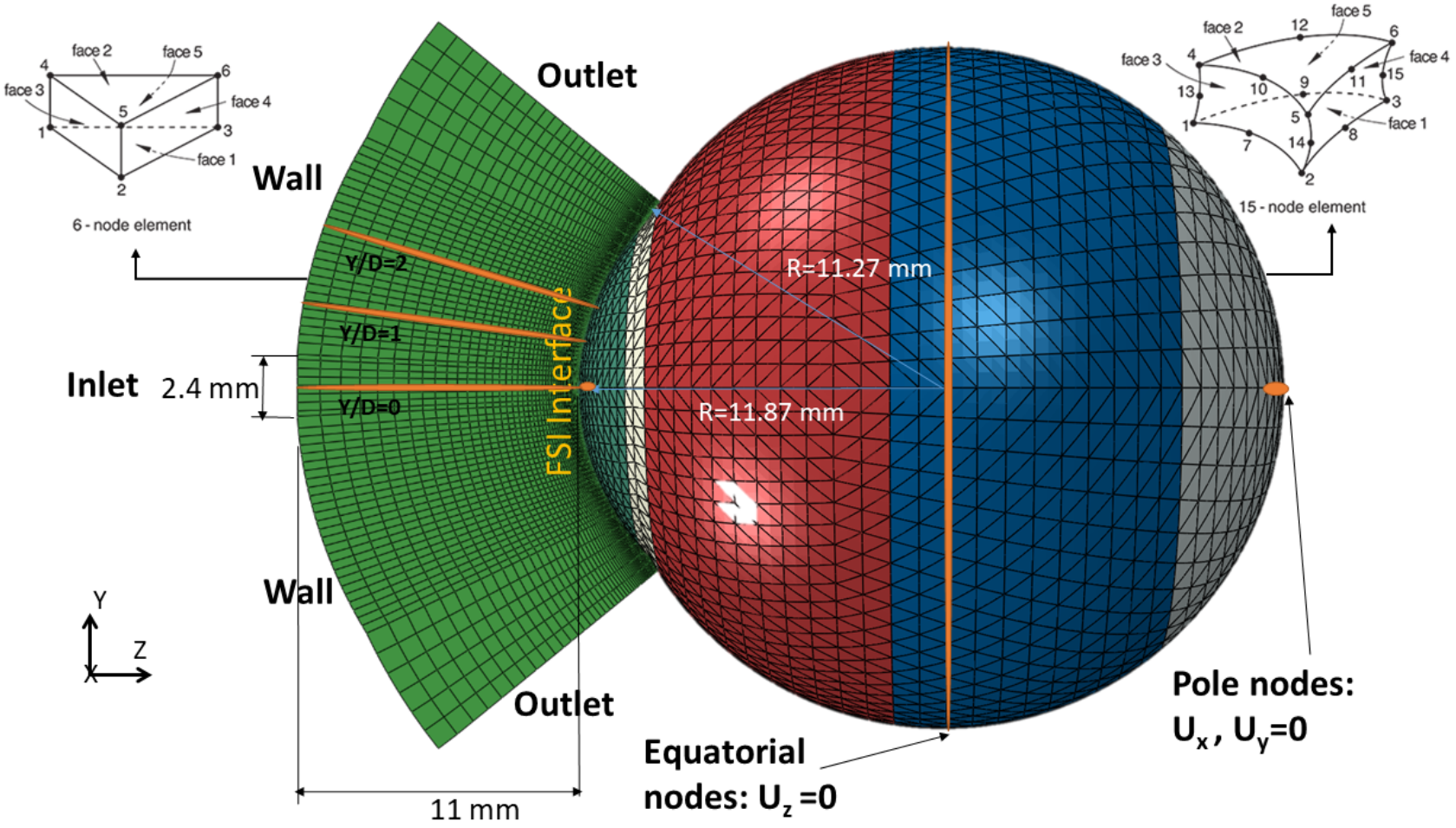

Figure 4.3 Geometry definition of the CFD and eye domains showing key dimensions, element types and boundary conditions. U_x, U_y, U_z are deformations in the three dimensions

It was important to generate a code which was applicable for all geometries of the eye, idealised and healthy patient-specific or with certain pathological conditions. The code was built in Matlab and was made able to take the eye model; input, material and node files and produce a modified eye input file and an air input file with air domain node and element files ready for the co-simulation coupling.

$$\frac{X_1}{X_2} = \frac{Y_1}{Y_2} = \frac{Z_1}{Z_2} = \frac{L_1}{L_2} \tag{4.1}$$

Material properties of air were defined in terms of density ($1.204 Kg/m^3$) and viscosity ($1.83 \times 10^{-5} Kg/(m.s)$) [138–140]. Amplitude of the air jet velocity, and its variation with time were defined along with the initial turbulent kinematic eddy viscosity ($68 \times 10^{-6} m^2/s$) [100, 138–140]. The CFD solution parameters are then specified in terms of momentum, pressure and transport equation solvers and which turbulence model is to be used to resolve the turbulent eddies.

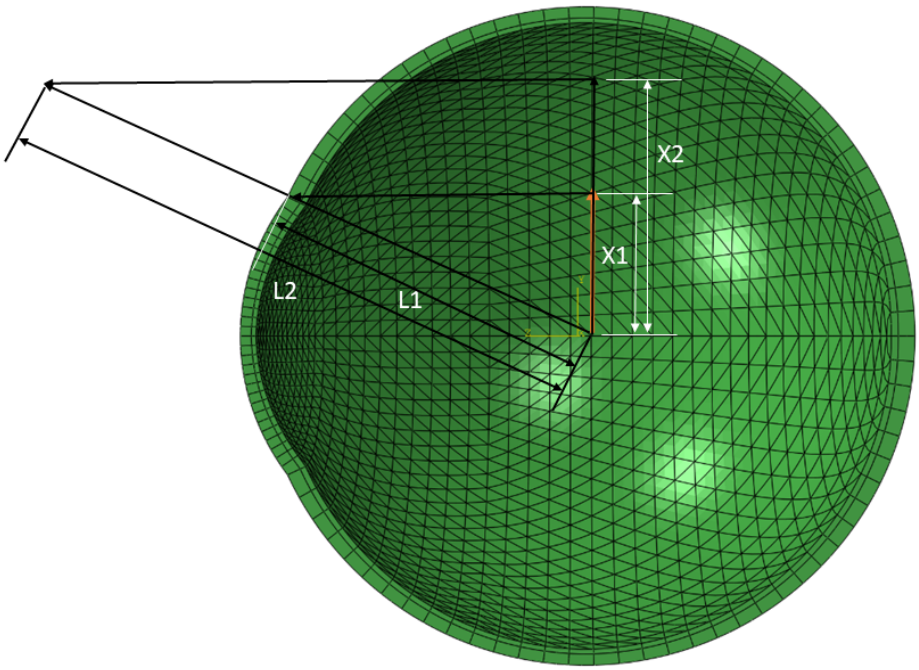

Figure 4.4 Projection principle used in generation of air domain mesh

In the CFD model, the air jet inlet diameter was set to 2.4 mm, the same as measured for the nozzle of CorVis-ST [68], and the air maximum velocity at the inlet was set to 167.8 m/s based on the air piston velocity. The change in velocity with time is shown in Figure 4.5, based on experimental data obtained from the CorVis-ST manufacturers [68, 21] which will be explained in details in next subsection 4.2.3. The surface that surrounds the jet diameter is set as a no-slip wall boundary condition while the side is open to the air with pressure equal to zero. Lastly, the cornea and 3 rings from sclera, where there is no deformation beyond this distance from cornea centre [129, 101], were set to co-simulation interface and data exchange surface. Table 4.2 summarises the initial and boundary conditions used in the CFD model. The air puff model geometry and boundary conditions' parameters are shown in Figure 4.3. The air puff device is equipped with a high speed camera (4330 images/s, 576 measuring point per image (80 640 per examination)) to capture corneal deformation under the effect of air puff over a period of 30 ms, where the conea returns to its original shape [68, 21]. The cornea shows first applanation around time t=9.66 $\pm$ .97 ms, maximum deformation around t=16.2 $\pm$ .36 ms and second applanation around t=22 $\pm$ 0.8 ms.

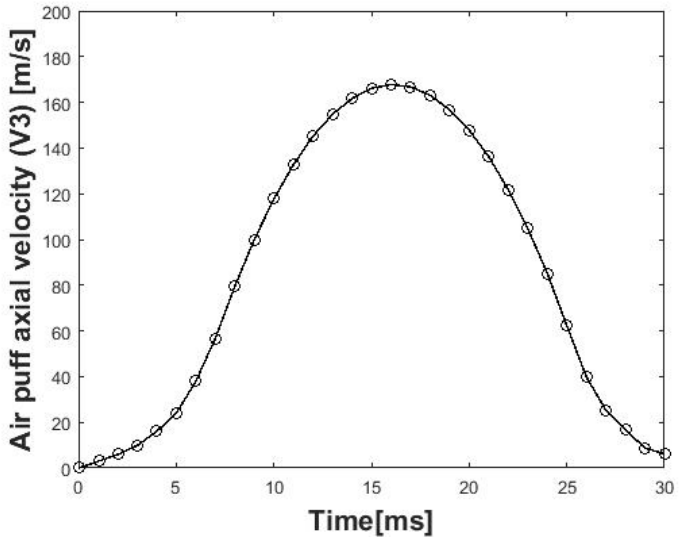

Figure 4.5 Temporal velocity profile at the air puff nozzle fed as inlet boundary condition to CFD air puff model

Table 4.2 Initial & Boundary Conditions used for the CFD model

Condition	Value
Characteristic length	Orifice Diameter = 2.4 mm
Reynolds number	23702.26
Turbulent kinematic viscosity IC	$68 \times 10^{-6}\ m^2/s$
Turbulent Kinetic Energy IC (k)	$87.23457\ m^2/s^2$
Turbulent Dissipation IC (ε)	$760092\ m^2/s^3$
Inlet BC	$Vx = 0, Vy = 0, Vz = -167.891\ m/s$ maximum velocity with amplitude with time
Outlet BC	$P = 0\ N/mm^2$
Wall BC	No slip Boundary Condition
FSI interface	Fluid structure interaction surface

C O S I M U L A T I O N I N T E R F A C E S

Surface	Import/Export	Field
CORNEA-SCLERA	Import	U
CORNEA-SCLERA	Import	V
CORNEA-SCLERA	Export	LUMPEDMASS
CORNEA-SCLERA	Export	TRSHR

Note: BC is boundary condition, IC is initial condition, U is deformation, V is velocity, TRSHR is surface shear traction.

4.2.3 CFD simulation of flow inside CorVis-ST

In order to obtain the right boundary conditions for CFD model of the air puff, a contact was made with CorVis-ST manufactureres [68] to get information about the temporal velocity distribution at the device nozzle. The manufacturer provided a three dimensional CAD

drawing of the internal components of the device, Figures 4.6, 4.7, a video for the piston movement during applying the air puff, Figure 4.8 and data about the piston speed, piston's distance and chamber pressure, Figure 4.9. The manufacturer mentioned that there is no velocity measurement at the nozzle tip, but from calculation using incompressible continuity equation 4.2, the maximum air velocity at the nozzle was obtained to be 168 m/s knowing that the maximum piston speed equals to 2 m/s, piston diameter is 22 mm and nozzle diameter is 2.4 mm.

$$A_{Piston} \times V_{Piston} = A_{Nozzle} \times V_{Nozzle} \tag{4.2}$$

where A is the cross sectional area and V is air velocity at the piston or nozzle locations. A CFD simulation of the flow inside the internal geometry of CorVis-ST was made as a further validation of air exit velocity from the device nozzle. Figure 4.10 shows velocity contours of air inside the device as obtained using commercial CFD code ANSYS Fluent R14.5 (ANSYS, Inc, Pennsylvania, USA) [141]. By probing value of velocity at the nozzle, it was equal to 167.89 m/s. By applying the same temporal velocity distribution of the piston to the nozzle, inlet boundary condition of the air puff model was obtained, as shown previousley in Figure 4.5. Figures 4.11 and 4.12 show the air streamlines and pressure values inside device, respectively.

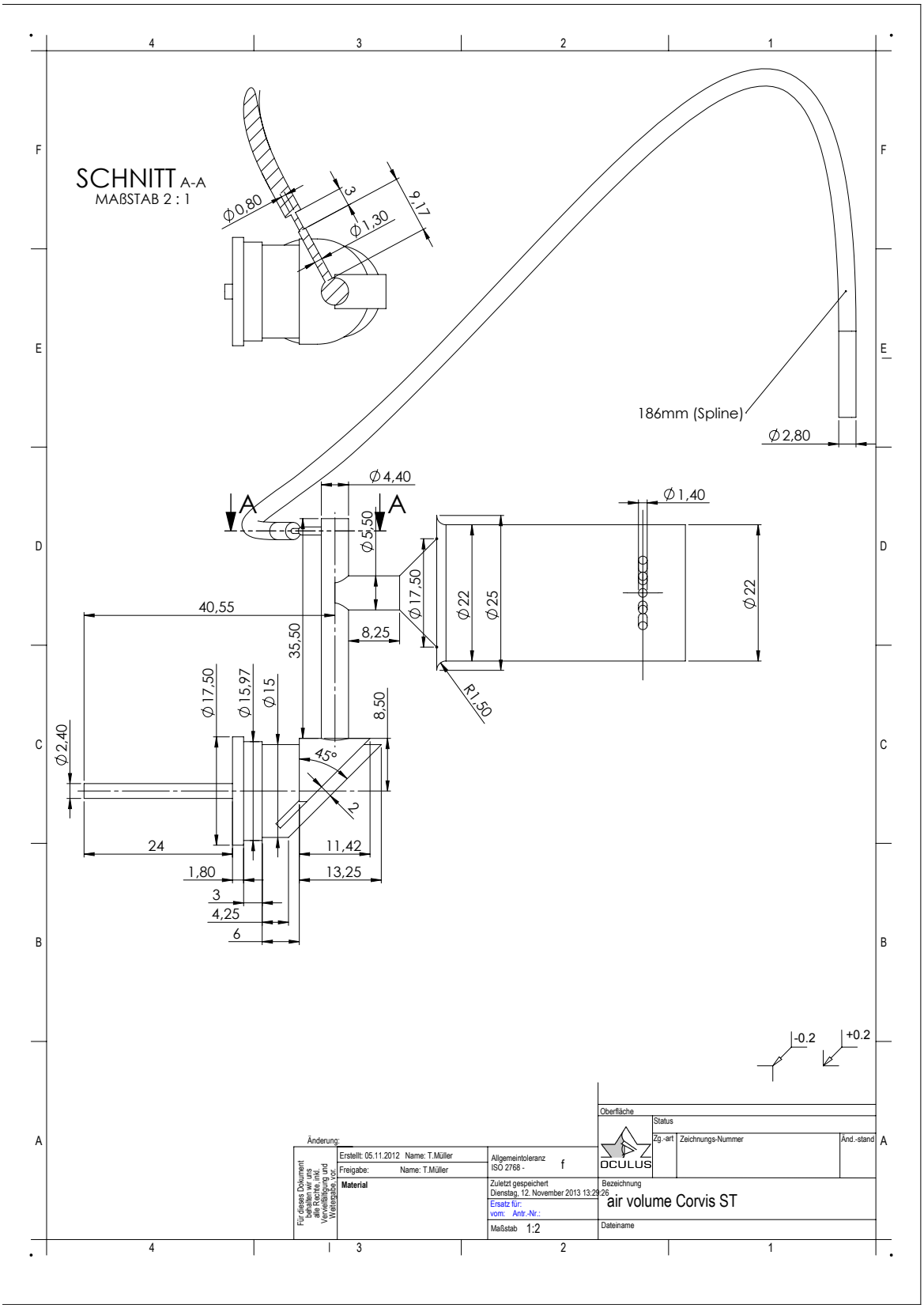

Figure 4.6 Internal geometry of CorVis-ST starting from piston to nozzle exit [68]

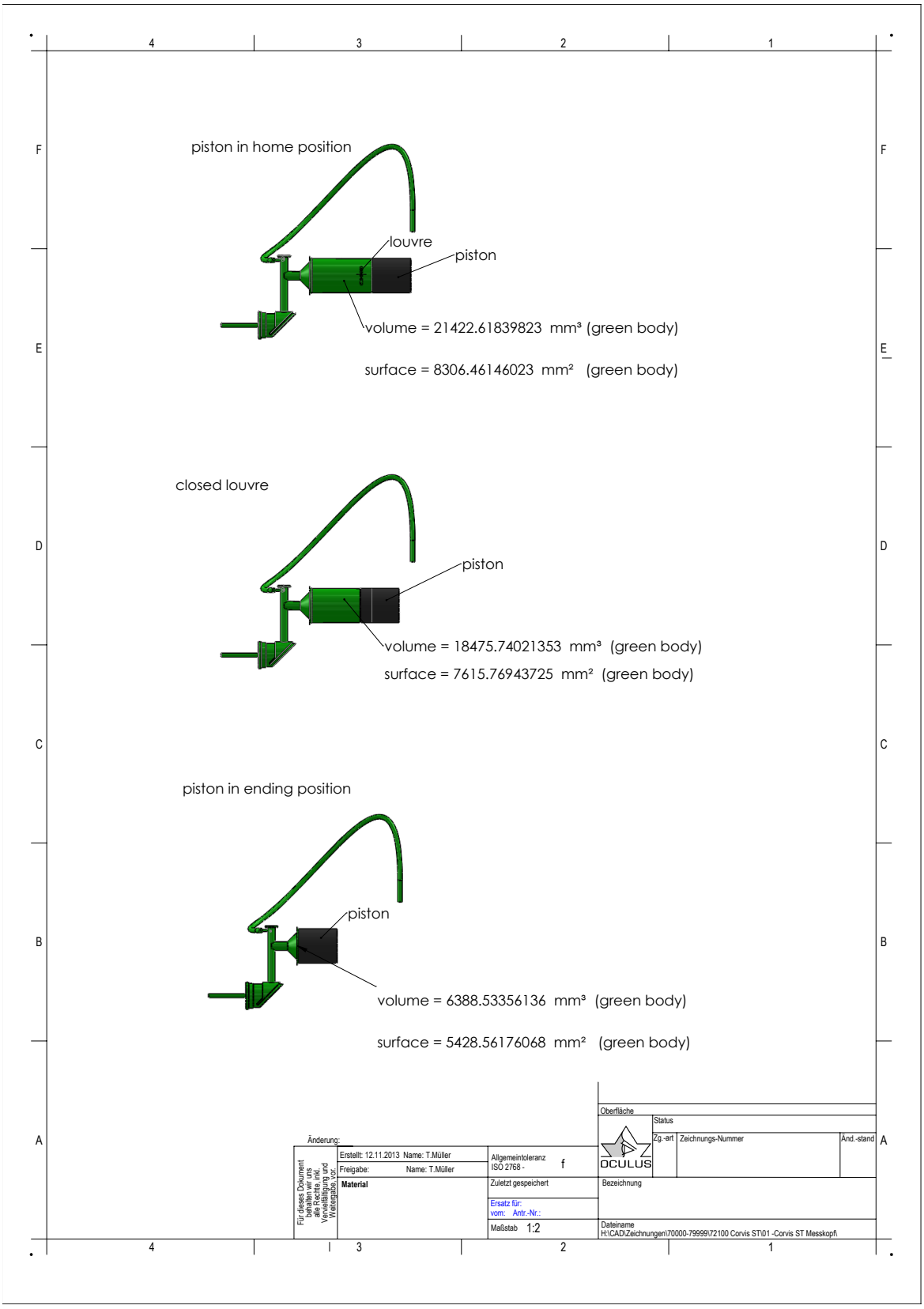

Figure 4.7 Air volume inside CorVis-ST starting from piston to nozzle exit [68]

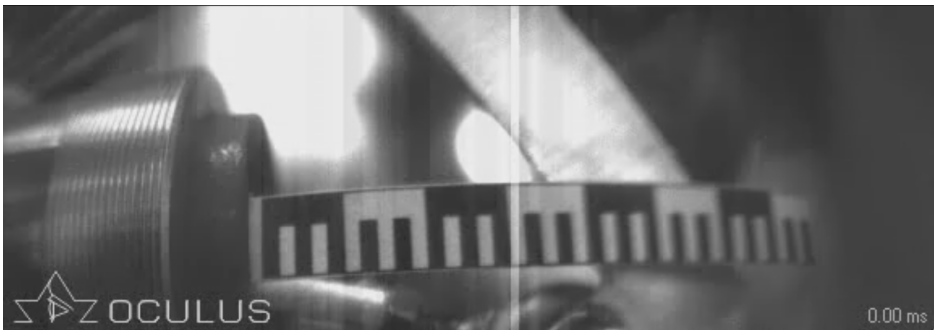

(a) Piston at initial state, time = 0 ms

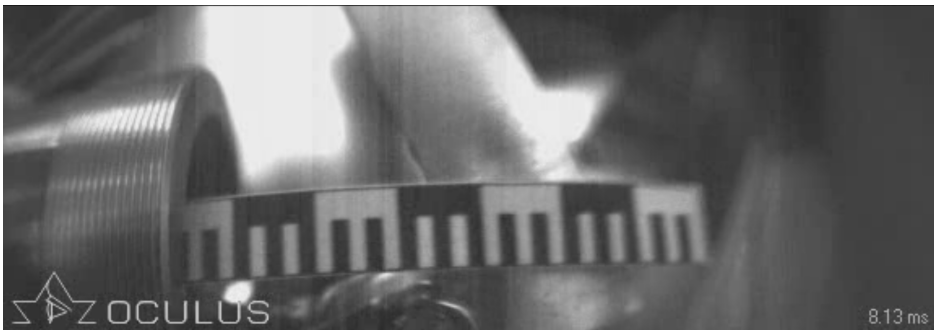

(b) Piston at time = 8.13 ms

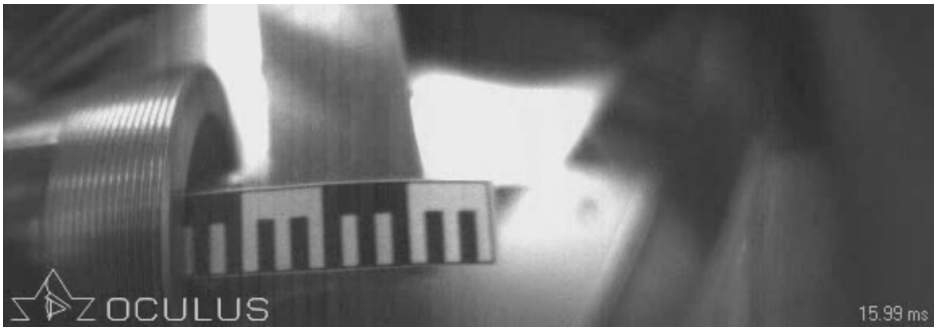

(c) Piston at time = 15.99 ms

Figure 4.8 CorVis air piston movement during air puff test at times 0, 8.13, 15.99 ms [68]

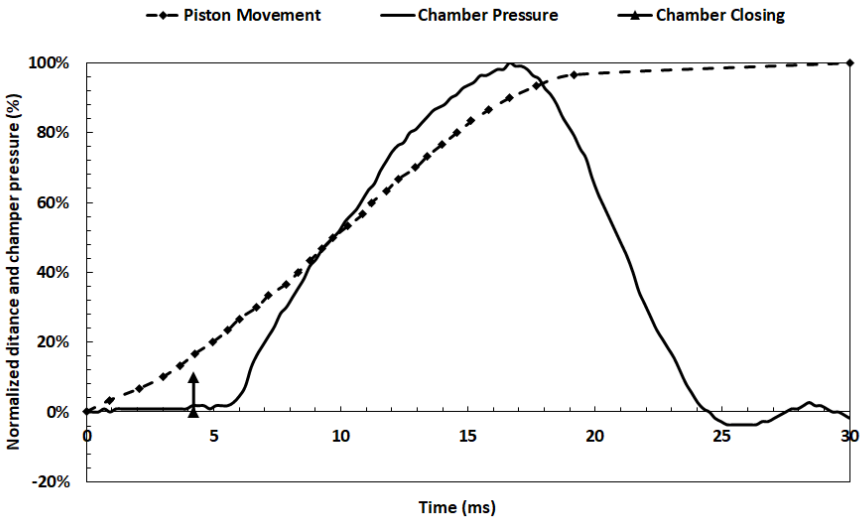

(a) Normalised piston movement and normalised champer pressure against time

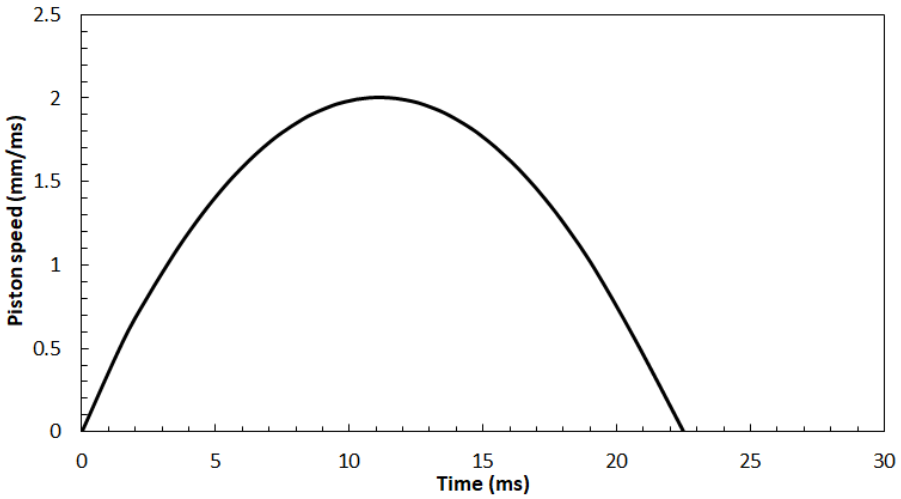

(b) Piston speed

Figure 4.9 CorVis air piston movement and its effect on pressure champer (a) and piston speed (b) [68]

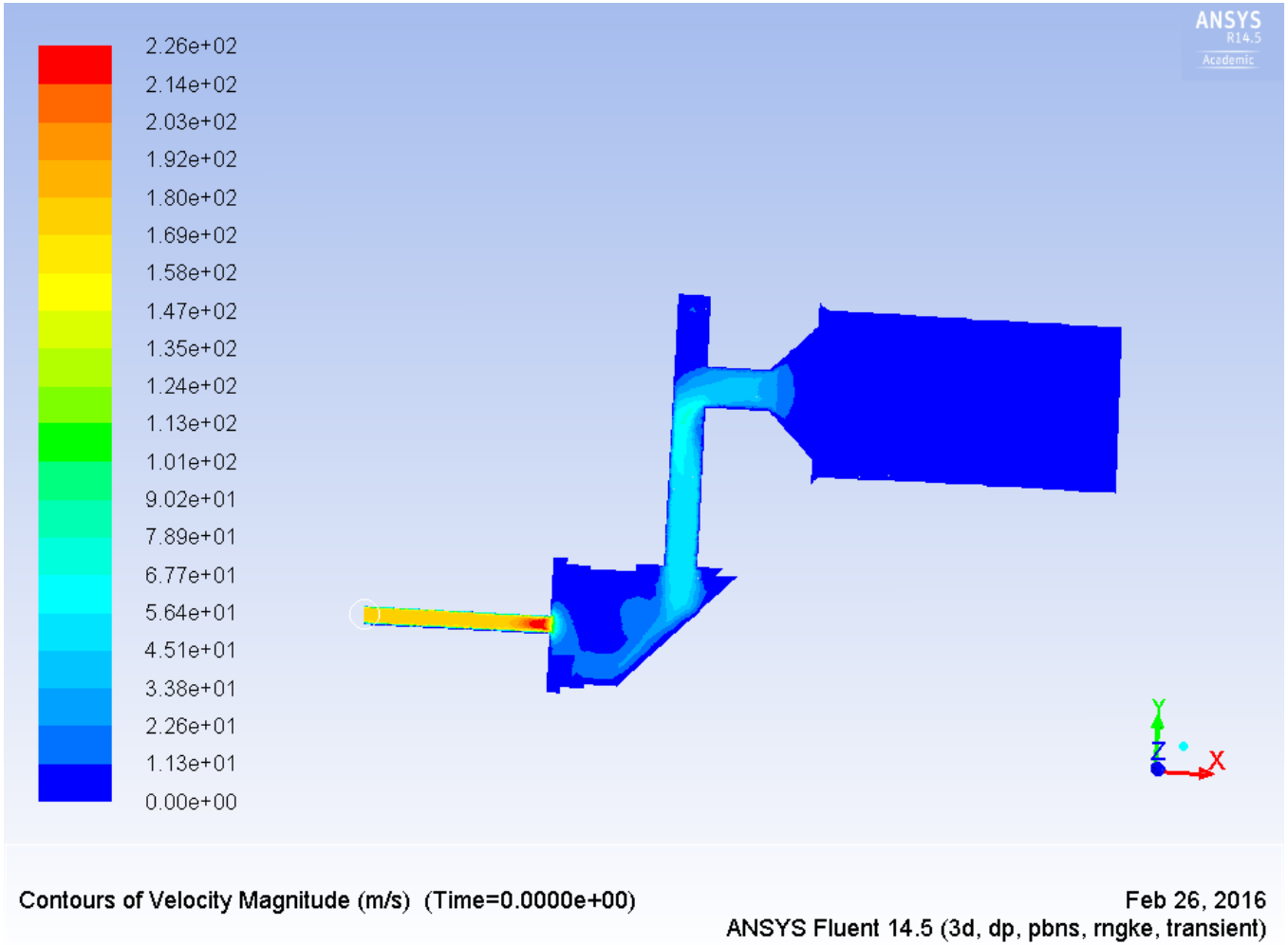

Figure 4.10 Velocity contours inside CorVis-ST

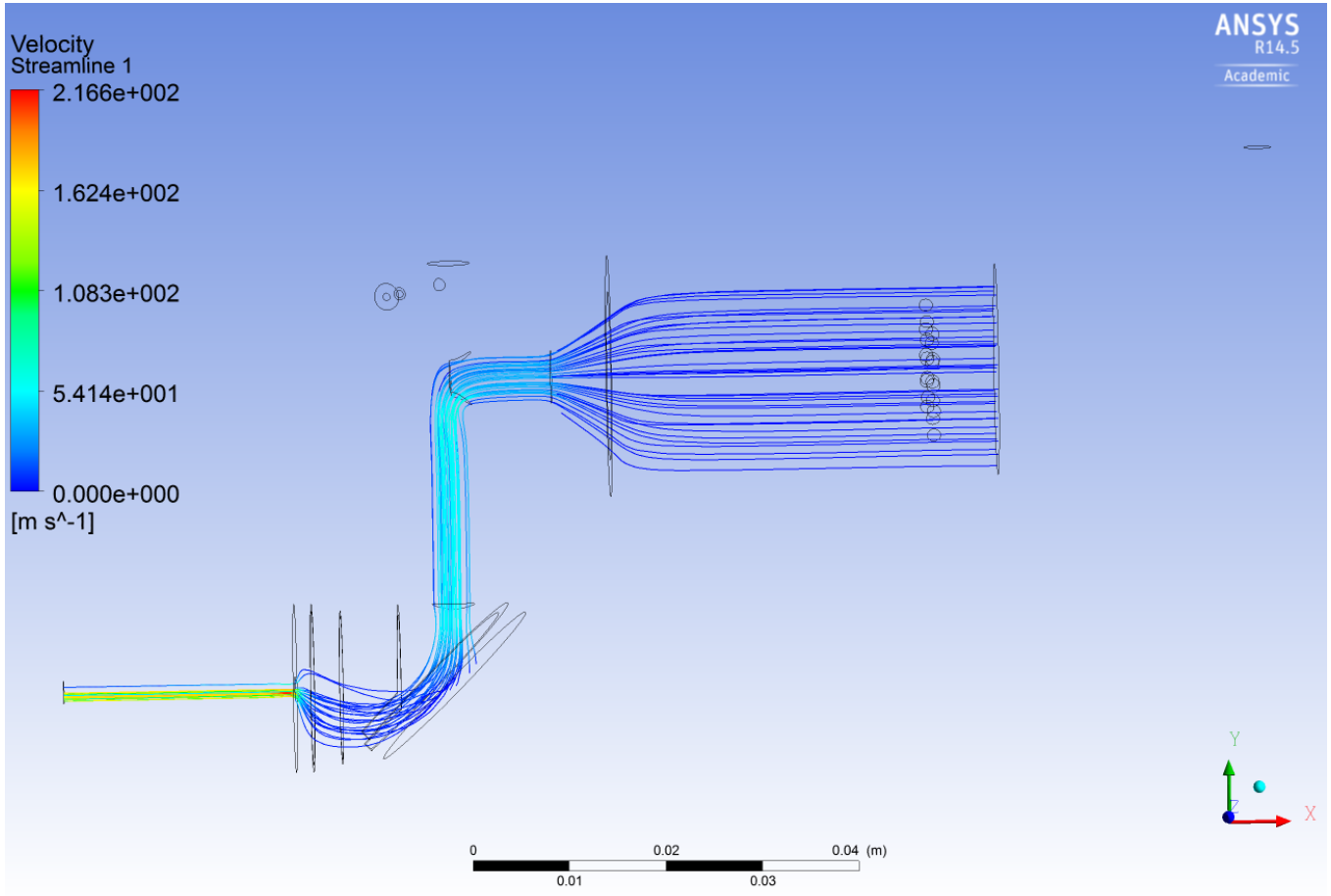

Figure 4.11 Streamlines of air inside CorVis-ST

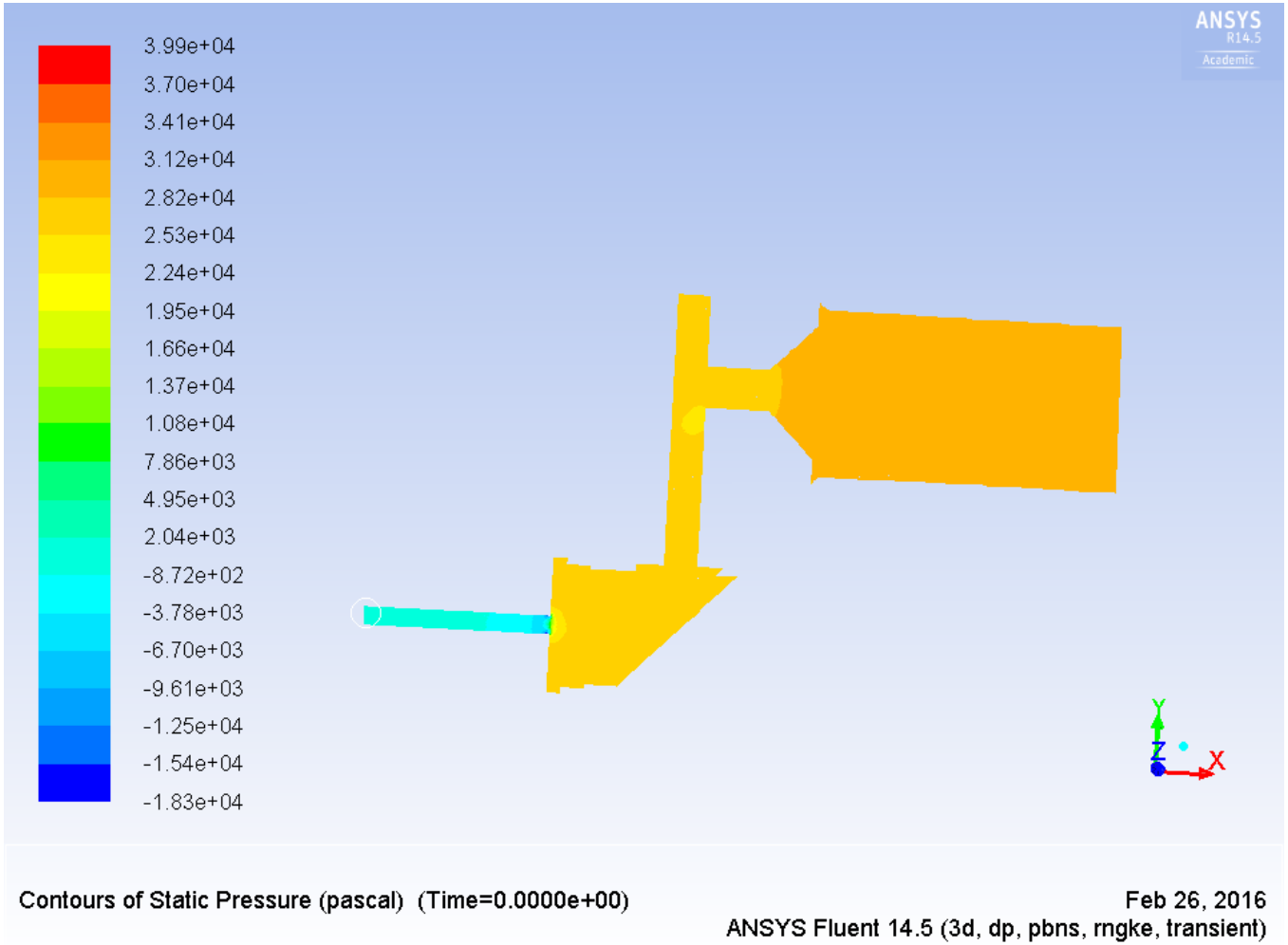

Figure 4.12 Pressure values inside CorVis-ST

4.2.4 Fluid structure interaction co-simulation

For the co-simulation step to run successfully, the interaction surfaces in the eye and air models should be exactly the same with the same node numbering. The eye model imports the Concentrated Force (CF) and the Lumped Mass from the CFD model and exports the deformations (U) and the velocities (V) back to the CFD model, see Table 4.2. For transient problems, Abaqus/CFD uses an advanced second-order projection method to create an arbitrary deforming mesh [117]. It uses node-centred finite-element discretization for the pressure and a cell-centred finite volume discretisation of all other transported variables (such as velocity, temperature, turbulence, etc.)[100]. This hybrid meshing approach removes the need for any artificial dissipation, while preserving the traditional conservation properties associated with the finite volume method. The main concept of projection methods is the separation between the velocity and the pressure fields for more efficient solutions of Navier-Stokes equations. The projection purpose is to separate the divergence free part of the velocity field using Helmholtz decomposition providing that the boundary conditions are satisfied.

Arbitrary Lagrangian-Eulerian (ALE) deforming mesh

In FSI applications, where there are large solid deformations, the adaptive mesh is important for stability of the solution and to prevent distortion of the fluid mesh [142–148, 45]. This was done using Arbitrary Lagrangian-Eulerian (ALE) deforming mesh method which has the following characteristics; the mesh motion is constrained only at the free boundaries but everywhere else the material and mesh motion are independent [142, 143, 148, 45]. The adaptive meshing incorporates two main tasks; creating a new mesh and remapping the solution variables, through a process named advection, from the old mesh to the new mesh [144–148]. The meshing is created at a prespecified frequency accompanied by a combination of mesh smoothing methods [100]. Then, remapping the solution variables to

the new mesh is of second-order accuracy and conserves mass and momentum. Moreover, for FSI stabilisation, the solution control parametrs are used to maintain mesh quality and control the mesh motion. Figure 4.13 shows the adaptive deformable mesh of the air puff model [100].

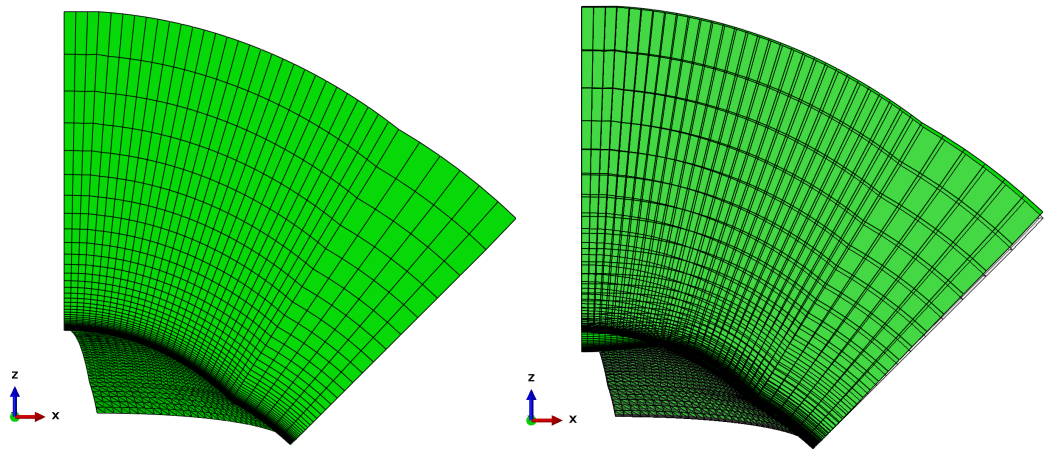

(a) (b)

Figure 4.13 ALE adaptive mesh. Original mesh (a), Deformed mesh (b)

Linear equations solvers

The parallel preconditioned Krylov solvers (DSGMRES-ILUFGMRES) [149–151] are the main solution methods for transport equations including momentum and turbulence with prescribed iteration limit and convergence criteria. The pressure and distance function equations are solved with one of Krylov solvers and strong multigrid algebraic preconditioner such as (AMG-SSORCG-DSCG) [117, 152, 153].

Integration and time incrementation

The time was integrated using second-order accuracy and all other diffusive and advective terms were integrated using the Crank-Nicolson method or the trapezoidal rule [154]. The CFL (Courant-Friedrichs-Lewy) stability condition was satisfied also by continually adjusting

the time increment size. The maximum value for CFL number was kept at 0.45. The CFL condition was necessary for partial differential equations' solution convergence [155, 156]. It must be less than one for explicit solvers to converge since the full numerical domain of dependence must contain the physical domain of dependence like Laney's definition [157]. Equation 4.3 illustrates the value of CFL number as the ratio between the real physical distance over the numerical distance and if this number is greater than one, the numerical viscosity will have negative values which is invalid.

$$C = \frac{u_x.\Delta t}{\Delta x} + \frac{u_y.\Delta t}{\Delta y} + \frac{u_z.\Delta t}{\Delta z} \leq C_{max} \tag{4.3}$$

Initial and boundary conditions

The specified initial conditions for velocity, density and turbulent kinematic eddy viscosity must satisfy boundary conditions of the model in order to have a well-posed flow problem and satisfy the solvability conditions [118, 100, 147]. During the FSI analysis, the pressure and velocity at interaction interface are described through definition of the co-simulation region [100].

4.2.5 Graphical user interface of mesh generator

To conduct the parametric study in an efficient and reliable way, an important step was to be performed first to plan the study and generate a graphical user interface (GUI) to easily change parameters of the model. Another crucial aspect is to link between the eye model generator and the new air model generator taking into account the two interactive meshes and co-simulation procedure and how to make the process automated with no need for a specialist to generate the air puff test model and run it successfully. Figure 4.14 shows the outline of the air puff model generator. It consists of 4 main sections:

- The eye model section to specify the input files and the eye mesh details to enable generating the air domain mesh above any specific eye geometry. The eye model mesh's most important details are the number of rings in the cornea and in the whole eye, number of eye segments and number of material sections in cornea and sclera as any change in these factors will directly affect the air model and its mesh. This section provides a file explorer to locate directory of the eye model input files.

- The air model section is set to choose between the mesh options and specify the output files' directory. The mesh options are to decide how many sclera element rings to cover, radius of the air jet at nozzle and type of the mesh projected above the cornea, which can have a linear or logarithmic element size distribution. Number of the air element layers is specified as well as the distance between air jet nozzle and the cornea.

- The velocity boundary condition can be controlled and the turbulence model used in simulation of the air jet can be one of two options; either Spallart Allmaras or RNG K-ε models. Density and viscosity of the fluid is set and the initial value of turbulent kinematic viscosity is specified.

- Last part of the GUI is to choose between two different shapes of the mesh, inclined or vertical with a zoom in at the inlet of the air jet. In mesh discretisation, the tip of the air jet stays constant and remains equal to the specified value of the radius in the second section of the GUI.

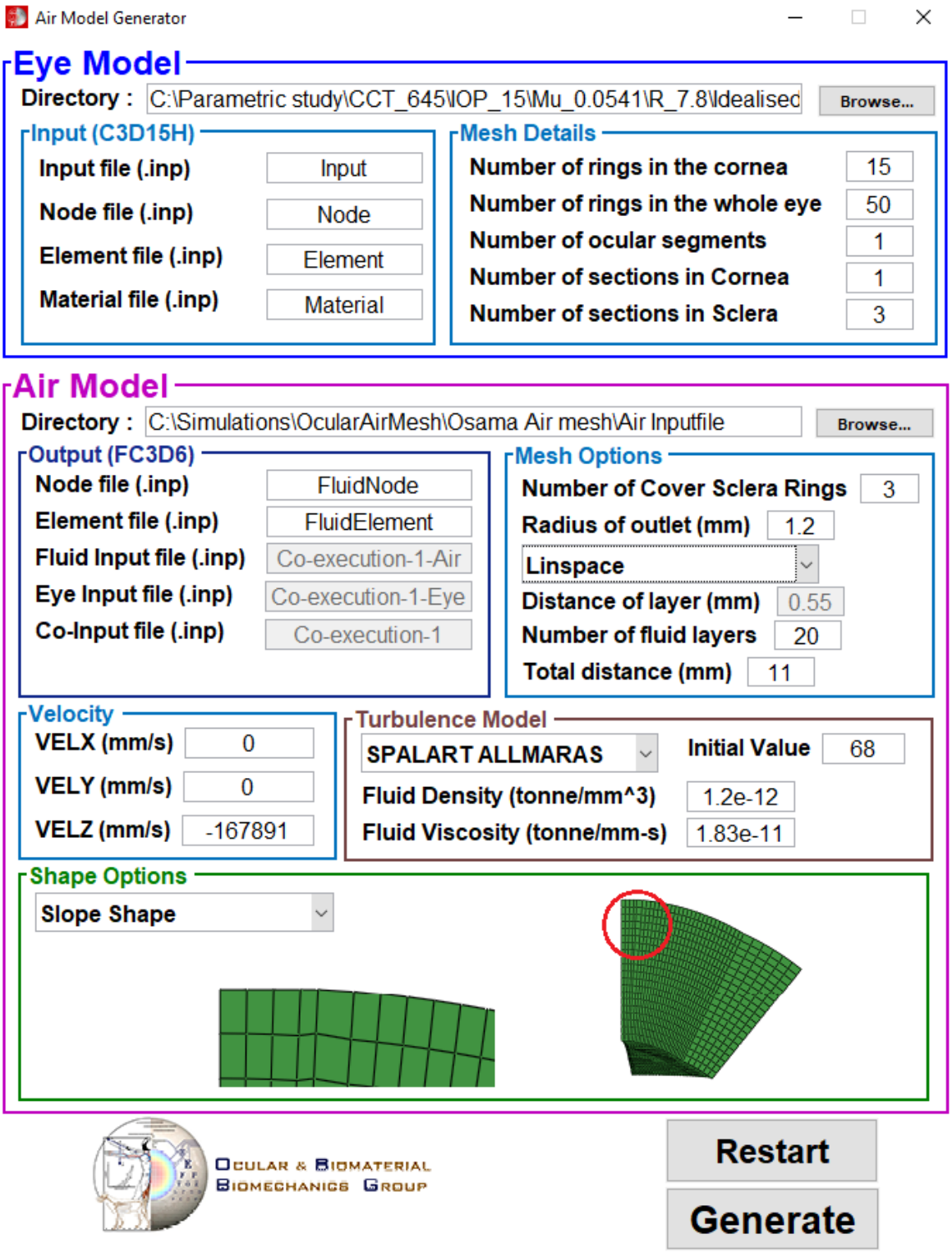

Figure 4.14 Graphical user interface of coupled fluid structure interaction model generator of the air puff test

Mesh sensitivity analysis

Mesh of the air jet domain was produced by projection of layers above the cornea and part of the sclera to a distance of 11 mm from the cornea apex as in the typical air puff test. The mesh sensitivity in the eye model was tested by varying the number of rings in the cornea and sclera and recording the effect on model output. The study was performed with 10 different mesh densities with total number of nodes ranging between 24743 and 48283; with cornea rings from 11 to 22 and number of elements from 18780 to 55146, more details are shown in Table 4.3. Figure 4.15 shows an example for three densities of the eye and the air meshes for a quartre model. Three output parameters were observed; the cornea apical maximum deformation, the maximum air pressure on cornea and the tests' run time.

Table 4.3 Details of the tests involved in the mesh sensitivity analysis

No. of cornea element Rings	Air No. of Nodes	Air No. of Elements	Eye No. of Nodes	Eye No. of Elements
11	9135	15680	15608	3100
12	10416	18000	15907	3226
13	11781	20480	16234	3364
14	13230	23120	16589	3514
15	14763	25920	16972	3676
16	16380	28880	17383	3850
17	18081	32000	17822	4036
18	19866	35280	18289	4234
19	21735	38720	18784	4444
22	27846	50000	20437	5146

Model	Eye model mesh	Air model mesh
Models with 11 element rings	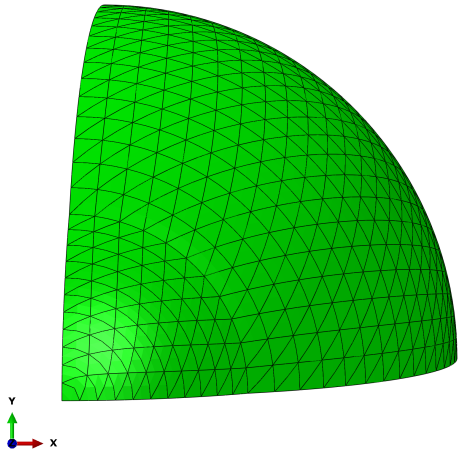	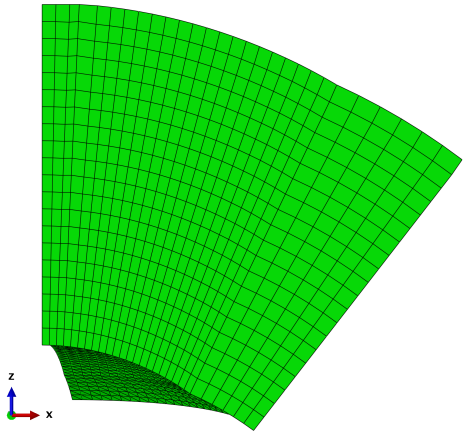
Models with 15 element rings	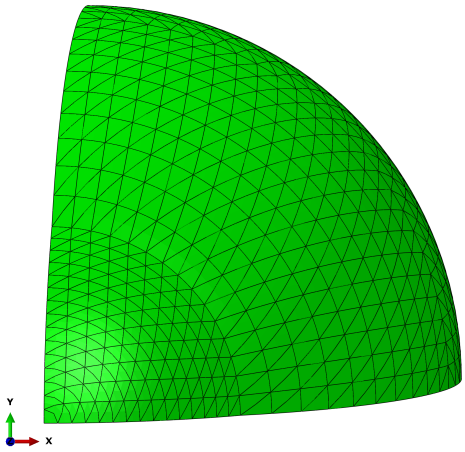	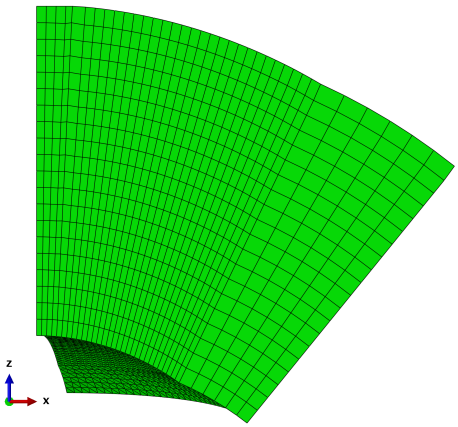
Models with 22 element rings	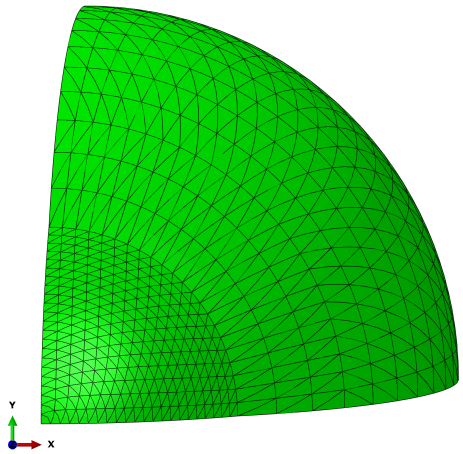	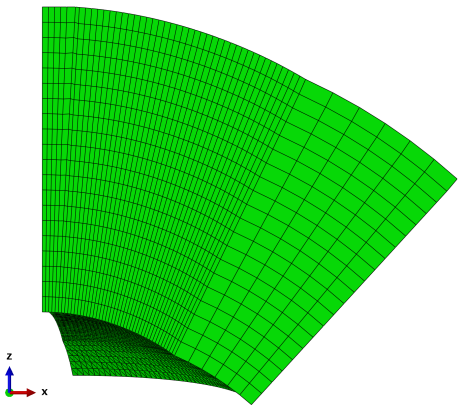

Figure 4.15 Mesh configurations for eye and air models for 11, 15 and 22 element rings on the cornea as changing parameter

4.3 Validation of fluid structure interaction model

After building the coupled fluid structure interaction model of the air puff test, it needs to be validated against clinical and experimental measurements. The two approaches that were used in the validation process were:

- Experimental validation of the CFD code that was used in modelling of the turbulent air puff
- Validation of corneal response in the coupled model between the air puff and the eye model using in-vivo patient specific tests

4.3.1 Validation of CFD code

The CFD code in Abaqus was validated against experimental laser doppler measurements of the turbulent flow in the impingement region of a single impinging jet of a circular pipe with diameter D and at a distance 2D from a flat impingement surface as shown in Figure 4.16(a) [158]. Reynolds number of the problem was based on the pipe diameter and flow bulk velocity and it equals 2.3×10^4. The mean axial and radial velocity components of the numerical model produced on Abaqus/CFD were compared against the experimental measurements determined by the two-component LDA of the experiment. Total number of nodes for the model was 398697 nodes, total number of elements was 2266509 elements and the mesh is shown in Figure 4.16(b). All the results were extracted after the jet has reached steady state condition.

4.3.2 Clinical validation of corneal response to air puff tonometry test

Clinal data of 6 healthy patients choosen from the clinical dataset provided by Vincieye Clinic in Milan, Italy and Rio de Janeiro Corneal Tomography and Biomechanics Study Group, Brazil, was used to validate the numerical model results and later the whole dataset

used for validation of the IOP and cornea material algorithms. Institutional review boards (IRB) of these clinical centres ruled that approval was not obligatory for this record review study. However, the ethical standards set in the 1964 Declaration of Helsinki, and revised in 2000, were observed.

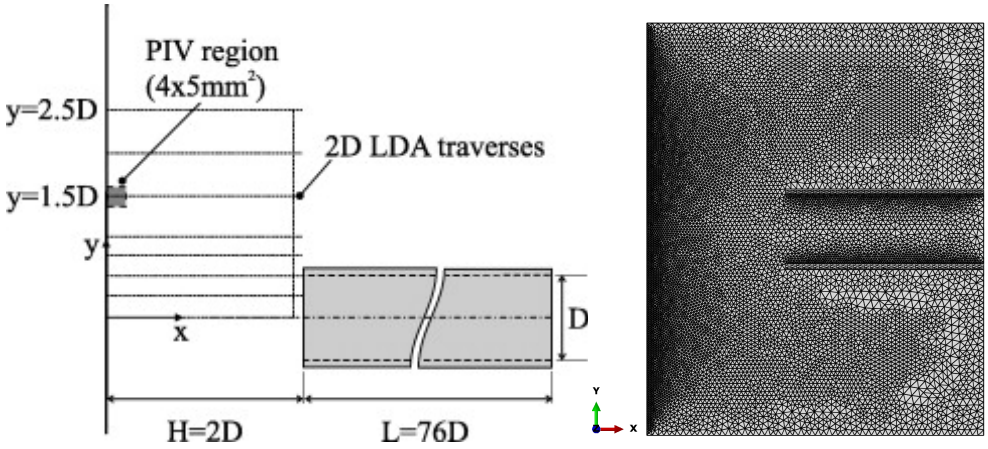

(a) (b)

Figure 4.16 Experimental configuration of impinging jet used in Tummers et al. experiments [158](a) and mesh of the produced model on Abaqus/CFD (b)

All patients provided informed consent before using their data in the study. All patients had a complete ophthalmic examination, including the CorVis ST and Pentacam (OCULUS Optikgeräte GmbH; Wetzlar, Germany) exams. The inclusion criteria of healthy subjects were a Belin/Ambrósio Enhanced Ectasia total deviation index (BAD-D) of less than 1.6 standard deviations (SD) from normative values in both eyes, no previous ocular surgery and disease, myopia less than 10D and no concurrent or previous glaucoma or hypotonic therapies [159]. Moreover, to confirm the diagnosis, all exams of each clinic were blindly re-evaluated by a corneal expert at the other clinic.

Cornea biomechanical parameters were collected from CorVis-ST and included maximum deformation, applanation pressure, applanation times, highest concavity radius, spatial and temporal corneal deformations. Participants had age between 10 and 87 years, central

corneal thickness of 455 to 630 μm and IOP of 9 to 25 mmHg. Patient specific eye tests were produced using built in house Matlab code based on the CCT, IOP and the material properties, in relation to the patient's age, starting from the stress-free geometry [101]. Their deformation patterns, as a response to the air puff, were analysed and compared against the clinical behaviour.

4.4 Parametric study

A parametric study was carried out to gauge the influence of cornea biomechanical parameters on its response to the air puff since this provides valuable information on how healthy the cornea is and to help correcting the effect of biomechanics on IOP measurement. The eye parameters that were varied in the parametric study were central corneal thickness (CCT), intraocular pressure (IOP), corneal curvature radius (R) and corneal material coefficient (μ). A graphical user interface of the model generation was created to simplify the process and easily change input parameters when generating the eye and air puff models. The total number of tests included in the study were 110 tests with wide parametric ranges for CCT, IOP, R and corneal material coefficient (μ) representing the change in stiffness with patient's age, more details about μ are given in Section 4.5.2. After the tests were finished, a Matlab code was used to extract the corneal response paramters, explained in table 4.4 [160, 161] and generate a parametric database, which formed the starting point towards the estimation algorithms of IOP measurement and corneal material behaviour considering the influence of fluid structure interaction.

Figure 4.17 shows the extracted temporal pressure and apical deformation for one model of the parameteric study which will help in calculating corneal response parameters. The peak distance, which is the distance between the two corneal peaks at highest concavity moment, was calculated by detecting the peak points via fitting the corneal curve and getting the points with maximum Z-coordinate and then finding the distance from corneal centre (X-coordinate),

as explained in Figure 4.18. To get the information at first applanation moment, first and second derivatives of the corneal curve were calculated at cornea centre for every time step until they reach zero, this idicates the flattened corneal surface moment as shown in Figure 4.19. Once the first applanation time (A1T) was found, the first applanation pressure (AP1) and first applanation deformation amplitude were calculated from the temporal profiles. First applanation length was estimated by calculating the difference between Apex Z-coordinate and its neigbouring points until a tolerance of 0.01 is broken, then the point index number is specified and A1 length is calculated through the X-coordinate values as shown in Figure 4.20.

4.4.1 Pearson correlation analysis of corneal response parameters

Previous efforts were made to perform a multivariable correction algorithm for intraocular pressure [59, 62, 64, 162, 163]. The first step towards this objective was to know the association, or relationship significance, between IOP and corneal response parameters to the air puff which are extracted from corneal deformation profiles, explained in table 4.4 [160, 161].

Corneal response parameters were extracted, by built in-house Matlab and Python codes, from the tests produced in parametric study, presented in Sections 4.4 & 5.6, and the full clinical dataset presented in Sections 4.3.2 & 4.7. A bivariate correlation analysis using SPSS statistics 24 (SPSS Inc., IL) between model input parameters (IOP, CCT, R and μ (Representing corneal stiffness)) and corneal response parameters was done to select the parameters with highest correlation coefficients (r).

Pearson's correlation coefficient (r) gives an indication on how strong is the association between two variables and the direction of this association. It ranges between -1, for perfectly negative linear relationship, and 1, for perfectly positive linear relationship.

Table 4.4 Corvis corneal response parameters to the air puff test [160, 161].

Corvis parameter	Description
A1 DeflAmp (mm)	Corneal deflection amplitude during the first applanation, determined as the displacement of corneal apex in relation to the initial state without the whole eye movement
A1 length (mm)	Length of the flattened cornea at the first applanation
A1 time (ms)	Time from the measurement beginning to the first applanation moment
A1 velocity (mm/ms)	Velocity of the corneal apex during the first applanation
DA (mm)	Maximum deformation amplitude (measured at the moment of the highest corneal concavity). It is the actual sum of corneal deflection amplitude and whole eye movement
DA ratio (2 mm)	Deformation amplitude ratio at 2 mm
DefA ratio (2 mm)	Deflection amplitude ratio at 2 mm
HC radius (mm)	Radius of corneal curvature during the moment of its highest concavity
HC time (ms)	Time from the measurement beginning to the moment of reaching the highest concavity
HCDeflAmp (mm)	Corneal deflection amplitude at the moment of the highest corneal concavity
Peak distance (mm)	Distance between the corneal peaks at the moment of the highest corneal concavity
SP-HC	Stiffness parameter HC
WEMmax (mm)	Maximum whole eye movement

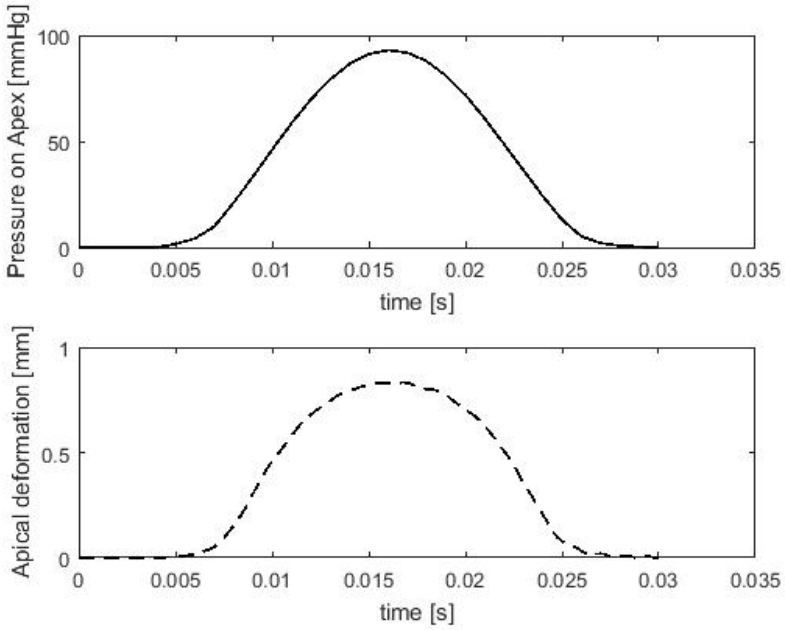

Figure 4.17 Temporal pressure and apical deformation profiles

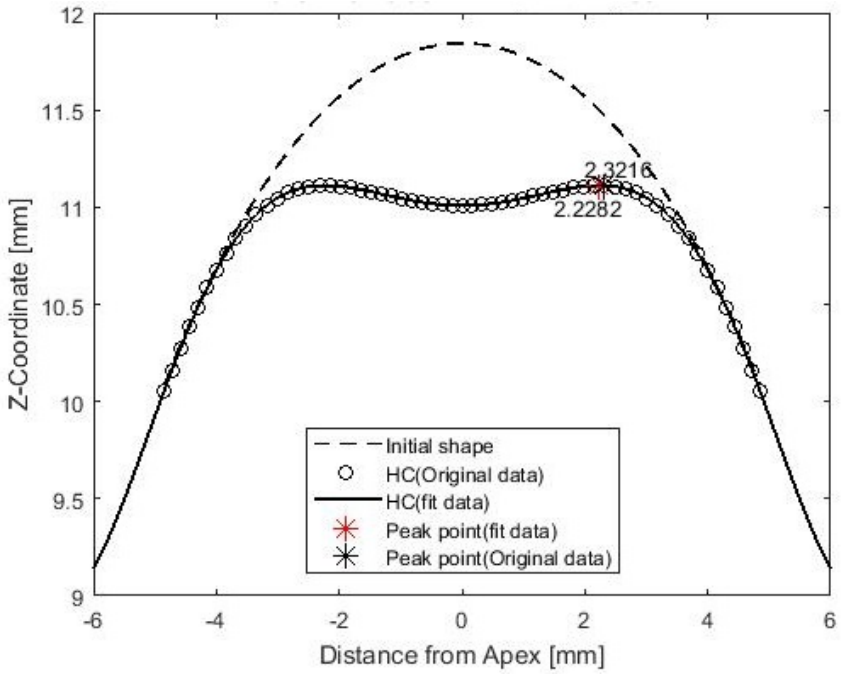

Figure 4.18 Peak point location at highest corneal concavity to calculate peak distance

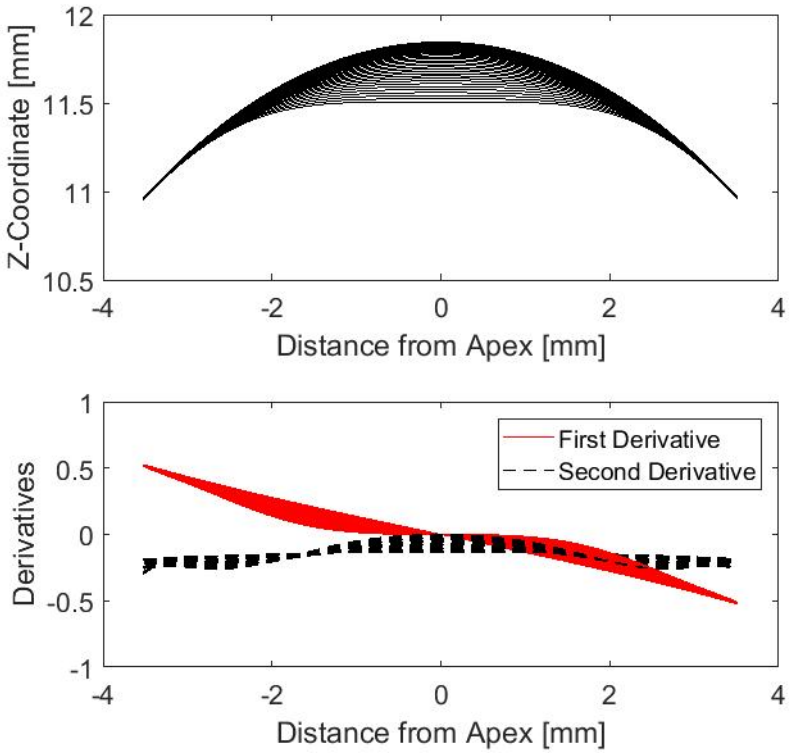

Figure 4.19 Estimation of first applanation moment by calculating first and second derivatives of corneal curve over 7 mm of central zone

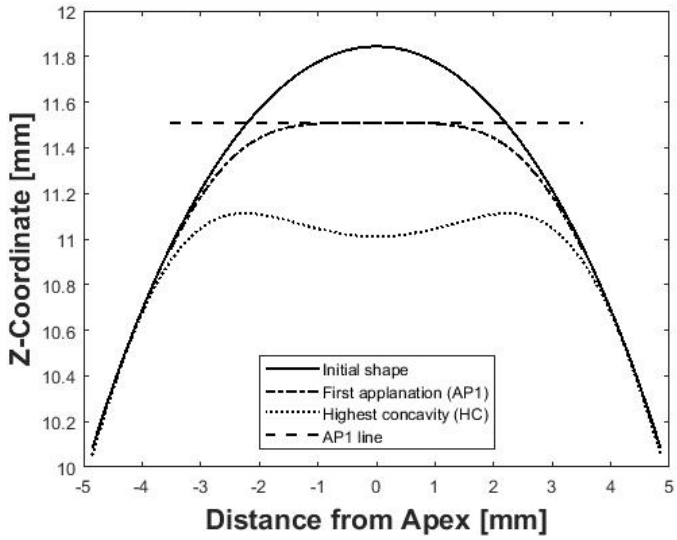

Figure 4.20 Three main corneal stages; initial shape, first applanation and highest concavity. First applanation line is shown to calculate first applanation length

More importantly is the significance or confidence level of statistical relationships which was quantified by the P-value representing probability of accepting the null hypothesis, which assumes that relationships are due to chance and not significant. The correlation analysis revealed which response parameters are more correlated to IOP and corneal stiffness than central corneal thickness (CCT) and patient's age to minimise their influence on the new IOP estimation algorithm.

4.5 Algorithms to estimate intraocular pressure and corneal material behaviour

The ultimate goals of this study, after building and validating the coupled fluid structure interaction model of the air puff test, are to use it for:

- Developing a new algorithm for estimating the value of intraocular pressure which will be known as (fIOP) algorithm.
- Developing a corneal material characterisation algorithm based on the change in patient's age and corneal biomechanical parameters which will be known as (β_f) material algorithm.

Development of these algorithms requires a database of corneal deformation parameters, sometimes called CorVis parameters, for different eyes with wide range of corneal biomechanical input parameters of central corneal thickness (CCT), corneal curvature (R), cornea material stiffness coefficient (μ) and Intraocular pressure (IOP). The fluid structure interaction model of the air puff test was used in the parametric study , Section 4.4, to produce the database of Corvis parameters in order to take apart in the algorithms' development.

4.5.1 Development of fIOP algorithm

IOP measurements were found in earlier studies to be affected by biomechanical properties of the cornea including central corneal thickness, corneal curvature and tissue stiffness [5, 57, 31, 160, 164, 165]. Several studies were conducted to provide multivariable correction algorithms to the IOP measurements [57–64], but most of them were structural in nature with assumptions made on the fluid structure interaction effect between the air puff and cornea. The flow chart in Figure 4.21 summarises the development process of the estimation algorithm in the current study.

After preparing the parametric study database, a correlation analysis was performed to see the association of IOP with Corvis corneal response parameters to reduce the dependence of IOP measurments on cornea central thickness (CCT), corneal curvature (R) and patients' age (corneal stiffness). Further to that, Matlab and Python codes were developed to perform a non-linear least square optimization, Equation 4.4, for fIOP equation parameters to get a close match with the true value of IOP (IOPt). The best equation for fIOP was extracted from the code and validated against previous corrections for IOP, clinical datasets and experimental measurments for true IOP.

$$\min_{x} \|F(x,xdata) - ydata\|^2 = \min_{x} \sum_{i} (F(x,xdata) - ydata)^2 \tag{4.4}$$

Intraocular pressure estimation equation (fIOP)

Following the correlation analysis of clinical and numerical databases, an exercise of finding the lower polynomial was needed for each variable in Equation 4.5 before performing a least square optimisation process for the polynomials' coefficients. The objective function of this optimisation was the root mean square of the difference between true IOP (IOPt) and fIOP.

$$fIOP = f(CCT, R, \mu, Responseparameters) \tag{4.5}$$

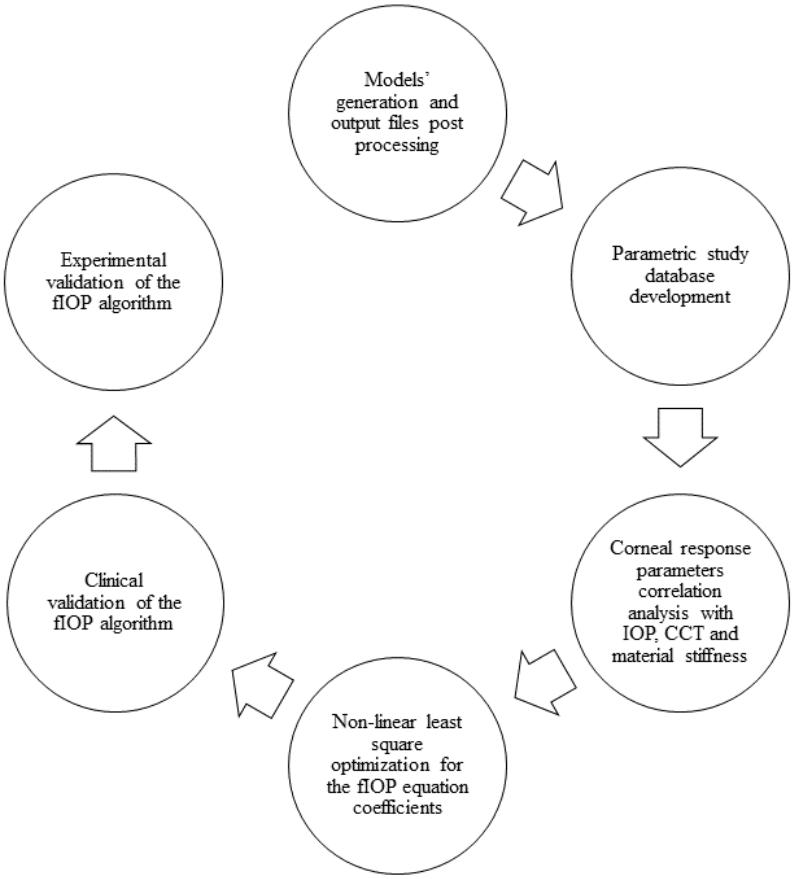

Figure 4.21 Development process of a biomechanical estimation algorithm for intraocular pressure (fIOP)

4.5.2 Development of corneal material estimation algorithm (β_f)

The material properties applied in the eye model was different for the main five parts of the eye; cornea, limbus, anterior sclera, equatorial sclera and posterior sclera as shown in Figure 4.22 [5, 6, 65]. A first-order hyper-elastic Ogden material model was used in the material definition for every segment with different values for model input coefficients (μ *and* α) as obtained from uniaxial experimental analysis of corneal and scleral tissues [5, 6, 65]. Ogden models were first produced by Raymond Ogden [99], to describe the material behaviour through strain energy density function. They were primarily used to define non-linear stress-strain behaviour of complex materials such as biological tissues and

rubber-like materials. In the present study, the hyperelastic model's coefficients and their change with age for limbus and sclera were fixed to the values obtained by Elsheikh et. al shown in table 4.5 [5, 6] as they are not significantly affected by the air puff tonometry under investigation. What was considered in the parametric study is changing the corneal material coefficients according to their relation with patients' age to reflect corneal tissue stiffening. It was found in earlier experimental study by Elsheikh et al. that the ratio between, μ for a specific age and μ for age 50, was changing with age and stress-strain curves don't cross with each other [5, 6]. This ratio was named β, Equation 4.6, to represent the corneal stiffening with age, but there is no developed algorithm to accurately estimate β and relate it to different age groups. β for age 50 was considered equal to 1 and it was found from the experimental data by Elsheikh et al. that age groups, significantly higher than 50 years with stiff corneas, showed values of $\beta > 1$ and for age groups, significantly less than 50 with softer corneas, showed values of $\beta < 1$ as shown in Figure 4.23 [5, 6].

$$\beta = \frac{\mu}{\mu_{Age50}} \tag{4.6}$$

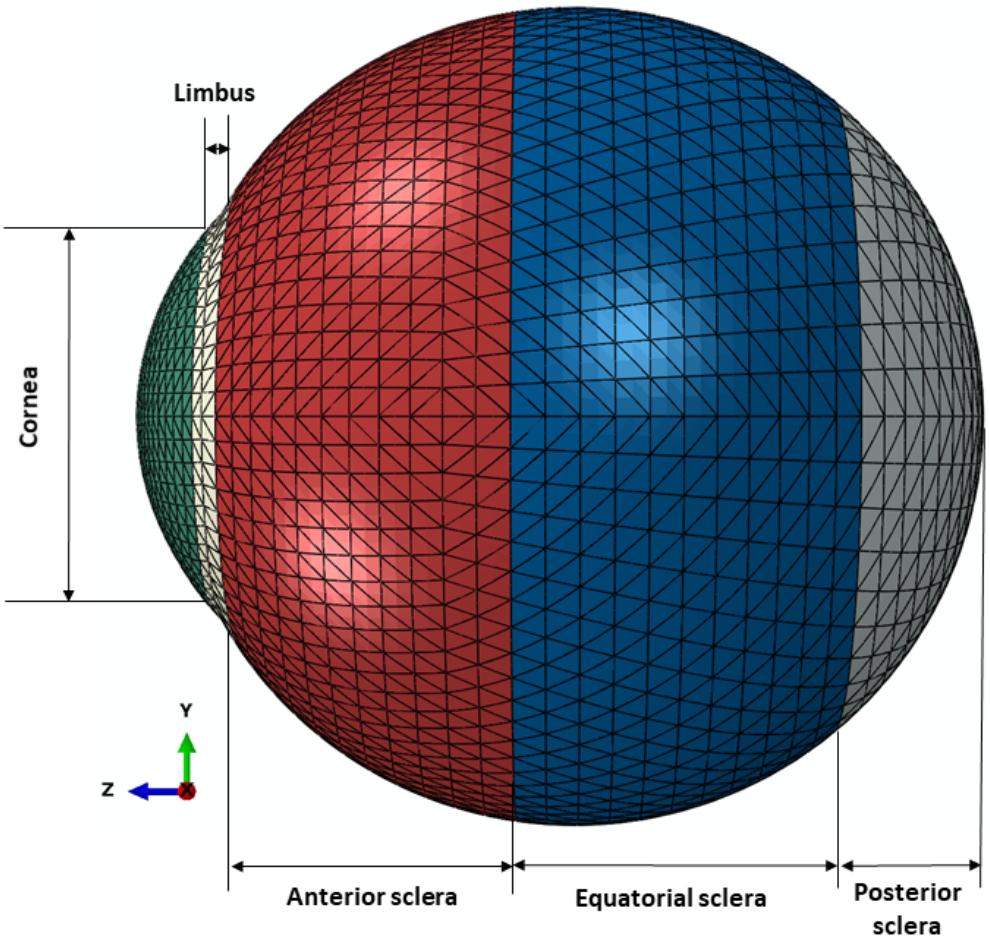

Figure 4.22 Material regional variation across the ocular globe [5, 6, 65]

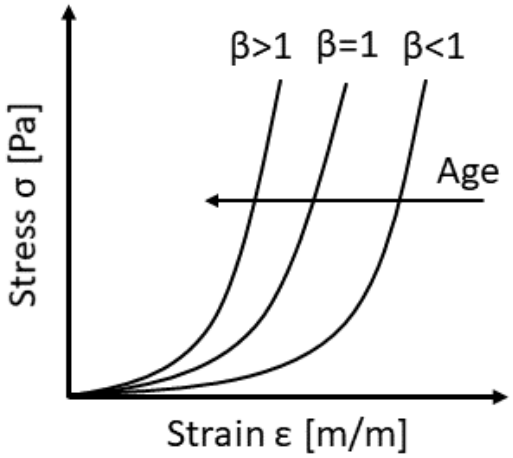

Figure 4.23 β corneal material parameter and its relation with age [32, 166, 6, 65]

Table 4.5 First-order Ogden material model coefficients for eye material regional variation in cornea, limbus & anterior sclera, equatorial sclera and posterior sclera [166, 5, 6, 65]

Region	Age	μ	α
Cornea	30	0.049	108.595
	40	0.051	109.590
	50	0.054	110.836
	60	0.057	112.333
	70	0.061	114.083
	80	0.066	116.087
	90	0.071	118.348
	100	0.077	120.867
Limbus & Anterior Sclera	50	2.318	39.128
	55	2.322	41.070
	60	2.350	42.915
	65	2.403	44.621
	70	2.479	46.164
	75	2.579	47.534
	80	2.703	48.731
	85	2.851	49.762
	90	3.021	50.642
Equatorial Sclera	50	1.301	47.294
	55	1.343	47.704
	60	1.391	48.331
	65	1.443	49.128
	70	1.500	50.049
	75	1.563	51.050
	80	1.631	52.097
	85	1.705	53.157
	90	1.785	54.210
Posterior Sclera	50	0.717	53.418
	55	0.788	52.082
	60	0.864	51.280
	65	0.945	50.943
	70	1.030	50.986
	75	1.120	51.319
	80	1.215	51.864
	85	1.314	52.551
	90	1.419	53.329

It was also found by Elsheikh et al. that tangent modulus (E_t) is changing linearly with the applied stress to cornea according to Figure 4.24. Tangent modulus (E_t) is the slope of a stress-strain curve at a specific stress value. More importantly, it was found that the tangent modulus ratio equals β ratio which represents corneal stiffening with age, Equation 4.7 [6, 32, 65, 166].

$$\frac{E_{t1}}{E_t} = \frac{\beta_1}{\beta} \tag{4.7}$$

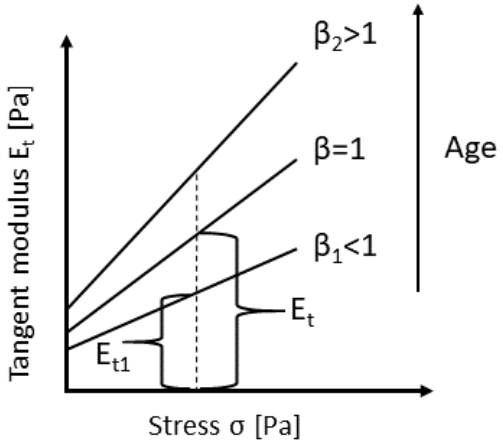

Figure 4.24 Tangent modulus relation with stress for different β values [6, 32, 65, 166]

In the current study, a new algorithm was developed to estimate the corneal material behaviour which is known through the thesis as "β_f" algorithm due to the fact that correlation of corneal stiffening with age is not strong enough to accurately estimate the corneal material behaviour. the new β_f material algorithm uses the corneal response parameters along with CCT and IOP to obtain the material model coefficients with less dependence on patient's age. After building the numerical model of air puff test, a parametric study was performed on the eye model with different corneal material coefficients (μ) values. Then, Pearson correlation analysis was done to study corneal response parameters' association with the change in corneal material in order to extract the most correlated parameters. Further to that, a three

dimensional plot of β_f and the correlation parameters were ploted to get the five material sufaces involved in the study. Based on these surfaces, the value of β_f can be estimated and used in numerical analyses, which is not only depending on age of the patient, but also depends on corneal response parameters extracted from CorVis measurement providing better accuracy of material representation in patient specific tests in finite element analyses. The flowchart shown in Figure 4.25 summarises the algorithm development process.

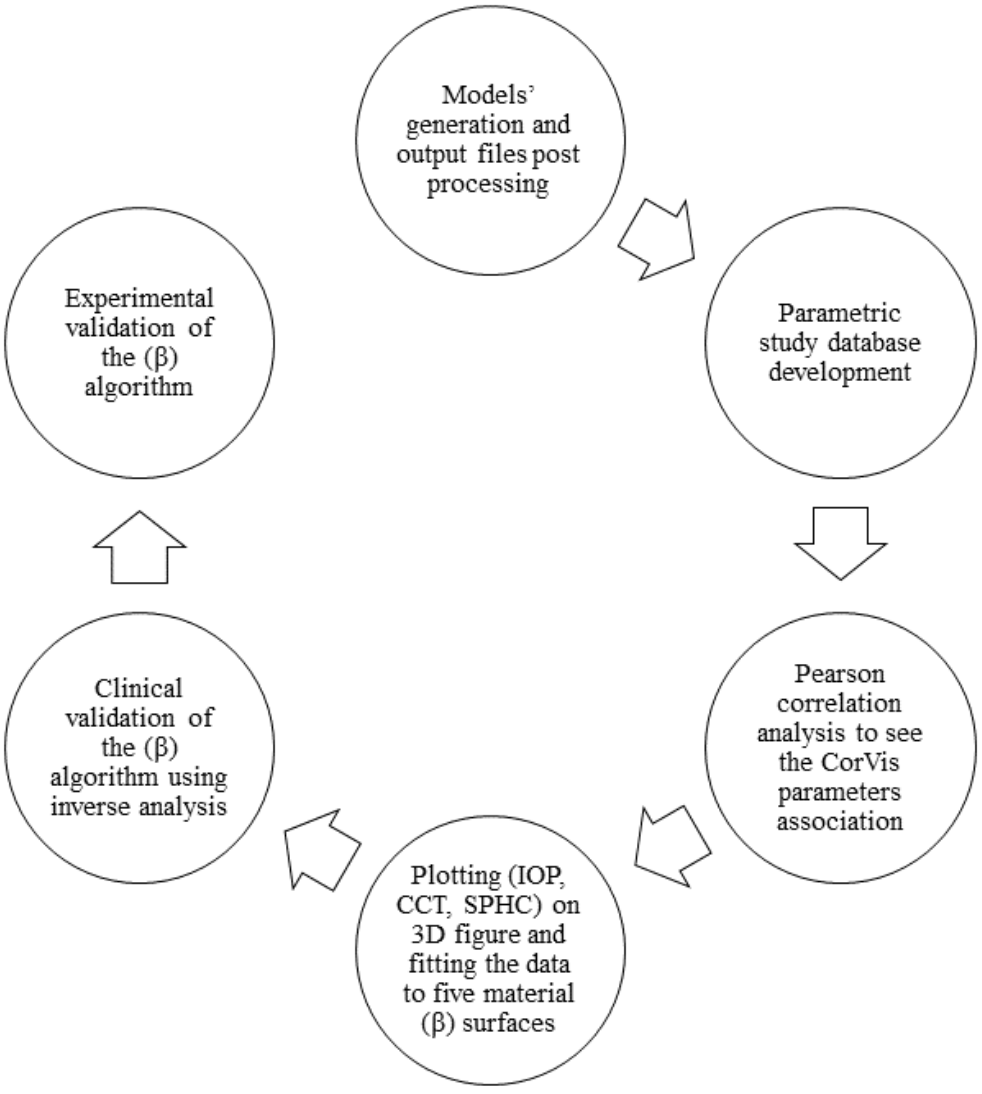

Figure 4.25 The cornea material estimation algorithm flowchart

4.6 Experimental validation of fIOP and corneal material algorithms

Experimental validation of the new estimation algorithms included performing the air puff test on human eyes using CorVis-ST device and built-in house eye pressure control system to extract deformation profiles of the cornea and sclera by the existing high speed Scheimpflug imaging camera, Figure 4.26. These profiles were compared with the numerical results as a validation to the numerical model. CorVis-ST was used to measure IOP of five ex-vivo donated human eyes with age range (69$\pm$3 years) obtained from the Fondazione Banca degli Occhi del Veneto Onlus, Venice, Italy, were tested during a time frame of 3 to 5 days post-mortem. To use the specimens, ethical approvals were issued by the eye bank in Italy and by the biomechanical engineering group in Liverpool (RETH000753) in accordance with the Declaration of Helsinki.

4.6.1 Specimen preparation protocol

The specimens are prepared according to the protocol in Figure 4.27 and the following steps:

1. After the eye was recieved, it was cleaned from any external ocular tissues using curved scissors and crucible tongs.

2. The superior (top) direction was marked on the eye and corneal thickness is measured using a DGH 55 Pachymate pachymeter (DGH Technology, Exton, USA).

3. A G14 needle was inserted at the posterior of the eye with a help of 3D printed box.

4. The internal fluids, including retina and ocular lens, were removed without letting any air to enter the eye.

5. The needle stayed in place, but the syringe was removed to be cleaned and filled with Phosphate Buffered Saline (PBS, P4417, Sigma-Aldrich, Darmstadt, Germany)

solution to clean the ocular globe from inside. This step can be repeated if needed, until the flow of solution through the needle is smooth enough.

6. Using a pencil tip, the needle was glued enough to posterior of the eye to prevent fluid leakage under pressure during the test.

7. Then, the eye was inflated by 10% Dextran solution (Sigma-Aldrich, Darmstadt, Germany) to prevent swelling of the tissues during experiment and to provide control of pressure inside the eye using a syringe pump system.

8. To prevent the cornea from drying out, a viscous tear film supplement (Everclear, Melleson Pharma, Breda, Netherlands) was used through the experiments' time.

4.6.2 Experimental set-up and test protocol

The test rig used in the experiments tried to mimic the real condition of the in-vivo human eye. A needle clamp holder was fixed to a built in house round steel table as shown in Figure 4.28(a). The needle was connected via transparent PVC tubes of diameter 4 mm to a syringe pump and pressure transducer to control and monitor pressure in the system. The needle's horizontal level was made at the same level of pressure transducer and the syringe pump to eliminate any head pressure differences. Motion of the syringe pump plunger was controlled by a stepper motor, connected to a control circuit, connected to a LabVIEW code on the computer. After sample preparation in Section 4.6.1, the eye is ready for Corvis testing, the needle that was glued to the eye, was fixed by the needle clamp and connected to the PVC tubes as shown in Figure 4.29. The Corneal Visualisation Scheimpflug Technology (CorVis-ST) device was then put in front of the cornea at a distance of 11 mm as specified by the manufactureres and clinical practice [68, 21]. The CorVis-ST provides two important components for the test, the air puff via high speed piston movement and the high speed Scheimpflug imaging to capture the corneal deformation in real time.

(a)

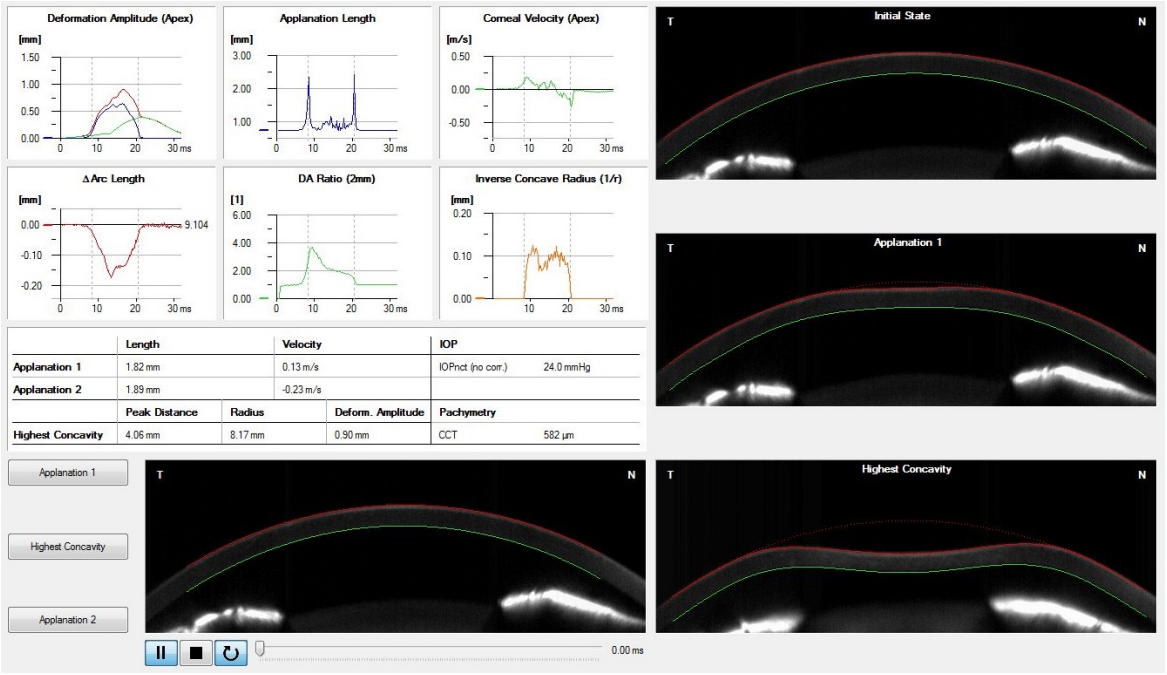

(b)

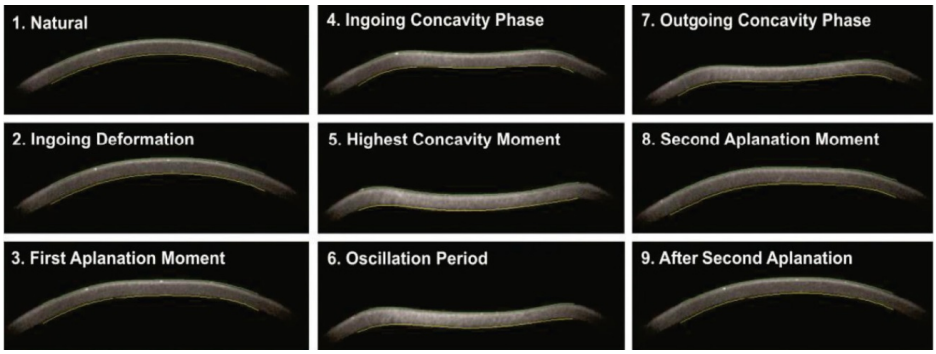

(c)

Figure 4.26 CorVis air puff test device (a) and images of cornea deformation stages as output from the device screen (b,c), ®OCULUS Corvis ST

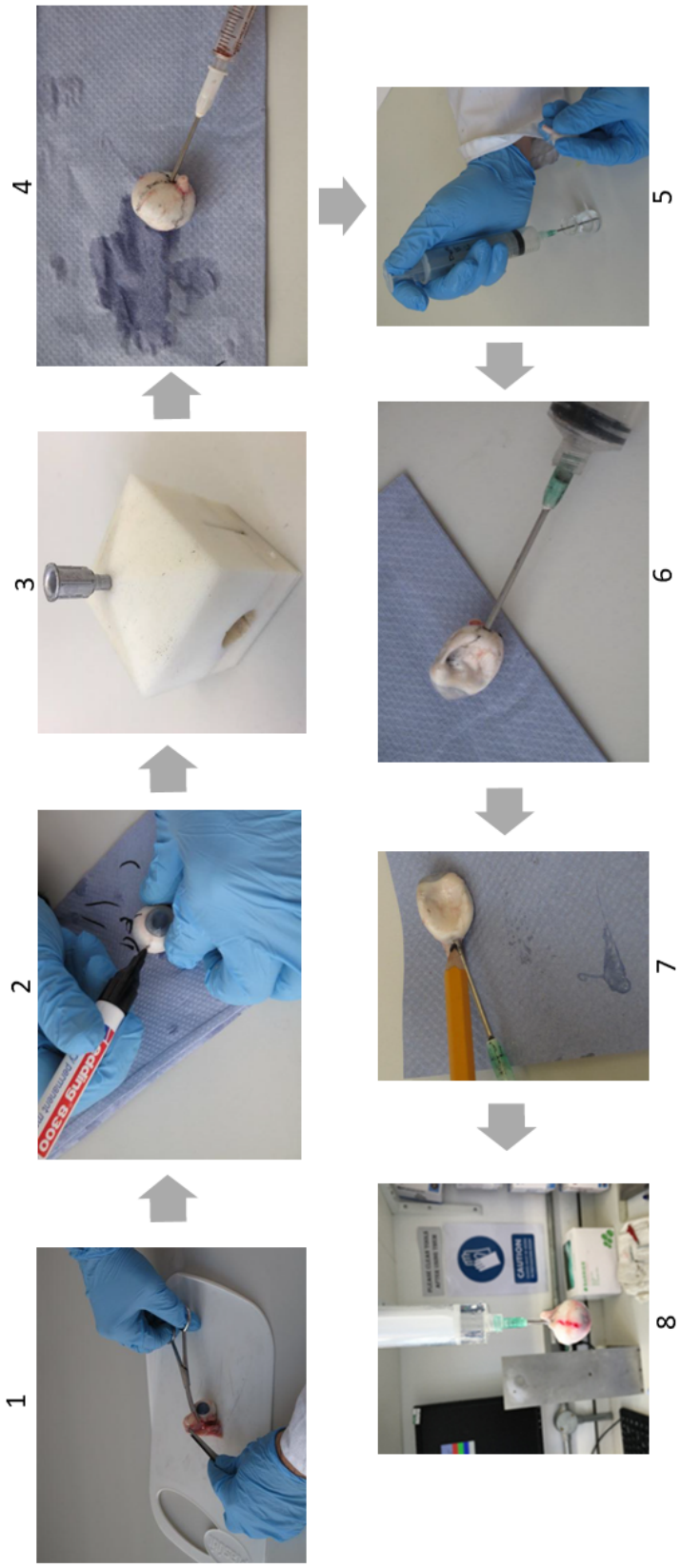

Figure 4.27 Experimental protocol sequence of specimen preparation

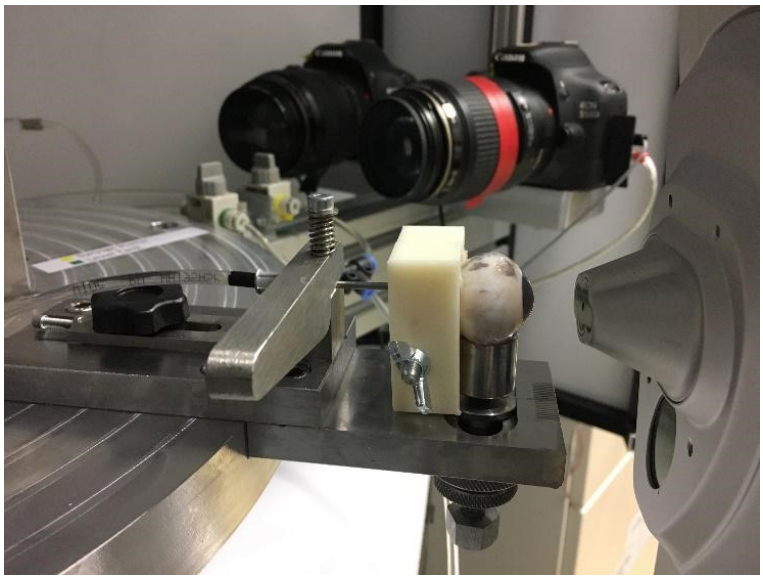

(a)

(b)

Figure 4.28 The Corvis-ST device is put in front of an ex-vivo human eye ready for the air puff test [167]. Front view (a), Rear view (b)

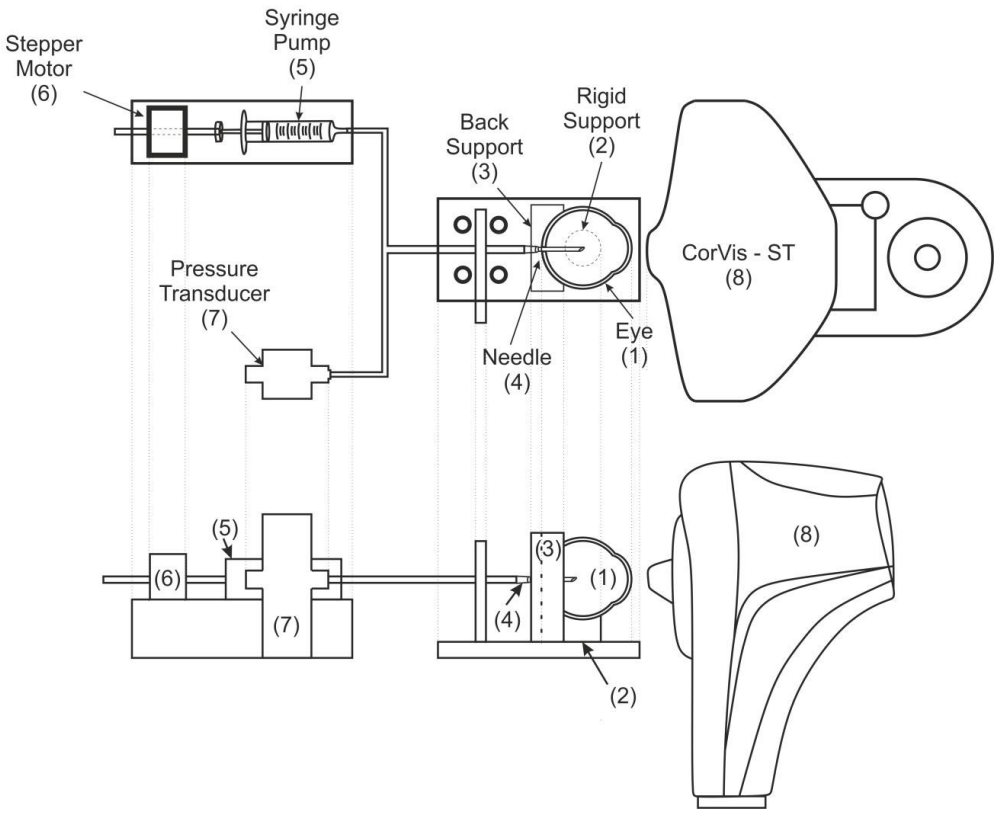

Figure 4.29 Schematic diagram of the experimental setup [167]

The digital camera gives 4330 images per second, 576 measuring point per image (80 640 point per examination).The tested eye is supported by a mechanism allowing it to be on its natural position with the cornea being aligned horizontally with CorVis-ST nozzle tip, while being prevented from horizontal and vertical rigid body motion. Soft silicone rubber padding (Ecoflex Series, Smooth-On, Pennsylvania, USA) was placed on the support mechanism to reflect the fatty tissue effect around the eye. The IOP was controlled through a stepper motor and measured by an FDW pressure transducer (RDP Electronics, Wolverhampton, UK) through a pre-set cycle on LabView to cover a range from 0 to 30 mmHg. These pressure measurements were considered true IOP (IOPt) and the reference value to compare with CorVis IOP reading (CVS-IOP) and the biomechanically corrected value fIOP. Every eye was tested at different IOP values starting from 10 to 30 mmHg by increase of 5 mmHg. At each value of IOP, 3 to 5 tests were performed on the eye to minimize the error in measuremenet

of CCT, CVS-IOP and the rest of Corvis output parameters. The Corvis air puff shooting and cornea deformation were recorded and taken for each test, but the eye was left to stabilise for 60 seconds after every pressure change. All data were exported to excel files for validation purposes and statistical analysis.

4.7 Clinical validation of fIOP and corneal material algorithms

A clinical dataset of 476 healthy patients from the Vincieye Clinic in Milan, Italy and Rio de Janeiro Corneal Tomography and Biomechanics Study Group, Brazil, was used to validate the fIOP and cornea material parameter (β_f) algorithms. Cornea biomechanical parameters were collected from CorVis-ST and included maximum deformation, applanation pressure, applanation times, highest concavity radius, spatial and temporal corneal deformations. Participants had age between 10 and 87 years, central corneal thickness of 455 to 630 μm and IOP of 9 to 25 mmHg. Table 4.6 provides descriptive statistics of the clinical dataset for Milan and Rio's centres.

Table 4.6 Clinical dtatsets used in the validation of fIOP and cornea material characterisation algorithms

Database		Patients	Age (years)	CCT (μm)	CVS-IOP (mmHg)
Dataset 2 (Milan)	Healthy	225	38 ± 17.2 (7–91)	543 ± 31.5 (458–635)	15.7 ± 2.35 (11–25)
Dataset 1 (Rio)	Healthy	251	43 ± 16.5 (8–87)	539 ± 33.2 (454–629)	14.8 ± 3.06 (6–34)

The idea was to make sure there is minimal or no relationship between fIOP measurement and corneal thickness (CCT), age and corneal curvature (R), otherwise the IOP measurement will be affected by changing these parameters between different patients. The second check is the association of cornea material characterisation parameter (β_f) with CCT, R and age. It shouldn't show a change with CCT and R variations, but shows direct relationship with age as the cornea material gets stiffer in older people [6, 166].

A final important validation was applying fIOP and β_f to the six clinical cases, used in validation of the corneal response in Section 4.3.2, and observe improvement of the numerical results compared to the clinical behaviour of both corneal deformations and response parameters.

Chapter 5

Presentation of results

5.1 Introduction

In this chapter, the verification and validation results of the fluid structure interaction model, IOP and corneal material estimation algorithms will be introduced. Verification and validation (V & V) are the measures needed to provide the sufficient proof on the reliability of computational models to be used for a specific purpose. In the recent years, there has been a rapid increase in the use of numerical simulations in the biomechanics field for surgical planning and optimisation [130]. Computational models can provide numerous information for the entire domain of study which gives an advantage in specific applications where experimental measurements is impossible or expensive. Moreover, the growth in computational power, geometry reconstruction and imaging techniques made analysing patient specific models more achievable to clinicians [130]. However, clinicians and scientists will not accept any algorithm or virtual reality model to make clinical decisions until certain credibility measures have been met. Some of these credibility measures are:

1. Are the mathematical governing equations of the model implemented correctly?
2. Is the model representative to the real physical problem?
3. Have the error and uncertainty been assessed and take into account in the model predictions?

In order to answer these three questions, a combination of experimental and numerical data must be integrated to verify and validate the model through specific algorithms and protocols. Verification is the procedure of checking if the model accurately describes the physical concept and solution of the problem, while validation is the comparison between

the computational results and experimental measurements to estimate the model uncertainty. In simple words, verification is working on "solving the equations correctly" and validation is dealing with "solving the correct equations" [130–132].

Figure 5.1 summarises the results that are presented in this chapter. General validation of the CFD code and turbulence model that were used in the modelling are introduced in the beginning. The impinging jet on a flat surface was chosen to be validated against laser Doppler anemometer velocity field obtained experimentally from the literature. Then, these results are followed by the coupled numerical fluid structure interaction model of the air puff test and the mesh sensitivity analysis. Further to that, the air puff analysis is presented discussing the axial and parallel velocity fields, pressure distribution on cornea showing the fluid structure interaction influence. This is followed by the parametric study results which is performed on the FSI coupled model to see association of the corneal response parameters with IOP material stiffness. Then the clinical and experimental validation of the corneal deformations are presented. These results have led to a new estimation algorithm for IOP measurements taking into account the fluid structure interaction effect and a new material parameter β_f describing the corneal matrial behaviour. Finally, the expeimental and clinical validation of IOP estimation and corneal matrial behaviour algorithms are introduced.

Figure 5.1 Summary of the results introduced in this chapter

5.2 Validation of CFD code

To validate the CFD code available in Abaqus, experimental measurements of the axial and radial velocities of a turbulent air jet impinging normally on a flat plate was used in the comparison with the same model produced on Abaqus/CFD. Tummers et al. [158] have reported detailed experimental measurements of the turbulent flow field at the stagnation region of a single impinging jet pumped out from a circular pipe of diameter D and a distance 2D between the impingement flat plate and the pipe outlet. Reynolds number of the problem was 2.3×10^4 which is the same order of magnitude of the maximum Reynolds number for the air puff test. A two-component laser doppler anemometer (LDA) was used to determine mean velocity components of the jet and Reynolds stresses. Another modified LDA one-component was used to obtain near wall measurements with 40 μm minimum wall distance. Also, particle image velocimetry (PIV) was used in a small region of (4×5 mm) to examine the instantaneous reversals at the region near the wall [158].

5.2.1 Experimental set-up configuration

The air is pumped through the pipe using a centrifugal fan uniform flow system equipped with a flow meter. The inner diameter of the pipe was $D = 37$ mm and the outer diameter was 50 mm. The pipe-to-wall distance was 2D as shown in figure 5.2. Reynolds number is 2.3×10^4 which was calculated based on the pipe internal diameter and a bulk velocity of 9.6 m/s which was determined from the flow meter measurement [158]. The impingement flat plate size was 1×1.2 m and placed in a large sealed enclosure to guarantee stable air conditions. Oil droplets were used to seed the ambient air and the jet to work as tracing particles for the LDA and the PIV. Origin of the coordinate system was the intersection between axes of the impingement surface and the pipe. X-coordinate was the distance normal to the wall, parallel to pipe axis and y and z-coordinates are on the impingement plate [158].

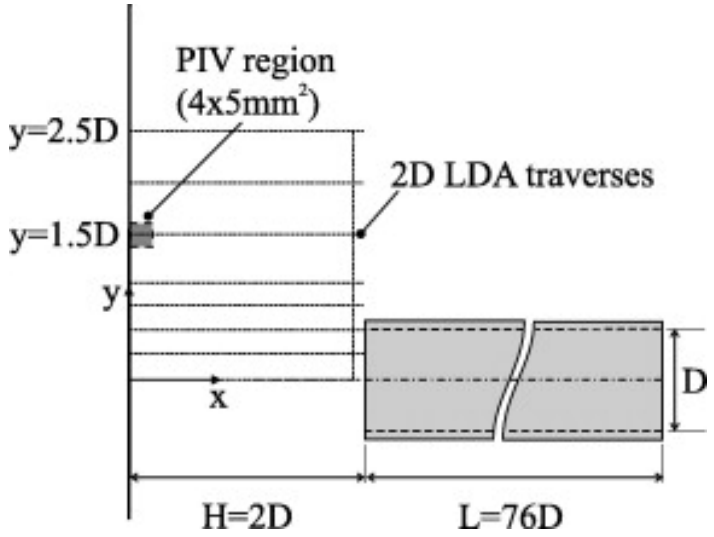

Figure 5.2 Experimental configuration of impinging jet used in Tummers et al. experiments [158]

Laser doppler anemometer (LDA) functionality

Two-component laser doppler anemometer (LDA) was used to measure the axial and radial velocity components of the jet. The green colour beam (514 nm) of a 4 W Argon-ion laser was used to measure the radial velocity, v, and the blue colour beam (488 nm) of the same laser was used to measure the axial velocity, u [158].

5.2.2 Experimental observations

It was observed that the jet travels towards the impingement wall with gradual radial growth and decrease of the flow velocity associated with deflection of the flow in the radial direction for $x/D < 0.5$. Following impingement at the stagnation point, the flow gets accelerated again forming a radial wall jet and this wall jet caused entrainment of the outer layers of air into the inner layers forming large recirculation bubbles [158, 168].

A numerical model of the same air turbulent jet was produced on Abaqus CFD and applying Spallart Allmaras turbulence model. The total number of nodes was 398697 and total number of elements was 2266509. The time step was 0.01 S, but all the results were

extracted after the jet has reached steady state condition. Comparison results of the flow field are shown in figure 5.3. It showed a good agreement for the mean flow field, while the mean axial velocity at different axial trajectories normal to the impingement surface are shown in figures 5.4 and 5.5. The values of root mean square error (RMSE) for every trajectory is shown on the top of every plot. The highest value was (0.103) for the axial velocity at $\frac{y}{D} = 0.5$. The mean radial velocity at the same axial trajectories normal to the impingement surface are shown in figures 5.6 and 5.7. The highest value for root mean square was (0.253) for the radial velocity at $\frac{y}{D} = 2$ This could be due to the high turbulence intensity in this region where the turbulence model couldn't catch every detail in the flow. Figures 5.8 and 5.9 present distribution of the turbulent kinematic viscosity which is the main output of the turbulence model. Static pressure conours is shown in figures 5.10 and 5.11 indicating the impingment effect on the impingment surface and conversion of the dynamic to static pressure at the stagnation point.

Another important analysis of the properties was done at distance 1 mm from the impingment surface. In Figure 5.12, the pressure coefficient (C_p) is presented in the first plot, it equals 1 at the stagnation point and zero where the maximum velocity exists. The second plot is showing the normalised mean axial velocity (v_1/V_b) normal to the wall and negative values were observed the impingment region to indicate reflection of some of the air from wall. The third plot is showing the normalised mean radial velocity distribution (v_2/V_b) and it is symmetric about the diagonal axis. The fourth plot is showing the normalised static pressure (P/P_{max}) equal 1 at the centre and decreasing to zero as going further from the stagnation point. The last plot is presenting the normalised mean turbulent kinematic viscosity distribution (ν/ν_{max}) equal to zero at the wall and starting kicking off at slightly before $\frac{y}{D} = 1$ until it reaches its peak at $\frac{y}{D} = 1.2$ and then starts decreasing again reching half peak at edges of the domain.

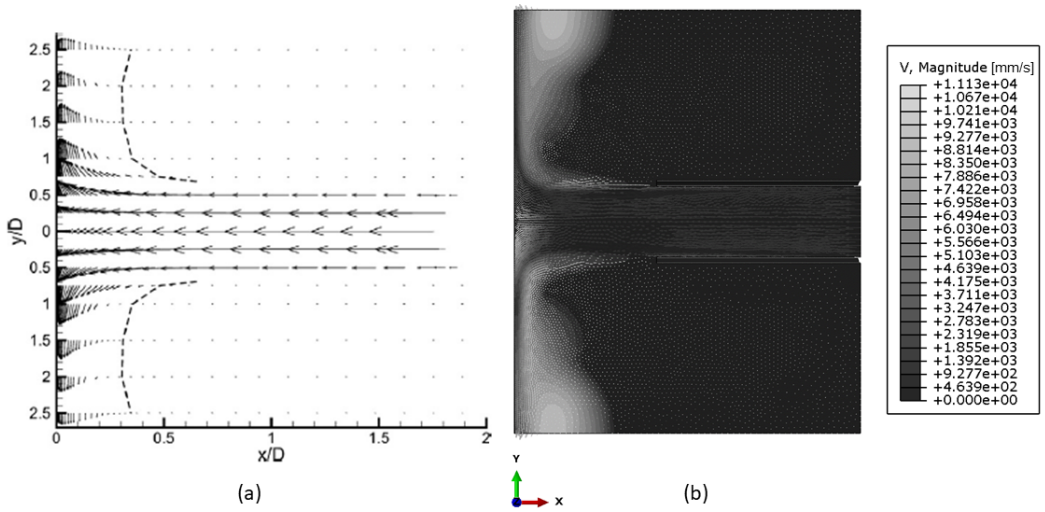

Figure 5.3 Laser Doppler Anemometer (LDA) mean flow field for Tummers experiments [158] (a) and the numerically reproduced flow field predicted by Abaqus-CFD (b)

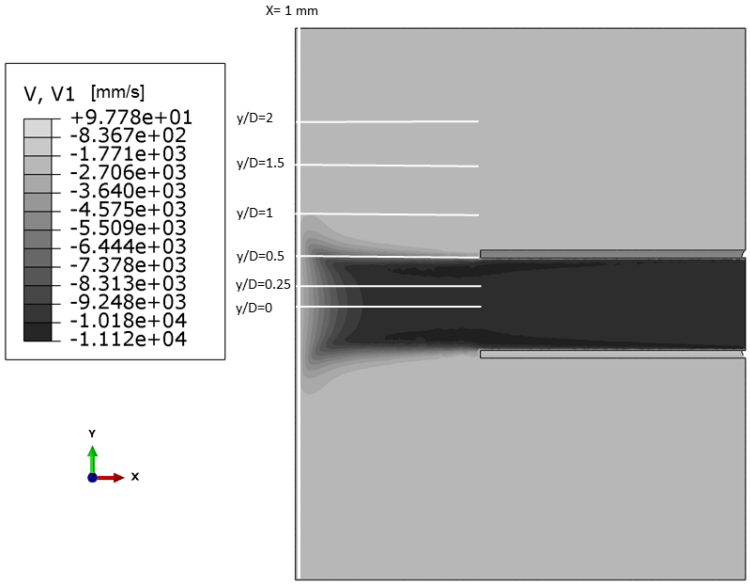

Figure 5.4 Mean axial velocity component from numerical CFD model of the impinging jet. $\frac{y}{D}$ is the normalised distance on the wall plotted at six trajectories normal to the wall

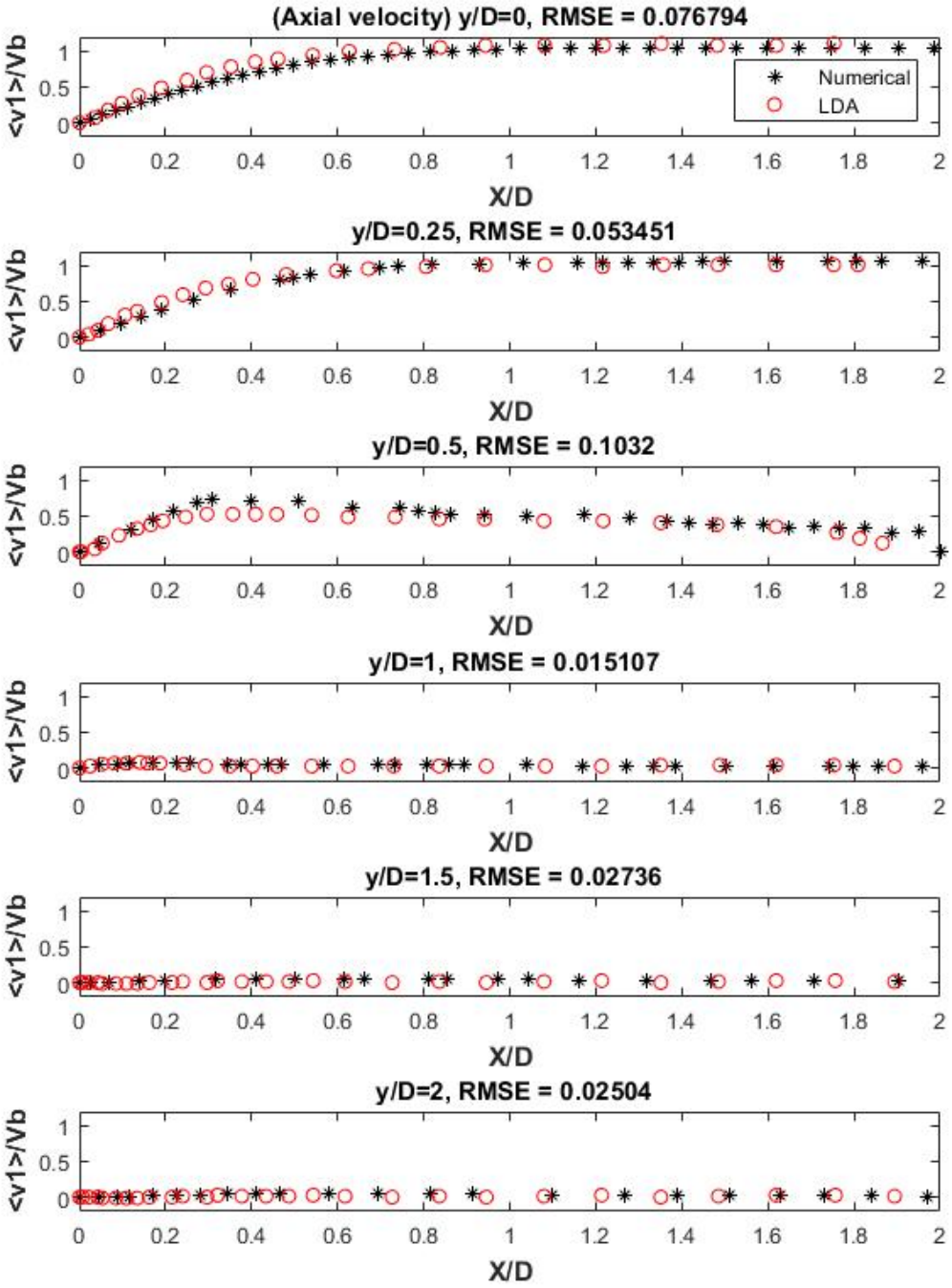

Figure 5.5 Mean normalised axial velocity component at six axial trajectories normal to the wall compared against laser doppler anemometer (LDA) data from Mark J. Tummers et al. [158]. $\frac{X}{D}$ is the normalised distance Perpendicular to the wall and $\frac{y}{D}$ is the normalised distance on the wall. $< v1 >$ is the mean axial velocity and Vb is flow bulk velocity

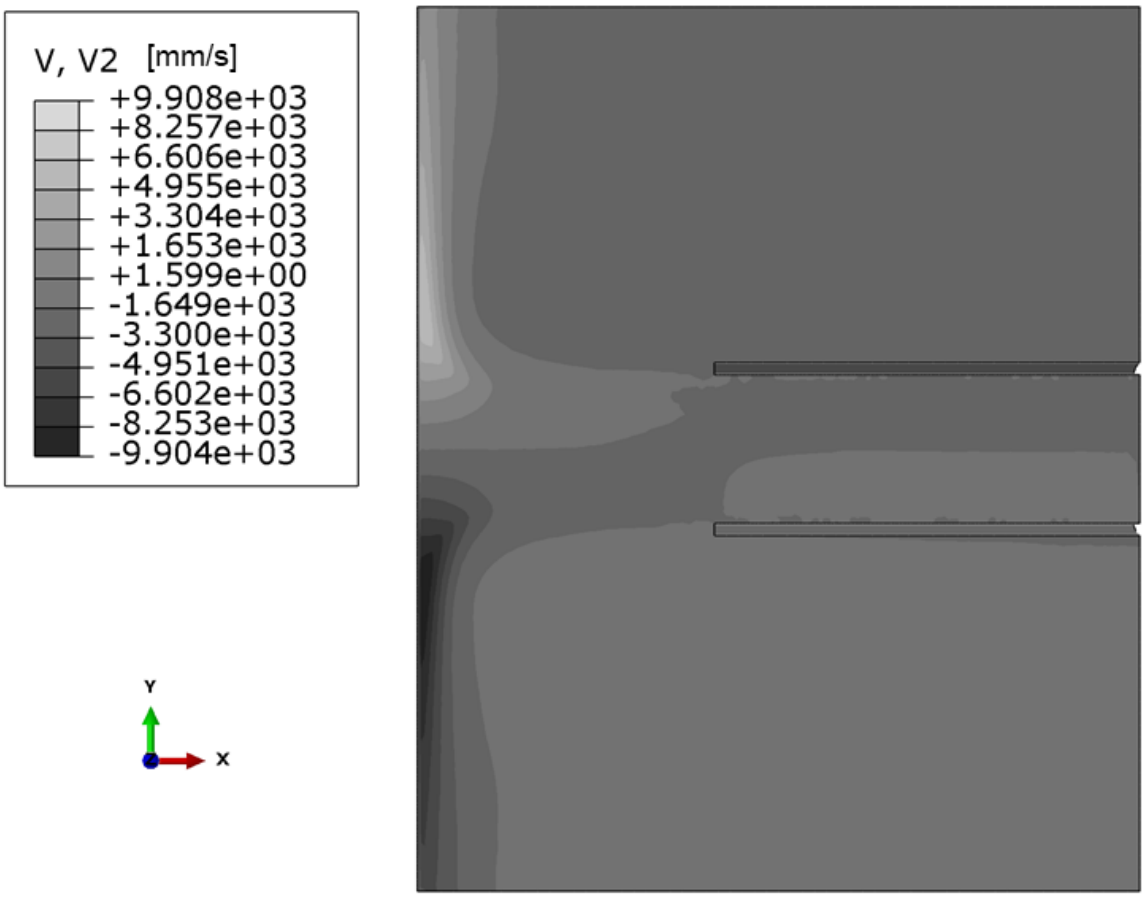

Figure 5.6 Mean radial velocity component from the numerical CFD model of the impinging jet

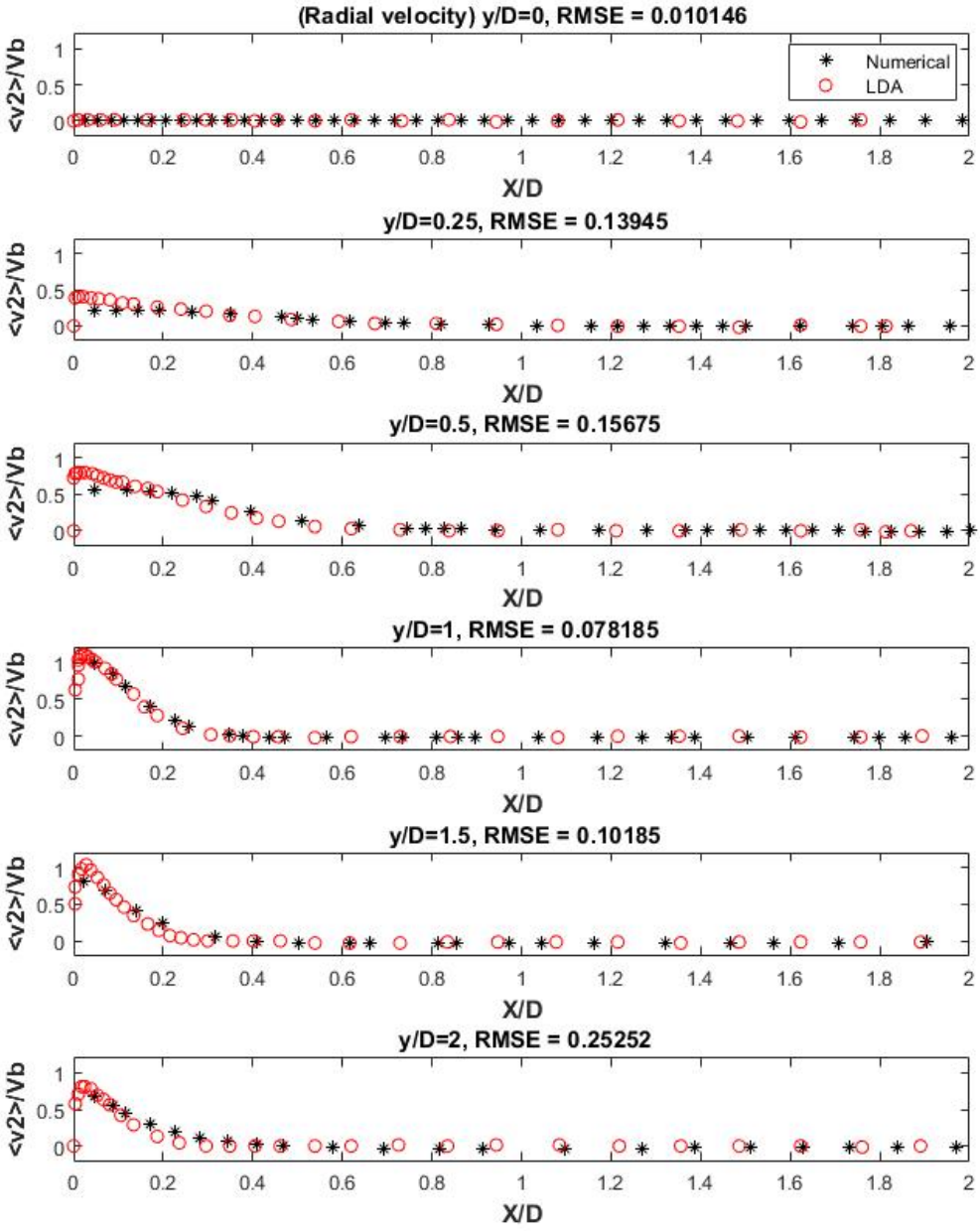

Figure 5.7 Mean normalised radial velocity component at six axial trajectories normal to the wall compared against laser doppler anemometer (LDA) data from Mark J. Tummers et al. [158]. $\frac{X}{D}$ is the normalised distance perpendicular to the wall and $\frac{y}{D}$ is the normalised distance on the wall. $< v2 >$ is the mean radial velocity and Vb is flow bulk velocity

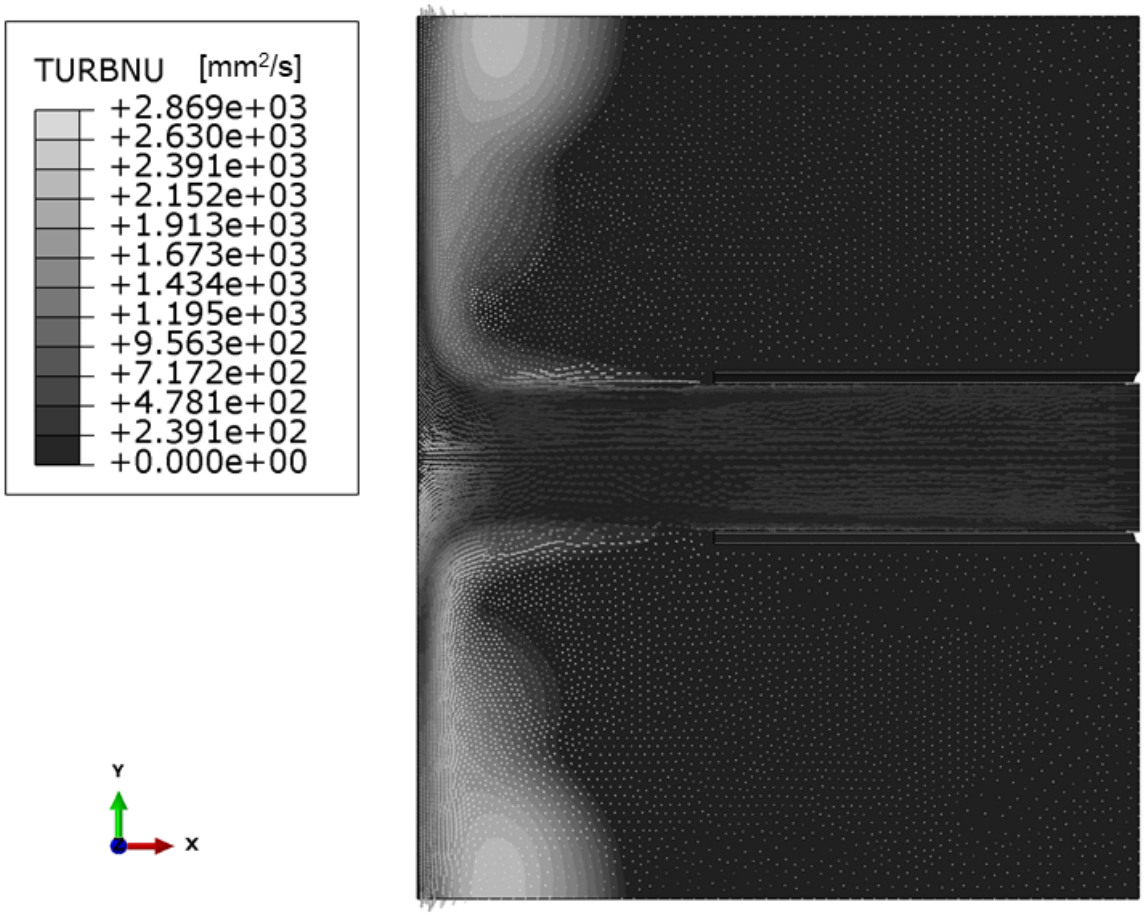

Figure 5.8 Mean turbulent kinematic viscosity from the numerical CFD model of the impinging jet

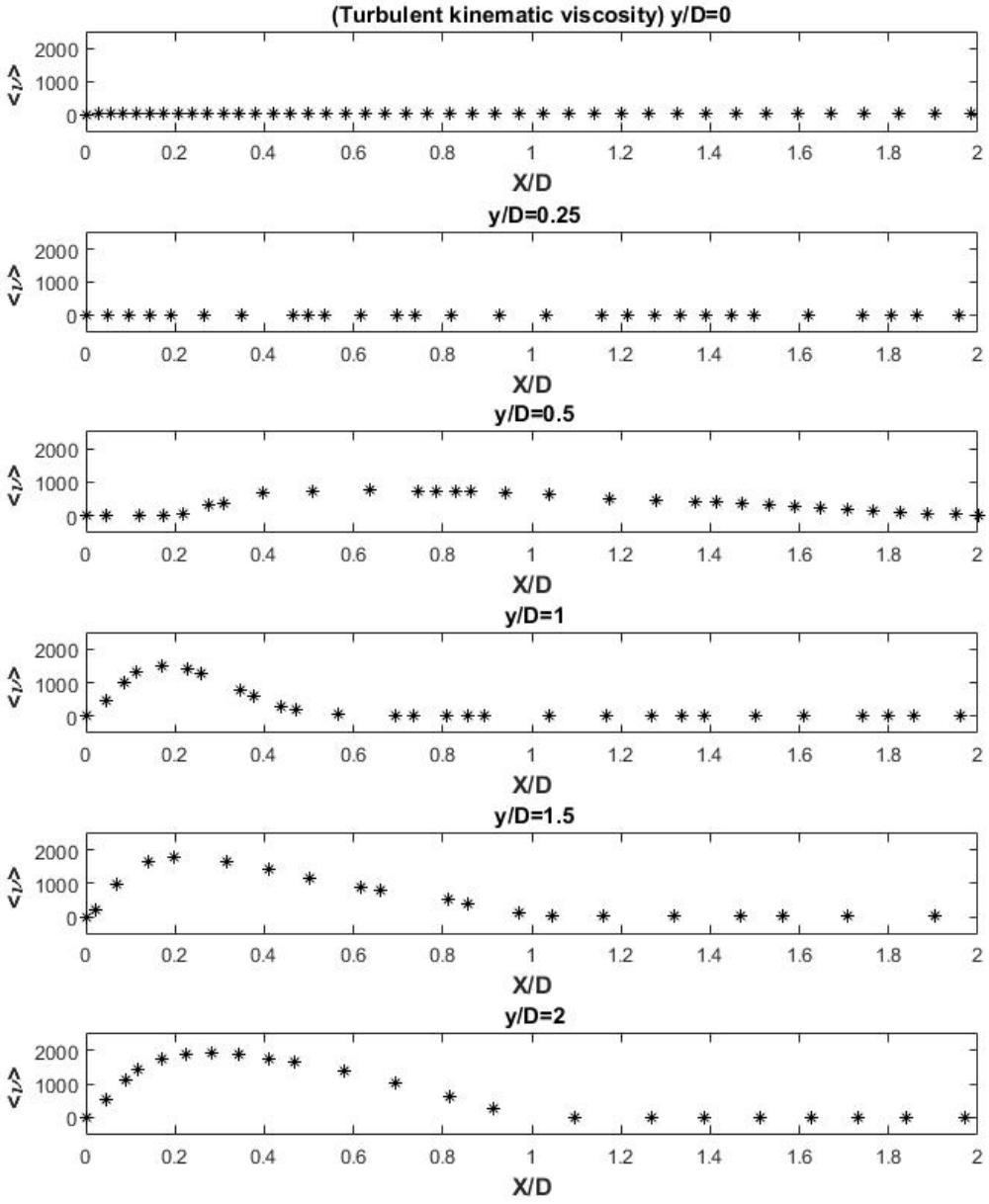

Figure 5.9 Mean turbulent kinematic viscosity at six axial trajectories normal to the wall. $\frac{X}{D}$ is the normalised distance perpendicular to the wall and $\frac{y}{D}$ is the normalised distance on the wall

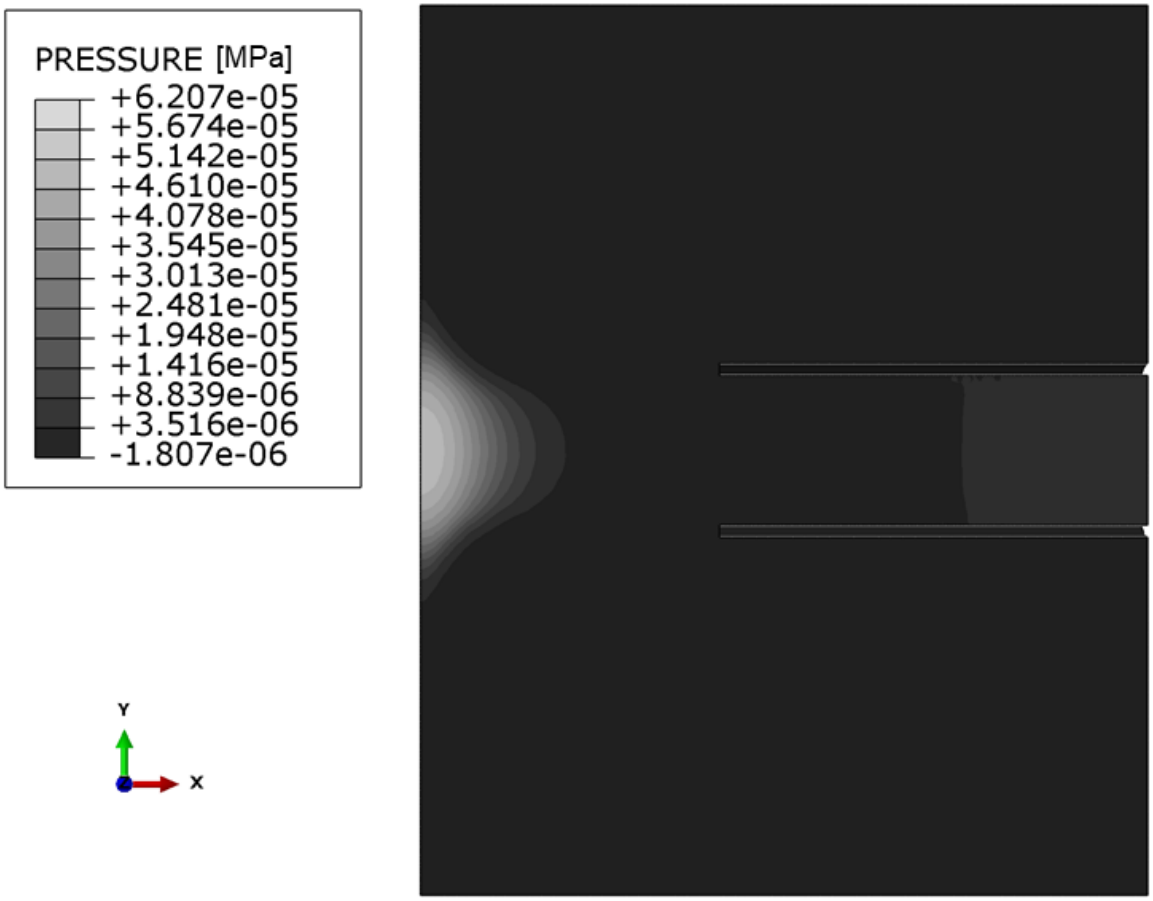

Figure 5.10 Static pressure distribution for the numerical CFD model of the impinging jet

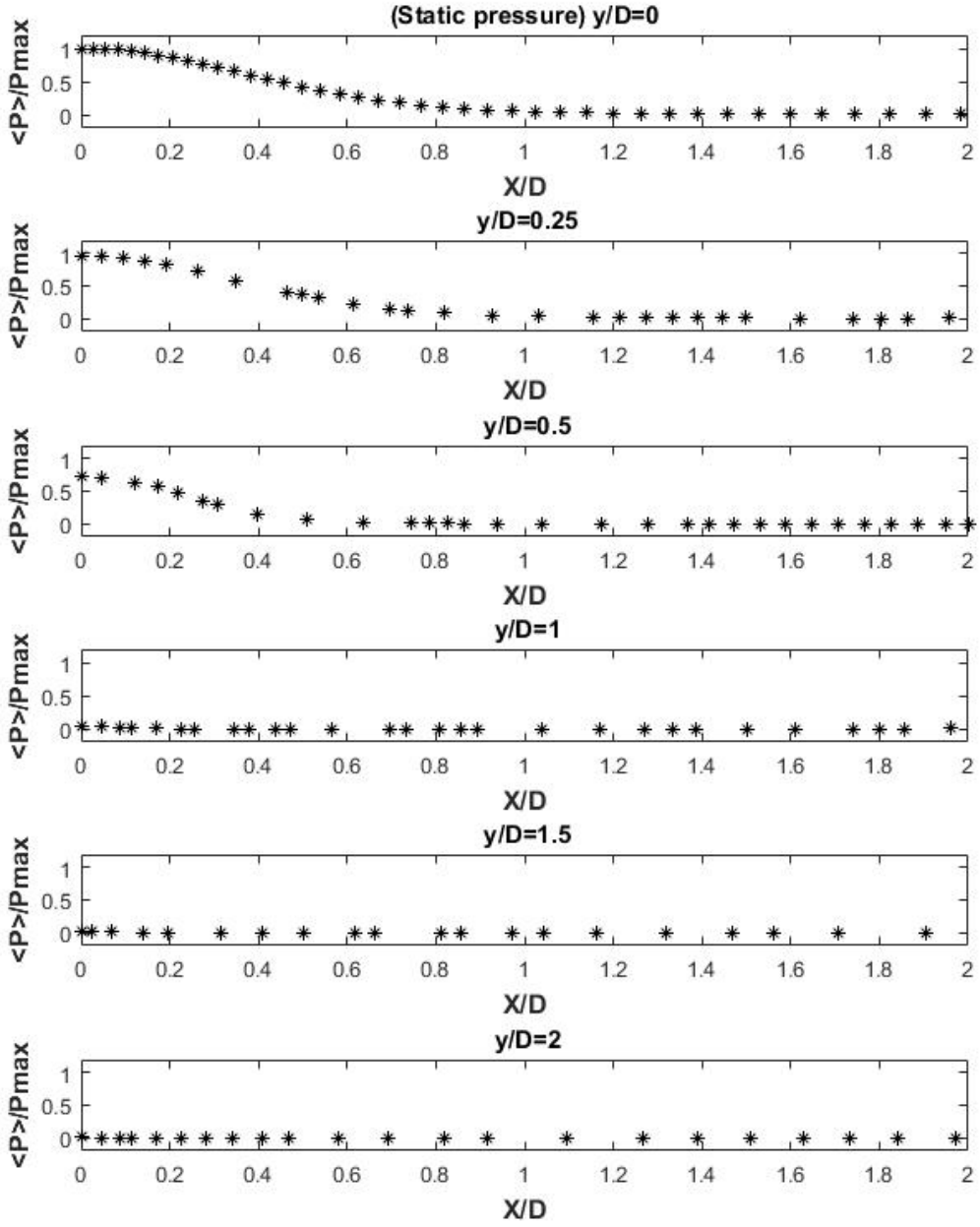

Figure 5.11 Normalised static pressure along six axial trajectories normal to the wall. $\frac{X}{D}$ is the normalised distance perpendicular to the wall and $\frac{y}{D}$ is the normalised distance on the wall

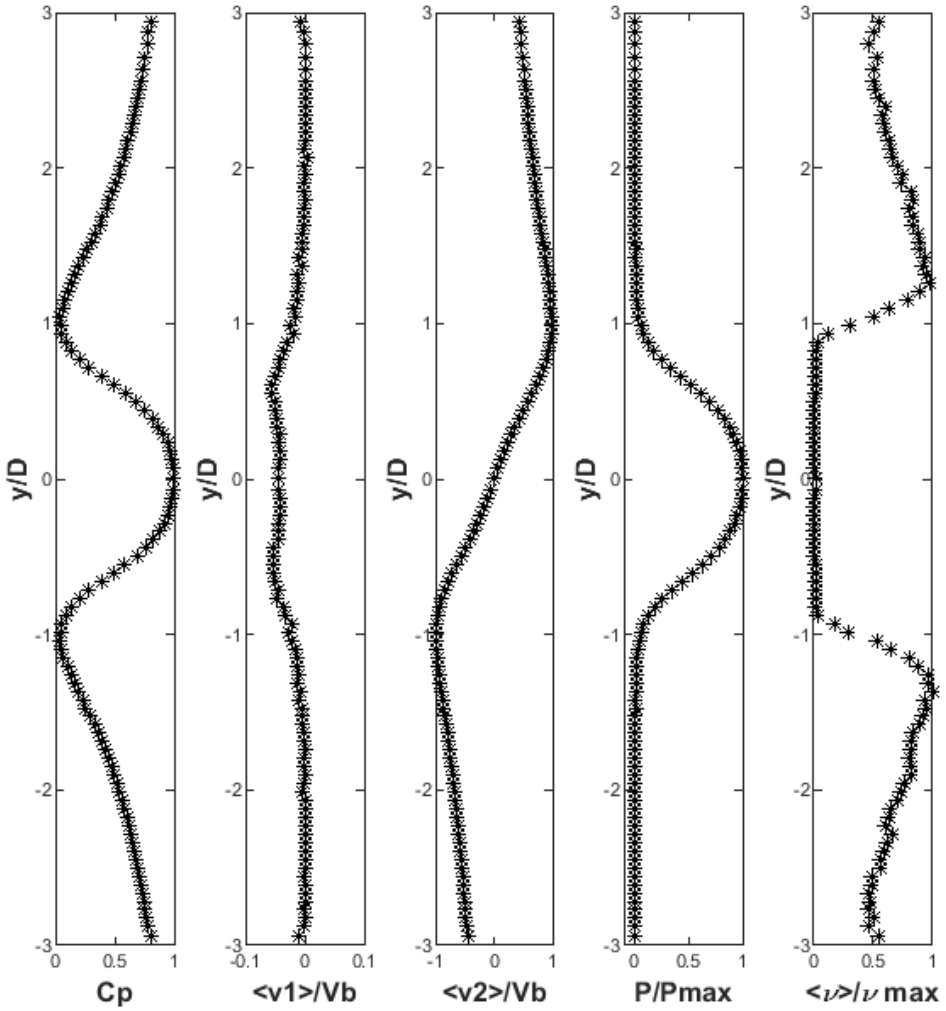

Figure 5.12 Pressure coefficient, normalised mean axial, mean radial velocities, normalised pressure and normalised turbulent kinematic viscosity at trajectory parallel to the wall at distance X= 1 mm from the wall. $\frac{y}{D}$ is the normalised distance on the wall

5.3 Coupled FSI model of the non-contact tonometry test

Model of the air puff test consists of two different domains and governing physics. The first domain is the finite element model of the eye and the second domain is for model of the turbulent air jet.

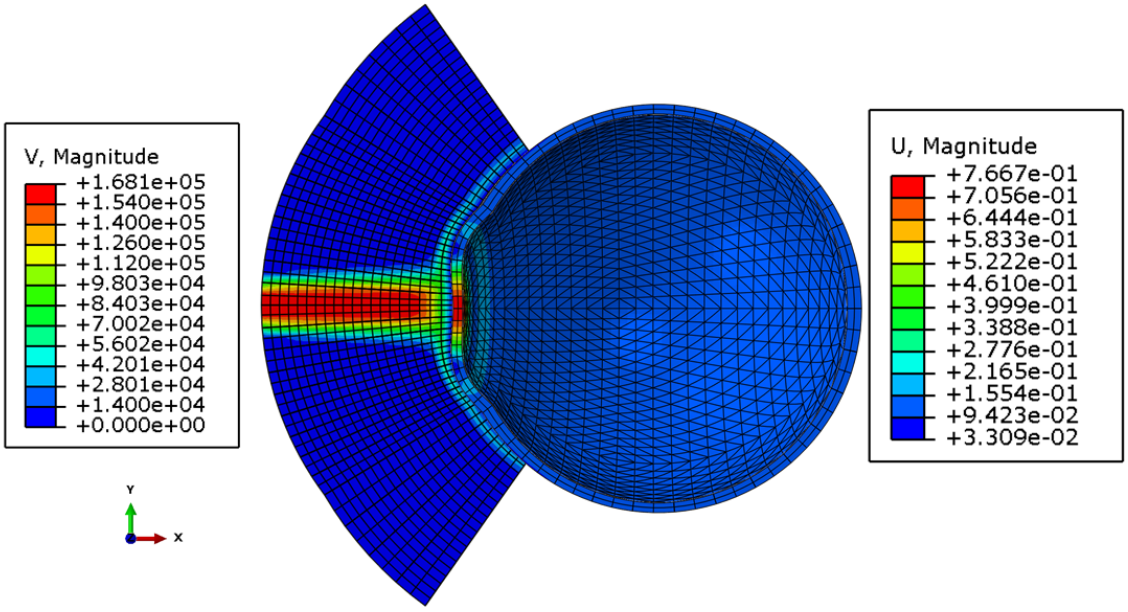

Figure 5.13 Fluid Structure Interaction coupled model of the air puff test, the left legend represents velocity values of the air puff in (mm/s) and the right legend represents deformation values of the eye model in (mm)

The eye model has two layers with thicknesses of 70% and 30% of the total thickness for both cornea and sclera. The surface between the two layers of cornea was subject to a contact boundary condition with friction coefficient of 0.072 to give cornea the required flexibility under the air puff loading to give similar behaviour to the clinical deformations. The air jet domain consists of 20 layers above the cornea surface with total distance of 11 mm from the cornea which is the typical distance between the Corvis-ST device and the human eye under testing [169–171].

5.3.1 Mesh sensitivity analysis results

The mesh sensitivity study shown in figure 5.14 was performed with 10 different mesh densities with total number of nodes ranging between 24743 and 48283; with cornea rings from 11 to 22 and number of elements from 18780 to 55146. Graphs (a) and (b) show the change of cornea apical deformation with different mesh densities. Graphs (c) and (d) show the change of air pressure on cornea Apex at time 15 ms with the mesh change. Graphs (e) and (f) show the running time of every model to reach the maximum deformation performed on the same machine on the Chadwick cluster. The running time is an important parameter in the current study as a parametric study of 110 different eye tests have to be conducted for validation purposes and generating the new IOP algorithm.

For the first three tests from 11 rings model to 13 rings model, the deformation of the cornea apex is decreasing significantly to a stable value of (0.73 mm). The air puff pressure on the CFD model showed the same behaviour for rings from 11 to 13 and decreased to a stable value of (0.009 MPa). The 15 rings model marked with red point is the chosen number of rings to enter the parametric study and the future calculations with total number of nodes (31735), in both models (air and eye), and total number of elements (29596) with running time of 17 Hrs.

Differences between Quarter-segment and full eye models

Due to rotational symmetry of the results in both domains, only quarter of the two domains was simulated in the parametric study to save the running time. Figure 5.15 shows the two coupled domains for the quarter model in (a) and the full model in (b). The difference in corneal deformations is shown in figure 5.16. Tha maximum error in the deformation was 0.3% which was negligible compared to the differnce between numerical and clinical deformations.

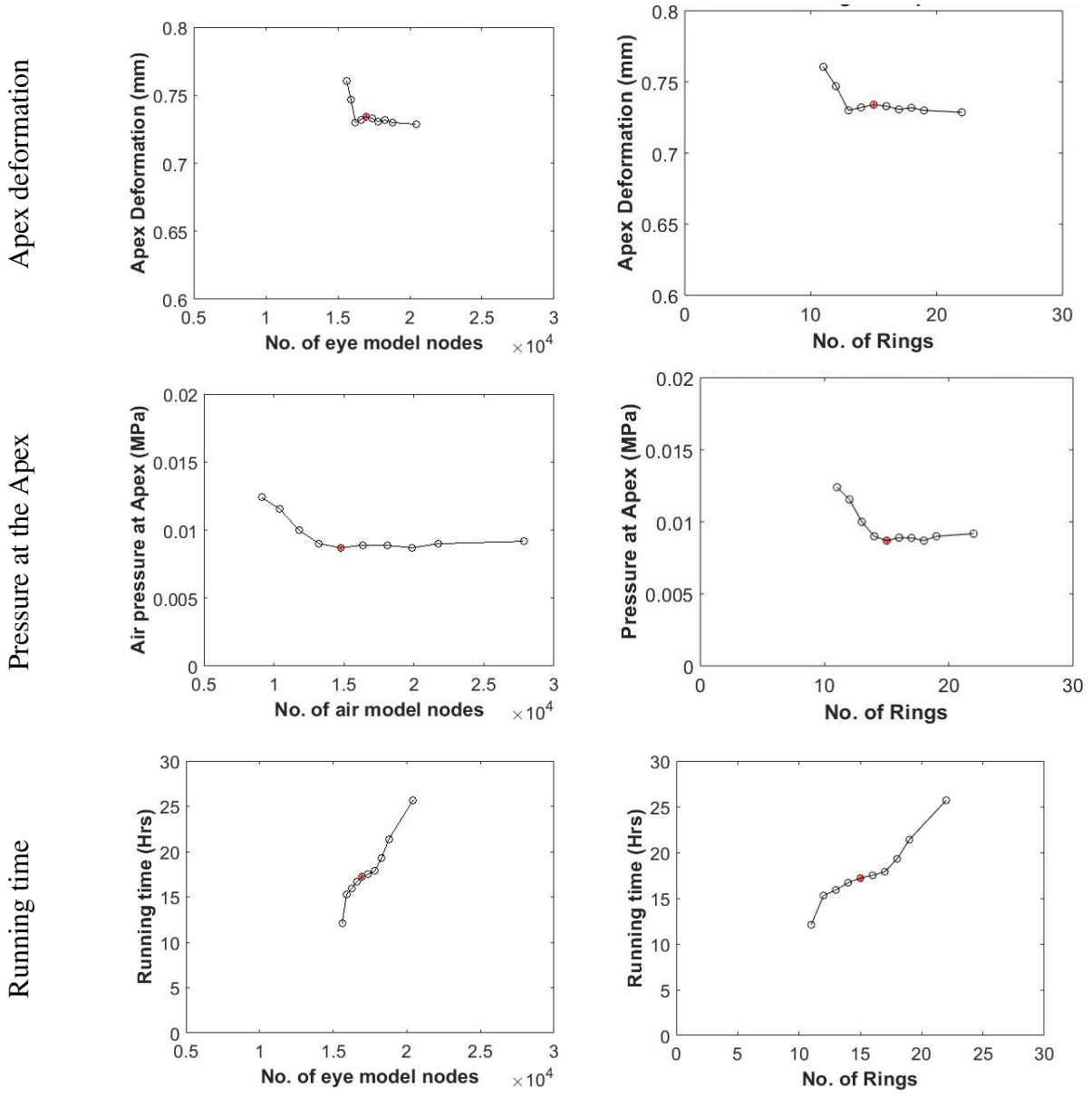

Figure 5.14 Mesh sensitivity analysis results, Deformation of the cornea apex, the air pressure at the apex and the running time against the total number of nodes and the number of element rings in the cornea, the red marker represents the chosen mesh density

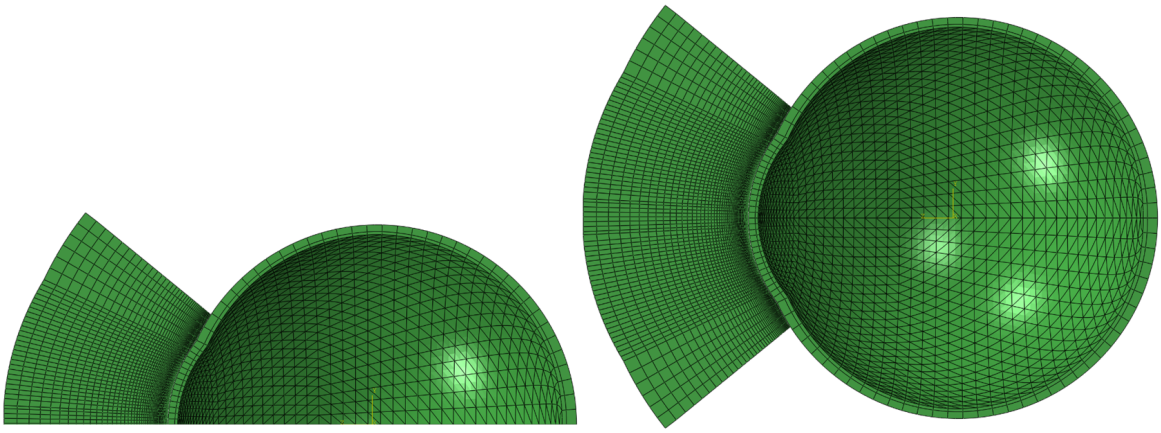

(a) (b)

Figure 5.15 Mesh of (a) quarter-segment model and (b) full eye model

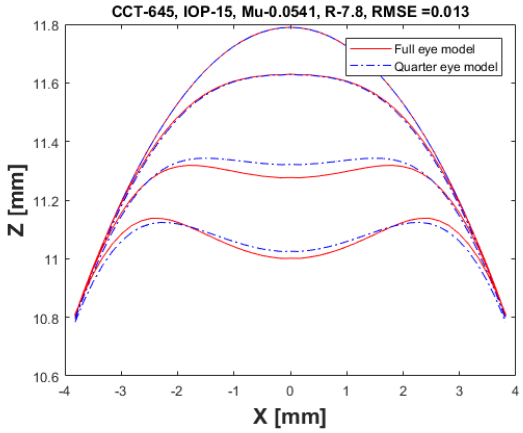

Figure 5.16 Difference in corneal deformations between full eye and quarter segment eye models

5.4 Air puff analysis

The air puff was analysed to see the change of velocity, pressure and mesh deformation during the test. Figure 5.18 shows two velocity components of the air puff, the axial velocity (V3) normal to the cornea and velocity component (V1) parallel to the cornea at three normal trajectories (Y/D=0, Y/D=1, Y/D=2), that are explained in figure 5.17, and 4 time steps (T= 5, 8, 10, 16 ms). By the time, the puff gets stronger to reach its maximum strength at T=

16 ms and as distance from the puff orifice increases, normal velocity (V3) decreases until it reaches zero at the stagnation point on cornea surface. By changing the axial trajectory further away from cornea centre, the puff gets weaker and is noticed at (Y/D = 1 and 2), there are some negative values for the normal velocity indicating reflection of the air from cornea surface in the opposite direction to the flow [171]. The jet accelerates parallel to the cornea forming a radial wall jet, developing with time and by going further from the cornea centre axis. This explains why there is negative pressure observed at the same location of the cornea, which will be presented later in the next subsection 5.4.1.

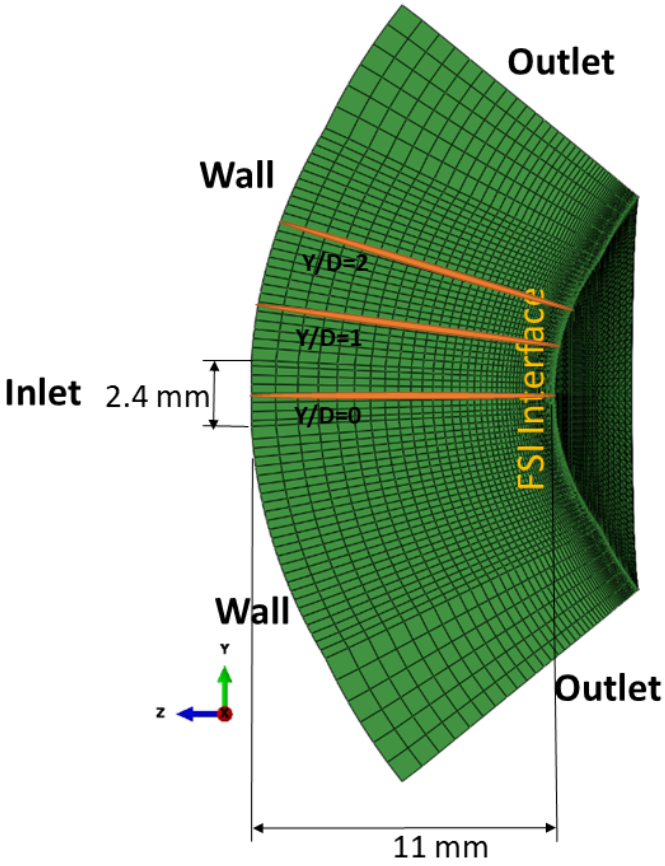

Figure 5.17 Locations of the axial trajectories normal to cornea at which velocity and pressure were monitored

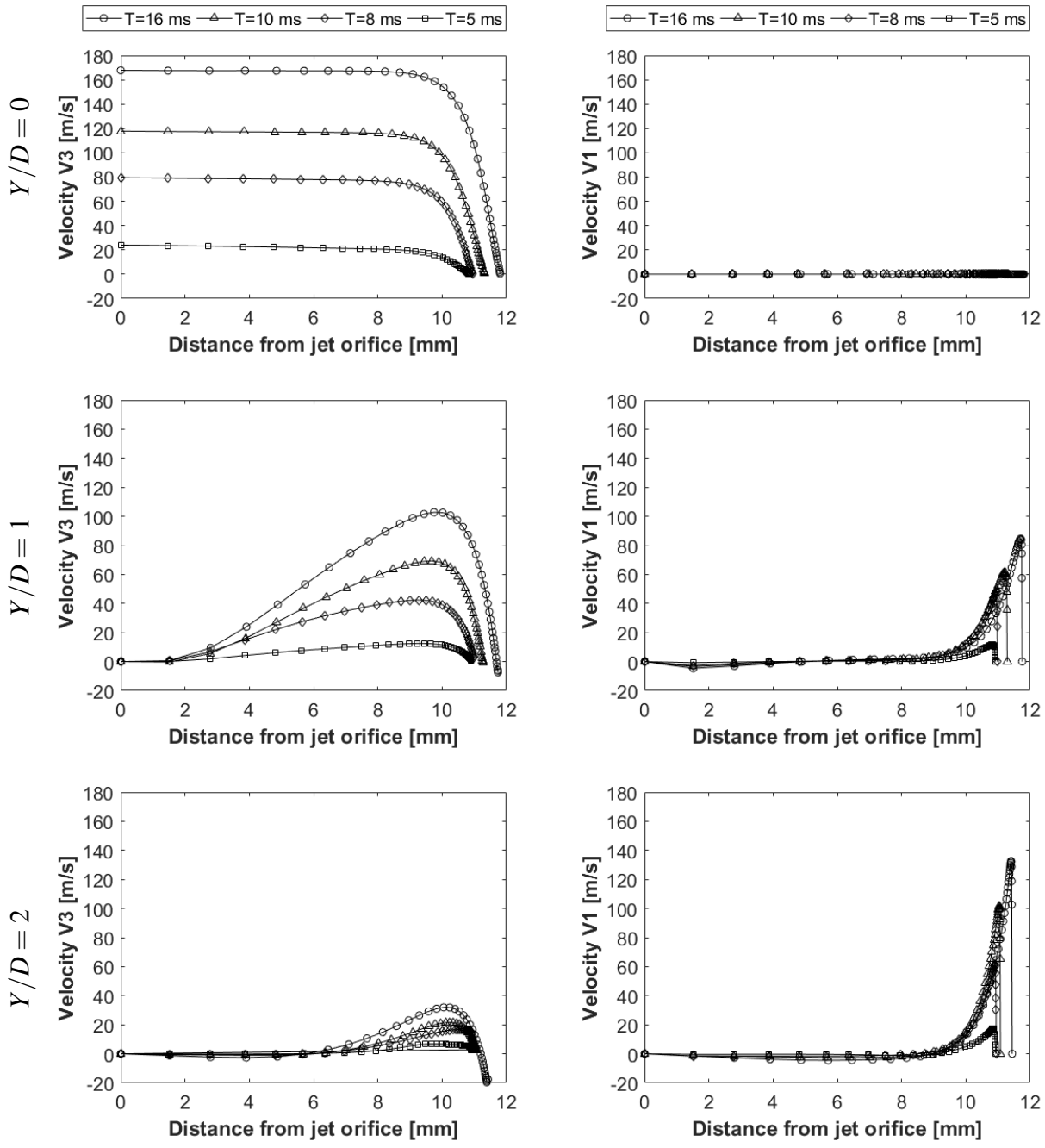

Figure 5.18 Air puff velocity components analysis at axial trajectories Y/D=0, Y/D=1, Y/D=2 and 4 time steps at T= 5, 8, 10, 16 ms

On the other hand, pressure was found to change with corneal deformation and time steps as illustrated in figure 5.19. Pressure here represents the static pressure, it starts with zero at the jet orifice and increase gradually towards the cornea because of transforming the dynamic pressure into static pressure. This is also explained in the plots of pressure coefficient, it starts at zero and becomes 1 at the stagnation points on corneal surface which is a quantitative value of the conversion from dynamic to static pressure. It was also noticed from the pressure trajectories that distance from the jet at end of every curve is increasing because of movement of cornea with time. In terms of the CFD mesh motion during the test, Figure 5.20 shows the axial (U3) and parallel (U1) deformations as they develop with time and at the same three trajectories studied earlier. As the axial trajectory go further from cornea centre, the axial deformation (U3) decreases, but the opposite happens with parallel deformations (U1) [171].

5.4.1 Velocity, pressure and deformation profiles

Fluid structure interaction was found to have an effect on pressure distribution on cornea during time of the air puff test. Figure 5.21 shows the pressure distribution on the cornea at different time steps during the test. Graph (a) shows the pressure distribution change with time and the region where there is negative pressure. Graph (b) shows the progression of corneal deformation with time and Graph (c) indicates corneal nodes deformation with time at three locations; cornea centre (Apex), at distances 1.7 mm and 2.4 mm from apex. To show the effect of corneal deformations on pressure values of the jet, two different simulations of the turbulent jet were performed; one impinging on a rigid cornea surface with no moving boundaries and no slip wall boundary condition and the other using FSI coupling between CFD and finite element to consider corneal deformations. When the results of these two models were compared, it illustrated a change of 6.29 % in the maximum pressure at apex, as shown in Figure 5.22 [169–171].

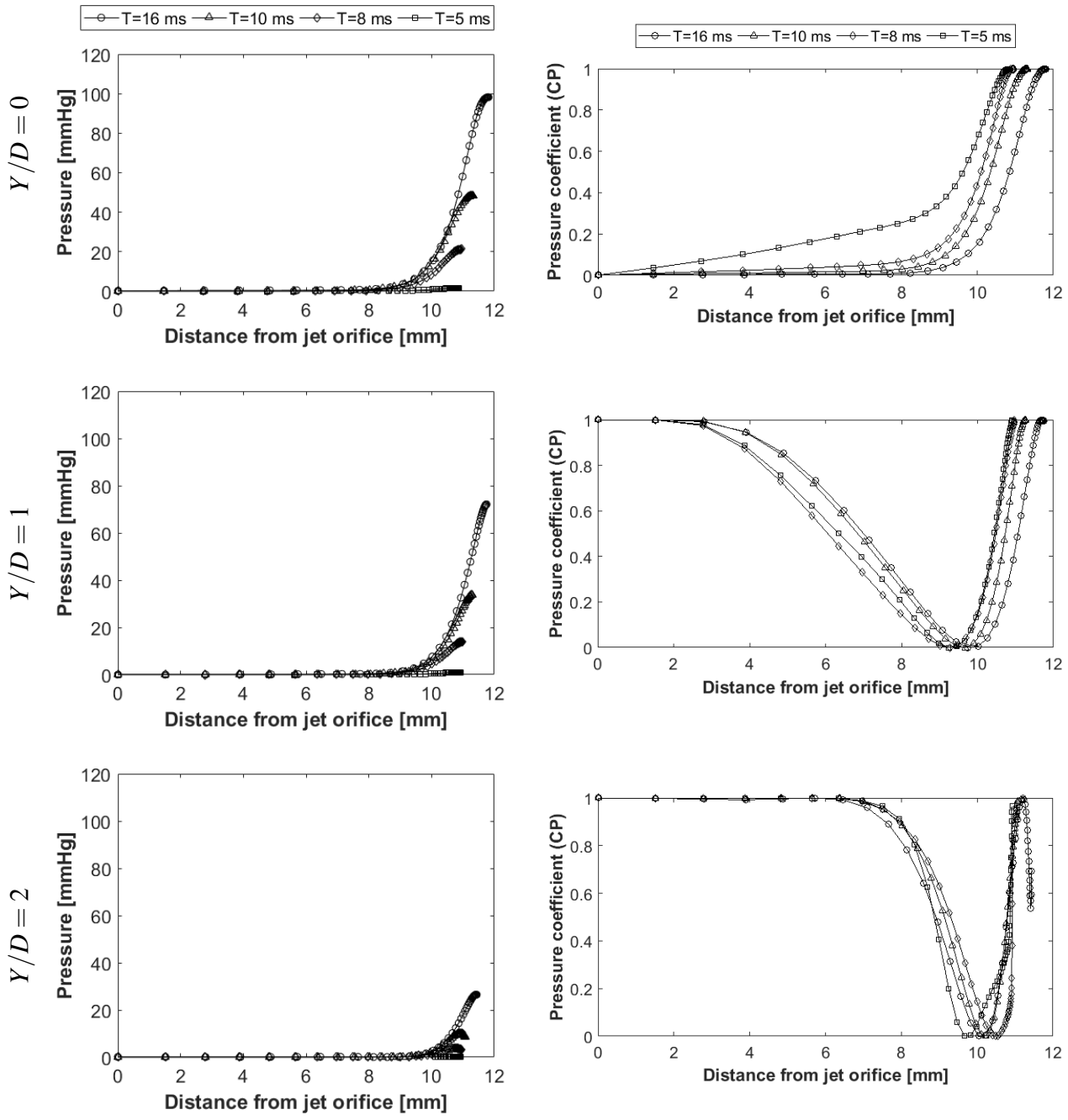

Figure 5.19 Air puff static pressure and pressure coefficients' traverses, at Y/D=0, Y/D=1, Y/D=2 and 4 time steps at T= 5, 8, 10, 16 ms [171]

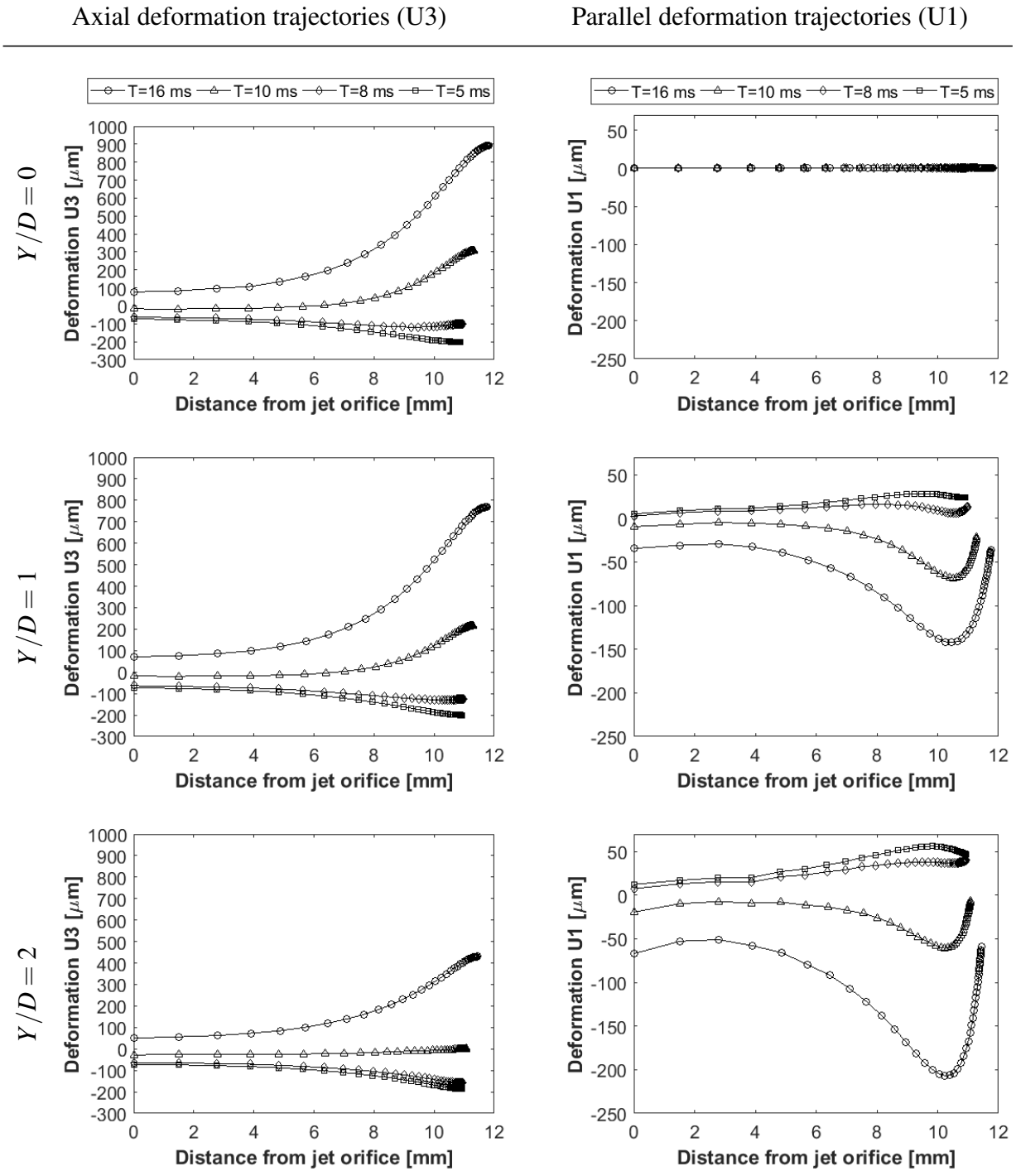

Figure 5.20 Air puff mesh deformation components analysis at axial trajectories Y/D=0, Y/D=1, Y/D=2 and 4 time steps at T= 5, 8, 10, 16 ms

Description	Figure
(a) Spatial pressure distribution	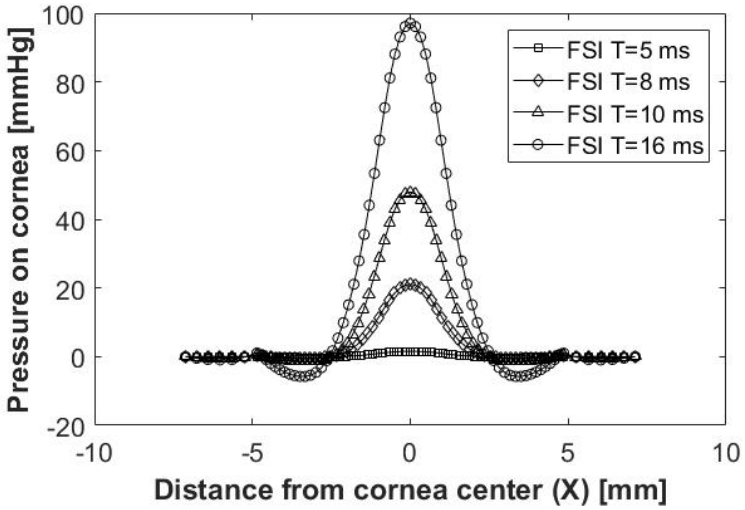
(b) Spatial cornea deformation profiles	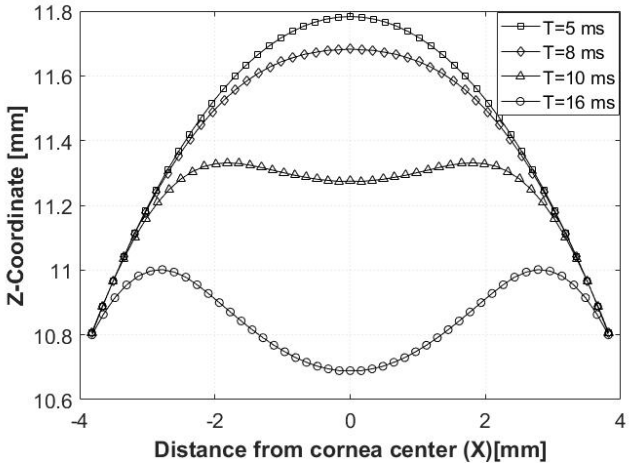
(c) Temporal apical rise	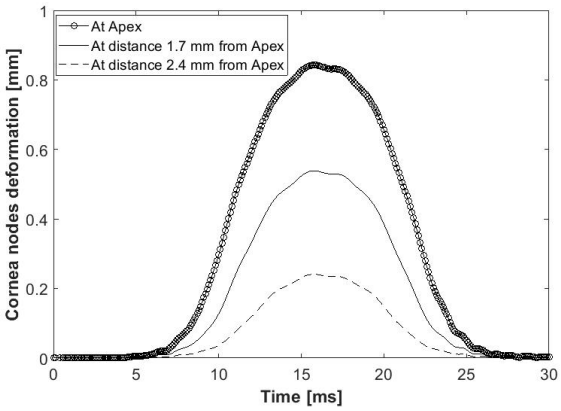

Figure 5.21 Pressure and deformation profiles on the cornea. Spatial pressure distribution on the cornea (a), cornea deformation profiles (b), and Temporal apical rise at three locations on the cornea (c) [169–171]

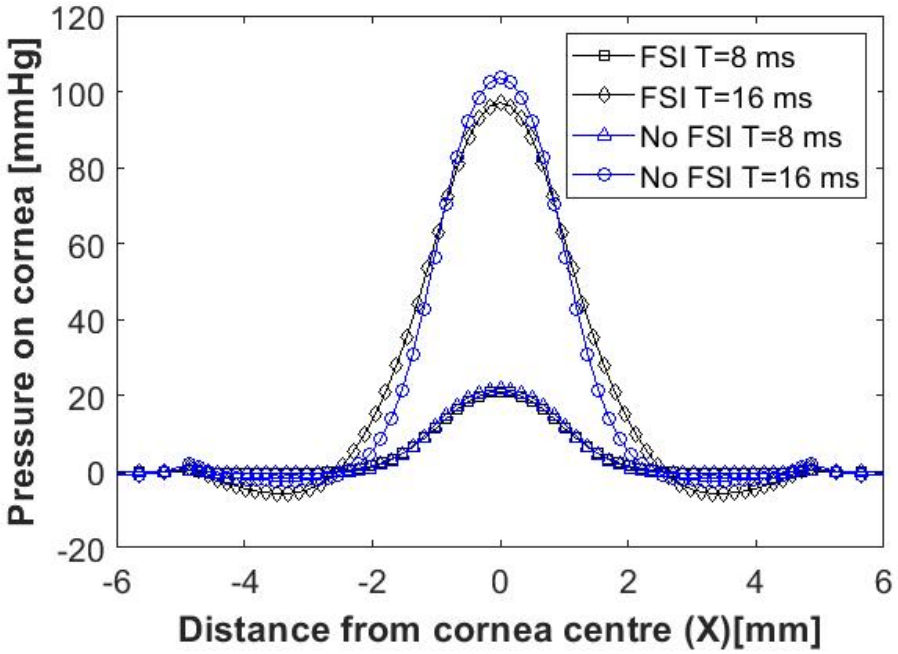

Figure 5.22 Pressure distribution comparison on the cornea with and without FSI effect

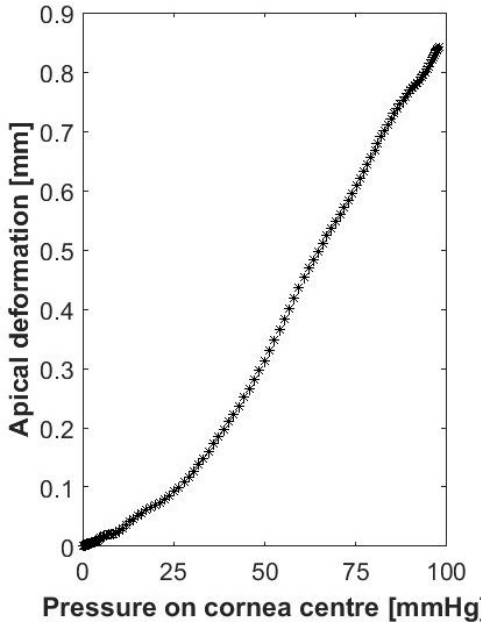

Figure 5.23 Corneal apical deformation against pressure loading on cornea centre

In order to show the mechanical response of corneal material to air puff loading, pressure was plotted against apical deformation, in Figure 5.23, to analogue the stress-strain curve or corneal material showing the nonlinear mechanical behaviour of the cornea. Comparison of the normalised air puff pressure distribution with distributions presented in the literature for Muench et al. [73] and kling et al. [11] are shown in Figure 5.25. It shows good agreement with the spatial pressure distribution profile at 3 time steps (T= 5, 10, 16 ms).

A nother analysis of velocity, pressure coefficient and corneal deformation magnitude was carried out at distance of 1 mm from the cornea. Figure 5.26 shows in the first plot, distribution of velocity magnitude ratio (V/Vmax) and how it reaches zero at cornea apex and one at distance equal 2 mm from the centre. The same conclusion was found from the second plot of pressure coefficient reaching one at the centre representing the stagnation point and go to zero at distance = 2 mm. The third plot is more interesting, it shows distribution of the axial velocity ratio (V3/V3max) along the cornea. It is showing zero at the centre, but negative values up to the 2 mm ring of the cornea, explaining the reflection of air away from cornea surface. The fourth plot is the pressure coefficient based on V3 and the fifth plot is showing the deformation magnitude along the cornea.

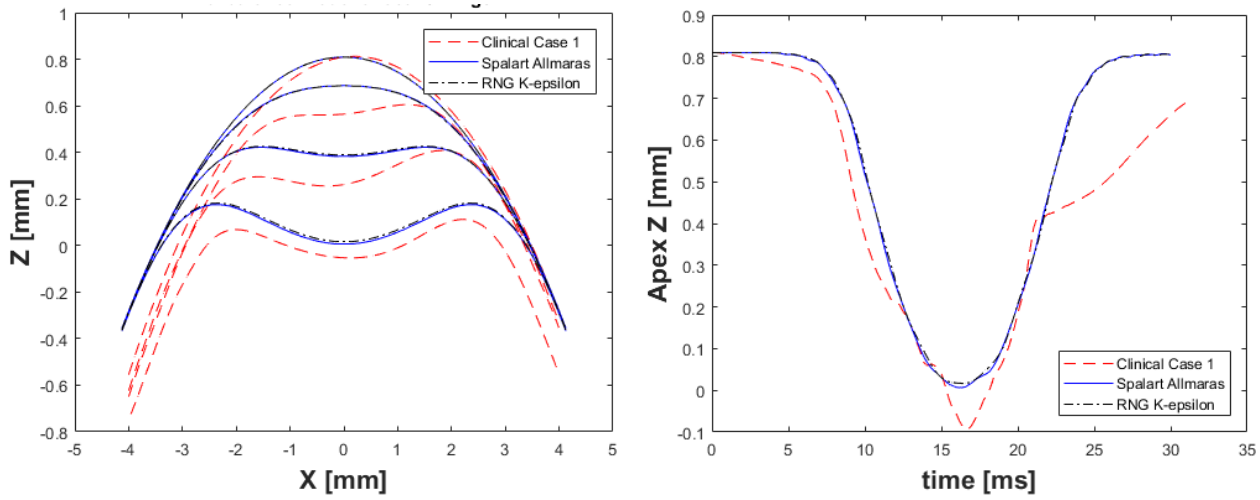

(a) (b)

Figure 5.24 Turbulence model effect and comparison with the clinical data

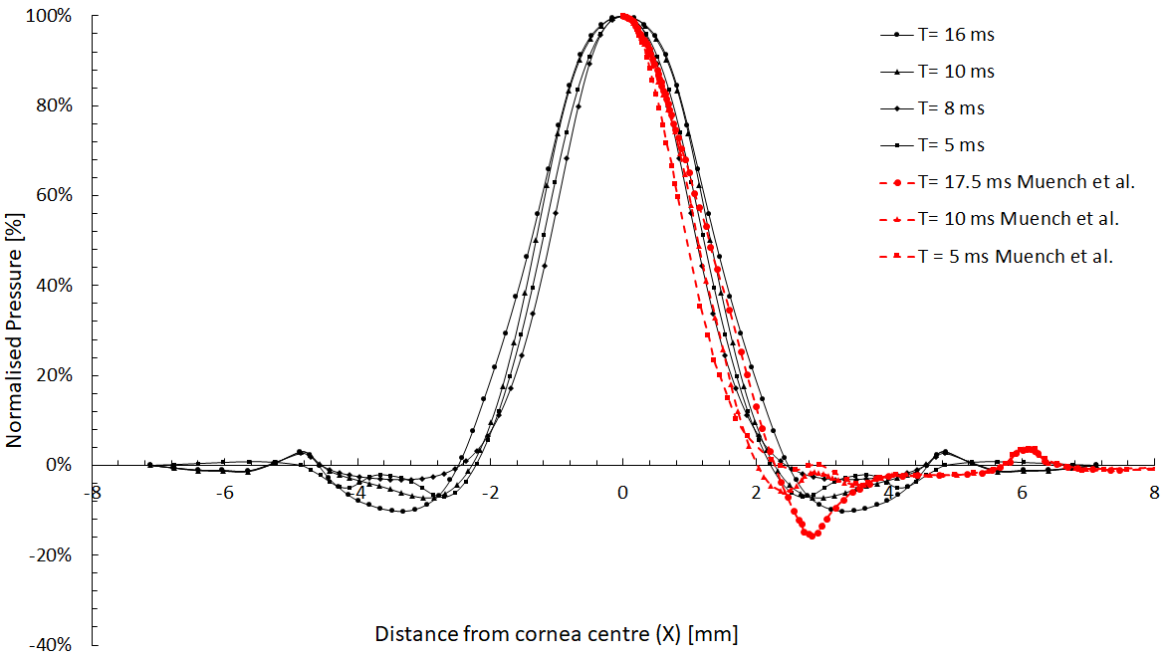

(a)

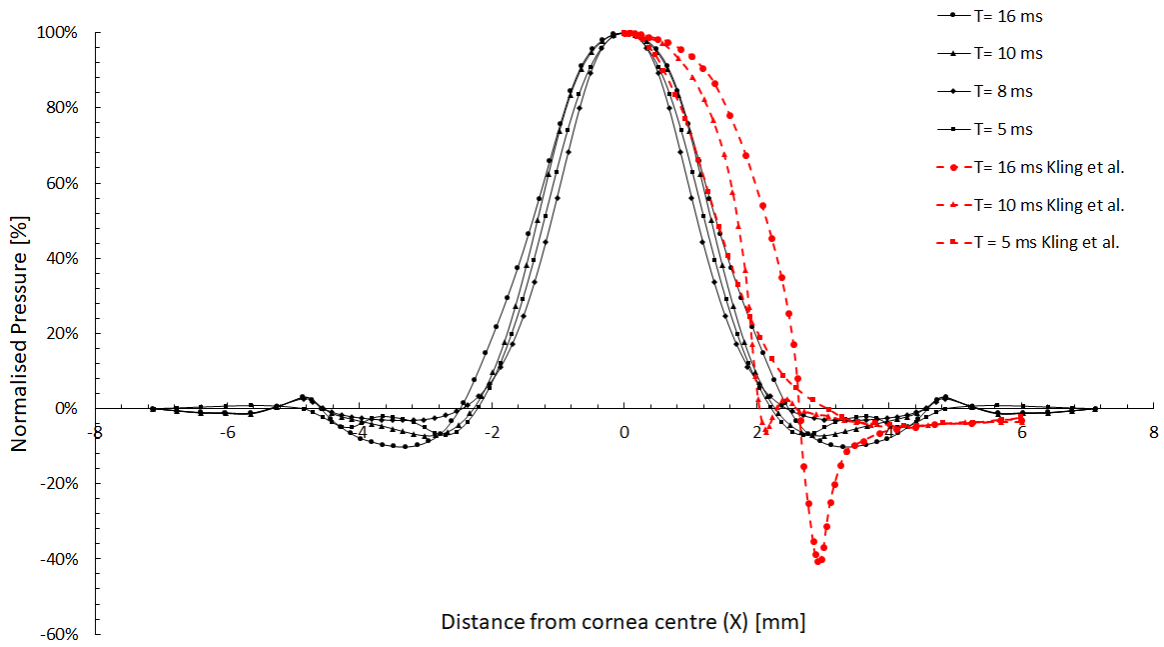

(b)

Figure 5.25 Comparison of pressure distribution on the cornea with two studies from literature Muench et al. [73] (a) and kling et al. [11] (b)

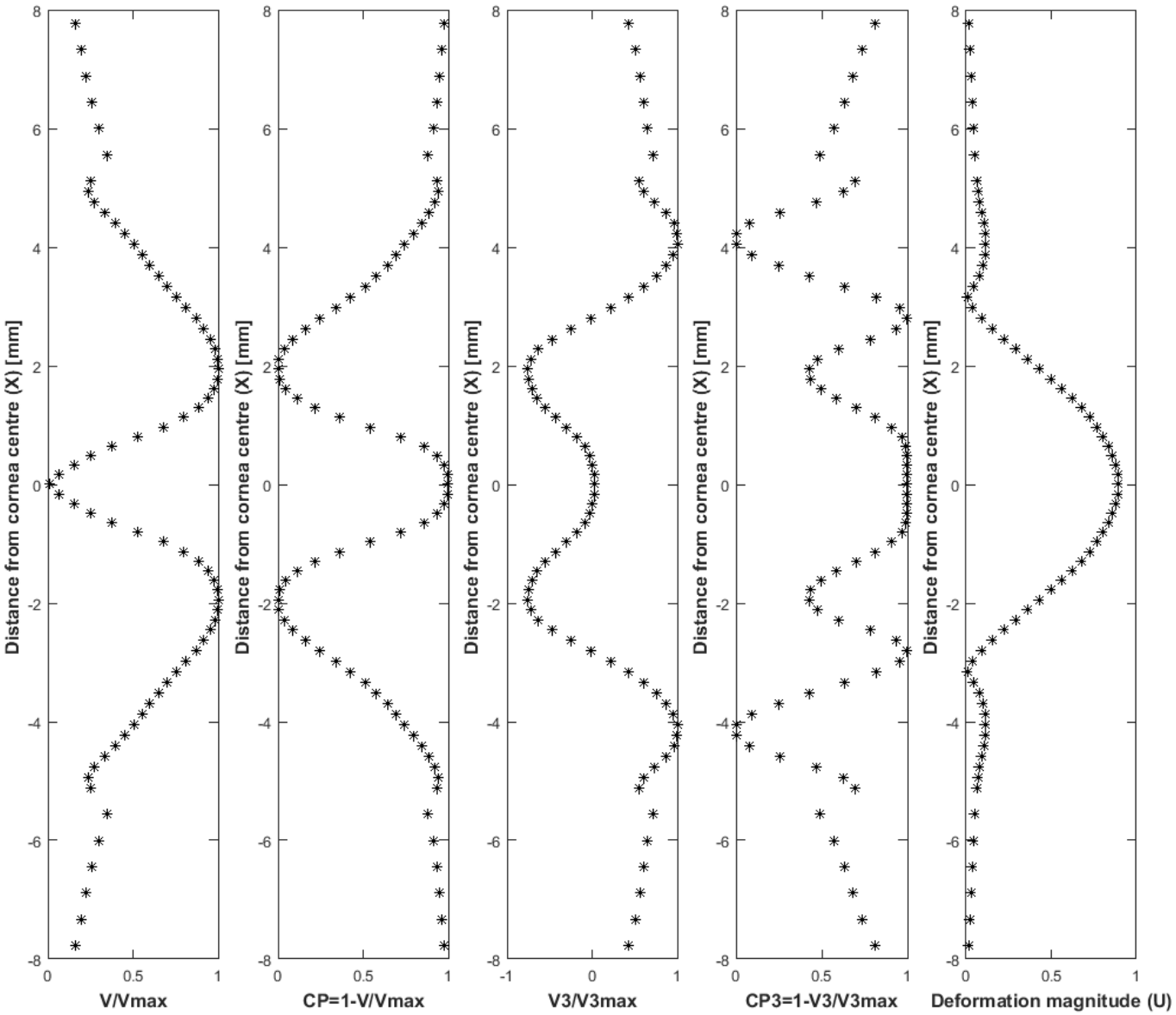

Figure 5.26 Velocity (V) magnitude distribution, axial velocity (V3), pressure coefficients based on V and V3 and deformation magnitude distribution on the cornea at distance (X= 1mm) from the cornea surface

Also, the comparison between effect of turbulence models, Spallart Almaras and RNG k-epsilon, on cornea deformation profiles was performed, as shown in Figure 5.24. There was no difference in results between the two models.

5.5 Clinical validation of dynamic corneal response to air puff test

A set of clinical data for six healthy patients was choosen from the clinical dataset with wide range of corneal parameters, provided by Vincieye Clinic in Milan, Italy and Rio de Janeiro Corneal Tomography and Biomechanics Study Group, Brazil. They were used for comparison with the numerical data that was obtained from the patient specific fluid-structure interaction model. A good agreement and close behaviour to the real corneal behaviour was achieved. Figure 5.27 shows results for the six tests and their comparison with clinical data. The left column of graphs shows corneal deformation profiles at four time steps T= 5, 8, 10, 16 ms. The difference in profiles is due to the fact that biological tissue is different in responding to the air puff and is not gauranteed that the puff is applied to the cornea centre with the same angle and distance from the nozzle. The right column of figures shows the apical deformation with time numerically and clinically.

Figure 5.28 provides comparison of the temporal pressure profile on cornea centre clinically and numerically, the last plot in this figure provides comparison of the temporal pressure profiles between the six cases. The temporal and spatial pressure profiles are different from case to case which makes the consideration of FSI effect between the air puff and cornea, more important in IOP measurements. Figure 5.29 presents the apical deformations as a function of pressure applied on cornea to show the mechanical response of the cornea to loading. Analysis of error for apical deformations, pressure on cornea, and highest concavity corneal profile, is summarised in Table 5.1 by presenting the values of root mean square error (RMSE) between the clinical and numerical behaviour. The highest RMSE was in the temporal pressure profile on corneal apex due to the difference at in the unloading part of the test. Clinically, the cornea has a hysterisis effect due to the visco-elastic material behaviour causing it to have some delay in returning back to the original geometry. This is

not considered in the material model of the eye which is affecting the accurate prediction of pressure on cornea from CFD model of the air puff.

Table 5.1 Root mean square error (RMSE) between the clinical and numerical results

Variable	N	Mean	Std. Deviation	Minimum	Maximum
HC corneal profile RMSE (mm)	6	0.187	0.167	0.067	0.645
Apical deformation RMSE (mm)	6	0.28	0.10	0.127	0.41
Pressure on apex (Loading part) RMSE (mmHg)	6	0.103	0.052	0.046	0.214
Temporal pressure on apex (Full curve) RMSE (mmHg)	6	10.31	5.76	4.07	17.24

Comparison of corneal response parameters

Using built in-house Python and Matlab codes, the dynamic corneal response parameters were extracted from the numerical model to compare them against the same parameters available for the clinical dataset. Table 5.3 gives descriptive statistics of corneal response parameters for the six tests involved in the comparison while table 5.4 provides the same parameters from the clinical cases. Figure 5.30 shows a graphical comparison of the mean values via a bar chart and error bars for standard deviation representaion. The biggest difference was for the first applanation deformation amplitude with 52.6% higher, followed by the first applanation pressure (AP1) with 25.6 % lower and stiffness parameter (SP-HC) with 23% lower. A correlation analysis was required to select the parameters with highest association with IOP and corneal material stiffness in order to build estimation algorithms for them considering fluid structure interaction effect between the air puff and cornea. These results for the six cases were encouraging to start a parameteric study for 110 cases with wide range of eye biomechanical parameters.

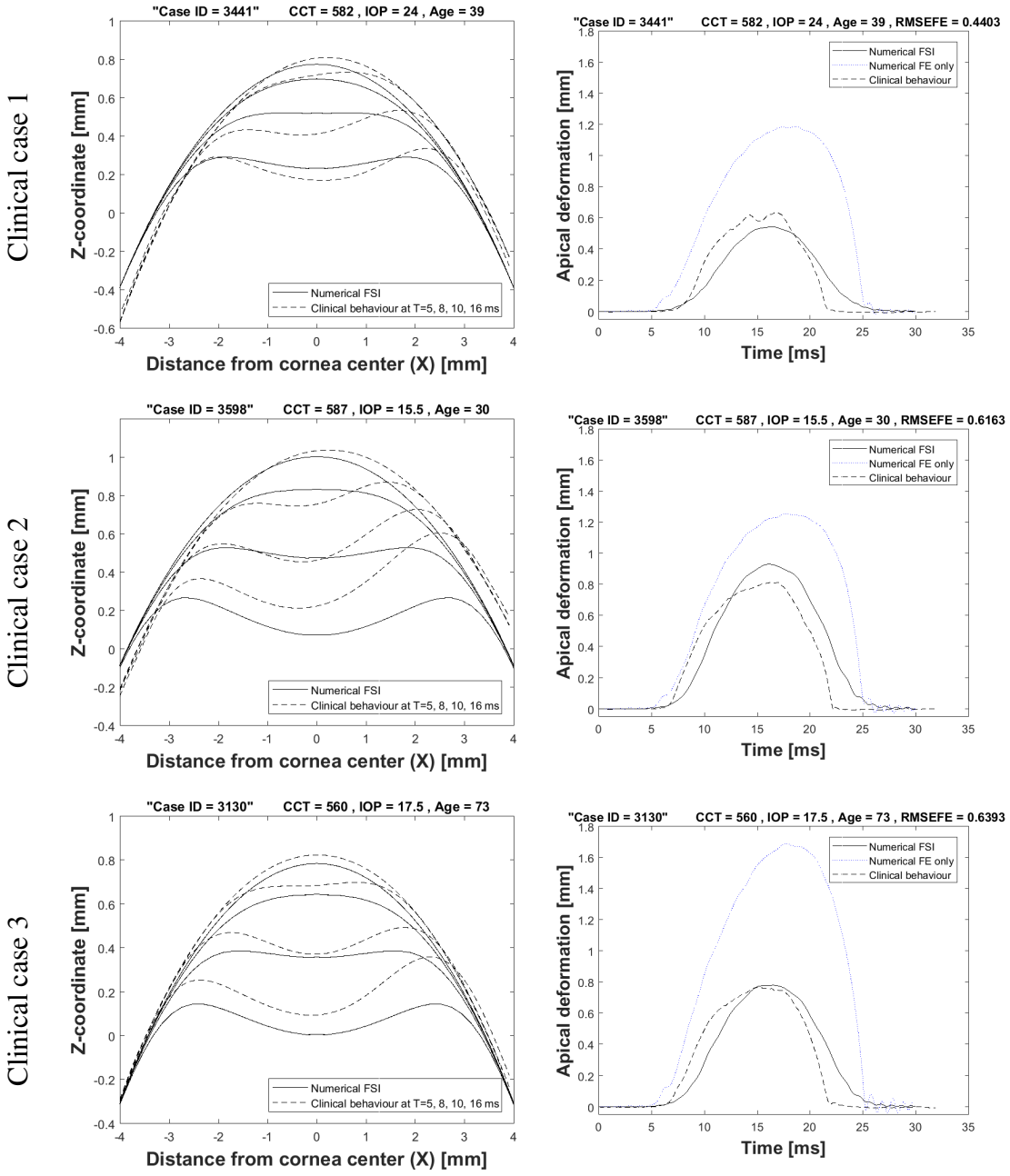

Clinical validation results with six patients

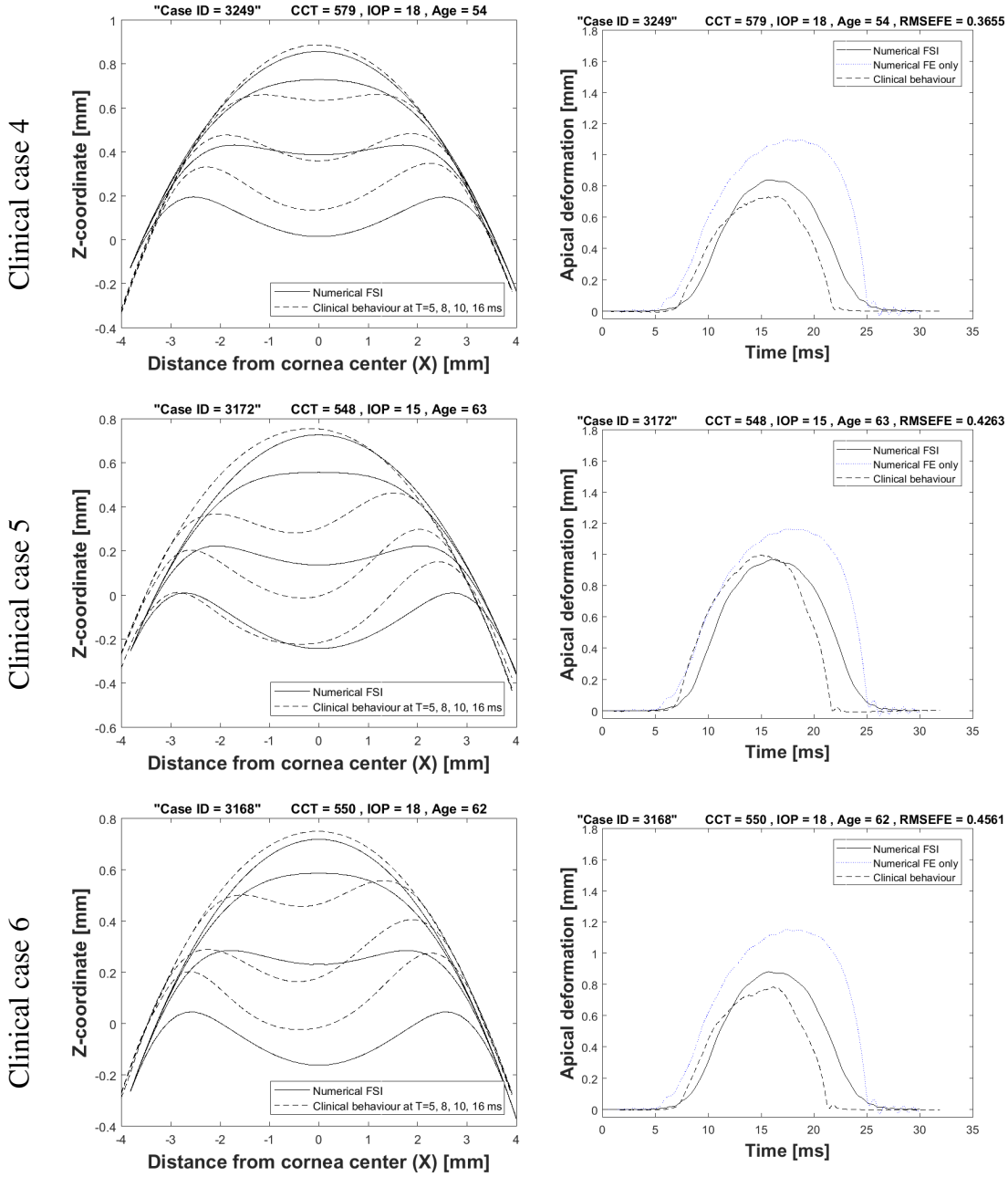

Figure 5.27 Continued: clinical validation results with six patients presented by the spatial corneal deformations and temporal apical deformation

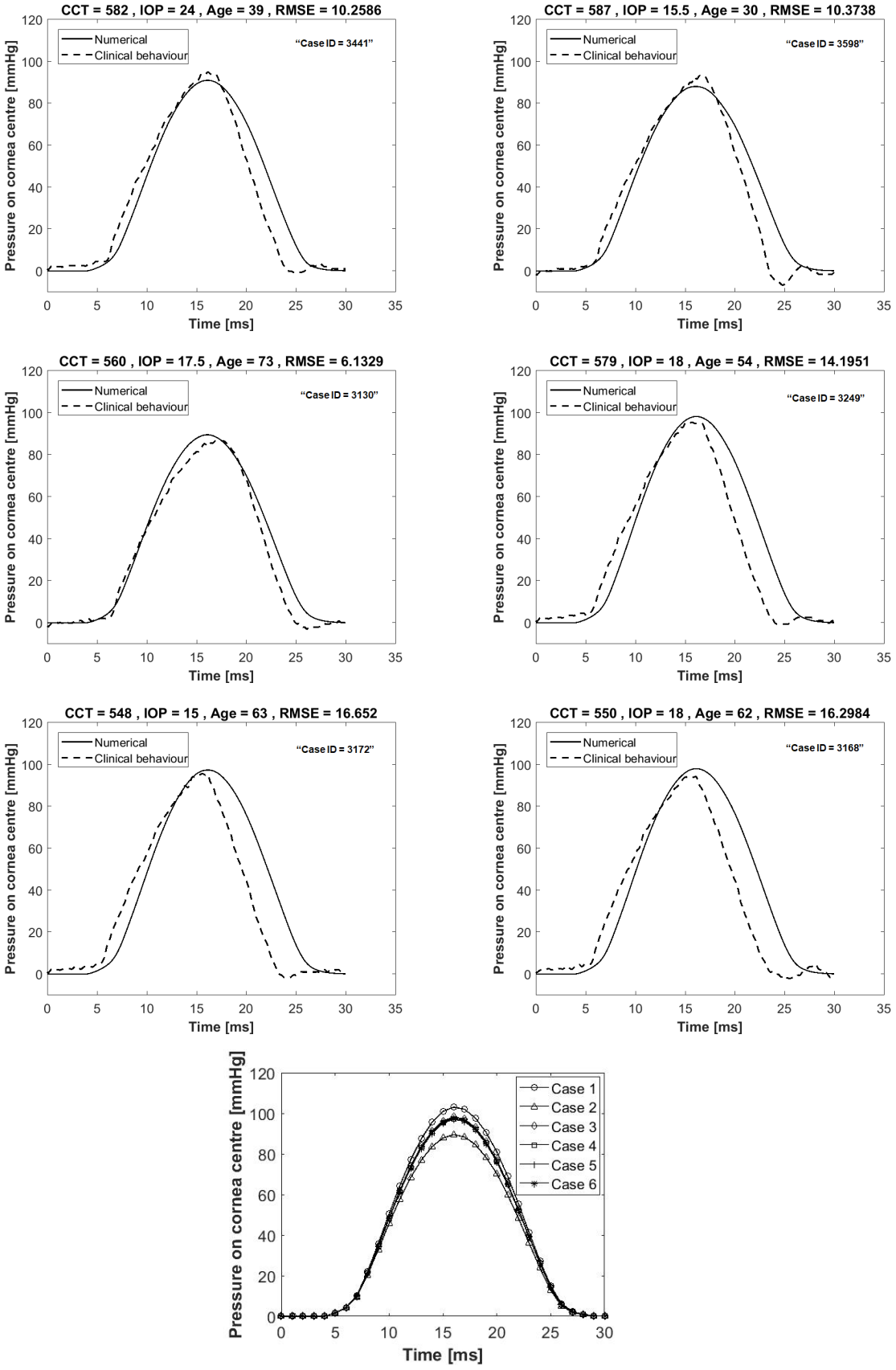

Figure 5.28 Temporal pressure profile on cornea centre numerically and clinically for six clinical cases and the last plot gathers numerical results in one plot

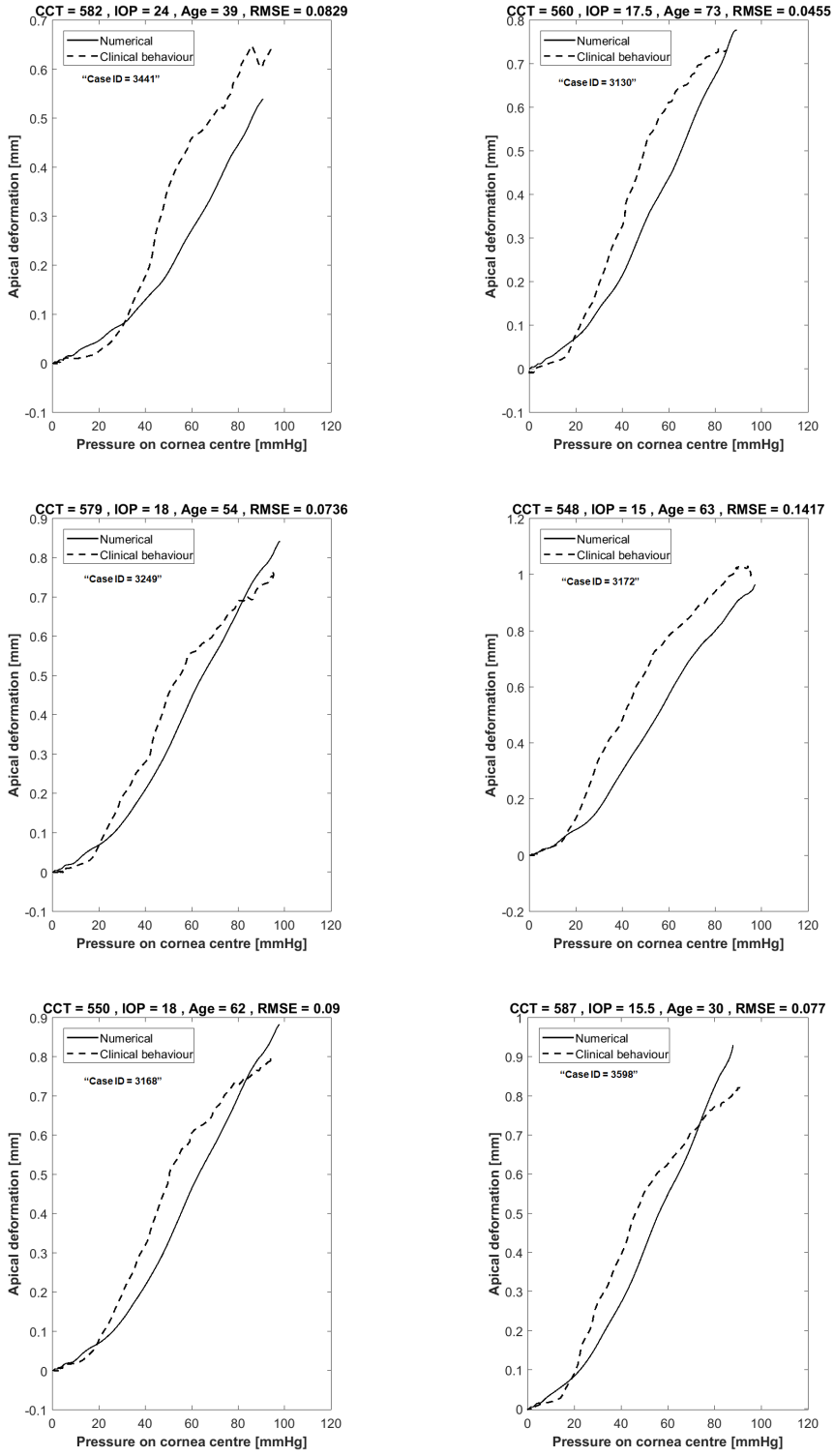

Figure 5.29 Apical deformation against pressure on cornea centre numerically and clinically for six clinical cases and the last plot gathers numerical results in one plot

Table 5.3 Descriptive statistics of the numerical corneal response parameters for six tests of clinical cases, the bold line separates input from output parameters

Parameter	N	Mean	Std. Deviation	Minimum	Maximum
IOP(mmHg)	6	16.50	3.37	11.00	24.00
CCT(μm)	6	554	23.4	512	587
μ	6	0.0564	0.0046	0.0485	0.0638
R(mm)	6	7.45	0.30	6.95	8.03
A1 Time(ms)	6	9.04	0.41	8.36	9.53
A1 Length(mm)	6	2.08	0.04	2.01	2.16
A1 Velocity(mm/s)	6	0.1482	0.02	0.12	0.18
HC Time(ms)	6	16.12	0.25	15.70	16.50
Peak Dist.(mm)	6	5.15	0.35	4.55	5.68
A1 Deformation Amp.(mm)	6	0.21	0.01	0.21	0.22
HC Deformation Amp.(mm)	6	0.94	0.11	0.78	1.09
AP1(mmHg)	6	34.66	5.68	25.87	41.87
SP-HC Stiffness parameter	6	26.67	8.92	14.21	38.82

Table 5.4 Descriptive statistics of the clinical response parameters for the six cases used in validation, the bold line separates input from output parameters

Parameter	N	Mean	Std. Deviation	Minimum	Maximum
IOP(mmHg)	6	16.50	3.37	11.00	24.00
CCT(μm)	6	554.50	23.24	512	587
Age (Years)	6	56.30	13.93	30	75
R(mm)	6	7.45	0.30	6.95	8.03
A1 Time(ms)	6	7.46	0.49	6.97	8.65
A1 Length(mm)	6	1.81	0.10	1.54	1.90
A1 Velocity(mm/s)	6	0.16	0.02	0.13	0.19
HC Time(ms)	6	16.61	0.84	15.71	18.25
Peak Dist.(mm)	6	4.87	0.46	4.06	5.81
A1 Deformation Amp.(mm)	6	0.14	0.02	0.12	0.17
HC Deformation Amp.(mm)	6	1.05	0.14	0.89	1.34
AP1(mmHg)	6	46.58	10.99	36.30	73.60
SP-HC Stiffness parameter	6	34.62	14.35	20.20	67.57

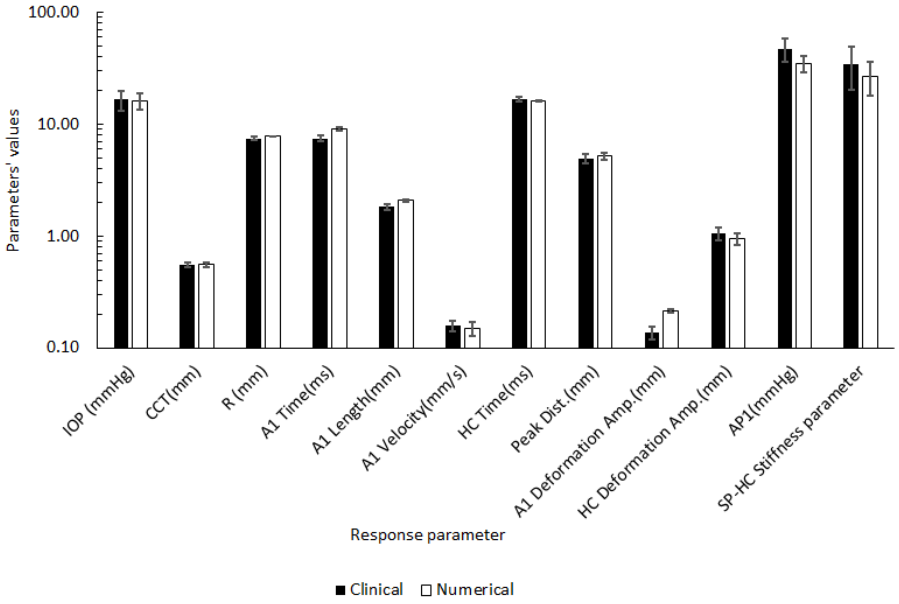

Figure 5.30 Visual representation of corneal response parameters comparison between clinical and numerical results

5.6 Results of parametric study

After validation of fluid structure interaction model of the air puff test, it was important to expand the model to wider range of eye biomechanical parameters to gauge their effect on the dynamic corneal response parameters. Also, Pearson correlation analysis was required to choose which dynamic reponse parameters were more associated with the change in IOP and corneal stiffness to use them in the estimation algorithms. The four parameters involved in the study were:

- Cornea material stiffness coefficient (μ)
- Central corneal thickness (CCT)
- Corneal curvature radius (R)
- Intraocular pressure (IOP)

A graphical user interface of the model generation was created to simplify the process and easily change input parameters when generating the eye and air puff models. The total number of tests included in the study were 110 tests with parametric ranges summarised in Table 5.5 for CCT, IOP, R and corneal material coefficient (μ) representing the change in stiffness with patient's age.

Table 5.5 Ranges of corneal biomechanical parameters used in parametric study

CCT [μm]	445	495	545	595	645
μ	0.0422	0.0541	0.0683	0.0811	0.1082
IOP [mmHg]	10	15	20	25	
R [mm]	7.4	7.8	8.4		

Note: CCT is corneal central thickness, μ is corneal material coefficient representing the change in stiffness with patient's age, IOP is intraocular pressure and R is cornea curvature radius.

Figure 5.31 provides example of comparison between three models by changing one parameter, while keeping other parameters the same. The plots show how each parameter affects the corneal spatial and temporal deformation which is a direct factor in changing intraocular pressure measurement. In the first row of graphs , by increasing stiffness of corneal material, the amount of deformation decreases. The second row illustrates the influence of central corneal thickness which is inversely proportional to corneal deformation. The third row shows the effect of corneal curvature and how it is affecting the deformation after eye inflation and after applying the air puff pressure. The last row shows the effect of intraocular pressure on corneal deformations, by increasing IOP, resistance of the cornea to deform is higher.

Parameter	Spatial corneal deformations	Temporal apical deformation

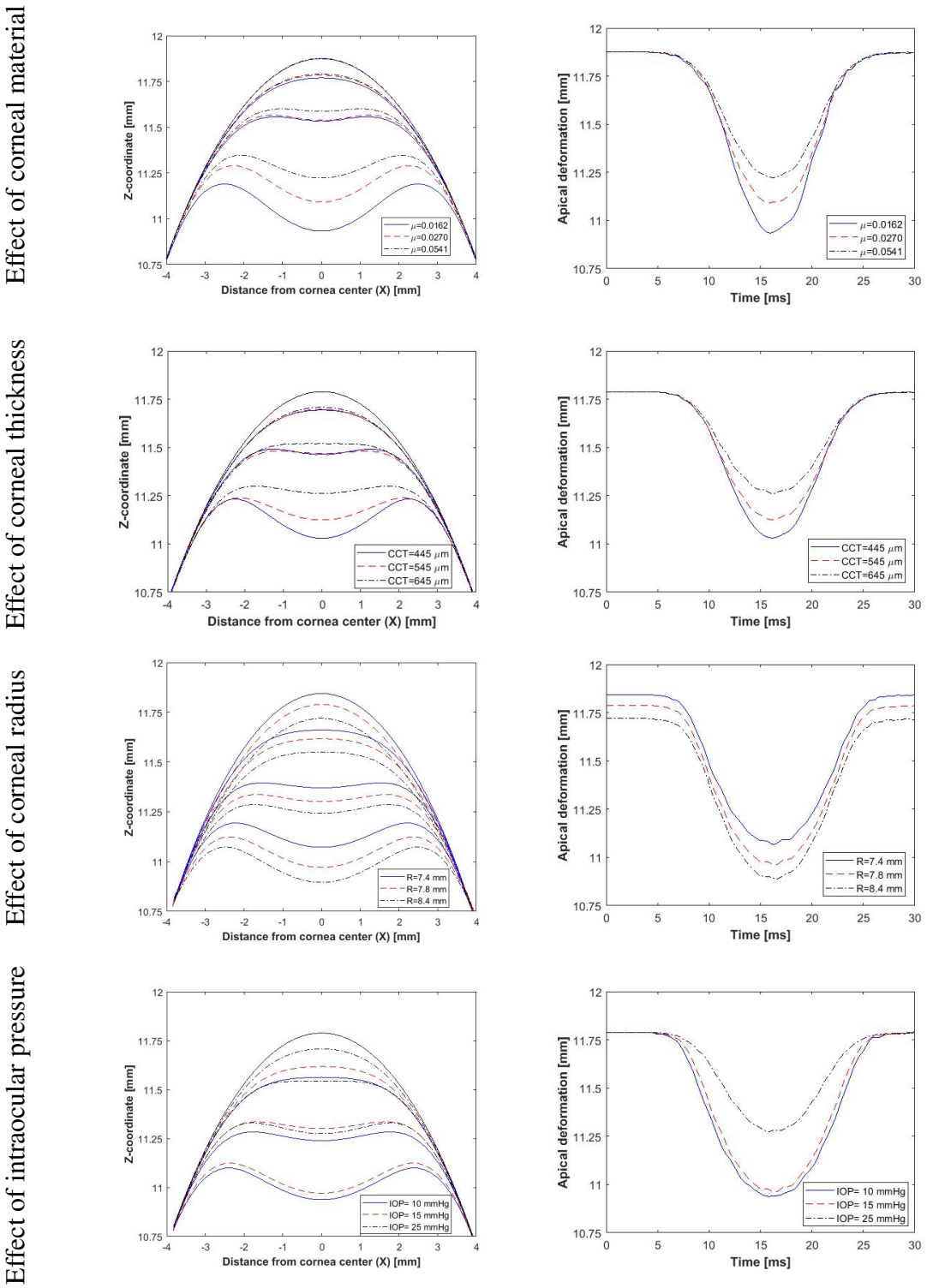

Figure 5.31 Effect of corneal material, corneal thickness, corneal radius and intraocular pressure on cornea deformation profiles and apical deformation with time

Figures 5.32, 5.33, 5.34 and 5.35 show, visually, the influence matrix of every input parameter in the parametric study on dynamic corneal response parameters with different colour for each value.

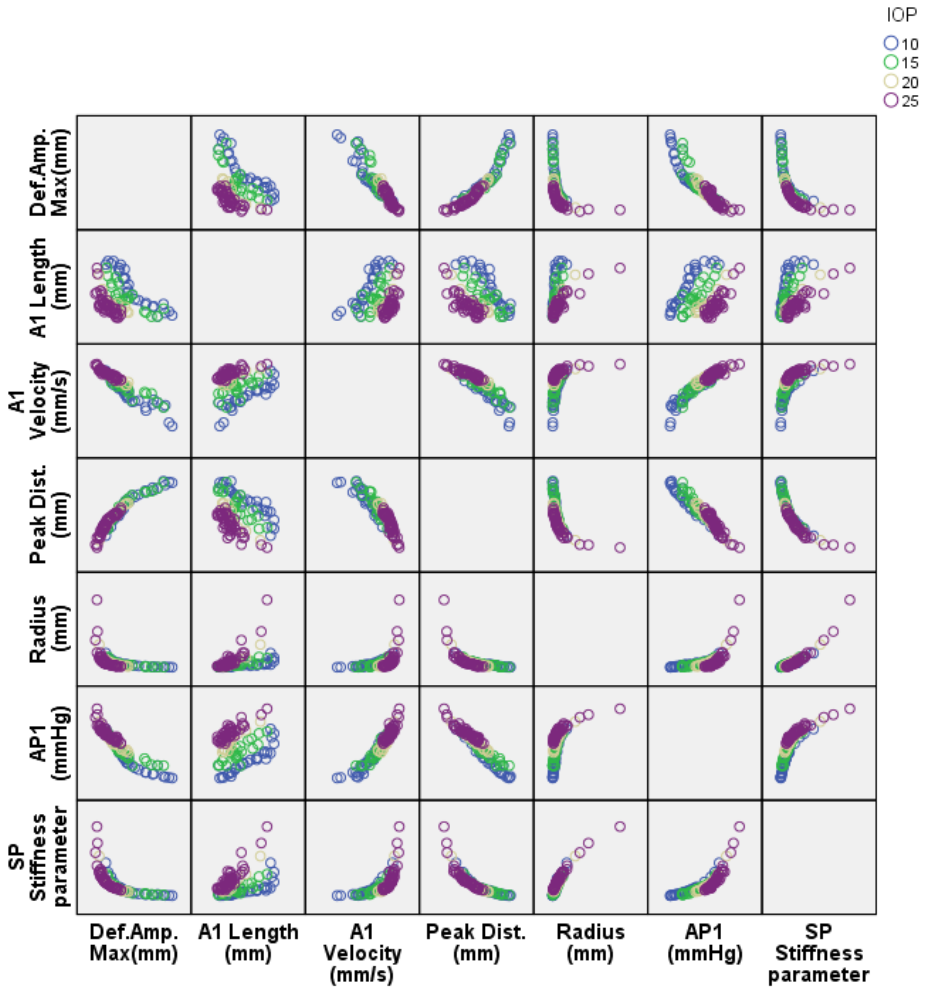

Figure 5.32 Influence matrix of changing intraocular pressure (IOP) on corneal response parameters

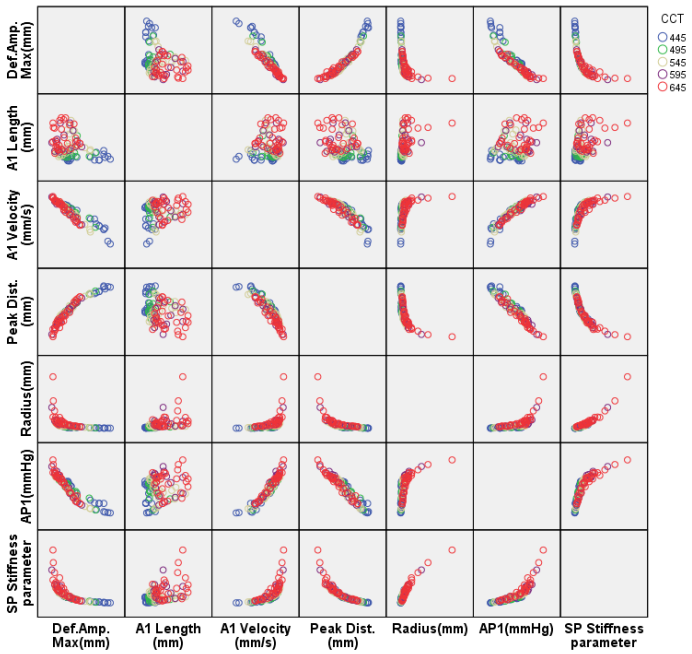

Figure 5.33 Influence matrix of changing central corneal thickness (CCT) on corneal response parameters

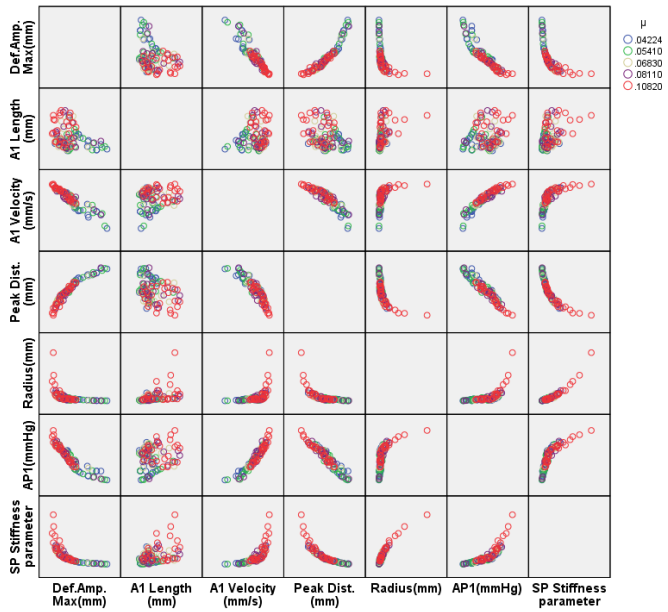

Figure 5.34 Influence matrix of changing corneal stiffness (μ) on corneal response parameters

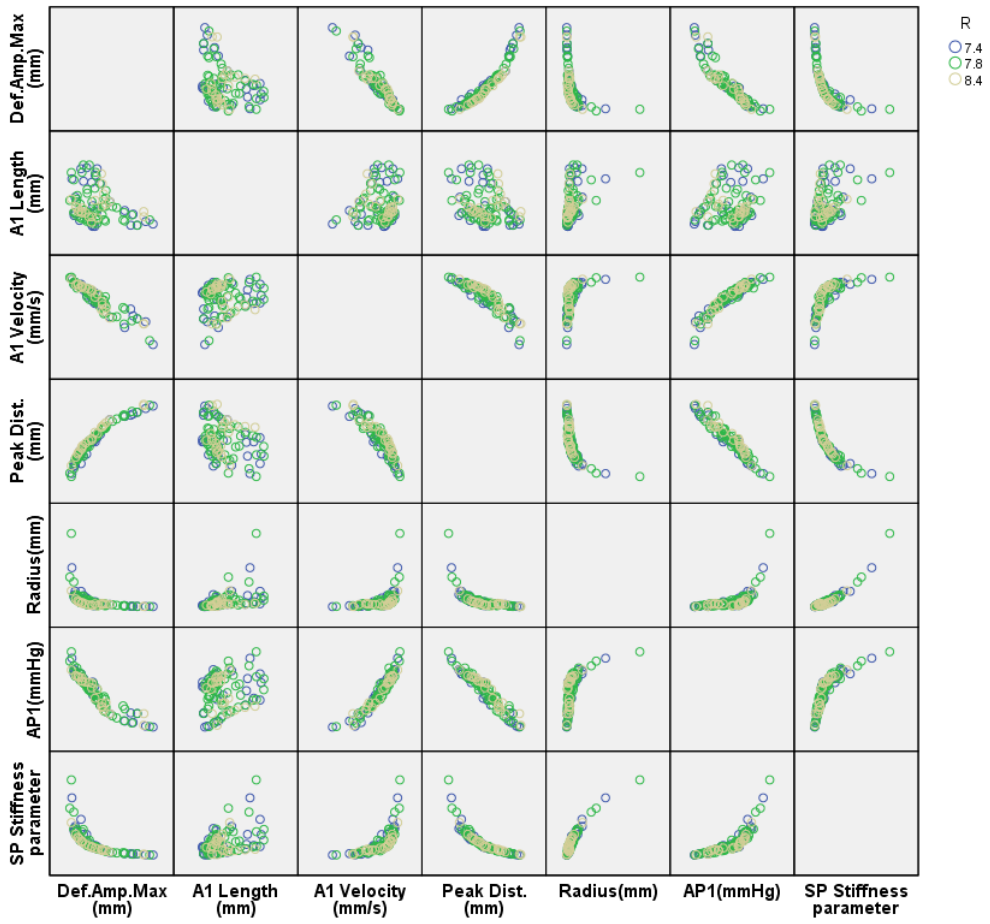

Figure 5.35 Influence matrix of changing corneal curvature radius (R) on corneal response parameters

5.6.1 Correlation analysis results of corneal response parameters

After showing, graphically, the influence of parameters involved in the parametric study, it was vital to quantify correlations and significance of relationships between parametric study's input and output parameters, to choose which response parameters were influenced more by changing IOP and corneal stiffness. This was an important outcome of the present study, as estimation algorithms for IOP and corneal material behaviour were required to correct fluid structure interaction effect between the air puff and human cornea. A bivariate correlation analysis using SPSS statistics 24 (SPSS Inc., IL) was performed to obtain Pearson's correlation coefficient (r) and two-tailed significance t-test to know the

significance level of correlations (P-value). Descriptive statistics of the parameteric study are shown in Table 5.6 providing mean, standard deviation, minimum and maximum of input and output parameters for 110 different eye models.

Table 5.6 Descriptive statistics of parametric study, the bold line separates input from output parameters

Variable	N	Mean	Std. Deviation	Minimum	Maximum
IOP	110.00	18.36	6.25	10.00	25.00
CCT	110.00	550.45	73.99	445.00	645.00
μ	110.00	0.0712	0.0236	0.0422	0.1082
R	110.00	7.82	0.33	7.40	8.40
A1 Time(ms)	110.00	9.66	0.97	7.81	12.47
A1 Length(mm)	110.00	2.15	0.19	1.91	2.62
A1 Velocity(mm/s)	110.00	0.13	0.04	0.06	0.21
HC Time(ms)	110.00	16.21	0.36	15.30	16.90
Peak Dist.(mm)	110.00	4.58	0.95	2.46	6.62
A1 Def. Amp.(mm)	110.00	0.23	0.05	0.17	0.39
HC Def. Amp.(mm)	110.00	0.84	0.30	0.42	1.77
AP1(mmHg)	110.00	42.09	12.09	18.82	75.24
SP-HC Stiffness parameter	110.00	34.69	21.92	5.00	109.59

Table 5.7 provides values of Pearson's correlation coefficient (r) between input and output response parameters which gives an indication on correlation's strength and direction. The highest correlated parameters to IOP change were; first applanation pressure (AP1), first applanation velocity (A1 velocity), first applanation time (A1 time) with r= 0.736, .731, .725 respectively and all of them at significance level of 0.0001 ($P < 0.0001$) referenced by the double asterisk next to the value of r. One of these three corneal response parameters was chosen to enter the estimation algorithm along with central corneal thickness (CCT), corneal

curvature (R) and corneal material stiffness parameter (μ). On the other hand, the first applanation length (A1 length) and stiffness parameter (SP-HC) were the most associated response parameters to corneal material change with correlation coefficients of 0.471 and 0.442 respectively at significance level of 0.01 ($P < 0.01$).

5.6.2 Validation of numerical parametric study

In order to validate the parametric study, the same descriptive statistics and correlation analysis that was done for parametric study, were done to the clinical dataset to see where the differences are, in order to consider it in the estimation algorithms. Table 5.8 provides descriptive statistics of the clinical corneal response parameters. In comparison to the parametric study statistics, Figure 5.36, provides a barchart to compare the means and standard deviations. The biggest difference was in the first applanation deformation amplitude with 76.9 % higher and HC deformation amplitude with 22.2 % less. In terms of pearson's correlations, the clinical dataset showed that the first applanation pressure remained the highest correlated parameter to IOP (r=.927, $p < .0001$) followed by A1 time (r=.889, $p < .0001$) and stiffness parameter (SP-HC) (r=.857, $p < .0001$) which is the same as the numerical database apart from A1 velocity which was found the highest after AP1, Section 5.6.1.

Table 5.7 Correlation and relationship significance analysis between input and output parameters of parametric study

Variable		A1 Time (ms)	A1 Length (mm)	A1 Velocity (mm/s)	HC Time (ms)	Peak Dist. (mm)	A1 Def. Amp. (mm)	HC Def. Amp. (mm)	AP1 (mmHg)	SP-HC (mmHg /mm)
IOP [mmHg]	Pearson Correlation	.725**	-.455**	-.731**	-.255**	-.616**	-.403**	-.635**	.736**	.442**
	Sig. (2-tailed)	0.000	0.000	0.000	0.007	0.000	0.000	0.000	0.000	0.000
CCT [µm]	Pearson Correlation	.382**	.637**	-.206*	-0.122	-.500**	.673**	-.493**	.385**	.468**
	Sig. (2-tailed)	0.000	0.000	0.031	0.204	0.000	0.000	0.000	0.000	0.000
μ	Pearson Correlation	.338**	.421**	-.367**	-.280**	-.407**	.432**	-.377**	.355**	.434**
	Sig. (2-tailed)	0.000	0.000	0.000	0.003	0.000	0.000	0.000	0.000	0.000
R [mm]	Pearson Correlation	-0.007	-0.056	-0.067	0.032	0.088	-.253**	-0.052	0.007	-0.088
	Sig. (2-tailed)	0.946	0.564	0.486	0.741	0.362	0.008	0.592	0.945	0.362

**. Correlation is significant at the 0.01 level (2-tailed).

*. Correlation is significant at the 0.05 level (2-tailed).

Table 5.8 Descriptive statistics of the clinical dataset used in the validation, the bold line separates input from output parameters

Variable	N	Mean	Std. Deviation	Minimum	Maximum
IOP [mmHg]	476.00	15.15	2.57	6.00	25.00
CCT [µm]	476.00	541.31	32.40	454.00	634.00
Age [Years]	476.00	40.49	16.97	7.00	91.00
R [mm]	476.00	7.65	0.34	6.79	8.75
A1 Time [ms]	476.00	7.26	0.32	6.59	8.65
A1 Length [mm]	476.00	1.82	0.07	1.25	1.96
A1 Velocity [m/s]	476.00	0.16	0.02	0.07	0.22
HC Time [ms]	476.00	16.59	0.73	14.09	18.71
Peak Dist. [mm]	476.00	5.05	0.28	3.98	5.81
A1 Def. Amp. [mm]	476.00	0.13	0.01	0.09	0.17
HC Def. Amp. [mm]	476.00	1.08	0.10	0.79	1.47
AP1 (device internal) [mmHg]	476.00	42.46	6.66	26.20	73.60
SP-HC [mmHg/mm]	476.00	31.15	8.48	16.97	79.61

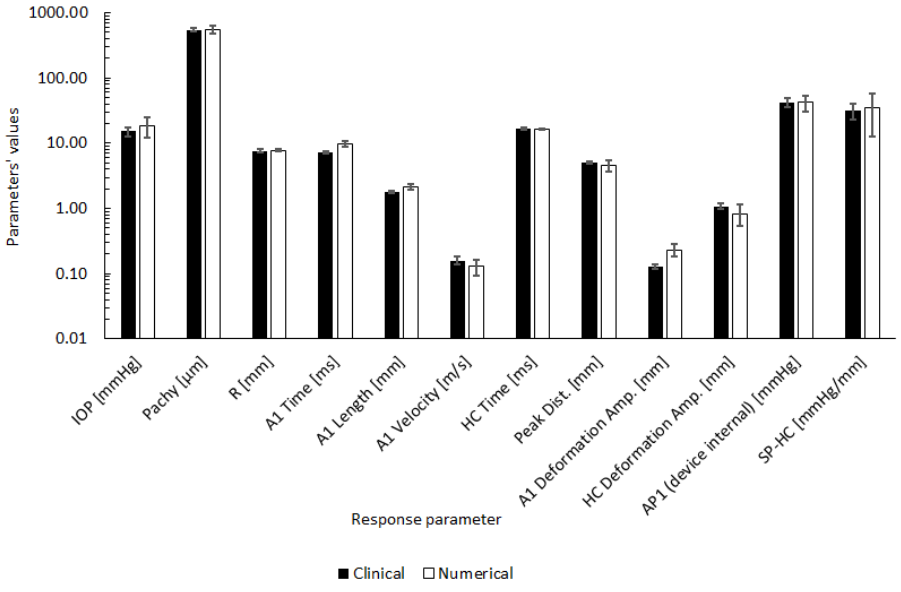

Figure 5.36 Visual representation of corneal response parameters comparison between clinical and numerical results of the parametric study

Table 5.9 Correlation and relationship significance analysis between input and output parameters for the clinical dataset used in the validation

Variables		A1 Time [ms]	A1 Length [mm]	A1 Velocity [m/s]	HC Time [ms]	Peak Dist. [mm]	A1 Def. Amp. [mm]	HC Def. Amp. [mm]	AP1 [mmHg]	SP-HC [mmHg /mm]
IOP [mmHg]	Pearson Correlation	.889**	.096*	-.593**	-.143**	-.641**	.266**	-.650**	.927**	.857**
	Sig. (2-tailed)	0.000	0.036	0.000	0.002	0.000	0.000	0.000	0.000	0.000
CCT [µm]	Pearson Correlation	.234**	.135**	-.217**	-0.031	-.237**	.204**	-.287**	.245**	.238**
	Sig. (2-tailed)	0.000	0.003	0.000	0.497	0.000	0.000	0.000	0.000	0.000
Age [Years]	Pearson Correlation	0.089	.097*	-.106*	-0.061	-.110*	.163**	-.126**	0.065	0.045
	Sig. (2-tailed)	0.052	0.035	0.021	0.186	0.017	0.000	0.006	0.159	0.332
R [mm]	Pearson Correlation	-.152**	.279**	-.111*	-.300**	.335**	-.398**	0.070	-.228**	-.198**
	Sig. (2-tailed)	0.001	0.000	0.016	0.000	0.000	0.000	0.129	0.000	0.000

**. Correlation is significant at the 0.01 level (2-tailed).

*. Correlation is significant at the 0.05 level (2-tailed).

5.7 Intraocular pressure estimation algorithm (fIOP)

The clinical IOP measurements from CorVIs-ST device have shown an association with CCT (R^2=0.0884, slope= 0.0236 mmHg/μm), intermediate association with the cornea radius (R^2=0.0208, slope= 1.1054 mmHg/mm) and weaker association with Age (R^2=0.0047, slope= 0.01 mmHg/year). This was the motivation to bimechanically correct CorVis IOP measurements by including one of the corneal response parameters, studied in Section 5.6.1, into the estimation equation to reduce association of IOP with CCT, R and patient's age.

According to the correlation analysis between corneal response parameters, it was found that AP1 was the highest associated parameter with IOP ($r = 0.736, P < 0.0001$). AP1 was chosen along with CCT, R and μ, representing corneal stiffening with patient's age, to eliminate IOP's association with CCT and age. An exercise was made to know the lowest possible polynomial for each parameter in the equation and based on the lowest RMSE, equation formula was chosen. AP1 has second order polynomial, CCT effect represented by fourth order, μ third order and corneal curvature was included as first order polynomial. Matlab and Python codes were used to perform a non-linear least square optimization for the equation parameters to get a close match with the true value of IOP (IOPt). The best equation for fIOP was extracted from the code and validated against, clinical datasets and experimental measurments of true IOP. Based on the patient's geometry parameters and age, the value of fIOP was calculated from Equation 5.1 and compared to readings of the Corvis device as shown in Figure 5.37.

$$fIOP = C_{AP1} \times C_{CCT} \times C_{Age} \times C_R + C$$

where fIOP is the biomechanically FSI corrected IOP, C_{CCT} is the influence of change in corneal central thickness, C_{Age} is the patient's age influence, C_R is the corneal curvature variation effect and C is an offset constant.

$$fIOP = (2.30\times10^{-3}\times AP1^2 + 1.68\times10^{-1}\times AP1 + -6.40)\times$$
$$(-9.76\times10^{-9}\times CCT^4 + 1.68\times10^{-5}\times CCT^3 + -1.07\times10^{-2}\times CCT^2 + 2.74\times CCT + 0.952)\times$$
$$(8.71\times10^{-2}\times\mu^3 + -6.88\times\mu^2 + -1.53\times\mu + 6.93\times10^{-1})\times$$
$$(1.23\times10^{-3}\times R + -2.13\times10^{-3}) + 11.21 \tag{5.1}$$

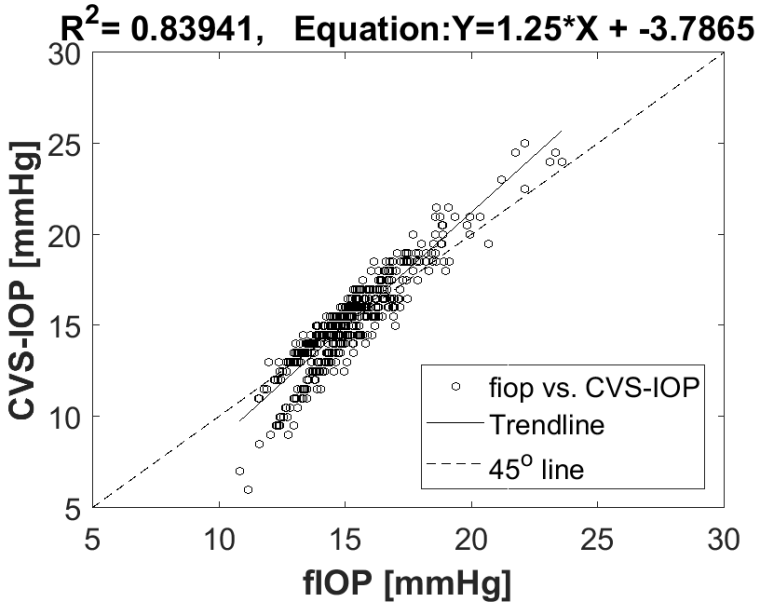

Figure 5.37 The IOP value comparison between fIOP algorithm and Corvis reading

5.7.1 Ex-vivo experimental validation of fIOP estimation algorithm

In order to validate the new IOP estimation algorithm taking into account the fluid structure interaction effect, an ex-vivo experimental testing to human eye specimens was performed. The main reason for the experimental testing is that the value of true IOP (IOPt) in the eye is unknown during the air puff test using CorVis-ST. This value only can be measured with intrusive methods which needs a surgery to perform it safely. Five human eyes were

tested ex-vivo, connected to a pressure control circuit filled with 10% Dextran solution (Sigma-Aldrich, Darmstadt, Germany). The true IOP value (IOPt) was measured via an FDW pressure transducer (RDP Electronics, Wolverhampton, UK) and compared against the CorVis-ST measurement (CVS-IOP) and fIOP calculated from the new estimation algorithm. The true IOP was controlled during the experiment by a stepper motor and syringe pump to range from 10 to 30 mmHg with 5 mmHg increments. The eye was left to stabilise for 60 s after reaching each pressure level before applying the air puff from CorVis-ST. At least three measurements were taken for every pressure level, leaving at least two minutes between every successive measurements to enable the ocular tissue to relax to original condition.

Table 5.10 presents descriptive statistics for every specimen at five pressure levels showing values of CCT, true IOP, CVS-IOP readings, fIOP values and the difference between them performed with SPSS statistics 24 (SPSS Inc., IL). Mean of the readings at every pressure level is shown along with standard deviation and range for CorVis and fIOP values. The average difference between CVS-IOP and IOPt for all specimens at different pressure levels was $7.8 \pm 4.1 (1.2 - 17.3)$ while for fIOP was $0.44 \pm 1.6 (-3.1 - 5.0)$ with 94% reduction in error of mean difference. Figure 5.38 shows graphically the comparison between CorVis IOP readings (CVS-IOP) and fIOP against the measured true IOP (IOPt) for every specimen. A 45^o line was shown to see the amount of agreement between the readings, fitting equation and R^2 are also shown. For CorVis readings ($R^2 = 0.975 \pm 0.023\ (0.94 - 1)$) while for fIOP ($R^2 = 0.968 \pm 0.031\ (0.92 - 0.99)$). In terms of gradients, for CorVis readings ($slope = 0.999 \pm 0.12\ (0.86 - 1.14)$) while for fIOP values ($slope = 1.07 \pm .09\ (0.94 - 1.17)$).

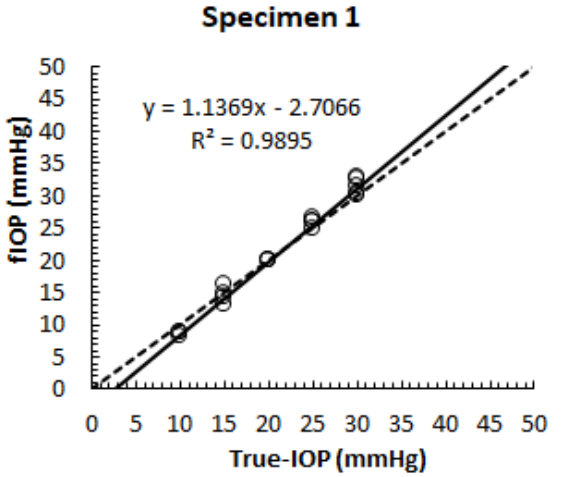
Specimen 1
y = 1.1369x - 2.7066
R² = 0.9895
fIOP (mmHg)
True-IOP (mmHg)

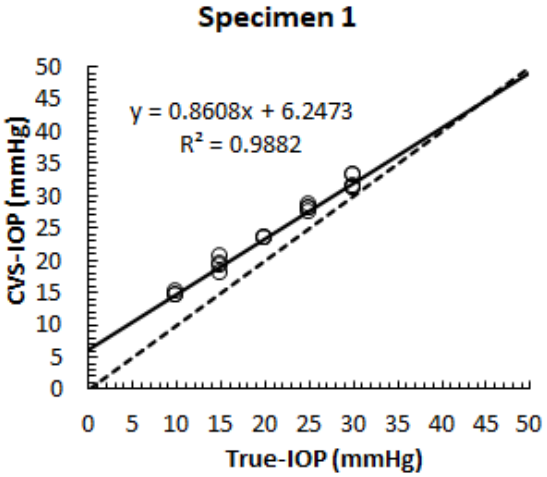
Specimen 1
y = 0.8608x + 6.2473
R² = 0.9882
CVS-IOP (mmHg)
True-IOP (mmHg)

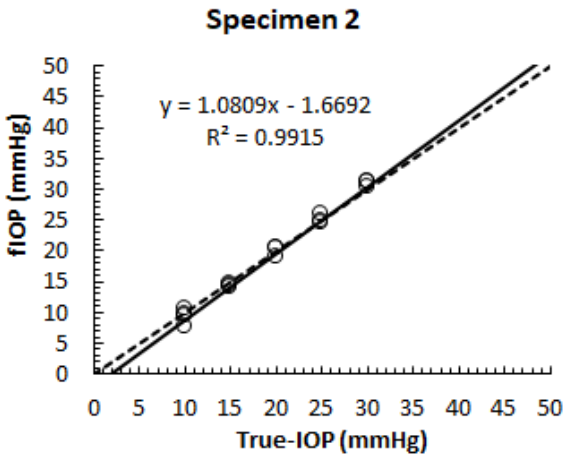
Specimen 2
y = 1.0809x - 1.6692
R² = 0.9915
fIOP (mmHg)
True-IOP (mmHg)

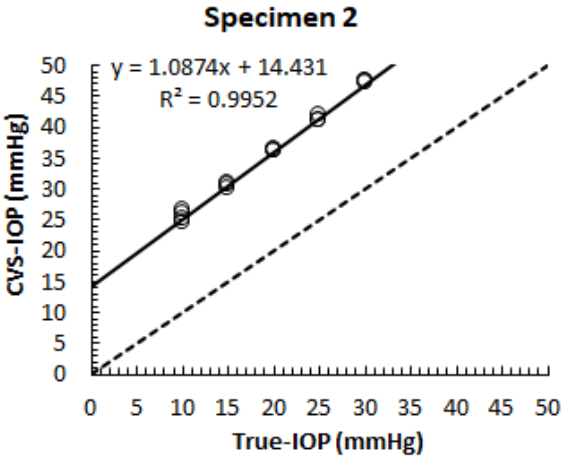
Specimen 2
y = 1.0874x + 14.431
R² = 0.9952
CVS-IOP (mmHg)
True-IOP (mmHg)

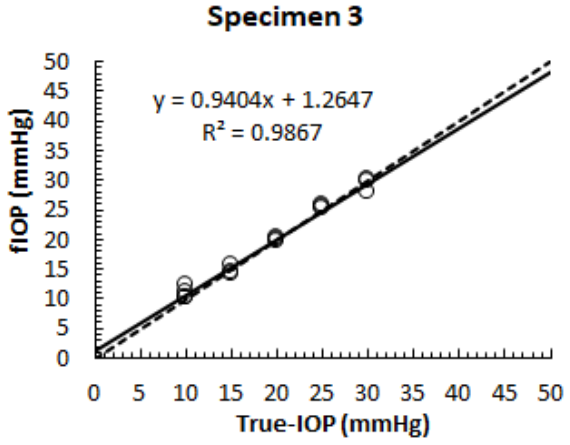
Specimen 3
y = 0.9404x + 1.2647
R² = 0.9867
fIOP (mmHg)
True-IOP (mmHg)

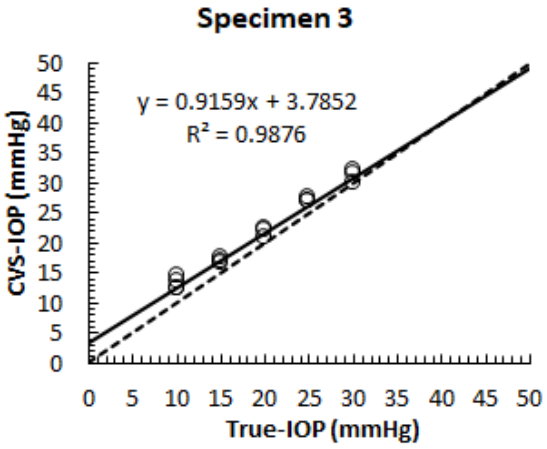
Specimen 3
y = 0.9159x + 3.7852
R² = 0.9876
CVS-IOP (mmHg)
True-IOP (mmHg)

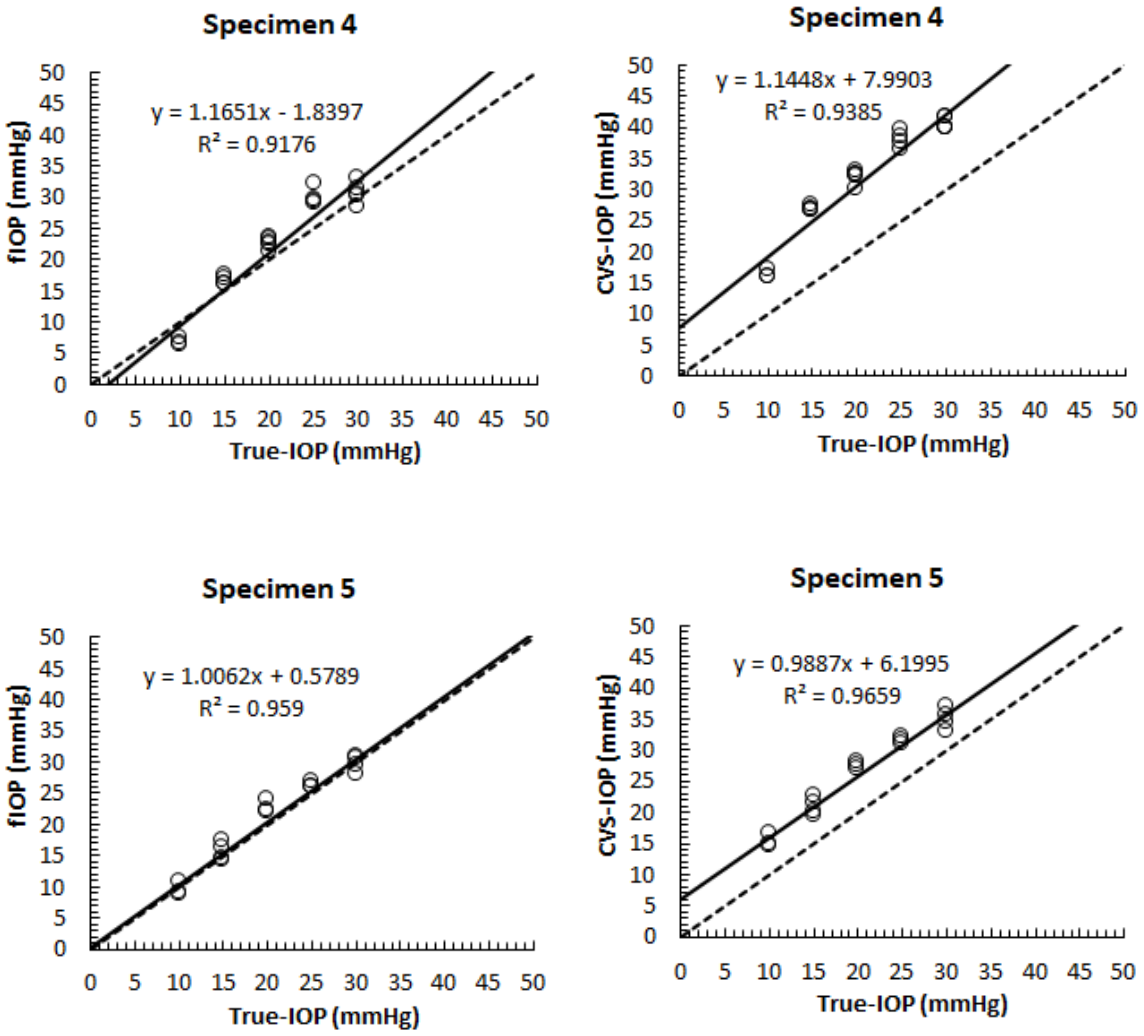

Figure 5.38 Validation of the fIOP algorithm using five ex-vivo experimental specimens through comparing fIOP against CorVis IOP and true IOP, solid line is the fitting trendline and dash line is a 45^o line to show difference in the readings

Table 5.10 Improvment of the IOP measurements after applying the fIOP estimation algorithm on five ex-vivo human eye specimens at five eye pressure levels, mean standard deviation and range are included for every pressure level

Specimen	Age (years)	CCT (μm)	IOPt (mmHg)	CVS-IOP			fIOP		
				IOP (mmHg)	Δ IOP (mmHg)	Error (%)	IOP (mmHg)	Δ IOP (mmHg)	Error (%)
S1	67	465±6 (458-469)	10	14.7±0.3 (14.5-15.0)	4.7	47%	8.5±0.3 (8.1-8.7)	-1.5	-15%
		488±13 (476-507)	15	19.3±1.0 (18.0-20.5)	4.3	29%	14.6±1.1 (13.2-16.2)	-0.4	-3%
		493±2 (492-496)	20	23.5±0.0 (23.5-23.5)	3.5	18%	19.9±0.1 (19.8-20.0)	-0.1	-1%
		498±1 (496-499)	25	28.0±0.4 (27.5-28.5)	3	12%	25.8±0.6 (24.8-26.5)	0.8	3%
		487±6 (477-494)	30	31.9±1.0 (31.0-33.0)	1.9	6%	31.4±1.1 (30.1-32.8)	1.4	5%
S2	67	619±18.6 (598-639)	10	25.5±0.9 (24.5-26.5)	10.5	70%	9.3±1.1 (7.6-10.5)	-0.7	-7%
		620±1 (618-622)	15	30.5±0.4 (30.0-31.0)	15.5	103%	14.3±0.3 (14.0-14.7)	-0.7	-5%
		621±9 (613-632)	20	36.2±0.3 (36.0-36.5)	10.5	53%	19.9±0.7 (19.0-20.5)	-0.1	-0.4%
		624±2 (622-627)	25	41.3±0.6 (41.0-42.0)	11.2	45%	25.1±0.6 (24.6-25.9)	0.1	1%
		624±2 (622-627)	30	47.3±0.2 (47.0-47.5)	17.3	116%	30.4±0.4 (30.4-31.3)	1	7%
S3	76	607±10 (597-618)	10	17.0±0.5 (16.5-17.5)	7	70%	10.9±0.8 (10.2-12.2)	0.9	9%
		599±18 (584-619)	15	21.8±0.8 (21.0-22.5)	6.8	45%	14.8±0.6 (14.1-15.6)	-0.2	-2%
		594±4 (590-598)	20	27.2±0.3 (27.0-27.5)	7.2	36%	19.9±0.3 (19.5-20.1)	-0.1	-1%
		603±1 (602-604)	25	31.2±1.0 (30.0-32.0)	6.2	25%	25.5±0.3 (25.1-25.8)	0.5	2%
		609±1 (608-610)	30	31.2±0.8 (30.0-32.0)	1.2	4%	29.2±0.9 (27.9-30.0)	-0.8	-3%
		829±68 (750-870)	10	16.3±0.6 (16.0-17.0)	6.3	63%	6.9±0.5 (6.4-7.5)	-3.1	-31%
		808±3 (805-810)	15	26.9±0.5 (26.5-27.5)	11.9	79%	16.7±0.6 (16.1-17.5)	1.7	11%

Table 5.10 Continued: Improvement of the IOP measurements after applying the fIOP estimation algorithm

Specimen	Age	CCT	IOPt	CVS-IOP (mmHg)			fIOP (mmHg)		
S4	68	834±8 (828-840)	20	32.0±1.2 (30.0-33.0)	12	60%	22.7±0.8 (21.4-23.6)	2.7	13%
		808±3 (805-810)	25	38.0±1.3 (36.5-39.5)	13	52%	30±1.2 (28.9-32.1)	5	20%
		870±14 (860-880)	30	40.6±0.8 (40.0-41.5)	10.6	35%	30.7±1.5 (28.4-33.0)	0.7	2%
S5	67	553±6 (548-557)	10	15.8±1.1 (15.0-16.5)	5.8	58%	9.6±0.9 (8.8-10.8)	-0.4	-4%
		576±5 (572-584)	15	20.9±1.4 (19.5-22.5)	5.9	39%	15.6±1.2 (14.2-17.3)	0.6	4%
		582±15 (565-593)	20	27.5±0.5 (27.0-28.0)	7.5	38%	22.8±0.8 (22.1-23.9)	2.8	14%
		603±4 (599-608)	25	31.5±0.5 (31.0-32.0)	6.5	26%	26.3±0.4 (25.9-26.9)	1.3	5%
		605±12 (596-624)	30	35.0±1.7 (33.0-37.0)	5	17%	29.7±1.1 (27.9-30.8)	-0.3	-1%

Note:IOPt is true IOP, CVS-IOP is CorVis IOP reading, fIOP is the corrected value of IOP considering FSI effect and Δ IOP is the difference in values for every respective IOP reading with ture IOP.

5.7.2 Clinical validation of fIOP estimation algorithm

In comparison of fIOP to CorVis readings (CVS-IOP), Figure 5.37 shows the scatter plot of fIOP against CVS-IOP and a 45^o line to explain how close are the readings. At values of IOP less than 15 mmHg, fIOP was giving higher values than CVS-IOP reached 100% increase in some cases. For IOP values more than 20 mmHg, fIOP showed slightly higher values than CVS-IOP. The association of corneal biomechanical parameters (CCT, patient's age affecting corneal stiffness and corneal curvature) with CorVis-ST and fIOP values are shown in figure 5.39. The main target was to make sure that slope of the fitting line is close to zero as possible which indicates that IOP readings don't depend on the change of various patients' eye parameters. Improvement of CCT association was from (R^2=0.0884 to 0.026) which is less by 70.6 %, age association improved by 94.7 % and corneal curvature association developed by 43.1 %.

Table 5.11 Descriptive statistics of fIOP, CVS-IOP and the difference between both values

Variable	N	Minimum	Maximum	Mean	Std. Deviation
fIOP [mmHg]	476	6.99	28.88	15.15	3.18
CVS-IOP [mmHg]	476	6.00	25.00	15.15	2.57
Difference	476	-4.88	3.71	0.00	1.24

Parameter	Corvis-IOP Association	fIOP Association
Association with cornea central thickness	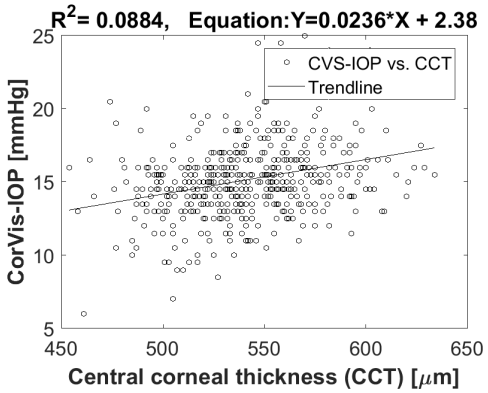	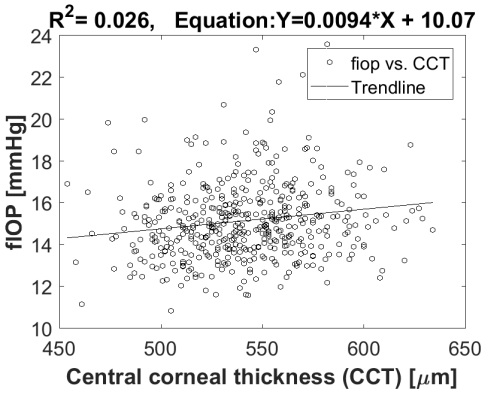
Association with age	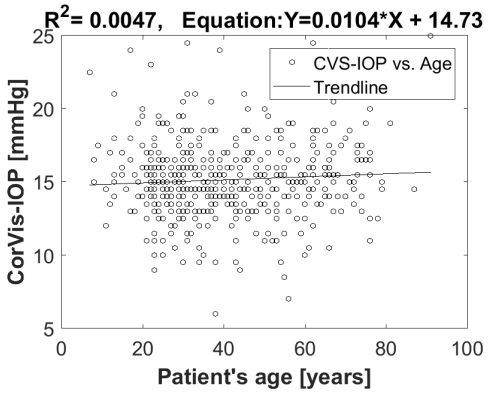	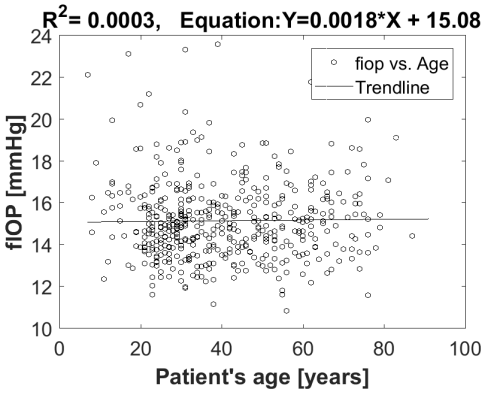
Association with cornea apical radius	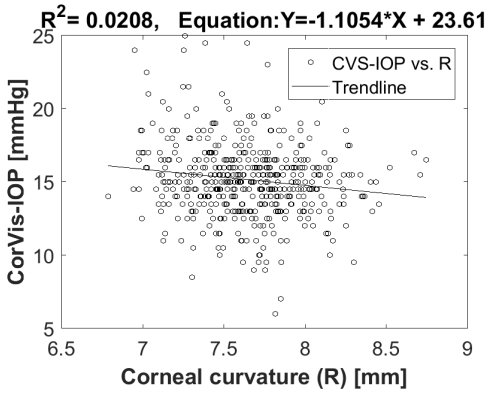	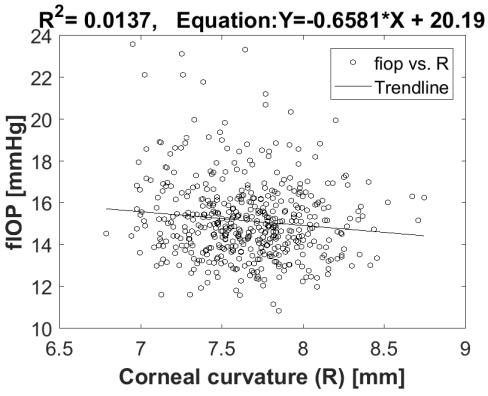

Figure 5.39 The association of the corneal biomechanical parameters (CCT, cornea stiffness represented by age and corneal curvature) with the IOP reading for the CorVis-ST and the fIOP values

5.8 Cornea material estimation algorithm (β_f)

The corneal tissue is a hyperelastic non-linear material which, sometimes, can not be predicted accurately for numerous reasons. One important reason is that knowing the true loading is difficult, either the intraocular pressure (IOP) or the air puff pressure during an air puff test. For better representation of corneal material behaviour, a parameter β, was introduced by Elsheikh et al. to represent the corneal material behaviour under loading [5, 6]. The present algorithm β_f is proposing an accurate way of knowing the corneal material behaviour for patient specific models taking into account fluid structure interaction effects between the air puff and cornea. The present algorithm is providing better accuracy of corneal material estimation using three test parameters rather than relying on patient's age only. The process started after finishing the parametric study, IOP estimation algorithm (fIOP) and its validation. It is well known from previous studies that intraocular pressure (IOP) and central cornal thickness (CCT) are the most biomechanical parameters affecting the corneal response to loading [31, 62, 161, 164]. From the correlation analysis of parametric study, Section 5.6.1, the parameters with highest association with material change were identified. The stiffness parameter (SP-HC) was the highest correlated parameter with (r=.434, P<0.0001) followed by first applanation deformation amplitude (A1 Def. Amp) with (r=.432, P<0.0001). The stiffness parameter (SP-HC), Equation 5.2, was found in earlier study to be the strongest parameter in correlation with corneal material change [172] so it was chosen to enter the estimation algorithm.

$$SP-HC=\frac{AP1-IOP}{HC\ deflection-A1\ deflection} \tag{5.2}$$

where AP1 is the first applanation pressure on cornea, IOP is the intraocular pressure and can be replaced by bIOP or fIOP, HC deflection is the maximum deformation of cornea apex

without whole eye movement and A1 deflection is the deformation amplitude at the first applanation moment without whole eye movement.

Figure 5.40 provides the five level surfaces of β_f representing values of (0.5, 1, 1.5, 1.9, 3.1), by knowing the IOP, CCT and SP-HC of the patient from CorVis-ST measurement, 5 values of β_f can be obtained according to Equations 5.3, 5.4 and then by fitting a second order polynomial through the five points, value of β_f can be estimated from the value of Ln(SP-HC) as explained in Figure 5.41. The surfaces show strong correlations between (SP-HC & CCT) and (SP-HC & IOP). Each surface equation is in the form of Equation 5.4 with surface parameters shown in Table 5.12. IOP is normalised via dividing by 20 (mmHg) and CCT was normalised by the average clinical CCT of 545 μm.

$$\beta_f = f(IOP, CCT, Ln(SP-HC)) \tag{5.3}$$

$$\beta_f = P1 + P2 \times (IOP/20) + P3 \times (CCT/545) \tag{5.4}$$

Table 5.12 The surface coefficients for the five levels of β_f

Surface coefficient	P1	P2	P3
$\beta_f = 0.5$	0.026	1.83	2.62
$\beta_f = 1$	0.68	1.44	2.36
$\beta_f = 1.5$	0.85	1.49	2.35
$\beta_f = 1.9$	1.11	1.02	2.55
$\beta_f = 3.1$	1.33	1.05	2.54

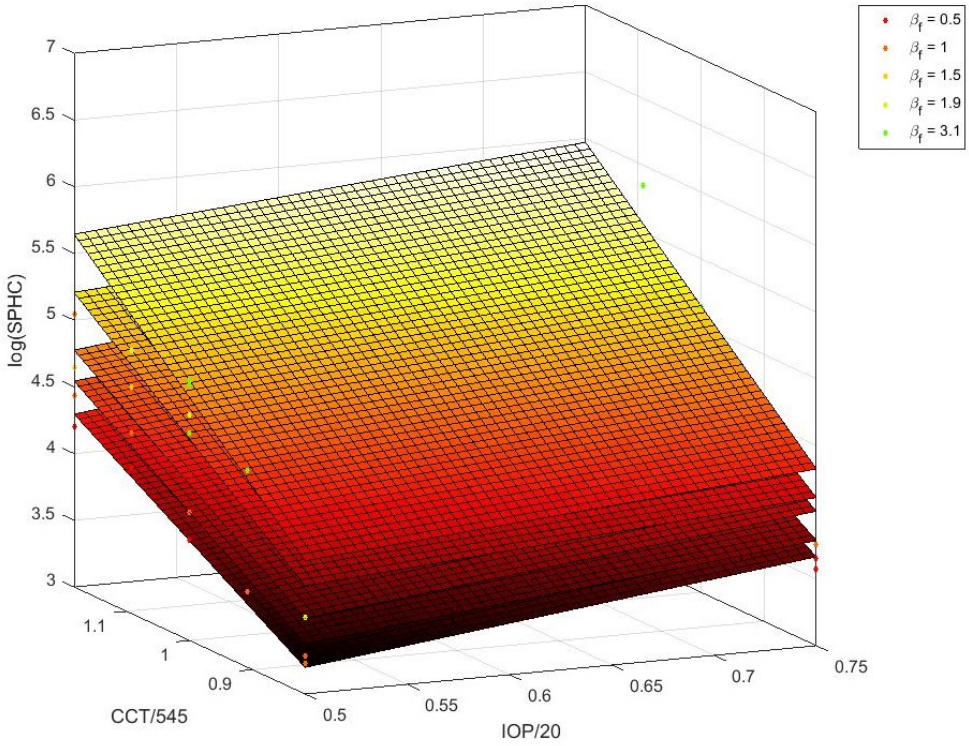

Figure 5.40 The five levels of beta that have been tested with relation to IOP, CCT and the stiffness parameter SP-HC

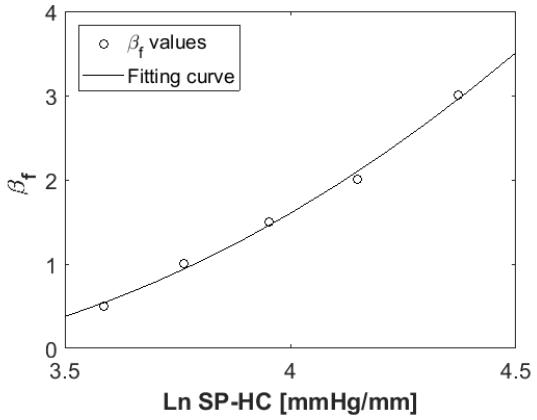

Figure 5.41 Second order polynomial fitting of the five values of β_f at a specific value of (IOP=11.3 mmHg) and (CCT=525 μm)

5.8.1 Clinical validation of cornea material behaviour algorithm

In order to validate the corneal material behaviour parameter β_f, it was applied to the clinical dataset to see the association with central corneal thickness (CCT), intraocular pressure (fIOP), corneal curvature R and patient's age, Figure 5.42. It was found that β_f has low association with CCT (R^2=0.0498, slope = -0.0017), fIOP (R^2=0.0014, slope = 0.0042) and R (R^2=0.0154, slope = -0.08), and moderate association with age (R^2=0.4146, slope = -0.0083) which is consistent with Elsheikh et al.'s previous findings of corneal stiffening with age [5, 6]. The descriptive statistics of β_f and association parameters are shown in Table 5.13 providing mean, standard deviation, minimum and maximum. Pearson's correlation analysis results are provided in Table 5.14, for fIOP and R, there was no significant correlation with (P-value > 0.05) = 0.644 and .122, respectively. Correlation with CCT was very weak (r=.223 and P-value = 0.005) and strong correlation with age (r=.644 and P-value <0.0001).

Another validation is shown in the last plot of Figure 5.42, β_f was plotted against true β which was obtained from previous experimental inverse analysis done on the eye model [5, 6, 134].

Table 5.13 Descriptive statistics of β_f and the association parameters for the clinical dataset used in validation

Parameter	N	Mean	Std. Deviation	Minimum	Maximum
β_f	156	1.045	0.21	0.55	1.86
fIOP [mmHg]	156	15.2	1.9	11.4	26.1
R [mm]	156	7.66	0.34	6.99	8.8
Age [Years]	156	40.00	16.73	7	81
CCT [μ m]	156	544.6	28.6	487	621
$\beta_{Inverse}$	156	0.924	0.204	0.47	1.53

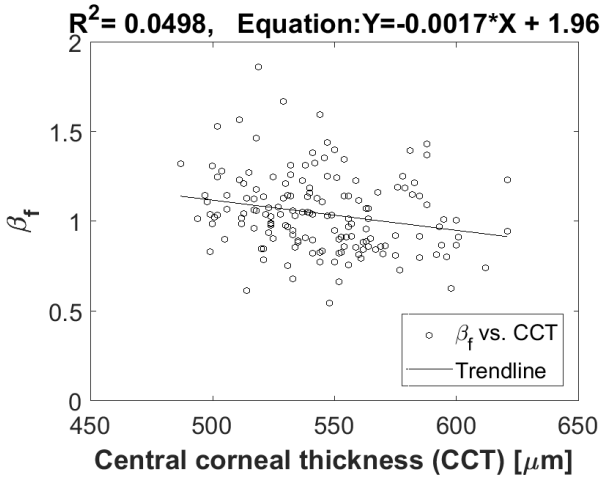

(a)

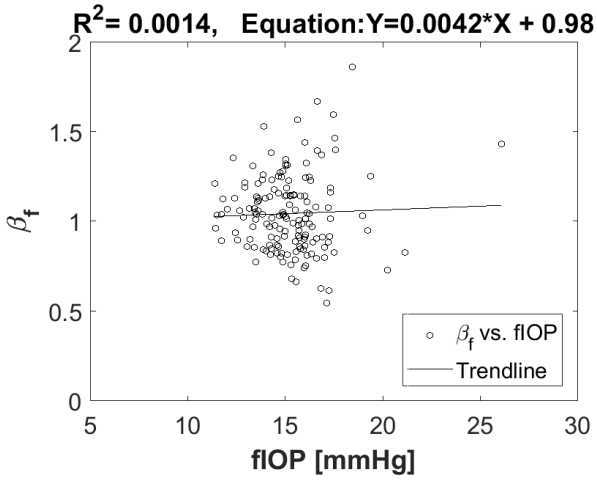

(b)

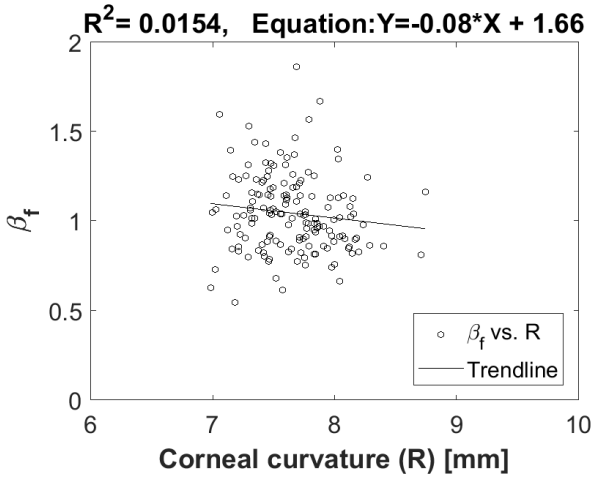

(c)

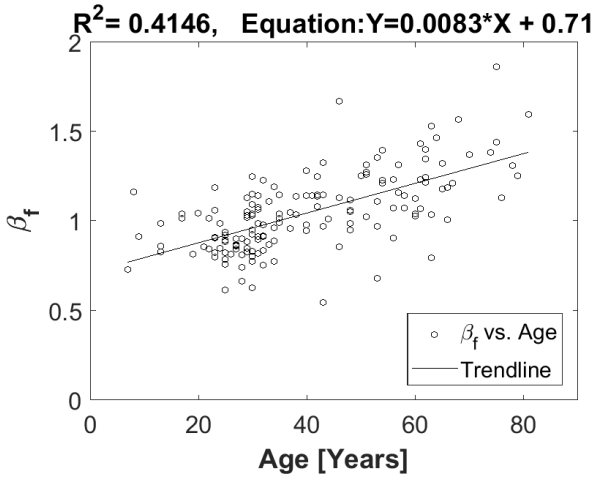

(d)

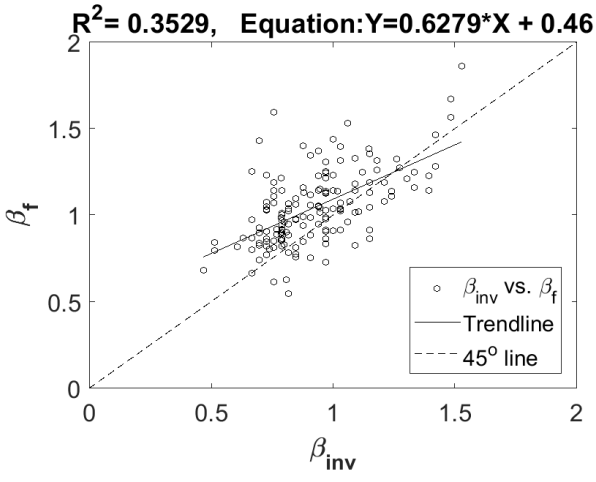

(e)

Figure 5.42 Association of the corrected corneal material parameter β_f with CCT in (a), fIOP in (b), R in (c), age in (d) and comparison with values of β obtained from previous inverse analysis [5, 6, 134]

Table 5.14 Correlation and relationship significance analysis between β_f and association parameters for the clinical dataset used in the validation

Correlations		β_f	fIOP [mmHg]	R [mm]	Age [Years]	CCT [μ m]	$\beta_{Inverse}$
	Pearson Correlation	1	.037	-.124	.644**	-.223**	.594**
β_f	Sig. (2-tailed)		.644	.122	.000	.005	.000
	Pearson Correlation	.037	1	-.033	-.111	.230**	.074
fIOP [mmHg]	Sig. (2-tailed)	.644		.680	.170	.004	.359
	Pearson Correlation	-.124	-.033	1	-.151	.052	.097
R [mm]	Sig. (2-tailed)	.122	.680		.060	.520	.230
	Pearson Correlation	.644**	-.111	-.151	1	-.056	.099
Age [Years]	Sig. (2-tailed)	.000	.170	.060		.489	.218
	Pearson Correlation	-.223**	.230**	.052	-.056	1	-.439**
CCT [μ m]	Sig. (2-tailed)	.005	.004	.520	.489		.000
	Pearson Correlation	.594**	.074	.097	.099	-.439**	1
$\beta_{Inverse}$	Sig. (2-tailed)	.000	.359	.230	.218	.000	

**. Correlation is significant at the 0.01 level (2-tailed).

*. Correlation is significant at the 0.05 level (2-tailed).

Comparison of corneal response parameters after applying β_f and fIOP on six clinical cases

After validation of the new estimation algorithms for intraocular pressure (fIOP) and corneal material behaviour (β_f), they were applied to the same six clinical cases that were presented in Section 5.5 for initial model validation. The same Python and Matlab codes, were applied again to extract the corneal response parameters from the numerical models after applying the new values of β_f and fIOP to compare them against the clinical behaviour. Table 5.15 gives descriptive statistics of corneal response parameters for the six models involved in the comparison and Figure 5.43 shows a graphical comparison of the values via a bar chart and error bars for standard deviation representaion. The biggest difference after applying the new algorithms still was for the first applanation deformation amplitude with 57.1% higher, followed by the highest concavity deformation with 22.9 % lower. The stiffness parameter (SP-HC) and first applanation pressure have improved in accuracy after applying the new algorithms by 48.6 and 13 %, respectively. Figure 5.16 shows corneal deformation results for the six models and their comparison with the original results and clinical behaviour. The left column of graphs shows corneal spatial deformation profiles at four time steps T= 5, 8, 10, 16 ms and the right column of figures shows the apical deformation with time, numerically and clinically, before and after correction.

Figure 5.45 provides comparison of the temporal pressure profile on cornea centre clinically and numerically, the last plot in this figure provides comparison of the temporal pressure profiles between the six cases. Figure 5.46 presents the apical deformations as a function of pressure applied on cornea to show development of the mechanical response of cornea to loading after applying the new algorithms. Analysis of error for apical deformations, pressure on cornea, and highest concavity corneal profile, is summarised in Table 5.17, by presenting the values of root mean square error (RMSE) between the clinical and numerical behaviour.

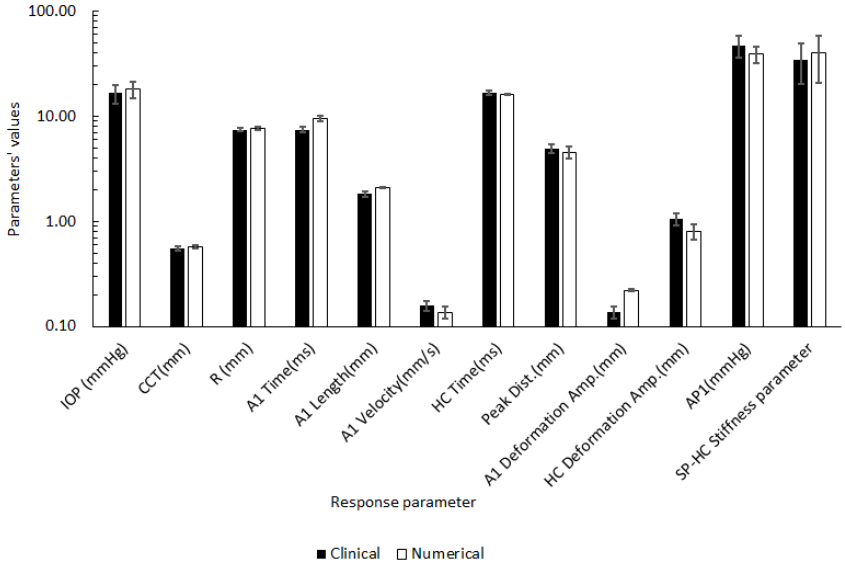

Figure 5.43 Visual representation of corneal response parameters comparison between clinical and corrected numerical results

Table 5.15 Descriptive statistics of the numerical corneal response parameters after applying β_f and fIOP on the six models of clinical cases, the bold line separates input from output parameters

Parameter	N	Mean	Std. Deviation	Minimum	Maximum
IOP (mmHg)	6.00	18.00	3.21	15.00	24.00
CCT(mm)	6.00	0.57	0.02	0.55	0.59
μ	6.00	0.0583	0.006	0.0502	0.0656
R (mm)	6.00	7.65	0.23	7.29	7.88
A1 Time(ms)	6.00	9.47	0.55	8.83	10.49
A1 Length(mm)	6.00	2.09	0.04	2.02	2.13
A1 Velocity(mm/s)	6.00	0.14	0.02	0.11	0.16
HC Time(ms)	6.00	16.03	0.29	15.60	16.50
Peak Dist.(mm)	6.00	4.56	0.58	3.54	5.20
Radius(mm)	6.00	10.94	1.84	8.14	13.94
A1 Deformation Amp.(mm)	6.00	0.22	0.01	0.21	0.23
HC Deformation Amp.(mm)	6.00	0.81	0.14	0.58	1.01
AP1(mmHg)	6.00	39.20	6.94	31.35	52.03
β_f	6.00	1.06	0.11	0.91	1.19
fIOP (mmHg)	6.00	17.32	3.35	13.88	23.60
SP-HC Stiffness parameter	6.00	39.64	19.01	20.70	76.52

	Spatial corneal deformations	Temporal apical deformations
Clinical case 1	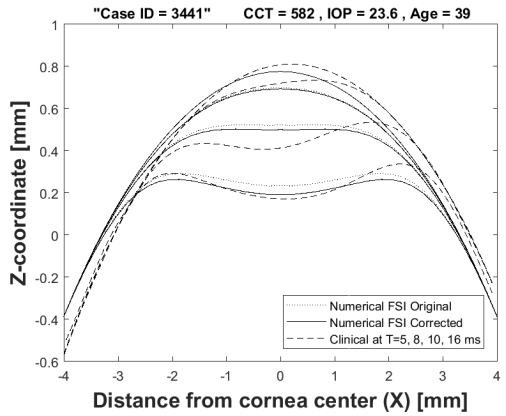	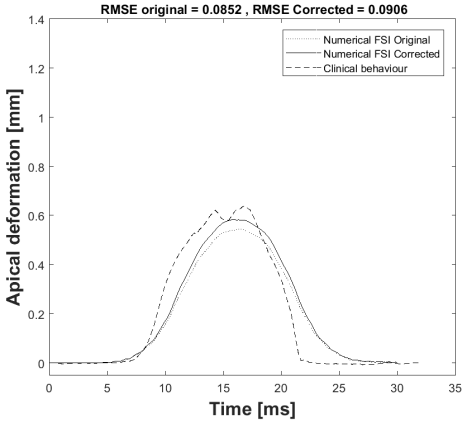
Clinical case 2	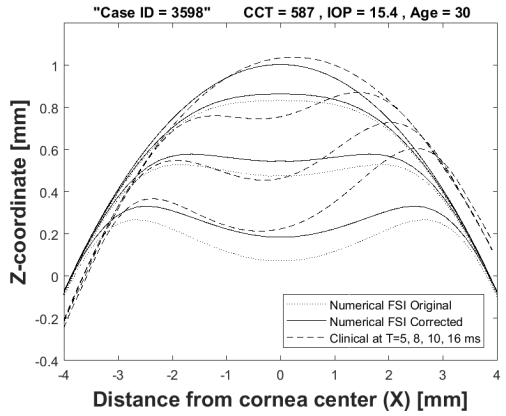	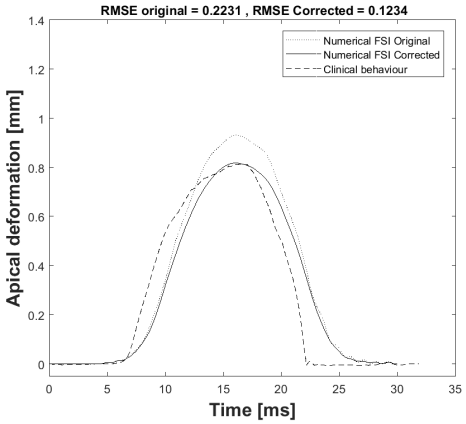
Clinical case 3	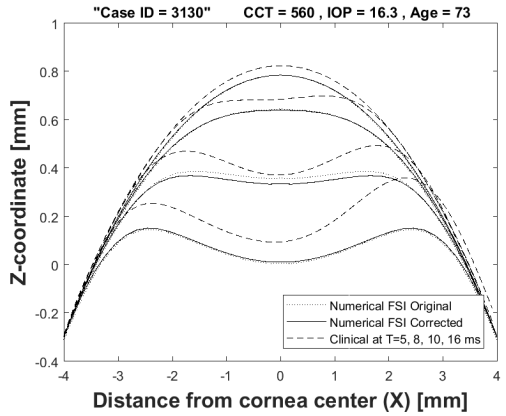	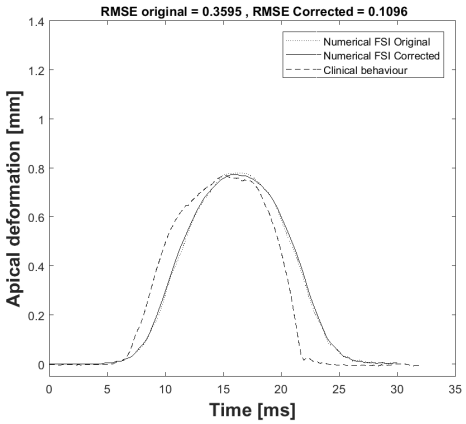

Clinical validation results with six patients after applying the new estimation algorithms

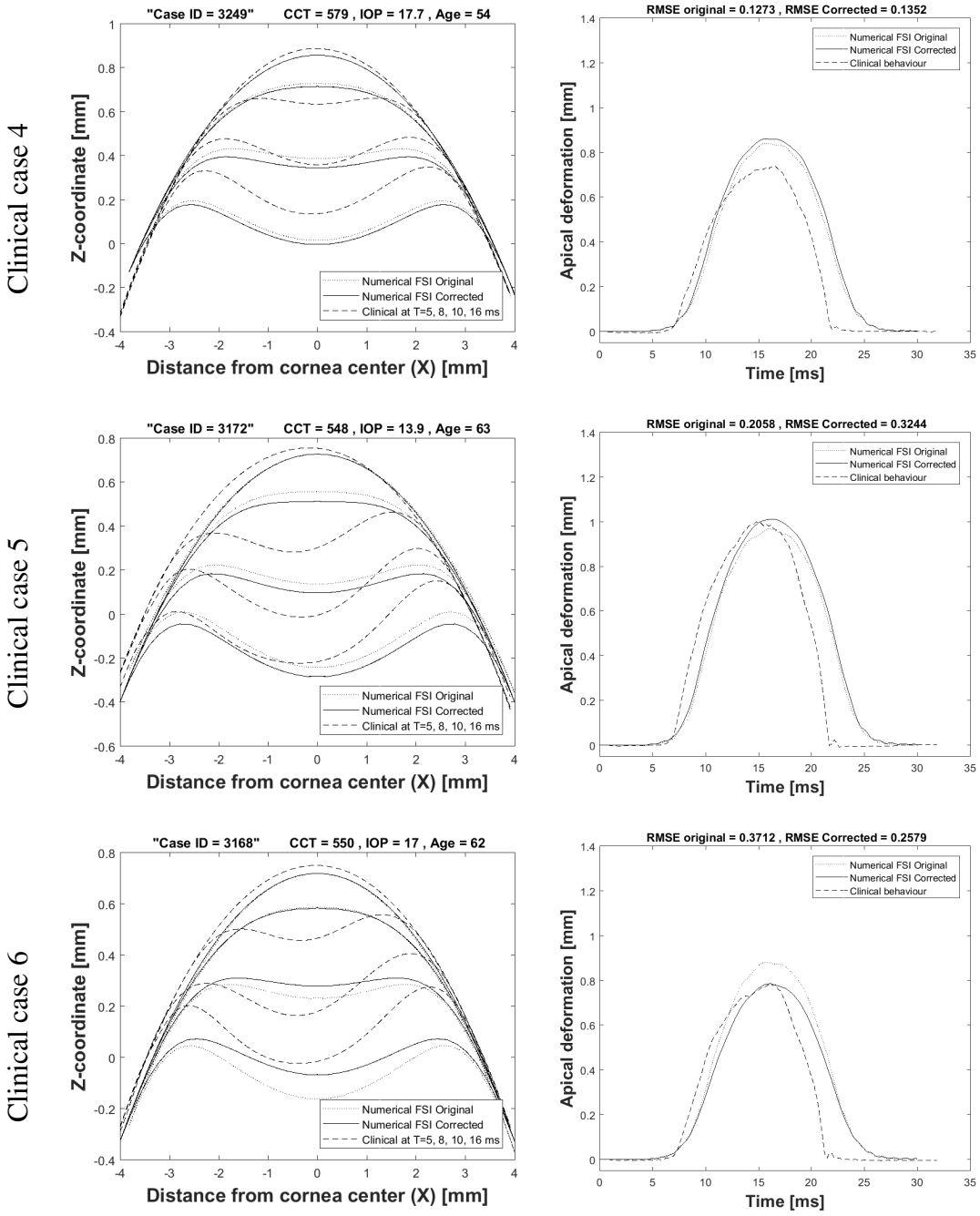

Figure 5.44 Continued: clinical validation results with six patients presented by the spatial corneal deformations and temporal apical deformation after applying the new estimation algorithms

The influence of applying the corneal material algorithm to the cases was more significant than just applying fIOP. The difference in IOP was smaller than the difference on the corneal stiffness which indicates the importance of accurate corneal material characterisation which will lead naturally to accurate IOP measurements. Value of the mean RMSE of Apical deformation and loading part of the pressure on apex have developed by 37.9% and 20.4%, respectively, however the highest concavity corneal profile and full curve of temporal pressure on cornea have raised by 60.3% and 12.6%, respectively, due to air puff shooting angle and material hysterisis effects.

Table 5.17 Root mean square error (RMSE) between the clinical and numerical results

Variable	N	Mean	Std. Deviation	Minimum	Maximum
HC corneal profile RMSE	6	0.299	0.249	0.081	0.662
Apical deformation RMSE	6	0.174	0.095	0.091	0.324
Pressure on apex (Loading part) RMSE	6	0.082	0.031	0.040	0.129
Temporal pressure on apex (Full curve) RMSE	6	11.625	3.532	5.840	14.870

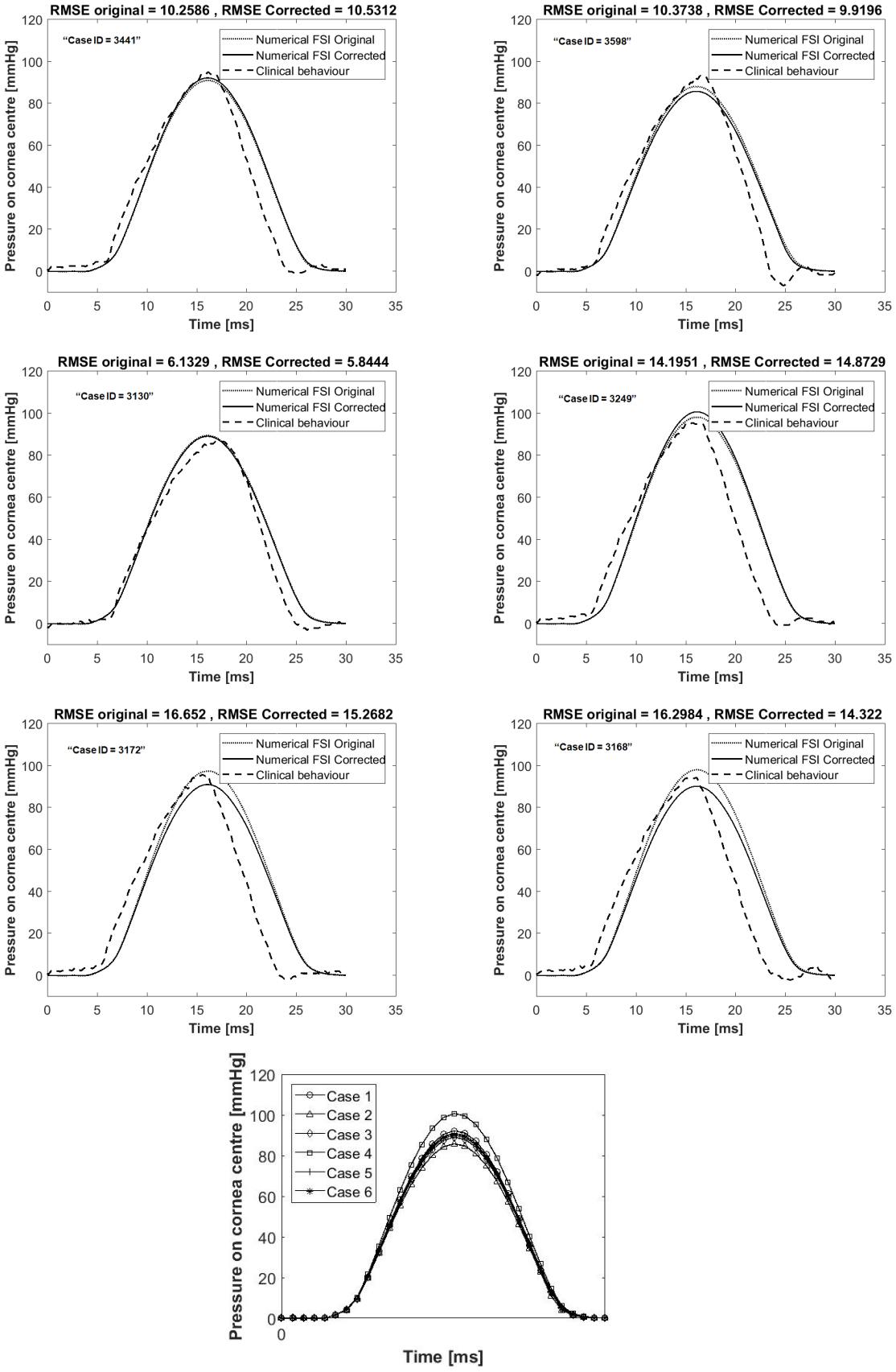

Figure 5.45 Temporal pressure profile on cornea centre numerically and clinically for six clinical cases and the last plot gathers numerical results in one plot

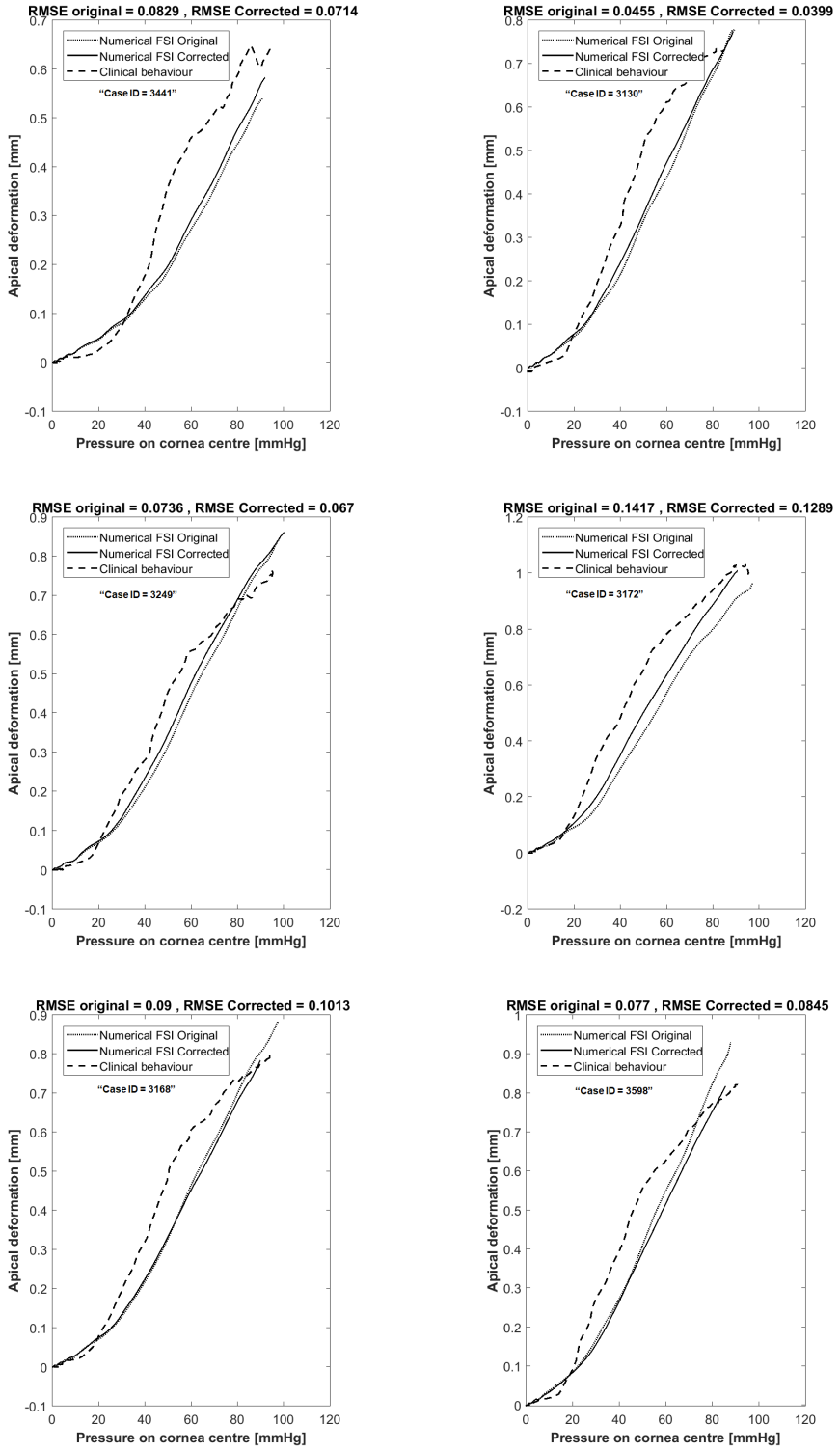

Figure 5.46 Apical deformation against pressure on cornea centre numerically and clinically for six clinical cases and the last plot gathers numerical results in one plot

Chapter 6

Overall discussion and conclusions

6.1 Overall discussion

The ocular biomechanics has been growing in the last thirty years as a result of increasing support to interdisciplinary research. One biomechanics project can incorporate many physics and scientific aspects which need flexible learning attitude and open perspective. The motivations for ocular biomechanics' studies are diverse as large number of people are affected by ocular diseases starting from simple refractive errors to complicated and progressive eye conditions.

The cornea has a visco-hyperelastic nonlinear material behaviour and numerous studies were performed before to understand this behaviour under different types of loadings. Examples of these tests are uni-axial and biaxial testing of ocular tissues, ocular globe inflation and air puff test, in-vivo and ex-vivo, which led to various developments in ocular devices, better diagnosis and wiser clinical decisions. The intraocular pressure (IOP) reading is a vital measurement in studing the eye or any associated disease, especially glaucoma risk management. Many techniques were developed to measure IOP as accurate as possible, some of these techniques require direct contact with the cornea such as Goldmann applanation tonometer or nonintrusive techniques such as the air puff non-contact tonometers (NCT).The NCT techniques are more prefered by patients, however it was found influenced by the biomechanical properties of the eye, either the geometry parameters like corneal thickness, curvature, or the material properties which was reported to change from person to another and with age variation [6, 107, 59]. The main question is how this technique can be valid for every patient having the eye test, with no measurement error. The answer to that question is the primary argument introduced in this chapter and a discussion of the results obtained in Chapter 5, is presented.

The biomechanical correction of IOP measurement has been the focus of many previous studies. Some focused on the association of IOP with central corneal thickness (CCT), corneal curvature (R) and other studies focused on corneal material properties' effect, but most of them were structural in nature suggesting assumptions for the fluid structure interaction (FSI) effect during the air puff test. Some of these assumptions can work effectively if the ratio between time scales of the two models in interaction is very small or very large to neglect the effect of one domain over the other or make a reasonable approximation, this ratio is known as the reduced velocity (U_R). But this is not the case in air puff test as the two time scales of the fluid velocity and the eye deformations are within the same order of magnitude and the time scales are changing through the unsteady application of the air jet on cornea during

the test. This is the start point to calssify the fluid structure interaction problem and choose which numerical method is suitable to solve the problem.

In order to accurately take into account, fluid structure interaction effect on the corneal response to loading, the two domains need to be solved simultaneously to exchange the data between them at each time step of the solution. The finite element model of the eye was based on the mass, force and stiffness matrices to calculate the structural material deformation. On the other hand, the CFD model of the air jet was governed by momentum and continuity equations to calculate pressure and velocity fields of the flow.

The coupled model of fluid structure interaction (FSI) between the eye and an air jet was successfully built and a mesh sensitivity analysis was performed to choose the most feasible and acceptable mesh [169–171]. Then the model was validated through three ways. Firstly, validation of the CFD code by simulating a turbulent jet impinging to a stationary flat surface and comparing the flow parameters against Laser Doppler Anemometry (LDA) experimental data. Secondly, comparison of the corneal deformations from the numerical model against clinical corneal response data from CorVis-ST for in-vivo human eyes. Thirdly, clinical and experimental validations of the estimation algorithms of IOP and cornea material behaviour extracted from the parametric study performed using the FSI model.

The clinical comparisons were presented in two forms; the first form was by presenting cornea deformation profiles at 4 time captures of the test (5, 8, 10, 16 ms) along with the cornea apical deformation with time. The second form was through calculating dynamic corneal response (DCR) parameters (A1 Time (ms), A1 Length (mm), A1 Velocity (mm/s), HC Time (ms), Peak Distance (mm), HC Radius (mm), A1 Deformation Amplitude (mm), HC Deformation Amplitude (mm), AP1 (mmHg), SP-HC Stiffness parameter) and comparing them against the same parameters obtained clinically.

After the validation process, a parametric study was performed to see the effect of cornea geometrical and material parameters on the corneal response to the air jet loading in order

to come up with an estimation algorithm for the intraocular pressure, taking into account the fluid structure interaction effect. The new estimation algorithm was verified against the clinical CorVis measurements and the experimental measurements done on five ex-vivo human eyes using the same device. Then, an estimation algorithm to the corneal material behaviour was built to accurately determine the corneal material parameter β_f describing the change of corneal material stiffness from patient to another, taking into account, fluid structure interaction effect.

Numerical analysis of the turbulent impinging jet was done in the context of hybrid finite volume solution of Navier-Stokes equations and Spallart allmaras or RNG-k epsilon turbulence models to simulate the production and dissipation of the turbulent kinetic energy which produce an approximate solution for the pressure and velocity fields over cornea surface. The produced solution for pressure distribution on cornea and its progression with time produced corneal deformations which were in a good agreement with the clinical deformations.

The numerical analysis of finite element model of the eye was created based on previous studies performed by Elsheikh et al. [5, 6, 20, 129]. It uses variational formulation method to produce the matrix equations relating between the nodal values of deformation and the element material properties. In the past, air puff pressure was based on a constant pressure distribution loading on different rings of the cornea, changing in magnitude during time of the test. This pressure distribution was provided by Oculus based on a pressure tranceducer reading inside the piston chamber and pressure on the cornea was approximated to be half of piston pressure [19, 5, 65, 66, 20].

6.1.1 Validation of air puff test numerical model

The numerical results of the CFD model of impinging jet on a flat surface showed a close agreement with the laser doppler anemometer (LDA) experimental measurement of Tummers

experiment [158]. The axial and radial velocities at different trajectories normal to the impingement surface were presented. These results provided a sufficient confidence on the CFD capabilities within Abaqus and effectiveness of the co-simulation engine for fluid structure interaction problems. The model showed that it is robust and can be reliable in doing the parametric study. A graphical user interface was generated to enable building the orphan mesh of the air jet domain projected over the eye model.

The second important validation of the coupled model of the air puff test was the comparison with clincial deformations of the cornea. The results of six different clincal cases were presented. The IOP ranges from 15 to 24 mmHg, CCT from 548 to 587 μm, Age from 30 to 73. All the deformations showed close material response to the clincal deformations. There is a difference in some clinical cases due to the air puff shooting angle, sometimes it is not exactly at center of the cornea which was modified in the mesh genrator after the validation process.

The parametric study contained 110 different eye models with wide ranges of biomechanical parameters which has led to a better understanding of the association of these parameters to the IOP measurements and the corneal stiffness. As presented in Section 5.6, the influence matrices of corneal biomechanical parameters showed their effects on corneal response parameters. The target was to calculate the dynamic corneal response parameters and choose the most significant parameters to be included in the IOP biomechanical estimation algorithm (fIOP). In that table some of the parameters are input parameters to the numerical model such as (CCT, IOP, μ and R), but rest of the parameters are output from the results files such as (Highest concavity (HC) deformation, peak distance, A1 time, A1 length, A1 deformation, AP1, Stiffness parameter (SP-HC)).

Another benefit from the parametric study was to get the parameters that determine the cornea unique material parameter β_f without knowing the age. It was been found that IOP, CCT and SP-HC (Stiffness parameters) are the three parameters with the highest association

with the material stiffnes change. The main job was to fit all the parametric study data into 5 different surfaces which represent the β_f surfaces for the five material settings involved in the study. Based on value of IOP, CCT and SP-HC, the material parameter β_f can be identified.

6.1.2 Intraocular pressure estimation algorithm (fIOP)

The separation of corneal biomechanical parameters effect from IOP measurements has been the objective of several studies in the past and to date it has not been completely possible. This was a major problem in Goldmann applanation tonometery (GAT) when it comes to direct contact with the cornea, flattening the cornea is affected by the corneal thickness, corneal curvature and material stiffness [2–4]. The CorVis-ST was considered an attempt to resolve this challenge and minimze dependence of the readings on corneal topographic and material parameters. The data collected for an eye test from CorVis-ST acquires digital video of the corneal response to a rapid air puff. These cross-sectional profiles of the corneal anterior and posterior surfaces provide an understanding on the mechanical behaviour of human corneas and can deffrenitiate between healthy and diseased ones.

After previous conducted studies on the performance of CorVis-ST to provide accurate IOP measurements, it was also found that CorVis-ST IOP readings are still associated with corneal thickness (CCT), corneal curvature (R) and corneal stiffness but not at the same level as GAT measurements [5, 57, 31, 160, 164, 165]. Some multivariable correction studies were performed to address this issue in CorVis-ST [167, 57–64, 173], however little attention was made to the fluid structure interaction effect between air puff and the cornea. The presented estimation algorithm in the current study was an attempt to consider the FSI effect on IOP measurements.

After validation of the coupled model between the air puff and finite element model of the eye, the parameteric study was performed. The corneal response parameters were extracted from the output files and a correlation analysis was performed to find that first applanation

pressure (AP1) was the highest associated parameter with IOP ($r = 0.736, P < 0.0001$), Table 5.7. AP1 was chosen along with CCT, R and μ, representing corneal stiffening with patient's age, to eliminate IOP's association with CCT and age. An exercise was made to know the lowest possible polynomial for each parameter and the best equation formula was chosen based on the lowest RMSE. AP1 has second order polynomial, CCT effect represented by fourth order, μ by third order polynomial and corneal curvature was included as first order polynomial. Matlab and Python codes were used to perform a non-linear least square optimization for the equation parameters to get a close match with the true value of IOP (IOPt). The best equation for fIOP was extracted from the code and validated against, clinical datasets and experimental measurments of true IOP. Based on the patient's geometry parameters and age, the value of fIOP was calculated.

To validate the new fIOP algorithm, five ex-vivo donated human eyes, with age range (69$\pm$3 years) obtained from the Fondazione Banca degli Occhi del Veneto Onlus, Venice, Italy, were tested during a time frame of 3 to 5 days post-mortem. Ethical approvals were issued by the eye bank in Italy and by the biomechanical engineering group (RETH000753) in accordance with the Declaration of Helsinki. After the sample prepration, Section 4.6.1, the eye was ready to perform the air puff test on CorVis-St in order to collect the dynamic corneal response parameters for each eye at different levels of true IOP values (IOPt). True values of IOP were measured by an FDW pressure transducer (RDP Electronics, Wolverhampton, UK) and controlled by a stepper motor and syringe pump through a pre-set cycle on LabView to cover a range from 0 to 30 mmHg. The eye was left to stabilise for 60 s after reaching each pressure level before applying the air puff from corVis-ST. At least three measurements were taken for every pressure level, leaving at least two minutes between every successive measurements to enable the ocular tissue to relax to original condition. The average difference between CVS-IOP and IOPt for all specimens at different pressure levels

was $7.8 \pm 4.1 (1.2 - 17.3)$ while for fIOP was $0.44 \pm 1.6 (-3.1 - 5.0)$ with 94% reduction in error of mean difference.

To gauge the new algorithm's performance, it was applied to the clinical dataset and the association elimination was acheived. Age association improved by 94.7 %, CCT association improved by 70.6 % and corneal curvature association developed by 43.1 %. The current estimation algorithm is applicable to in-vivo clinical data which provided an advantage over previous studies that were done on ex-vivo tests and were not applicable to clinical tests [96, 89–91, 22, 23, 94, 92, 174].

6.1.3 Cornea material behaviour estimation algorithm (β_f)

The current study made use of numerical simulation of the non-contact tonometry test and the parametric study to provide an estimation algorithm of the corneal material behaviour from the output dynamic response parameters of the air puff test with less dependence on patient's age. The accurate material charecterisation for cornea can help ophtholmologists and surgions in treatment management and surgical planning before any physical intervention. Understanding the material mechanical response can be used in diagnosis of some diseases which alter the corneal stiffness such as keratoconus and ectatic diseases [88, 175–177]. Many experimental testing studies were conducted to understand behaviour of the cornea, some were based on uniaxial tests for corneal specimens [22–25], some other tests were based on inflation of the eye globe [89–92]. Some studies considered the corneal material to behave as linear homogenous elastic material [94, 95], other studies provided hyperelastic non-linear behaviour [96, 91, 97, 98].

According to the findings obtained by Elsheikh et al. for uniaxial testing [6] and inflation testing [32, 106, 178], there is a correlation between corneal stiffness and patient's age, however it was noticed that there is remarkable differences in material behaviour between patients within the same age group. Another problem is the non-linearity of corneal material

behaviour which means that material stiffness is different for different stress levels of intraocular pressure (IOP). This complicates the problem of separating between the effect of IOP and material stiffness on corneal deformations during the air puff test. That was the reason for developing a new corneal material parameter (β) to overcome these two issues and make it possible for the air puff test simulation to obtain the corneal material behaviour due to the fact that stress-strain curves for different ages don't cross over with each other as shown in Figure 6.1, [6, 32, 65, 166]. The average behaviour of corneas for patients of age 50 was considered as ($\beta = 1$) and softer or stiffer corneas are ratios of β, providing the whole stress-strain curve of the material behaviour not only at a certain stress level.

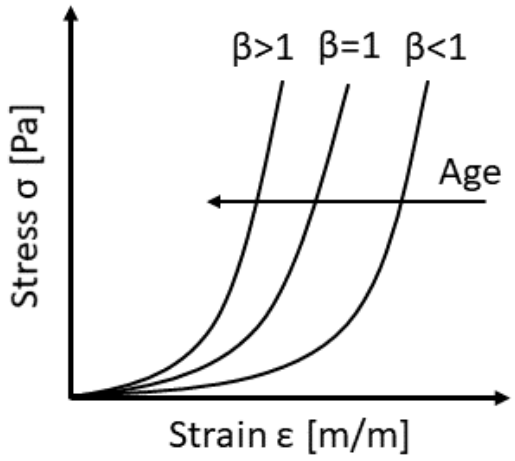

Figure 6.1 Tangent modulus relation with stress for different β values [6, 32, 65, 166]

There is another challenge related to the influence of intraocular pressure (IOP) and central corneal thickness (CCT) on the dynamic corneal response to the air puff. The influence of CCT on the dynamic response parameters is easier to compensate and correct for while the IOP effect is interlinked with material stiffness in a complicated closed loop as accurate estimation of corneal material requires an accurate estimation of IOP and air puff pressure and vice versa. This challenge was dealt with in the present study by involving the stiffness parameter (SP-HC) in the estimation algorithm of corneal material which was proven to have stronger correlation with corneal stiffness than intraocular pressure. The

stiffness parameter at the highest concavity (HC) is an output parameter from the CorVis-ST test results and is calculated from Equation 6.1.

$$SP-HC = \frac{AP1 - IOP}{HC\ deflection - A1\ deflection} \tag{6.1}$$

where AP1 is the first applanation pressure on cornea, IOP is the intraocular pressure and can be replaced by bIOP or fIOP, HC deflection is the maximum deflection of cornea apexand A1 deflection is the deflection amplitude at the first applanation moment.

Implementation of the new corneal material algorithm β_f can improve management and diagnosis of ocular diseases in clinical practice and eliminate the physical intervention with the eye. β_f algorithm also can be used to identify keratoconic eyes which are known by significant decrease in corneal stiffness than healthy corneas. The new algorithm also can improve the sensitivity of existing material indices applied clinically, for instance the topographic and biomechanical index (TBI) [107] and CorVis biomechanical index (CBI) [179]. Furthermore, it can assist in surgical planning of refractive surgery and detect patients with high risk of complications or ectasia progression after surgery [180–182]. The accurate estimation of corneal material behaviour also leads to improvement in IOP measurement as they are closely related to each other which in turn will help Glaucoma management [167, 58, 59, 61, 62].

6.2 Limitations of study

The clinical behaviour of biological tissues is known to be non-linear in nature and challenging to exactly simulate their behaviour numerically. From analysis of the obtained results in the current study, there were some limitations arised, which are important to be mentioned.

- The eye boundary conditions applied to prevent it from free body motion affect the accuracy of the numerical deformations to match with the corneal clinical deformations

as the whole eye move backward as a response to the air puff impact. The eye is surrounded by soft fatty tissue which gives the eye freedom to move backward and that is not considered in the current study.

- The hysteresis effect which is related to the viscoelastic behaviour of the cornea. When the cornea is unloaded and tries to return back to the original geometry, it reflects after a relaxation time and history effect. This effect was not considered in the current material model of the cornea.

- Clinically, the air puff shooting direction can be sometimes at an angle from the eye axis and a modification for the mesh was done to apply the air puff at an angle, same as the clinical shooting, but the problem is that it's not known how the air puff will hit the cornea in order to make a global correction which fits with all patients.

- Simulation of the internal fluids of the eye (aqueous and viterous) was not included in the current study and only their effect (intraocular pressure) was considered.

6.3 Conclusions

The primary objective of the current study was to develop and validate a numerical tool simulating the non-contact tonometry test in order to provide estimation algorithms for the intraocular pressure measurement and corneal material behaviour taking into consideration fluid structure interaction between cornea and the air puff based on the dynamic corneal response parameters from a non-contact tonometer CorVis-ST. Patient-specific models were used in the validation process of the numerical model to quantify the effect of biomechanical parameters on corneal deformations and air puff pressure distribution. The following conclusions were made:

- The full coupling between finite element model of the eye and a turbulent air puff model was accomplished successfully through two way fluid structure interaction simulation of the two models [169–171].

- The main finding was that, pressure distribution of the air puff is affected by the fluid structure interplay between, cornea and the air puff, which in turn affects the corneal deformations depending on geometric and stiffness parameters of the cornea.

- A parametric study was performed to see, effect of the corneal biomechanical parameters on IOP measurements and corneal material behaviour. Correlation analyses were performed to choose the parameters that were used in the estimation algorithms.

- An estimation algorithm of the intraocular pressure measurement (fIOP) was developed and validated against clinical and experimental data of in-vivo and ex-vivo eyes, respectively, showing reduced association between IOP, central corneal thickness and pateint's age.

- An estimation algorithm for cornea material behaviour (β_f) was developed and validated with clinical and experimental data of in-vivo and ex-vivo eyes, respectively. It showed low association with central corneal thickness (CCT), intraocular pressure (IOP) and corneal curvature (R), while showing direct relationship with age as expected by previous experimental investigation [6]. β_f algorithm can improve management and diagnosis of ocular diseases in clinical practice and eliminate the physical intervention with the eye. It can also lead to improvement in IOP measurements which helps in Glaucoma management and surgical planning.

6.4 Recommendations for future study

According to the achieved findings in the present study and the limitations observed, some recommendations for future research are listed below:

- Trying to consider the soft fatty tissue around the eye to reduce the boundary conditions effect for the eye model
- Developing the non-linear material model of the cornea to take hysteresis effect into account and considering the anisotropy or non-homogenity of the collagen fibres' distribution in the cornea
- Adding an algorithm to CorVis-ST to identify and correct the shooting angle of the air puff after measurement can lead to better accuracy in corneal deformations and pressure distribution on cornea such as the suggestion shown in Figure 6.2
- Simulation of the internal fluids of the eye can be benefitial in the study of retinal detachment or internal surgical planning such as vitrectomy [183–185]
- The fluid structure interactionj model can be applied to keratoconic eyes and using artificial intelligence, diseased eyes can be identified at early stages from the corneal response to the air puff.

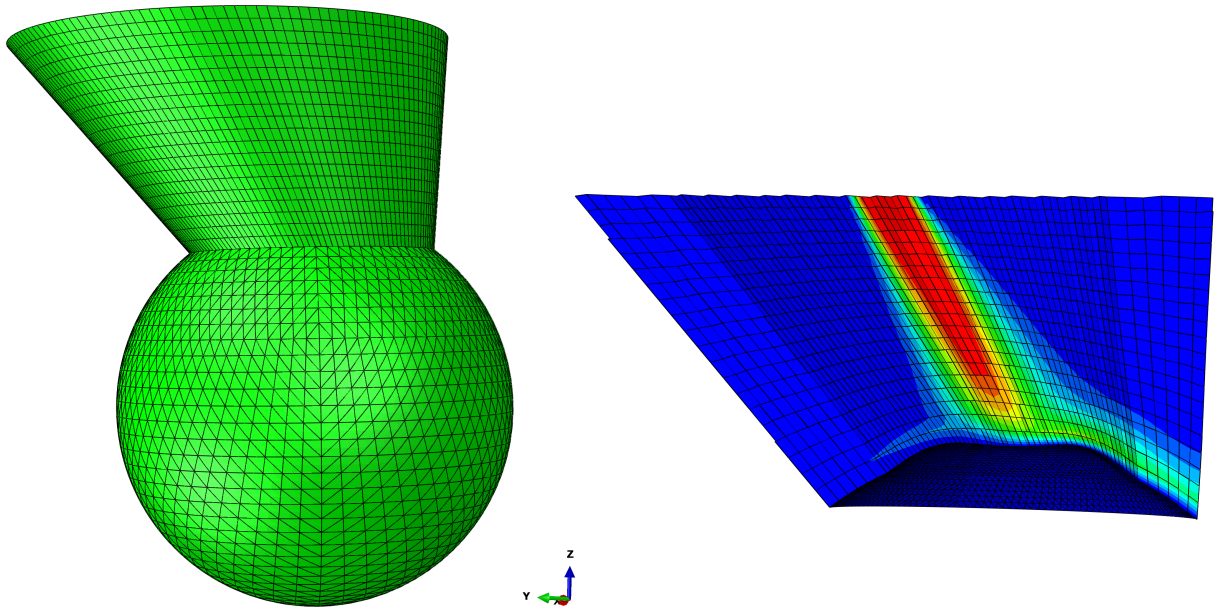

(a) (b)

Figure 6.2 Inclined shooting angle model of the air puff test. Full model (a), velocity and direction of the air puff from the CFD model (b)

References

[1] Jonathan N. Tinsley, Maxim I. Molodtsov, Robert Prevedel, David Wartmann, Jofre Espigulé-Pons, Mattias Lauwers, and Alipasha Vaziri. Direct detection of a single photon by humans. *Nature Communications*, 7(1):12172, dec 2016. ISSN 2041-1723. doi: 10.1038/ncomms12172. URL http://www.nature.com/articles/ncomms12172.

[2] Goldmann Applanation Tonometry. Multiparameter Correction Equation for. 88(1): 102–112, 2011.

[3] Robert A. Moses. The Goldmann applanation tonometer. *American Journal of Ophthalmology*, 46(6):865–869, 1958. ISSN 00029394. doi: 10.1016/0002-9394(58)90998-X.

[4] P G Davey, a Elsheikh, and D F Garway-Heath. Clinical evaluation of multiparameter correction equations for Goldmann applanation tonometry. *Eye (London, England)*, (January):1–9, mar 2013. ISSN 1476-5454. doi: 10.1038/eye.2013.23. URL http://www.ncbi.nlm.nih.gov/pubmed/23492859.

[5] Ahmed Elsheikh, Brendan Geraghty, Daad Alhasso, Jonathan Knappett, Marino Campanelli, and Paolo Rama. Regional variation in the biomechanical properties of the human sclera. *Experimental Eye Research*, 90:624–633, 2010. doi: 10.1016/j.exer.2010.02.010. URL https://ac.els-cdn.com/S0014483510000576/1-s2.0-S0014483510000576-main.pdf?{_}tid=4714681c-8246-43f3-bba2-83dc744d3ff6{&}acdnat=1548619419{_}73671e6befcf38056326cd32421ff5b1.

[6] Ahmed Elsheikh, Brendan Geraghty, Paolo Rama, Marino Campanelli, and Keith M Meek. Characterization of age-related variation in corneal biomechanical properties. doi: 10.1098/rsif.2010.0108. URL https://royalsocietypublishing.org/doi/pdf/10.1098/rsif.2010.0108.

[7] G. Boyer, C. Pailler Mattei, J. Molimard, M. Pericoi, S. Laquieze, and H. Zahouani. Non contact method for in vivo assessment of skin mechanical properties for assessing effect of ageing. *Medical Engineering & Physics*, 34(2):172–178, 2012. ISSN 13504533. doi: 10.1016/j.medengphy.2011.07.007.

[8] Vincent Fleury, Alia Al-Kilani, Olena P. Boryskina, Annemiek J. M. Cornelissen, Thi-Hanh Nguyen, Mathieu Unbekandt, Loïc Leroy, Georges Baffet, Ferdinand

le Noble, Olivier Sire, Elodie Lahaye, and Vincent Burgaud. Introducing the scanning air puff tonometer for biological studies. *Physical Review E*, 81(2): 021920, feb 2010. ISSN 1539-3755. doi: 10.1103/PhysRevE.81.021920. URL http://link.aps.org/doi/10.1103/PhysRevE.81.021920.

[9] Sabine Kling and Susana Marcos. Finite-Element Modeling of Intrastromal Ring Segment Implantation into a Hyperelastic Cornea. 54(1):881–889, 2013. doi: 10.1167/iovs.12-10852.

[10] Shang Wang, Jiasong Li, Ravi Kiran Manapuram, Floredes M Menodiado, R Davis, Michael D Twa, Alexander J Lazar, Dina C Lev, and Raphael E Pollock. HHS Public Access. 37(24):5184–5186, 2015.

[11] Sabine Kling, Nandor Bekesi, Carlos Dorronsoro, Daniel Pascual, and Susana Marcos. Corneal viscoelastic properties from finite-element analysis of in vivo air-puff deformation. *PloS one*, 9(8):e104904, jan 2014. ISSN 1932-6203. doi: 10.1371/journal.pone.0104904. URL http://journals.plos.org/plosone/article?id=10.1371/journal.pone.0104904.

[12] Yuan-Cheng Fung. *Biomechanics*. Springer New York, New York, NY, 1993. ISBN 978-1-4419-3104-7. doi: 10.1007/978-1-4757-2257-4. URL http://link.springer.com/10.1007/978-1-4757-2257-4.

[13] John V. Forrester, Andrew D. Dick, Paul G. McMenamin, Fiona Roberts, and Eric Pearlman. Chapter 1 - anatomy of the eye and orbit. In John V. Forrester, Andrew D. Dick, Paul G. McMenamin, Fiona Roberts, and Eric Pearlman, editors, *The Eye (Fourth Edition)*, pages 1 – 102.e2. W.B. Saunders, fourth edition edition, 2016. ISBN 978-0-7020-5554-6. doi: https://doi.org/10.1016/B978-0-7020-5554-6.00001-0. URL https://www.sciencedirect.com/science/article/pii/B9780702055546000010.

[14] The National Eye Institute (NEI). Facts About the Cornea and Corneal Disease, What is the cornea ? . page 2, 2016.

[15] H. R. Taylor. Refractive errors: Magnitude of the need, 2000. ISSN 09536833.

[16] David A. Luce. Determining in vivo biomechanical properties of the cornea with an ocular response analyzer. *Journal of Cataract & Refractive Surgery*, 31(1):156–162, jan 2005. ISSN 08863350. doi: 10.1016/j.jcrs.2004.10.044. URL http://www.ncbi.nlm.nih.gov/pubmed/15721708http://linkinghub.elsevier.com/retrieve/pii/S088633500401065X.

[17] Dolores Ortiz, David Piñero, Mohamed H. Shabayek, Francisco Arnalich-Montiel, and Jorge L. Alió. Corneal biomechanical properties in normal, post-laser in situ keratomileusis, and keratoconic eyes. *Journal of Cataract & Refractive Surgery*, 33(8):1371–1375, aug 2007. ISSN 08863350. doi: 10.1016/j.jcrs.2007.04.021. URL http://www.ncbi.nlm.nih.gov/pubmed/17662426http://linkinghub.elsevier.com/retrieve/pii/S0886335007008279.

[18] David Touboul, Cynthia Roberts, Julien Kérautret, Caroline Garra, Sylvie Maurice-Tison, Elodie Saubusse, and Joseph Colin. Correlations between corneal hysteresis, intraocular pressure, and corneal central pachymetry. *Journal of*

Cataract & Refractive Surgery, 34(4):616–622, apr 2008. ISSN 08863350. doi: 10.1016/j.jcrs.2007.11.051. URL http://www.ncbi.nlm.nih.gov/pubmed/18361984http://linkinghub.elsevier.com/retrieve/pii/S0886335008000953.

[19] D. Luce. Air–Jet Temporal and Spatial Pressure Properties of the Reichert Ocular Response Analyzer (ORA). *Investigative Ophthalmology & Visual Science*, 46(13): 5009–5009, may 2005. URL https://iovs.arvojournals.org/article.aspx?articleid=2404418.

[20] Ahmed Elsheikh, Stuart Ross, Daad Alhasso, and Paolo Rama. Numerical Study of the Effect of Corneal Layered Structure on Ocular Biomechanics. *Current Eye Research*, 34(1):26–35, jan 2009. ISSN 0271-3683. doi: 10.1080/02713680802535263. URL http://www.tandfonline.com/doi/full/10.1080/02713680802535263.

[21] Renato Ambrósio, Isaac Ramos, Allan Luz, Fernando Correa Faria, Andreas Steinmueller, Matthias Krug, Michael W. Belin, and Cynthia Jane Roberts. Dynamic ultra high speed scheimpflug imaging for assessing corneal biomechanical properties. *Revista Brasileira de Oftalmologia*, 72(2):99–102, 2013. ISSN 00347280. doi: 10.1590/S0034-72802013000200005.

[22] Theo Seiler, Michael Matallana, Sebastian Sendler, and Thomas Bende. Does Bowman's Layer Determine the Biomechanical Properties of the Cornea? *Journal of Refractive Surgery*, 8(2):139–142, 1992. doi: 10.3928/1081-597X-19920301-08.

[23] D A Hoeltzel, P Altman, K Buzard, and K Choe. Strip extensiometry for comparison of the mechanical response of bovine, rabbit, and human corneas. *Journal of biomechanical engineering*, 114(2):202–15, 1992. ISSN 0148-0731. URL http://www.ncbi.nlm.nih.gov/pubmed/1602763.

[24] Ira S. Nash, Peter R. Greene, and C. Stephen Foster. Comparison of mechanical properties of keratoconus and normal corneas. *Experimental Eye Research*, 35(5): 413–424, 1982. ISSN 00144835. doi: 10.1016/0014-4835(82)90040-9.

[25] J. GLOSTER, E. S. PERKINS, and M. L. POMMIER. Extensibility of strips of sclera and cornea. *The British journal of ophthalmology*, 41(2):103–110, 1957. ISSN 00071161. doi: 10.1136/bjo.41.2.103.

[26] In Glaucoma Management. The Role of Ocular Biomechanics. *Review of Optometry*, October:49–52, 2008.

[27] A Sommer. Intraocular pressure and glaucoma. *American journal of ophthalmology*, 107(2):186–8, feb 1989. ISSN 0002-9394. doi: 10.1016/0002-9394(89)90221-3. URL http://www.ncbi.nlm.nih.gov/pubmed/2913813.

[28] Harry A Quigley, Dana Center for Preventive Ophthalmology, and Johns Hopkins. Near East (African states not in Africa group, Arab states), Africa (African states south of 200 N latitude. *British Journal of Ophthalmology*, 80:389–393, 1996. doi: 10.1136/bjo.80.5.389. URL http://bjo.bmj.com/.

[29] Richard J. Symes and Frederick S. Mikelberg. Normal tension glaucoma management: a survey of contemporary practice. *Canadian Journal of Ophthalmology*, 52(4): 361–365, 2017. ISSN 17153360. doi: 10.1016/j.jcjo.2016.12.008. URL http://dx.doi.org/10.1016/j.jcjo.2016.12.008.

[30] Collaborative Normal-tension Glaucoma and Study Group. The Effectiveness of Intraocular Pressure Reduction in the Treatment of Normal-Tension Glaucoma. *American journal of ophthalmology*, 9394(98):498–505, 1998. ISSN 0002-9394 (Print). doi: 10.1016/S0002-9394(98)00272-4.

[31] Aachal Kotecha, Ahmed Elsheikh, Cynthia R. Roberts, Haogang Zhu, and David F. Garway-Heath. Corneal thickness- and age-related biomechanical properties of the cornea measured with the ocular response analyzer. *Investigative Ophthalmology and Visual Science*, 47(12):5337–5347, 2006. ISSN 01460404. doi: 10.1167/iovs.06-0557.

[32] Ahmed Elsheikh, Defu Wang, Michael Brown, Paolo Rama, Marino Campanelli, and David Pye. Assessment of corneal biomechanical properties and their variation with age. *Current Eye Research*, 32(1):11–19, jan 2007. ISSN 0271-3683. doi: 10.1080/02713680601077145. URL http://www.ncbi.nlm.nih.gov/pubmed/17364730.

[33] J. W. Gauntner, J. N. B. Livingood, and P. Hrycak. Survey of literature on flow characteristics of a single turbulent jet impinging on a flat plate. *NASA Technical Memorandum*, (February):43, 1970. URL http://www.fire.tc.faa.gov/pdf/fsr-0181.pdf.

[34] Coleman Dup D and D S Snedeker. A study of free jet impingement. Part 1. Mean properties of free and impinging jets. *Journal of Fluid Mechanics*, 45(2):281–319, 1971. ISSN 0022-1120. doi: 10.1017/S0022112071000053.

[35] Khaled J. Hammad and Ivana Milanovic. Flow Structure in the Near-Wall Region of a Submerged Impinging Jet. *Journal of Fluids Engineering*, 133(9):091205, 2011. ISSN 00982202. doi: 10.1115/1.4004907.

[36] S. Beltaos and N. Rajaratnam. Plane Turbulent Impinging Jets. *Journal of Hydraulic Research*, 11(1):29–59, 1973. ISSN 0022-1686. doi: 10.1080/00221687309499789. URL http://www.tandfonline.com/doi/abs/10.1080/00221687309499789.

[37] D R Miller and E W Comings. Static pressure distribution in the free turbulent jet. *J.{˜}Fluid Mech.*, 3(March 1957):1–16, 1957.

[38] D. Cooper, D. C. Jackson, B. E. Launder, and G. X. Liao. Impinging jet studies for turbulence model assessment-I. Flow-field experiments. *International Journal of Heat and Mass Transfer*, 36(10):2675–2684, 1993. ISSN 00179310. doi: 10.1016/S0017-9310(05)80204-2.

[39] T. Karimipanah. *Turbulent jets in confined spaces : application in mixing ventilation experimental and numerical studies*. Kungl. Tekniska Högskolan, 1996. ISBN 9789171706676. URL https://books.google.co.uk/books?id=Jfi5NAAACAAJ.

[40] Edward Seckel. Aeroelasticity. In *Stability and Control of Airplanes and Helicopters*, pages 152–162. 2014. doi: 10.1016/b978-0-12-634450-9.50014-2.

[41] Dewey H. Hodges and G. Alvin Pierce. *Introduction to structural dynamics and aeroelasticity, second edition*, volume 9780521195904. 2011. ISBN 9780511997112. doi: 10.1017/CBO9780511997112.

[42] DH Hodges, GA Pierce, and MA Cutchins. Introduction to Structural Dynamics and Aeroelasticity. *Applied Mechanics Reviews*, 56(3):B35, 2003. ISSN 00036900. doi: 10.1115/1.1566393.

[43] Grigorios Dimitriadis. *Introduction to Nonlinear Aeroelasticity*. 2017. doi: 10.1002/9781118756478.

[44] Xiaodong Sheldon. Wang. *Fundamentals of fluid-solid interactions : analytical and computational approaches*. Elsevier, 2008. ISBN 9780080559704.

[45] Jaroslav Hron and Stefan Turek. A Monolithic FEM/Multigrid Solver for an ALE Formulation of Fluid-Structure Interaction with Applications in Biomechanics. In *Fluid-Structure Interaction*, pages 146–170. Springer Berlin Heidelberg, Berlin, Heidelberg, 2006. doi: 10.1007/3-540-34596-5_7. URL http://link.springer.com/10.1007/3-540-34596-5{_}7.

[46] B. Cassin and M.L. Rubin. *Dictionary of Eye Terminology*. Triad Pub., 2006. ISBN 9780937404683. URL https://books.google.co.uk/books?id=3XKpPwAACAAJ.

[47] Jun Liu and Cynthia J. Roberts. Influence of corneal biomechanical properties on intraocular pressure measurement: Quantitative analysis. *Journal of Cataract and Refractive Surgery*, 31(1):146 – 155, 2005. ISSN 0886-3350. doi: https://doi.org/10.1016/j.jcrs.2004.09.031. URL http://www.sciencedirect.com/science/article/pii/S0886335004009599.

[48] Intraocular Pressure - Tonometry. URL https://retinavitreous.com/patientinfo/iop.php.

[49] Intraocular Pressure - Tonometry. URL https://retinavitreous.com/patientinfo/iop.php.

[50] Samin Hong, Je Seong Gong, and Jae Hong Young. Long-term intraocular pressure fluctuation and progressive visual field deterioration in patients with glaucoma and low intraocular pressures after a triple procedure. *Archives of Ophthalmology*, 125(8):1010–1013, 2007. ISSN 00039950. doi: 10.1001/archopht.125.8.1010.

[51] Joseph Caprioli and Anne L. Coleman. Intraocular Pressure Fluctuation. A Risk Factor for Visual Field Progression at Low Intraocular Pressures in the Advanced Glaucoma Intervention Study. *Ophthalmology*, 115(7), 2008. ISSN 01616420. doi: 10.1016/j.ophtha.2007.10.031.

[52] Christoph Kniestedt, Omar Punjabi, Shan Lin, and Robert L. Stamper. Tonometry Through the Ages. *Survey of Ophthalmology*, 53(6):568–591, nov 2008. ISSN 0039-6257. doi: 10.1016/J.SURVOPHTHAL.2008.08.024. URL https://www.sciencedirect.com/science/article/pii/S0039625708001495?via{%}3Dihub.

[53] Robert Stamper. A History of Intraocular Pressure and Its Measurement. *American Academy of Optometry*, 88(1):1–14, 2011.

[54] Elliot M., Ahmed Elsheikh, and Pinakin Gunvant. Tonometry – Past, Present and Future. *Glaucoma - Current Clinical and Research Aspects*, (May), 2011. doi: 10.5772/37393. URL http://www.intechopen.com/books/glaucoma-current-clinical-and-research-aspects/tonometry-past-present-and-future.

[55] Roberto Sampaolesi, Juan Roberto Sampaolesi, and Jorge Zárate. Applanation Tonometry. In *The Glaucomas*, pages 123–147. Springer Berlin Heidelberg, Berlin, Heidelberg, 2014. doi: 10.1007/978-3-642-35500-4_10. URL http://link.springer.com/10.1007/978-3-642-35500-4{_}10.

[56] Per Hallberg. *Applanation resonance tonometry for intraocular pressure measurement*. Number August. 2006. ISBN 9172640618.

[57] M J Doughty and M L Zaman. Human corneal thickness and its impact on intraocular pressure measures: a review and meta-analysis approach. *Survey of ophthalmology*, 44 (5):367–408. ISSN 0039-6257. URL http://www.ncbi.nlm.nih.gov/pubmed/10734239.

[58] Brian A. Francis, Amy Hsieh, Mei-Ying Lai, Vikas Chopra, Fernando Pena, Stanley Azen, and Rohit Varma. Effects of Corneal Thickness, Corneal Curvature, and Intraocular Pressure Level on Goldmann Applanation Tonometry and Dynamic Contour Tonometry. *Ophthalmology*, 114(1):20–26, jan 2007. ISSN 0161-6420. doi: 10.1016/J.OPHTHA.2006.06.047. URL https://www.sciencedirect.com/science/article/pii/S0161642006010086.

[59] FangJun Bao, ZiXu Huang, JinHai Huang, JunJie Wang, ManLi Deng, LinNa Li, AYong Yu, QinMei Wang, and Ahmed Elsheikh. Clinical Evaluation of Methods to Correct Intraocular Pressure Measurements by the Goldmann Applanation Tonometer, Ocular Response Analyzer, and Corvis ST Tonometer for the Effects of Corneal Stiffness Parameters. *Journal of Glaucoma*, 25(6):510–519, jun 2016. ISSN 1057-0829. doi: 10.1097/IJG.0000000000000359. URL http://content.wkhealth.com/linkback/openurl?sid=WKPTLP:landingpage{&}an=00061198-201606000-00010.

[60] Yasuaki Ito, Kotaro Ishii, Zhigang Sun, Tomoaki Ando, and Tetsuro Oshika. Numerical simulation of the goldmann applanation tonometer. *Folia Japonica de Ophthalmologica Clinica*, 5(8):744–748, 2012. ISSN 18825176.

[61] Nikhil S. Choudhari, Ronnie George, Mani Baskaran, Lingam Vijaya, and Namrata Dudeja. Measurement of Goldmann Applanation Tonometer Calibration Error. *Ophthalmology*, 116(1):3–8, 2009. ISSN 01616420. doi: 10.1016/j.ophtha.2008.06.020.

[62] Ahmed Elsheikh, Daad Alhasso, Pinakin Gunvant, and David Garway-Heath. Multiparameter correction equation for Goldmann applanation tonometry. *Optometry and Vision Science*, 88(1), 2011. ISSN 10405488. doi: 10.1097/OPX.0b013e3181fc3453.

[63] W Wiegand, B Schroeder, and A Hager. [Theoretical basis of goldmann applanation tonometry]. *Klinische Monatsblatter fur Augenheilkunde*, 222(7):552–7, 2005. ISSN 0023-2165. doi: 10.1055/s-2005-858112. URL http://www.pubmedcentral.nih.gov/articlerender.fcgi?artid=3032230{&}tool=pmcentrez{&}rendertype=abstract{%}0Ahttp://www.ncbi.nlm.nih.gov/pubmed/16034722.

[64] Akram Abdelazim Joda, Mir Mohi Sefat Shervin, Daniel Kook, and Ahmed Elsheikh. Development and validation of a correction equation for Corvis tonometry. *Computer Methods in Biomechanics and Biomedical Engineering*, 19(9):943–953, 2015. ISSN 14768259. doi: 10.1080/10255842.2015.1077515.

[65] Ahmed Elsheikh. Finite Element Modeling of Corneal Biomechanical Behavior. *Journal of Refractive Surgery*, 26(4):289–300, 2010. ISSN 1081-597X. doi: 10.3928/1081597X-20090710-01. URL http://www.healio.com/doiresolver?doi=10.3928/1081597X-20090710-01.

[66] Akram Abdelazim Joda, Mir Mohi Sefat Shervin, Daniel Kook, and Ahmed Elsheikh. Development and validation of a correction equation for corvis tonometry. *Computer Methods in Biomechanics and Biomedical Engineering*, 19(9):943–953, 2016. doi: 10.1080/10255842.2015.1077515. URL https://doi.org/10.1080/10255842.2015.1077515. PMID: 27049961.

[67] Eberhard Spoerl, Naim Terai, Freia Scholz, Frederik Raiskup, and Lutz E. Pillunat. Detection of Biomechanical Changes After Corneal Cross-Linking Using Ocular Response Analyzer Software. *Journal of Refractive Surgery*, 27(6):452–457, jun 2011. ISSN 1081-597X. doi: 10.3928/1081597X-20110106-01. URL http://www.slackinc.com/doi/resolver.asp?doi=10.3928/1081597X-20110106-01.

[68] OCULUS. OCULUS Corvis® ST - Tonometer - Highlights - OCULUS Optikgeräte GmbH. URL https://www.oculus.de/en/products/tonometer/corvis-st/highlights/.

[69] Chuanqing Zhou Zhaolong, Han, Dai, Zhou. Air Puff Induced Corneal Vibrations : Theoretical. (August 2015), 2014. doi: 10.3928/1081597X-20140212-02.

[70] Anna Pandolfic Irene Simoninia, Maurizio Angelillob. Theoretical and numerical analysis of the corneal air pu ff test.

[71] Makoto Kaneko, Kanichi Tokuda, and Tomohiro Kawahara. Dynamic sensing of human eye. *IEEE International Conference on Robotics and Automation*, (April): 2871–2876, 2005. ISSN 10504729. doi: 10.1109/ROBOT.2005.1570549.

[72] Miguel Á. Ariza-Gracia, Jesús F. Zurita, David P. Piñero, José F. Rodriguez-Matas, and Begoña Calvo. Coupled Biomechanical Response of the Cornea Assessed by Non-Contact Tonometry. A Simulation Study. *Plos One*, 10(3):e0121486, 2015. ISSN 1932-6203. doi: 10.1371/journal.pone.0121486. URL http://dx.plos.org/10.1371/journal.pone.0121486.

[73] S Muench, · M Roellig, · E Spoerl, and · D Balzani. Numerical and Experimental Study of the Spatial Stress Distribution on the Cornea Surface During a Non-Contact Tonometry Examination. 2018. doi: 10.1007/s11340-018-00449-0. URL https://doi.org/10.1007/s11340-018-00449-0.

[74] Abhijit Sinha Roy, Mathew Kurian, Himanshu Matalia, and Rohit Shetty. Air-puff associated quantification of non-linear biomechanical properties of the Human cornea in vivo. *Journal of the Mechanical Behavior of Biomedical Materials*, (APRIL), 2015. ISSN 17516161. doi: 10.1016/j.jmbbm.2015.04.010. URL http://linkinghub.elsevier.com/retrieve/pii/S1751616115001307.

[75] Vizzeri Edward P, Furlani, Gianmarco. Multiscale Biomechanical Modeling of the Multiscale Biomechanical Modeling of the Human Eye. (September), 2015.

[76] Sudip Nouran Bahr, Agrawal, Adam Wittek, Grand Joldes, Stuart Bunt, and Karol Miller. Mechanical Properties of Brain – Skull Interface in Compression. *Computational Biomechanics forMedicine*, pages 83–91, 2015. doi: 10.1007/978-3-319-15503-6.

[77] Miguel Ángel Ariza-Gracia, Wei Wu, Begoña Calvo, Mauro Malvè, Philippe Büchler, and José F. Rodriguez Matas. Fluid–structure simulation of a general non-contact tonometry. A required complexity? *Computer Methods in Applied Mechanics and Engineering*, 340:202–215, oct 2018. ISSN 0045-7825. doi: 10.1016/J.CMA.2018.05.031. URL https://www.sciencedirect.com/science/article/pii/S0045782518302755{#}sec2.

[78] B. Audrey Nguyen, Cynthia J. Roberts, and Matthew A. Reilly. Biomechanical Impact of the Sclera on Corneal Deformation Response to an Air-Puff: A Finite-Element Study. *Frontiers in Bioengineering and Biotechnology*, 6(January):1–8, 2019. ISSN 2296-4185. doi: 10.3389/fbioe.2018.00210. URL https://www.frontiersin.org/article/10.3389/fbioe.2018.00210/full.

[79] S. Salimi. Dynamic Response of Intraocular Pressure and Biomechanical Effects of the Eye Considering Fluid-Structure Interaction. *Journal of Biomechanical Engineering*, 133(9):091009, 2011. ISSN 0148-0731. doi: 10.1115/1.4005166. URL http://biomechanical.asmedigitalcollection.asme.org/article.aspx?doi=10.1115/1.4005166.

[80] Troels T. Andreassen, Anders Hjorth Simonsen, and Hans Oxlund. Biomechanical properties of keratoconus and normal corneas. *Experimental Eye Research*, 31(4):435–441, 1980. ISSN 00144835. doi: 10.1016/S0014-4835(80)80027-3.

[81] Cynthia J. Roberts and William J. Dupps. Biomechanics of corneal ectasia and biomechanical treatments, 2014. ISSN 18734502.

[82] J A. SCOTT. The Eye in Contact Lens Wear. *British Journal of Ophthalmology*, 83(12):1409g–1409g, 2008. ISSN 0007-1161. doi: 10.1136/bjo.83.12.1409g.

[83] John F. Stamler. The complications of contact lens wear, 1998. ISSN 10408738.

[84] Gary N. Foulks. Prolonging contact lens wear and making contact lens wear safer. *American Journal of Ophthalmology*, 141(2), 2006. ISSN 00029394. doi: 10.1016/j.ajo.2005.08.047.

[85] Robert Scott. The injured eye. In *Philosophical Transactions of the Royal Society B: Biological Sciences*, volume 366, pages 251–260, 2011. doi: 10.1098/rstb.2010.0234.

[86] Gustavo Corrales and Anthony Curreri. Eye Trauma in Boxing, 2009. ISSN 02785919.

[87] A. C. Mehta and N. B. Mehta. Eye Trauma. *Cleveland Clinic Journal of Medicine*, 59(5):554–554, 2013. ISSN 0891-1150. doi: 10.3949/ccjm.59.5.554-a.

[88] William J. Dupps and Steven E. Wilson. Biomechanics and wound healing in the cornea, 2006. ISSN 00144835.

[89] Jesper Hjortdal. Extensibility of the normo-hydrated human cornea. *Acta Ophthalmologica Scandinavica*, 73(1):12–17, 1995. ISSN 16000420. doi: 10.1111/j.1600-0420.1995.tb00005.x.

[90] Bill Jue and David M. Maurice. The mechanical properties of the rabbit and human cornea. *Journal of Biomechanics*, 19(10):847–853, 1986. ISSN 00219290. doi: 10.1016/0021-9290(86)90135-1.

[91] M R Bryant and P J McDonnell. Constitutive laws for biomechanical modeling of refractive surgery. *Journal of biomechanical engineering*, 118(4):473–81, 1996. ISSN 0148-0731. URL http://www.ncbi.nlm.nih.gov/pubmed/8950650.

[92] S. L.Y. Woo, A. S. Kobayashi, W. A. Schlegel, and C. Lawrence. Nonlinear material properties of intact cornea and sclera. *Experimental Eye Research*, 14(1):29–39, 1972. ISSN 00144835. doi: 10.1016/0014-4835(72)90139-X.

[93] J. L. Battaglioli and R. D. Kamm. Measurements of the compressive properties of scleral tissue. *Investigative Ophthalmology and Visual Science*, 25(1):59–65, 1984. ISSN 01460404.

[94] R P Vito and P H Carnell. Finite element based mechanical models of the cornea for pressure and indenter loading. *Refractive & corneal surgery*, 8(2):146–151, 1992. ISSN 1042-962X. URL http://www.ncbi.nlm.nih.gov/pubmed/1591210.

[95] S A Velinsky and M R Bryant. On the computer-aided and optimal design of keratorefractive surgery. *Refract Corneal Surg*, 8(2):173–182, 1992. URL http://www.ncbi.nlm.nih.gov/entrez/query.fcgi?cmd=Retrieve{&}db=PubMed{&}dopt=Citation{&}list{_}uids=1591213.

[96] W. Matthew Petroll, Partha Roy, Charles J. Chuong, Brian Hall, H. Dwight Cavanagh, and James V. Jester. Measurement of Surgically Induced Corneal Deformations Using Three-Dimensional Confocal Microscopy. *Cornea*, 15(2):154–164, 1996. ISSN 02773740. doi: 10.1097/00003226-199603000-00008.

[97] K D Hanna, F E Jouve, G O Waring, and P G Ciarlet. Computer simulation of arcuate keratotomy for astigmatism. *Refractive & corneal surgery*, 8(2):152–63, 1992. ISSN 1042-962X. URL http://www.ncbi.nlm.nih.gov/pubmed/1591211.

[98] W. O. Wray, E. D. Best, and L. Y. Cheng. A Mechanical Model for Radial Keratotomy: Toward a Predictive Capability. *Journal of Biomechanical Engineering*, 116(1):56, 2008. ISSN 01480731. doi: 10.1115/1.2895705.

[99] R. W. Ogden. Large Deformation Isotropic Elasticity - On the Correlation of Theory and Experiment for Incompressible Rubberlike Solids. *Proceedings of the Royal Society A: Mathematical, Physical and Engineering Sciences*, 326(1567):565–584, feb 1972. ISSN 1364-5021. doi: 10.1098/rspa.1972.0026. URL http://rspa.royalsocietypublishing.org/cgi/doi/10.1098/rspa.1972.0026.

[100] Hibbit, Karlsson, and Sorensen. *ABAQUS/CFD Analysis User's Manual*. Hibbit, Karlsson, Sorensen Inc., USA, 2007.

[101] Ahmed Elsheikh, Charles Whitford, Rosti Hamarashid, Wael Kassem, Akram Joda, and Philippe Büchler. Stress free configuration of the human eye. *Medical Engineering and Physics*, 2013. ISSN 13504533. doi: 10.1016/j.medengphy.2012.09.006.

[102] R. W. Ogden. *Non-linear elastic deformations*. Dover Publications, 1997. ISBN 9780486696485.

[103] R.C. Hibbeler. *Mechanics of Materials*, volume 152. 2008. ISBN 139789810679941. URL http://www.ncbi.nlm.nih.gov/pubmed/21513376.

[104] Sabine Kling and Susana Marcos. Contributing Factors to Corneal Deformation in Air Puff Measurements. *Investigative Opthalmology & Visual Science*, 54(7):5078, jul 2013. ISSN 1552-5783. doi: 10.1167/iovs.13-12509. URL http://www.ncbi.nlm.nih.gov/pubmed/23821200http://iovs.arvojournals.org/article.aspx?doi=10.1167/iovs.13-12509.

[105] Tukezban Huseynova, George O. Waring, Cynthia Roberts, Ronald R. Krueger, and Minoru Tomita. Corneal Biomechanics as a Function of Intraocular Pressure and Pachymetry by Dynamic Infrared Signal and Scheimpflug Imaging Analysis in Normal Eyes. *American Journal of Ophthalmology*, 157(4):885–893, apr 2014. ISSN 0002-9394. doi: 10.1016/J.AJO.2013.12.024. URL https://www.sciencedirect.com/science/article/pii/S0002939413008143.

[106] FangJun Bao, ManLi Deng, QinMei Wang, JinHai Huang, Jing Yang, Charles Whitford, Brendan Geraghty, AYong Yu, and Ahmed Elsheikh. Evaluation of the relationship of corneal biomechanical metrics with physical intraocular pressure and central corneal thickness in ex vivo rabbit eye globes. *Experimental Eye Research*, 137:11–17, aug 2015. ISSN 00144835. doi: 10.1016/j.exer.2015.05.018. URL http://www.ncbi.nlm.nih.gov/pubmed/26026878https://linkinghub.elsevier.com/retrieve/pii/S0014483515001712.

[107] Riccardo Vinciguerra, Ahmed Elsheikh, Cynthia J. Roberts, Renato Ambrósio, David Sung Yong Kang, Bernardo T. Lopes, Emanuela Morenghi, Claudio Azzolini, and Paolo Vinciguerra. Influence of Pachymetry and Intraocular Pressure on Dynamic Corneal Response Parameters in Healthy Patients. *Journal of Refractive Surgery*, 32(8):550–561, aug 2016. ISSN 1081-597X. doi: 10.3928/1081597X-20160524-01. URL http://www.ncbi.nlm.nih.gov/pubmed/27505316http://www.healio.com/doiresolver?doi=10.3928/1081597X-20160524-01.

[108] Jack P Holman and John Lloyd. Fluid Mechanics | |.

[109] L. J. Clancy. *Aerodynamics*. Wiley, 1975. ISBN 0470158379. URL https://books.google.co.uk/books/about/Aerodynamics.html?id=zaNTAAAAMAAJ{&}redir{_}esc=y.

[110] D. J. Kettle. The Design of Static and Pitot Static Tubes Jor Subsonic Speeds. *Journal of the Royal Aeronautical Society*, 58(528):835–837, dec 1954. ISSN 0368-3931. doi: 10.1017/S0368393100102159. URL https://www.cambridge.org/core/product/identifier/S0368393100102159/type/journal{_}article.

[111] B Hodkinson and M I E Mech. The Impact Tube. Technical report. URL https://journals.sagepub.com/doi/pdf/10.1243/PIME{_}PROC{_}1944{_}151{_}038{_}02.

[112] G. K. (George Keith) Batchelor. *An introduction to fluid dynamics*. Cambridge University Press, 1999. ISBN 0521663962. URL https://books.google.co.uk/books?id=Rla7OihRvUgC{&}pg=PA156{&}redir{_}esc=y{#}v=onepage{&}q{&}f=false.

[113] John W. Mitchell, Philip J. Pritchard, Alan T. McDonald, Robert W. Fox, and John W. Mitchell. *Fox and McDonald's introduction to fluid mechanics*. ISBN 9781118912652. URL https://www.wiley.com/en-us/Fox+and+McDonald{%}27s+Introduction+to+Fluid+Mechanics{%}2C+9th+Edition-p-9781118912652.

[114] Abaqus. ABAQUS/Standard analysis user's manual v14.2. *SIMULIA*, 2014. ISSN 2041-1723. doi: 10.1038/s41467-017-02648-0.

[115] Olivier De Langre, Emmanuel; Amandolese, Xavier; Doaré. Fundamentals of Fluid-Solid Interactions. URL https://www.coursera.org/learn/fluid-solid-interaction/home/welcome.

[116] A Aksenov, A Dyadkin, T Luniewski, and V Pokhilko. Fluid Structure Interaction Analysis Using ABAQUS and FlowVision. Technical report. URL http://www.scai.fraunhofer.de.

[117] David Shirokoff and Rodolfo Ruben Rosales. An efficient method for the incompressible Navier-Stokes equations on irregular domains with no-slip boundary conditions, high order up to the boundary. 2010. doi: 10.1016/j.jcp.2011.08.011. URL http://arxiv.org/abs/1011.3589{%}0Ahttp://dx.doi.org/10.1016/j.jcp.2011.08.011.

[118] H.K: Versteeg and W. Malalasekera. An Introduction to Computational Fluid Dynamics - The Finite Volume Method, 1995. ISSN 02104806.

[119] NASA. Turbulence Modeling Resource: The Spalart-allmaras Turbulence. *Recherche*, 45(10):1–8, 2011.

[120] H. Reichardt. Vollständige darstellung der turbulenten geschwindigkeitsverteilung in glatten leitungen. *ZAMM - Journal of Applied Mathematics and Mechanics / Zeitschrift für Angewandte Mathematik und Mechanik*, 31(7):208–219, 1951. ISSN 1521-4001. doi: 10.1002/zamm.19510310704. URL http://dx.doi.org/10.1002/zamm.19510310704.

[121] Bert Blocken, Ted Stathopoulos, and Jan Carmeliet. CFD simulation of the atmospheric boundary layer: wall function problems. *Atmospheric Environment*, 41(2):238–252, jan 2007. ISSN 1352-2310. doi: 10.1016/J.ATMOSENV.2006.08.019. URL https://www.sciencedirect.com/science/article/pii/S135223100600834X.

[122] G. K. Morris, S. V. Garimella, and R. S. Amano. Prediction of Jet Impingement Heat Transfer Using a Hybrid Wall Treatment With Different Turbulent Prandtl Number Functions. *Journal of Heat Transfer*, 118(3):562, aug 1996. ISSN 00221481. doi: 10.1115/1.2822668. URL http://heattransfer.asmedigitalcollection.asme.org/article.aspx?articleid=1442470.

[123] Th Alrutz and T Knopp. Near-wall grid adaptation for wall-functions. Technical report. URL http://num.math.uni-goettingen.de/bail/documents/proceedings/alrutz.pdf.

[124] M A Christon. Hybrid Wall Treatment for RANS in Complex Geometry Turbulent Flows $. Technical report. URL http://c-sciences.com/images/publications/2017/christon{_}wall{_}treatment.pdf.

[125] Robert H. Nichols and C. C. Nelson. Wall Function Boundary Conditions Including Heat Transfer and Compressibility. *AIAA Journal*, 42(6):1107–1114, jun 2004. ISSN 0001-1452. doi: 10.2514/1.3539. URL http://arc.aiaa.org/doi/10.2514/1.3539.

[126] Zhi-Feng Yao, Zheng-Jun Yang, and Fu-Jun Wang. Evaluation of near-wall solution approaches for large-eddy simulations of flow in a centrifugal pump impeller. *Engineering Applications of Computational Fluid Mechanics*, 10(1):452–465, jan 2016. ISSN 1994-2060. doi: 10.1080/19942060.2016.1189362. URL https://www.tandfonline.com/doi/full/10.1080/19942060.2016.1189362.

[127] Klaus-Jurgen. Bathe and Klaus-Jurgen. Bathe. *Finite element procedures*. [publisher not identified], 2006. ISBN 097900490X. URL https://books.google.co.uk/books/about/Finite{_}Element{_}Procedures.html?id=rWvefGICfO8C{&}redir{_}esc=y.

[128] G P Nikishkov. Introductio to the finite element method. 2004.

[129] Ahmed Elsheikh, Defu Wang, Paolo Rama, Marino Campanelli, and David Garway-Heath. Experimental Assessment of Human Corneal Hysteresis. *Current Eye Research*, 33(3):205–213, jan 2008. ISSN 0271-3683. doi: 10.1080/02713680701882519. URL http://www.tandfonline.com/doi/full/10.1080/02713680701882519.

[130] Andrew E Anderson, Benjamin J Ellis, and Jeffrey A Weiss. Verification, validation and sensitivity studies in computational biomechanics. *Computer methods in biomechanics and biomedical engineering*, 10(3):171–84, jun 2007. ISSN 1025-5842. doi: 10.1080/10255840601160484. URL http://www.ncbi.nlm.nih.gov/pubmed/17558646http://www.pubmedcentral.nih.gov/articlerender.fcgi?artid=PMC3361760.

[131] *Guide: Guide for the Verification and Validation of Computational Fluid Dynamics Simulations (AIAA G-077-1998(2002))*. American Institute of Aeronautics and Astronautics, Inc., Washington, DC, jan 1998. ISBN 978-1-56347-285-5. doi: 10.2514/4.472855. URL http://arc.aiaa.org/doi/book/10.2514/4.472855.

[132] L E Schwer. Verification and validation in computational solid mechanics and the ASME Standards Committee. Technical report, 2005. URL www.witpress.com,.

[133] E D Elasd. Side by side comparison chart of 72 mechanical Finite Element Analysis (FEA) programs . We welcome suggestions and additional information . Click any row for more details . Expand all Meaning of headings Sort by features Sort by price. pages 1–5, 2017.

[134] Charles Whitford, Akram Joda, Steve Jones, Fangjun Bao, Paolo Rama, and Ahmed Elsheikh. Ex vivo testing of intact eye globes under inflation conditions to determine regional variation of mechanical stiffness. *Eye and vision (London,*

England), 3:21, 2016. ISSN 2326-0254. doi: 10.1186/s40662-016-0052-8. URL http://www.ncbi.nlm.nih.gov/pubmed/27512719{%}0Ahttp://www.pubmedcentral.nih.gov/articlerender.fcgi?artid=PMC4979203.

[135] Oculus Optikgerate Gmbh. Pentacam measurement principle, 2019. URL https://www.pentacam.com/int/technology/measurement-principle-licences-network.html.

[136] Anna Pandolfi and Gerhard A. Holzapfel. Three-Dimensional Modeling and Computational Analysis of the Human Cornea Considering Distributed Collagen Fibril Orientations. *Journal of Biomechanical Engineering*, 130(6):061006, dec 2008. ISSN 01480731. doi: 10.1115/1.2982251. URL http://biomechanical.asmedigitalcollection.asme.org/article.aspx?articleid=1475577.

[137] Gordon J. (Gordon John) Van Wylen and Richard Edwin. Sonntag. *Fundamentals of classical thermodynamics*. Wiley, 1985. ISBN 0471800147.

[138] E. E. Shpilrain. AIR (PROPERTIES OF). *A-to-Z Guide to Thermodynamics, Heat and Mass Transfer, and Fluids Engineering*, a, 2006. ISSN 1113-1114. doi: 10.1615/atoz.a.airprop.

[139] P. J. Rigden. Viscosity of air [15], 1938. ISSN 00280836.

[140] The Engineering Toolbox. Dry Air Properties, 2014. URL www.engineeringtoolbox.com/dry-air-properties-d{_}973.html.

[141] ANSYS. ANSYS Fluent Theory Guide v16. *ANSYS 16.2 Documentation*, 15317 (July):80, 2015. ISSN 03067734. doi: 10.7860/JCDR/2017/28593.10594.

[142] M. Kcharik, R. Liska, P. Váchal, and M. Shashkov. Arbitrary Lagrangian-Eulerian (ALE) Method in compressible fluid dynamics. *Applied Mathematical Sciences*, pages 1–6, 2007.

[143] Jean Donea, Antonio Huerta, Jean-Philippe Ponthot, and Antonio Rodríguez-Ferran. Arbitrary Lagrangian-Eulerian Methods. In *Encyclopedia of Computational Mechanics Second Edition*, pages 1–23. 2017. ISBN 0470846992. doi: 10.1002/9781119176817.ecm2009.

[144] Yong Zhao and Xiaohui Su. Arbitrary Lagrangian–Eulerian (ALE) Method and Fluid-Structure Interaction. In *Computational Fluid-Structure Interaction*, pages 127–144. 2018. doi: 10.1016/b978-0-12-814770-2.00009-x.

[145] M. Souli, K. Mahmadi, and N. Aquelet. ALE and Fluid Structure Interaction. *Materials Science Forum*, 465-466:143–150, 2009. doi: 10.4028/www.scientific.net/msf.465-466.143.

[146] Pierre Henri Maire, Jérôme Breil, and Stéphane Galera. A cell-centred arbitrary Lagrangian-Eulerian (ALE) method. In *International Journal for Numerical Methods in Fluids*, volume 56, pages 1161–1166, 2008. doi: 10.1002/fld.1557.

[147] Josep Sarrate, Antonio Huerta, and Jean Donea. Arbitrary lagrangian-eulerian formulation for fluid-rigid body interaction. *Computer Methods in Applied Mechanics and Engineering*, 190(24-25):3171–3188, 2001. ISSN 00457825. doi: 10.1016/S0045-7825(00)00387-X.

[148] M. Souli and J. P. Zolesio. Arbitrary Lagrangian-Eulerian and free surface methods in fluid mechanics. *Computer Methods in Applied Mechanics and Engineering*, 191 (3-5):451–466, 2001. ISSN 00457825. doi: 10.1016/S0045-7825(01)00313-9.

[149] C T Kelley. Iterative Methods for Linear and Nonlinear Equations. *Society*, 16 (11):pp. 166, 1995. ISSN 0-89871-352-8. doi: 10.1137/1.9781611970944. URL http://link.aip.org/link/doi/10.1137/1.9781611970944.

[150] J. Drkošová, A. Greenbaum, M. Rozložník, and Z. Strakoš. Numerical stability of GMRES. *BIT Numerical Mathematics*, 35(3):309–330, 1995. ISSN 00063835. doi: 10.1007/BF01732607.

[151] Alberto Pueyo and David W. Zingg. Efficient Newton-Krylov Solver for Aerodynamic Computations. *AIAA Journal*, 1998. ISSN 0001-1452. doi: 10.2514/2.326.

[152] G. W. Su, J. T. Geller, J. R. Hunt, and K. Pruess. _A review of algebraic multigrid.pdf. *Vadose Zone J*, 3(2):592–601, 2004. doi: 10.2113/3.2.592. URL http://vzj.scijournals.org/cgi/content/abstract/3/2/592.

[153] David R. Kincaid, John R. Respess, David M. Young, and Rober R. Grimes. Algorithm 586: ITPACK 2C: A FORTRAN Package for Solving Large Sparse Linear Systems by Adaptive Accelerated Iterative Methods. *ACM Trans. Math. Softw.*, 8(3):302–322, 1982. ISSN 1557-7295. doi: 10.1145/356004.356009. URL http://portal.acm.org/citation.cfm?id=356009.

[154] J. Crank and P. Nicolson. A practical method for numerical evaluation of solutions of partial differential equations of the heat-conduction type. *Mathematical Proceedings of the Cambridge Philosophical Society*, 43(1):50–67, 1947. ISSN 14698064. doi: 10.1017/S0305004100023197.

[155] R. Courant, H. Lewy, and K. Friedrichs. Über die partiellen Differenzengleichungen der mathematischen Physik. *Mathematische Annalen*, 100:32–74, 1928. URL https://www.digizeitschriften.de/dms/img/?PID=GDZPPN002272636.

[156] Carlos A. de Moura and Carlos S. Kubrusly, editors. *The Courant–Friedrichs–Lewy (CFL) Condition*. Birkhäuser Boston, Boston, 2013. ISBN 978-0-8176-8393-1. doi: 10.1007/978-0-8176-8394-8. URL http://link.springer.com/10.1007/978-0-8176-8394-8.

[157] Culbert B. Laney. *Computational Gasdynamics*. Cambridge University Press, Cambridge, 1998. ISBN 9780511605604. doi: 10.1017/CBO9780511605604. URL http://ebooks.cambridge.org/ref/id/CBO9780511605604.

[158] Mark J. Tummers, Jeroen Jacobse, and Sebastiaan G J Voorbrood. Turbulent flow in the near field of a round impinging jet. *International Journal of Heat and Mass Transfer*, 54(23-24):4939–4948, 2011. ISSN 00179310. doi: 10.1016/j.ijheatmasstransfer.2011.07.007. URL http://dx.doi.org/10.1016/j.ijheatmasstransfer.2011.07.007.

[159] Ovette F Villavicencio, Fatimah Gilani, Maria A Henriquez, Luis Izquierdo, and Renato R Ambrósio. Independent Population Validation of the belin / Ambrósio Enhanced Ectasia display : Implications for Keratoconus studies and screening. URL https://www.semanticscholar.org/paper/

Independent-Population-Validation-of-the-belin-{%}2F-{%}3A-Villavicencio-Gilani/551073bb6526cce55ad8bfb2fd40367edc218df2.

[160] Magdalena Jędzierowska and Robert Koprowski. Novel dynamic corneal response parameters in a practice use: a critical review. *BioMedical Engineering OnLine*, 18(1):17, dec 2019. ISSN 1475-925X. doi: 10.1186/s12938-019-0636-3. URL https://biomedical-engineering-online.biomedcentral.com/articles/10.1186/s12938-019-0636-3.

[161] Cynthia J. Roberts and Jun Liu. *Corneal biomechanics : from theory to practice*. ISBN 9789062998760.

[162] Markus Kohlhaas, Eberhard Spoerl, Andreas G Boehm, and Katharina Pollack. A correction formula for the real intraocular pressure after LASIK for the correction of myopic astigmatism. *Journal of refractive surgery (Thorofare, N.J. : 1995)*, 22 (3):263–7, mar 2006. ISSN 1081-597X. URL http://www.ncbi.nlm.nih.gov/pubmed/16602315.

[163] Yoshitaka Nakao, Yoshiaki Kiuchi, and Satoshi Okimoto. A Comparison of the Corrected Intraocular Pressure Obtained by the Corvis ST and Reichert 7CR Tonometers in Glaucoma Patients. 2017. doi: 10.1371/journal.pone.0170206. URL https://journals.plos.org/plosone/article/file?id=10.1371/journal.pone.0170206{&}type=printable.

[164] Jun Liu and Cynthia J. Roberts. Influence of corneal biomechanical properties on intraocular pressure measurement: Quantitative analysis. *Journal of Cataract and Refractive Surgery*, 31(1):146–155, 2005. ISSN 08863350. doi: 10.1016/j.jcrs.2004.09.031.

[165] Ahmed Elsheikh, Daad Alhasso, Aachal Kotecha, and David Garway-Heath. Assessment of the Ocular Response Analyzer as a Tool for Intraocular Pressure Measurement. *Journal of Biomechanical Engineering*, 131(8):081010, jul 2009. ISSN 0148-0731. doi: 10.1115/1.3148462. URL http://biomechanical.asmedigitalcollection.asme.org/article.aspx?doi=10.1115/1.3148462.

[166] Ahmed Elsheikh, Defu Wang, and David Pye. Determination of the modulus of elasticity of the human cornea. *Journal of refractive surgery (Thorofare, N.J. : 1995)*, 23(8):808–18, oct 2007. ISSN 1081-597X. URL http://www.ncbi.nlm.nih.gov/pubmed/17985801.

[167] A. Eliasy, K.-J. Chen, R. Vinciguerra, O. Maklad, P. Vinciguerra, R. Ambrósio, C.J. Roberts, and A. Elsheikh. Ex-vivo experimental validation of biomechanically-corrected intraocular pressure measurements on human eyes using the CorVis ST. *Experimental Eye Research*, 175, 2018. ISSN 10960007. doi: 10.1016/j.exer.2018.06.013.

[168] M. Fairweather and G. Hargrave. Experimental investigation of an axisymmetric, impinging turbulent jet. 2. Scalar field. *Experiments in Fluids*, 33(4):539–544, 2002. ISSN 07234864. doi: 10.1007/s00348-002-0480-1.

[169] Osama Maklad, Ashkan Eliasy, Kai-jung Chen, Vassilios Theofilis, and Ahmed Elsheikh. Influence of Fluid Structure Interaction (FSI) on Prediction of Corneal Biomechanics under the Effect of Air Puff Tonometry. *Journal of The Royal Society Interface*, Manuscript(0).

[170] O. Maklad, V. Theofilis, and A. Elsheikh. Fluid Structure Interaction (FSI) Simulation of the human eye under the air puff tonometry using Computational Fluid Dynamics (CFD). In *ICCFD10*, number ICCFD10-017, Barcelona, 2018. URL http://www.iccfd.org/iccfd10/proceedings.html.

[171] Osama Maklad, Vassilis Theofilis, and Ahmed Elsheikh. Role of impinging jets in the biomechanical correction of the intraocular pressure (IOP) measurement. *ICFD13*, (December):ICFD13–EG–6095, 2018. URL http://icfd-egypt.com/index.html.

[172] Cynthia J. Roberts, Ashraf M. Mahmoud, Jeffrey P. Bons, Arif Hossain, Ahmed Elsheikh, Riccardo Vinciguerra, Paolo Vinciguerra, and Renato Ambrósio. Introduction of Two Novel Stiffness Parameters and Interpretation of Air Puff–Induced Biomechanical Deformation Parameters With a Dynamic Scheimpflug Analyzer. *Journal of Refractive Surgery*, 33(4):266–273, apr 2017. ISSN 1081-597X. doi: 10.3928/1081597X-20161221-03. URL http://www.healio.com/doiresolver?doi=10.3928/1081597X-20161221-03.

[173] T. H. Kwon, J. Ghaboussi, D. A. Pecknold, and Y. M.A. Hashash. Effect of cornea material stiffness on measured intraocular pressure. *Journal of Biomechanics*, 41(8):1707–1713, 2008. ISSN 00219290. doi: 10.1016/j.jbiomech.2008.03.004.

[174] M. J. Moseley, N. M. Evans, A. R. Fielder, and R. A. Hitchings. Comparison of a new non-contact tonometer with Goldmann applanation. *Eye (Basingstoke)*, 3(3):332–337, 1989. ISSN 14765454. doi: 10.1038/eye.1989.48.

[175] Anna Pandolfi, Giorgio Fotia, and Federico Manganiello. Finite element simulations of laser refractive corneal surgery. In *Engineering with Computers*, volume 25, pages 15–24, 2009. doi: 10.1007/s00366-008-0102-5.

[176] Amit Gefen, Ran Shalom, David Elad, and Yossi Mandel. Biomechanical analysis of the keratoconic cornea. *Journal of the Mechanical Behavior of Biomedical Materials*, 2(3):224–236, 2009. ISSN 17516161. doi: 10.1016/j.jmbbm.2008.07.002.

[177] Mark Ahearne, Ying Yang, Kong Y Then, and Kuo-Kang Liu. An indentation technique to characterize the mechanical and viscoelastic properties of human and porcine corneas. *Annals of biomedical engineering*, 35(9):1608–16, 2007. ISSN 0090-6964. doi: 10.1007/s10439-007-9323-9. URL http://www.ncbi.nlm.nih.gov/pubmed/17479366.

[178] Ahmed Elsheikh and Defu Wang. Numerical modelling of corneal biomechanical behaviour. *Computer methods in biomechanics and biomedical engineering*, 10(2):85–95, apr 2007. ISSN 1025-5842. doi: 10.1080/10255840600976013. URL http://www.ncbi.nlm.nih.gov/pubmed/18651274.

[179] Renato Ambrósio, Bernardo T. Lopes, Fernando Faria-Correia, Marcella Q. Salomão, Jens Bühren, Cynthia J. Roberts, Ahmed Elsheikh, Riccardo Vinciguerra, and Paolo Vinciguerra. Integration of Scheimpflug-Based Corneal Tomography and Biomechanical Assessments for Enhancing Ectasia Detection. *Journal of Refractive Surgery*, 33(7):434–443, 2017. ISSN 1081-597X. doi: 10.3928/1081597X-20170426-02. URL http://www.healio.com/doiresolver?doi=10.3928/1081597X-20170426-02.

[180] Mohammad-Reza Sedaghat, Hamed Momeni-Moghaddam, Renato Ambrósio, Hamid-Reza Heidari, Nasim Maddah, Zeynab Danesh, and Fatemeh Sabzi. Diagnostic Ability of Corneal Shape and Biomechanical Parameters for Detecting Frank Keratoconus. *Cornea*, 37(8):1025–1034, aug 2018. ISSN 0277-3740. doi: 10.1097/ICO.0000000000001639. URL http://www.ncbi.nlm.nih.gov/pubmed/29847493http://insights.ovid.com/crossref?an=00003226-201808000-00014.

[181] Renato Ambrósio, Fernando Faria Correia, Bernardo Lopes, Marcella Q Salomão, Allan Luz, Daniel G Dawson, Ahmed Elsheikh, Riccardo Vinciguerra, Paolo Vinciguerra, and Cynthia J Roberts. Corneal Biomechanics in Ectatic Diseases: Refractive Surgery Implications. *The open ophthalmology journal*, 11:176–193, 2017. ISSN 1874-3641. doi: 10.2174/1874364101711010176. URL http://www.ncbi.nlm.nih.gov/pubmed/28932334{%}0Ahttp://www.pubmedcentral.nih.gov/articlerender.fcgi?artid=PMC5585467.

[182] G Pron, L Ieraci, K Kaulback, and Medical Advisory Secretariat, Health Quality Ontario. Collagen cross-linking using riboflavin and ultraviolet-a for corneal thinning disorders: an evidence-based analysis. *Ontario health technology assessment series*, 11(5):1–89, 2011. ISSN 1915-7398. URL http://www.ncbi.nlm.nih.gov/pubmed/23074417http://www.pubmedcentral.nih.gov/articlerender.fcgi?artid=PMC3377552.

[183] J Martinez-Toldos Jos, E Hoyos Jairo, and Carme Guardia. Chapter-18 Posterior Vitrectomy Complications. In *Vitrectomy*, pages 343–368. 2014. doi: 10.5005/jp/books/11949_32.

[184] Thomas A. Albini, Stephen G. Schwartz, and Janet L. Davis. Vitrectomy. In *Intraocular Inflammation*, pages 493–499. 2016. ISBN 9783540753872. doi: 10.1007/978-3-540-75387-2_39.

[185] J Martinez-Toldos Jos, E Hoyos Jairo, and Jos Martnez-Toldos. Chapter-05.9 Phacoemulsification. In *Vitrectomy*, pages 99–101. 2014. doi: 10.5005/jp/books/11949_17.

Appendix A

Codes and Input Files

A.1 Eye model input file

```
*HEADING
Model of the whole ocular vessel: one segment
Number of corneal rings = 15
Number of total rings = 50
Number of cornea/sclera layers = 2
Anterior corneal central radius = 7.8 mm
Anterior corneal shape factor = 0.82
Central corneal thickness = 0.579 mm
Peripheral corneal thickness = 0.729 mm
Limbal radius = 4.85 mm
External scleral radius = 11.5 mm
Equatorial scleral thickness = 0.556 mm
Posterior scleral thickness = 0.834 mm
Axial length = 23.5784 mm
IOP = 18 mmHg
Friction coefficient = 0.072
**
```

```
**
**============================================
**Node classifications
**============================================
**
**
*NODE,NSET=AllNodes,INPUT=Node.inp
**
**
*NSET,NSET=PoleNodes
1,2601,2602,5202,5203,7803,7804,10404,10405,13005,15607
**
*NSET,NSET=LimbalNodes, GENERATE
466,496,1
3067,3097,2
5668,5698,1
8269,8299,2
10870,10900,1
**
*NSET,NSET=XZeroNodes
**List of nodes
**
*NSET,NSET=YZeroNodes
**List of nodes
**
*NSET,NSET=CVSMeridian
2,7,16,29,46,67,92,121,154,191,232,277
326,379,436
**
*NSET,NSET=EquatorialNodes, GENERATE
1699,1740
**
```

```
*NSET, NSET=DEFORMATIONNODES
1,2,4,7,11,16,22,29,37,46,56,67
79,92,106,121,137,154,172,191,211,232,254,277
301,326,352,379,407,436,466,497,529,562,596,631
667
**
**
**============================================
**Element classifications
**============================================
**
*ELEMENT, ELSET=AllElements, TYPE=C3D15H, INPUT=Element.inp
**
**
*ELSET,ELSET=C1, GENERATE
1,196
1251,1446
*SOLIDSECTION, ELSET=C1, MATERIAL=MC1
**
*ELSET,ELSET=Limbus, GENERATE
197,256
1447,1506
*SOLIDSECTION, ELSET=Limbus, MATERIAL=MLimbus
**
*ELSET,ELSET=S1, GENERATE
257,721
1507,1971
*SOLIDSECTION, ELSET=S1, MATERIAL=MS1
**
*ELSET,ELSET=S2, GENERATE
722,1106
1972,2356
```

```
*SOLIDSECTION, ELSET=S2, MATERIAL=MS2
**
*ELSET,ELSET=S3, GENERATE
1107,1250
2357,2500
*SOLIDSECTION, ELSET=S3, MATERIAL=MS3
**
*ELSET,ELSET=InternalElements ,GENERATE
1251,2500
**
**
*ELSET, ELSET=Layer1, GENERATE
1,196
**
*ELSET, ELSET=Layer2, GENERATE
1251,1446
**
*ELSET, ELSET=E_Cornea_Sclera
**List of elements
**
**
**============================================
**Surface classifications
**============================================
**
*SURFACE, type=ELEMENT, name=InternalSurface
InternalElements, S1
**
**
*SURFACE, type=ELEMENT, name=Surface1
Layer1, S1
**
```

```
*SURFACE, type=ELEMENT, name=Surface2
Layer2, S2
**
*SURFACE, TYPE=ELEMENT, NAME=Cornea_sclera
E_Cornea_Sclera, S2
**
**
**============================================
**Contact & Interaction
**============================================
**
*CONTACT PAIR,INTERACTION=Pair1, TYPE=SURFACE TO SURFACE
Surface1, Surface2
*SURFACE INTERACTION,NAME=Pair1
*FRICTION
0.07200
**
**
**============================================
**Material properties
**============================================
**
*Include, input=Material.inp
**
**
**============================================
**Boundary conditions
**============================================
**
*BOUNDARY
PoleNodes, 1, 2
EquatorialNodes, 3
```

```
XZeroNodes, 1
YZeroNodes, 2
**=========================================
**Loading conditions and record keeping
**=========================================
**
** STEP: Step-1
**
*STEP,NLGEOM,INC=500
*STATIC
0.2,1.0,,0.4
*DSLOAD
InternalSurface,P,0.002399801616400
**
** OUTPUT REQUESTS
**
*Restart, write, frequency=0
**
** FIELD OUTPUT: F-OUTPUT-1
**
*OUTPUT, FIELD, TIME INTERVAL=0.001, TIME MARKS=NO
*Element Output, directions=YES
S,
**
** FIELD OUTPUT: F-OUTPUT-2
**
*OUTPUT, FIELD, TIME INTERVAL=0.001, TIME MARKS=NO
*Node Output
U,
*OUTPUT,HISTORY,FREQUENCY=0
*END STEP
**
```

```
**=========================================
**
** STEP: Step-2
**
*Step, name=Step-2, nlgeom=YES, inc=1000000
*Dynamic, nohaf
0.0003,0.03,3e-10
** Interaction: fsi
*Co-simulation, name=fsi, program=MULTIPHYSICS
*Co-simulation Region, import, type=SURFACE
Cornea_sclera, CF
Cornea_sclera, LUMPEDMASS
*Co-simulation Region, export, type=SURFACE
Cornea_sclera, U
Cornea_sclera, V
**
** OUTPUT REQUESTS
**
*Restart, write, frequency=0
**
** FIELD OUTPUT: F-OUTPUT-3
**
*OUTPUT, FIELD, TIME INTERVAL=0.001, TIME MARKS=NO
*Element Output, directions=YES
S,
**
** FIELD OUTPUT: F-OUTPUT-4
**
*OUTPUT, FIELD, TIME INTERVAL=0.001, TIME MARKS=NO
*Node Output
U,
**
```

```
** HISTORY OUTPUT: H-Output-1
**
*OUTPUT,HISTORY,TIME INTERVAL=0.0001
*Node Output, nset=DEFORMATIONNODES
COOR1, COOR2, COOR3
*END STEP
```

A.2 Air puff model input file

```
*HEADING
Model of Air puff
Number of corneal rings = 15
Number of select sclera rings = 3
Number of Air layers = 20
Each Air layer gap = 0.55 mm
Total distance of Air model = 11 mm
**
**
*NODE,NSET=AllNodes,INPUT=FluidNode.inp
**
**
*NSET, NSET=PressureProfile
52021,52022,52024,52027,52031,52036,52042,52049,52057,52066,52076,52087
52099,52112,52126,52141,52157,52174,52192,52211,52231,52252,52274,52297
52321,52346,52372,52399,52427,52456,52486,52517,52549,52582,52616,52651
52687
**
*NSET, NSET=SYMMETRY1N
**List of nodes
**
```

```
*NSET, NSET=SYMMETRY2N
**List of nodes
**
**
*ELEMENT, ELSET=AllElements, TYPE=FC3D6, INPUT=FluidElement.inp
**
**
** Section: Air
*FLUID SECTION, TYPE=SINGLE FLUID, ELSET=AllElements
Air
**
*ELSET, ELSET=E_Cornea_Sclera
**List of elements
**
*SURFACE, TYPE=ELEMENT, NAME=Cornea_sclera
E_Cornea_Sclera, S1
**
*ELSET, ELSET=E_inlet
1,2,3,4,5,6,7,8,9,10,11,12
13,14,15,16
**
*SURFACE, TYPE=ELEMENT, NAME=inlet
E_inlet, S2
**
*ELSET, ELSET=E_outlet
**List of elements
**
*SURFACE, TYPE=ELEMENT, NAME=outlet
E_outlet, S5
**
*ELSET, ELSET=E_wall
**List of elements
```

```
**
*SURFACE, TYPE=ELEMENT, NAME=Wall
E_wall, S2
**
*ELSET, ELSET=E_SYMMETRY1
**List of elements
**
*SURFACE, TYPE=ELEMENT, NAME=SYMMETRY1
E_SYMMETRY1, S3
**
*ELSET, ELSET=E_SYMMETRY2
**List of elements
**
*SURFACE, TYPE=ELEMENT, NAME=SYMMETRY2
E_SYMMETRY2, S4
**
*ELSET, ELSET=PDF_WholeModel, ELSET=AllElements
**
**
*Amplitude, name=Amp-1
0, 0
1.000000e-03, 1.780930e-02
2.000000e-03, 3.561860e-02
3.000000e-03, 4.749147e-02
3.500000e-03, 7.123720e-02
5.000000e-03, 1.424744e-01
6.000000e-03, 2.255845e-01
6.500000e-03, 2.646774e-01
7.424000e-03, 3.990383e-01
8.579000e-03, 5.479442e-01
9.503000e-03, 6.518329e-01
1.019600e-02, 7.208617e-01
```

```
1.077350e-02, 7.725663e-01
1.146700e-02, 8.276657e-01
1.204400e-02, 8.676947e-01
1.250600e-02, 8.959385e-01
1.319900e-02, 9.319558e-01
1.366100e-02, 9.517350e-01
1.435400e-02, 9.750556e-01
1.481600e-02, 9.863704e-01
1.527800e-02, 9.942994e-01
1.574000e-02, 9.988426e-01
1.620200e-02, 1
1.678000e-02, 9.966803e-01
1.735700e-02, 9.880807e-01
1.770400e-02, 9.803659e-01
1.828100e-02, 9.633091e-01
1.874300e-02, 9.458446e-01
1.943600e-02, 9.132996e-01
1.989800e-02, 8.873706e-01
2.047600e-02, 8.501637e-01
2.105300e-02, 8.077354e-01
2.163000e-02, 7.600259e-01
2.232350e-02, 6.956954e-01
2.313000e-02, 6.112878e-01
2.417000e-02, 4.872112e-01
2.567300e-02, 2.775821e-01
2.610000e-02, 2.255845e-01
2.710000e-02, 1.424744e-01
2.860000e-02, 7.123720e-02
2.910000e-02, 4.749147e-02
3.010000e-02, 3.561860e-02
3.110000e-02, 1.780930e-02
3.210000e-02, 0
```

```
** Material
**
*Material, name=Air
*Density
1.2e-12
*Viscosity
1.83e-11
**
**
** PREDEFINED FIELDS
**
** Name: IC-2   Type: Fluid turbulence
*Initial Conditions, type=TURBNU, Element Average
PDF_WholeModel, 68
**
**
*Step, name=Step-1, nlgeom=NO
*CFD, incompressible navier stokes
0.01, 0.03, 0.25, 0.45, 1
1e-10, 0.5,  , 0.5, 0.5
*Momentum Equation Solver
50, 2, 1e-05
*Pressure Equation Solver
250, 2, 1e-05
ICC, 1, 1, CG
*Transport Equation Solver
50, 2, 1e-05
*Turbulence Model, type=SPALART ALLMARAS
0.1355, 0.622, 7.1, 5, 3.2391, 0.3, 2, 0.6667
0.41
0.8889
**
```

```
**
** BOUNDARY CONDITIONS
**
** Name: inlet Type: Fluid inlet/outlet
*Fluid Boundary, amplitude=Amp-1, type=Surface
inlet, VELX, 0
inlet, VELY, 0
inlet, VELZ, -167891
** Name: Symmetry1 Type: Fluid inlet/outlet
*Fluid Boundary, type=Surface
SYMMETRY1, VELX, 0
** Name: Symmetry2 Type: Fluid inlet/outlet
*Fluid Boundary, type=Surface
SYMMETRY2, VELY, 0
** Name: USymmetry1 Type: Displacement/Rotation
*Boundary
SYMMETRY1N, 1, 1
** Name: USymmetry2 Type: Displacement/Rotation
*Boundary
SYMMETRY2N, 2, 2
** Name: outlet Type: Fluid inlet/outlet
*Fluid Boundary, type=Surface
outlet, P, 0
** Name: wall Type: Fluid wall condition
*Fluid Boundary, type=Surface
wall, DIST, 0
*Fluid Boundary, type=Surface
wall, VELX, 0
wall, VELY, 0
wall, VELZ, 0
** Interaction: fsi
*Co-simulation, name=fsi, program=MULTIPHYSICS
```

```
*Co-simulation Region, import, type=SURFACE
Cornea_sclera, U
Cornea_sclera, V
*Co-simulation Region, export, type=SURFACE
Cornea_sclera, LUMPEDMASS
Cornea_sclera, TRSHR
**
**
*Restart, write, frequency=0
**
** FIELD OUTPUT: F-Output-1
**
*Output, field, time interval= 0.001
*Node Output
PRESSURE, U, V
*Output, history, time interval= 0.001
*Node Output, NSET=PressureProfile
COORD
*End Step
```

A.3 Co-simulation job submission batch file for HPC parallel computing

```
date_start=`date +%s`

echo ------------------------ O Maklad ----------------
echo ==========================================
echo 8 cpus on 1 nodes \( SMP=16 \)
echo Executable file: /lv1/data/abaqus/Commands/abaqus
```

```
. /usr/share/Modules/init/sh
module load intel
module unload gcc/4.4
module load abaqus
echo ----------------
cat ${PE_HOSTFILE} | cut -f 1 -d \. | sort | fmt -w 30
echo ================================================
echo Job output begins
echo ----------------
echo

#$ -N Co-execution-1
#$ -l h_rt=72:0:0
#$ -l h_vmem=4000M
#$ -pe smp 16
#$ -R y
#$ -l cputype=sandybridge
#$ -cwd -V -j y
#$ -l abaqus=1
#$ -o Co-execution-1.out
#$ -m bea
#$ -M osama@liv.ac.uk

echo Working directory is
pwd
echo Running on
hostname
MYWD=$PWD
cd $TMPDIR

# Copy common files
cp $MYWD/Co-execution-1.inp .
```

```
cp $MYWD/Co-execution-1-Air.inp .
cp $MYWD/Co-execution-1-Eye.inp .
cp $MYWD/Co-execution-1_config.xml .
cp $MYWD/FluidElement.inp .
cp $MYWD/FluidNode.inp .
cp $MYWD/Node.inp .
cp $MYWD/Element.inp .
cp $MYWD/Material.inp .

# Call Abaqus to run this setting
abaqus cosimulation cosimjob=Co-execution-1 job=Co-execution-1-Air,
Co-execution-1-Eye       mp_mode=mpi,mpi cpus=8,8 configure=Co-
execution-1_config interactive input=Co-execution-1-Air,
Co-execution-1-Eye
echo
echo ---------------
echo Job output ends
echo
ls -al
# Copy the results of the current setting back
cp *.msg $MYWD
cp *.sta $MYWD
cp *.txt $MYWD
cp *.dat $MYWD
cp *.log $MYWD
# odb file sometimes is not needed
cp *.odb $MYWD
# Finial record
cd $MYWD

date_end=`date +%s`
seconds=$((date_end-date_start))
```

```
minutes=$((seconds/60))
seconds=$((seconds-60*minutes))
hours=$((minutes/60))
minutes=$((minutes-60*hours))
echo ============================================================
echo SGE job: finished   date = `date`
echo Total run time : $hours Hours $minutes Minutes $seconds Seconds
echo ============================================================
```